UAB
Universitat Autònoma de Barcelona

Improvement and validation of a mechanistic physical model for the prediction of heat and mass transfer in higher plant growth in reduced gravity

Joanna KUŹMA

UNIVERSITÉ CLERMONT AUVERGNE

DOCTORAL SCHOOL OF ENGINEERING SCIENCES

UNIVERSITAT AUTÒNOMA DE BARCELONA

DOCTORAL PROGRAM IN BIOTECHNOLOGY

THESIS

presented by

Joanna KUŹMA

to obtain the degree of

DOCTOR OF PHILOSOPHY

Specialty: CHEMICAL ENGINEERING, BIOTECHNOLOGY

Improvement and validation of a mechanistic physical model for the prediction of heat and mass transfer in higher plant growth in reduced gravity

Publicly defended on 23rd of October 2025 in front of the jury:

Prof. Annalisa Molini	Reviewer
Dr. Stanislaus Schymanski	Reviewer
Prof. Céline Laroche	Examinator
Dr. Alexis Paillet	Examinator
Dr. Christophe Lasseur	Invited member
Prof. Claude-Gilles Dussap	Co-director
Prof. Jean-Pierre Fontaine	Co-director
Prof. Francesc Godia	Co-director
Dr. Lucie Poulet	Co-supervisor

UNIVERSITÉ CLERMONT AUVERGNE

ÉCOLE DOCTORALE SCIENCES POUR L'INGÉNIEUR

UNIVERSITAT AUTÒNOMA DE BARCELONA

PROGRAMA DE DOCTORAT EN BIOTECNOLOGIA

THÈSE

présentée par

Joanna KUŹMA

pour obtenir le grade de

DOCTEUR D'UNIVERSITÉ

Spécialité: GÉNIE DES PROCÉDÉS, BIOTECHNOLOGIE

Amélioration et validation d'un modèle physique mécaniste pour la prédiction des transferts de chaleur et de masse lors de la croissance des plantes supérieures en gravité réduite

Soutenue publiquement le 23 octobre 2025 devant le jury :

Prof. Annalisa Molini	Rapporteur
Dr. Stanislaus Schymanski	Rapporteur
Prof. Céline Laroche	Examinateur
Dr. Alexis Paillet	Examinateur
Dr. Christophe Lasseur	Invité
Prof. Claude-Gilles Dussap	Directeur de thèse
Prof. Jean-Pierre Fontaine	Directeur de thèse
Prof. Francesc Godia	Directeur de thèse
Dr. Lucie Poulet	Co-encadrante

Dr. Claude-Gilles Dussap, professor of the team *Génie des Procédés, Energétique and Biosystèmes* at *Université Clermont Auvergne* (UCA), Dr. Jean-Pierre Fontaine, full professor of the team *Génie des Procédés, Energétique and Biosystèmes* at *Université Clermont Auvergne* (UCA), Dr. Lucie Poulet Researcher in Bioastronautics & Life-Support Processes at *Institut Pascal* at *Université Clermont Auvergne*, and Dr. Francesc Gòdia, full professor at the *Departament d'Enginyeria Química, Biològica i Ambiental* of *Universitat Autònoma de Barcelona* (UAB) certify that:

Joanna Kuzma, BSc. in Chemical and Process Engineering by Wroclaw University of Science and Technology, has conducted with our direction in the group of *Génie des Procédés, Energétique and Biosystèmes* of UCA, with a Research stay in the *Departament d'Enginyeria Química, Biològica i Ambiental* of UAB, the PhD thesis titled "Improvement and validation of a mechanistic physical model for the prediction of heat and mass transfer in higher plant growth in reduced gravity". This PhD thesis has received funding from the MELiSSA Foundation within the framework of the *Pool of MELiSSA PhDs* (POMP) program and CNES PhD Program. The document presented constitutes the manuscript to achieve the degree of Doctor in Chemical Engineering by UCA and Doctor in Biotechnology by UAB.

And for it to be acknowledged and duly recorded for the appropriate purposes, we hereby sign this certificate:

Joanna Kuzma	Claude-Gilles Dussap	Jean-Pierre Fontaine	Lucie Poulet	Francesc Gòdia Casablancas
(author)	(co-director)	(co-director)	(co-supervisor)	(co-director)

Acknowledgments

First of all, I would like to thank my supervisors on the UCA side.

Prof. Claude-Gilles Dussap and Prof. Jean-Pierre Fontaine. Thank you for all the support I received from you, for the many scientific and technical discussions, and for all the advice you gave me. I really admire your scientific curiosity. I am also grateful for the financial support that allowed me to build the experiment, participate in two parabolic flight campaigns, attend several conferences, and conduct the ground reference experiment at UAB.

I would also like to thank Lucie Poulet, my co-supervisor, who guided me throughout the entire thesis, offering advice and helping me overcome every obstacle, whether technical, knowledge-based, or linguistic. It was a great pleasure to work under your guidance and supervision.

My thanks also go to my UAB-side supervisor, Prof. Francesc Gòdia Casablancas, for his guidance and support, for the incredible opportunity to work at the MELiSSA Pilot Plant, and for the suggestions that helped improve this work.

I am sincerely grateful to the entire MELiSSA Pilot Plant team for the help and support I received during my stay in Barcelona.

I would like to thank my CNES-side supervisor, Alexis Paillet, for the opportunity to be a CNES PhD student and for welcoming me into the program.

I also extend my thanks to the rest of the committee for participating in my defence and for the thoughtful questions and feedback you provided.

A special thanks goes to the two amazing interns I had the pleasure of working with - Célia and Noé. Thank you both for your help and expertise in building the experimental setup. The success of the experiment owes a great deal to your contributions. Thank you also for being such a fantastic team during both parabolic flight campaigns.

I also wish to thank David and Frédéric for their invaluable help in constructing the experiment, for your advice, and for dealing with every unexpected problem. This experiment would not have been possible without you.

I would like to thank CNES for approving our proposal twice and giving us the opportunity to take part in the 65th and 66th CNES Parabolic Flight Campaigns, as well as Novespace for organizing them. Special thanks to Thomas Villatte for coordinating our team during the campaigns.

Another person I would like to thank is Stanislaus Schymanski - thank you for your help with the development of the leaf replica, for sharing the recipe to create it, and for all the advice you provided throughout the experiment's development.

Special thanks also go to Christophe Lasseur, who welcomed me into the MELiSSA project six years ago, and without whom none of this would have happened.

I would also like to thank all the PhD students, interns, and young researchers at Institut Pascal for the great times we shared and the many interesting conversations. In particular, I would like to thank Ana, Martin, and Matheus for all the moments we spent together, whether on the climbing wall or around the table playing board games. You have made my stay in Clermont-Ferrand special.

Ogromne podziękowania dla Ani J, bez której spejsy nie byłyby nawet w połowie tak ciekawe – za wszystkie wspólne projekty, rozkminki oraz rozmowy, bez których nie miałabym odwagi pójść w tym kierunku.

Moim rodzicom oraz siostrom - za całe wsparcie, które od Was dostawałam przy wdrażaniu kolejnych pomysłów w życie i w ogóle za to, że jesteście, a także Filipowi, za czytanie, poprawianie pracy i całą pomoc którą od Ciebie dostałam w trakcie pisania pracy.

Wielkie podziękowania dla zespołów, których byłam częścią na Politechnice Wrocławskiej - FREDE, Scorpio oraz Space is More z którymi to wszystko się zaczęło i dzięki którym pomysł badania roślin w kosmosie w ogóle zaistniał.

Last but not least, I would like to thank CNES and the MELiSSA Foundation for funding this PhD, without which none of this would have been possible.

Table of Contents

Abbreviations

ALS	–	Advanced Life-Support
BL	–	Boundary Layer
BLSS	–	Bioregenerative Life-Support System
CEEF	–	Closed Ecology Experiment Facility
CELSS	–	Controlled Ecological Life-Support System
CM	–	Command Module
CNES	–	Centre national d'études spatiales
CNSA	–	China National Space Administration
CPU	–	Central Processing Unit
DAQ HAT	–	Data Acquisition Hardware Attached on Top
ECLSS	–	Environmental Control and Life-Support System
ECS	–	Environmental Control System
ESA	–	European Space Agency
GUI	–	Graphical User Interface
HPC	–	Higher Plants Chamber
IR	–	Infra-Red
ISS	–	International Space Station
LED	–	Light-Emitting Diode
LEO	–	Low Earth Orbit
LM	–	Lunar Module
LSS	–	Life-Support System
MSR	–	Multi Sensor Rack

NASA	–	National Aeronautics and Space Administration
NTP	–	Network Time Protocol
RH	–	Relative Humidity
SEM	–	Scanning Electron Microscope
SM	–	Service module
T	–	Temperature
RH	–	Relative Humidity

List of Figures

List of Tables

Abstract

Long-duration crewed space missions like those to the Moon, Mars, will demand reliable and self-sufficient closed-loop life-support systems to sustain crews for months or years with very limited resupply. In this context, bioregenerative life-support systems will become crucial. Those systems will incorporate higher plants to regenerate oxygen via photosynthesis, remove carbon dioxide, and recycle water through transpiration - plants are irrigated with treated wastewater that serves as a nutrient solution. They then transpire nearly all of the absorbed water (ca. 95%) as high-purity vapour via stomata, which can be condensed and recovered as clean, reusable water. However, currently existing plant growth models do not incorporate space-specific conditions such as microgravity, radiation exposure, and altered atmospheric parameters, resulting in a limited capability to predict plant behaviour and system performance in extra-terrestrial habitats.

This research addresses that gap by isolating and examining fundamental heat and mass transfer processes in plant–environment interactions using a leaf replica under controlled conditions. Using the leaf replica enables decoupling of purely physical phenomena from complex biological effects, allowing precise study of how gravity affects convective heat transfer and mass transfer. Experiments are conducted in both normal gravity on Earth and microgravity environments, achieved via parabolic flight campaigns, using an experimental platform that was designed and built as a part of this PhD. The platform consists of four units in which the leaf replica is subjected to controlled airflow and its position against the airflow can be adjusted. Key parameters monitored include airflow velocity, leaf orientation, gravitational acceleration, pressure, temperature, and relative humidity inside the units, and leaf replica surface temperature.

Data collected during these experiments enabled the identification of heat and mass transfer coefficients under both steady-state and transient conditions. Statistical analyses show significant effects of gravity, airflow, and orientation on surface temperature and mass transfer of the replica. The modelling work led to the development and validation of mechanistic models for convective heat and mass transfer that take into account natural and forced convection, boundary layer behaviour, and internal diffusion limitations (via porous of the leaf replica). The results confirm the role of gravity and air velocity in modulating heat and mass

transfer, and show the dominant contribution of the upper surface in heat loss. The model and data provide a physically grounded tool for analysing plant-environment interactions in altered gravity, with potential application in future space experiment.

All of the data collected in described experiments can be found on the following page: https://recherche.data.gouv.fr/fr, in the HAMSTER catalogue of Université Clermont-Auvergne. - https://entrepot.recherche.data.gouv.fr/dataverse/uca_ip_hamster

Résumé

Les missions spatiales habitées de longue durée, comme celles vers la Lune et Mars, nécessiteront des systèmes de survie en circuit fermé fiables et autonomes, capables de soutenir les équipages pendant des mois, voire des années, avec un ravitaillement très limité. Dans ce contexte, les systèmes de support vie biorégénératifs deviennent essentiels, avec la possibilité d'intégrer des plantes supérieures pour régénérer l'oxygène par photosynthèse, éliminer le dioxyde de carbone et recycler l'eau par transpiration. Cependant, les modèles de croissance végétale existants ne prennent pas en compte les conditions spécifiques à l'espace, telles que la microgravité, l'exposition aux radiations et les modifications des paramètres atmosphériques, ce qui limite la capacité à prédire le comportement des plantes et les performances des systèmes dans les habitats extraterrestres.

Cette recherche comble cette lacune en isolant et en examinant les processus fondamentaux de transfert de chaleur et de masse dans les interactions plante-environnement à l'aide d'une réplique de feuille dans des conditions contrôlées. L'utilisation de cette réplique de feuille permet de dissocier les phénomènes purement physiques des effets biologiques complexes, permettant ainsi d'étudier avec précision l'impact de la gravité sur le transfert de chaleur et de masse par convection. Les expériences sont menées en conditions de gravité normale sur Terre et de microgravité, grâce à des campagnes de vols paraboliques, à l'aide d'une plateforme expérimentale conçue et construite dans le cadre de cette thèse. Cette plateforme se compose de quatre unités dans lesquelles la réplique de feuille est soumise à un flux d'air contrôlé et sa position par rapport au flux d'air peut être ajustée. Les principaux paramètres surveillés comprennent la vitesse de d'air, l'orientation de la feuille, la gravité, la pression, la température et l'humidité relative à l'intérieur des unités, ainsi que la température de surface de la réplique de feuille.

Les données recueillies lors de ces expériences ont permis d'identifier les coefficients de transfert de chaleur et de masse en régime permanent et transitoire. Les analyses statistiques montrent des effets significatifs de la gravité, du flux d'air et de l'orientation sur la température de surface et le transfert de masse de la réplique. Les travaux de modélisation ont conduit au développement et à la validation de modèles mécanistes pour le transfert de chaleur et de masse par convection, prenant en compte la convection naturelle et forcée, le comportement

de la couche limite et les limitations de la diffusion interne. Les résultats confirment le rôle de la gravité et de la vitesse de l'air dans la modulation du transfert de chaleur et de masse, et montrent la contribution dominante de la surface supérieure aux pertes de chaleur. Le modèle et les données fournissent un outil physiquement fondé pour analyser les interactions plante-environnement dans une gravité altérée, avec une application potentielle dans de futures expériences spatiales.

Resumen

Las misiones espaciales tripuladas de larga duración, como las que se dirigen a la Luna o a Marte, requerirán sistemas de soporte vital en bucle cerrado, fiables y autosuficientes, capaces de sostener a las tripulaciones durante meses o años con un reabastecimiento muy limitado. En este contexto, los sistemas de soporte vital biorregenerativos se volverán cruciales. Estos sistemas incorporarán plantas superiores para regenerar oxígeno mediante la fotosíntesis, eliminar dióxido de carbono y reciclar agua a través de la transpiración. Sin embargo, los modelos actuales de crecimiento vegetal no incorporan condiciones específicas del espacio, como la microgravedad, la exposición a la radiación y parámetros atmosféricos alterados, lo que limita su capacidad para predecir el comportamiento de las plantas y el rendimiento del sistema en hábitats extraterrestres.

Esta investigación aborda esa brecha aislando y examinando los procesos fundamentales de transferencia de calor y masa en las interacciones planta–entorno, utilizando una réplica de hoja en condiciones controladas. El uso de la réplica permite desacoplar fenómenos puramente físicos de los efectos biológicos complejos, lo que permite un estudio preciso de cómo la gravedad afecta la transferencia convectiva de calor y masa. Los experimentos se llevan a cabo tanto en gravedad normal en la Tierra como en entornos de microgravedad, alcanzados mediante campañas de vuelos parabólicos, utilizando una plataforma experimental que fue diseñada y construida como parte de esta tesis doctoral. La plataforma consta de cuatro unidades en las que la réplica de hoja se somete a un flujo de aire controlado, y su posición respecto a dicho flujo puede ajustarse. Los parámetros clave monitorizados incluyen la velocidad del flujo de aire, la orientación de la hoja, la aceleración gravitacional, la presión, la temperatura, la humedad relativa dentro de las unidades y la temperatura de la superficie de la réplica.

Los datos recogidos durante estos experimentos permitieron identificar coeficientes de transferencia de calor y masa tanto en condiciones estacionarias como transitorias. Los análisis estadísticos muestran efectos significativos de la gravedad, el flujo de aire y la orientación sobre la temperatura superficial y la transferencia de masa de la réplica. El trabajo de modelado condujo al desarrollo y validación de modelos mecanicistas de transferencia convectiva de calor y masa que tienen en cuenta la convección natural y forzada, el

comportamiento de la capa límite y las limitaciones de difusión interna. Los resultados confirman el papel de la gravedad y la velocidad del aire en la modulación de la transferencia de calor y masa, y muestran la contribución dominante de la superficie superior en la pérdida de calor. El modelo y los datos proporcionan una herramienta basada en principios físicos para analizar las interacciones planta–entorno en condiciones de gravedad alterada, con potencial aplicación en futuros experimentos espaciales.

Resum

Les missions espacials tripulades de llarga durada, com les destinades a la Lluna o a Mart, requeriran sistemes de suport vital en bucle tancat, fiables i autosuficients, capaços de mantenir les tripulacions durant mesos o anys amb un subministrament molt limitat. En aquest context, els sistemes de suport vital biorregeneratius esdevindran crucials. Aquests sistemes incorporaran plantes superiors per regenerar oxigen mitjançant la fotosíntesi, eliminar diòxid de carboni i reciclar aigua a través de la transpiració. Tanmateix, els models actuals de creixement vegetal no incorporen condicions específiques de l'espai, com la microgravetat, l'exposició a la radiació i els paràmetres atmosfèrics alterats, la qual cosa limita la capacitat de predir el comportament de les plantes i el rendiment del sistema en hàbitats extraterrestres.

Aquesta recerca aborda aquesta mancança aïllant i examinant els processos fonamentals de transferència de calor i massa en les interaccions planta–entorn, utilitzant una rèplica de fulla en condicions controlades. L'ús de la rèplica permet desacoblar fenòmens purament físics dels efectes biològics complexos, permetent un estudi precís de com la gravetat afecta la transferència convectiva de calor i massa. Els experiments es duen a terme tant en gravetat normal a la Terra com en entorns de microgravetat, assolits mitjançant campanyes de vols parabòlics, utilitzant una plataforma experimental dissenyada i construïda com a part d'aquesta tesi doctoral. La plataforma consta de quatre unitats en les quals la rèplica de la fulla es sotmet a un flux d'aire controlat, i la seva posició respecte al flux es pot ajustar. Els paràmetres clau que es monitoritzen inclouen la velocitat del flux d'aire, l'orientació de la fulla, l'acceleració gravitacional, la pressió, la temperatura, la humitat relativa dins les unitats i la temperatura superficial de la rèplica.

Les dades recollides durant aquests experiments van permetre identificar coeficients de transferència de calor i massa tant en condicions estacionàries com transitòries. Les anàlisis estadístiques mostren efectes significatius de la gravetat, el flux d'aire i l'orientació sobre la temperatura superficial i la transferència de massa de la rèplica. El treball de modelatge va conduir al desenvolupament i validació de models mecanicistes de transferència convectiva de calor i massa que tenen en compte la convecció natural i forçada, el comportament de la capa límit i les limitacions de difusió interna. Els resultats confirmen el paper de la gravetat i la velocitat de l'aire en la modulació de la transferència de calor i massa, i mostren la contribució

dominant de la superfície superior en la pèrdua de calor. El model i les dades proporcionen una eina basada en principis físics per analitzar les interaccions planta–entorn en condicions de gravetat alterada, amb una possible aplicació en futurs experiments espacials.

Résumé étendu en Français

Le développement des systèmes de support vie biorégénératifs est essentiel pour les missions spatiales habitées de longue durée. De ce fait, les systèmes de support vie doivent être plus efficaces, plus fiables et plus optimaux d'un point de vue de la masse embarquée. Cela peut être réalisé en minimisant l'utilisation des ressources, la taille et les besoins énergétiques, tout en préservant la sécurité. Pour permettre une présence humaine durable dans l'espace, il est donc nécessaire de développer un système de support vie biorégénératif performant intégrant les plantes supérieures. Les plantes produisent de l'oxygène, éliminent le dioxyde de carbone, purifient l'eau et contribuent à la production alimentaire, autant de fonctions que les systèmes physico-chimiques seuls ne peuvent pleinement assurer. Cependant, l'un des principaux défis technologiques au développement de ces systèmes est de comprendre les processus de transfert de chaleur et de masse qui régissent les interactions plante-environnement dans des conditions gravitationnelles différentes de celles de la Terre.

Ce travail de thèse, co-financé par le Centre National d'Études Spatiales (CNES - France) et par l'Agence Spatiale Européenne (ESA – Europe), s'est inscrit dans ce cadre. Des objectifs fondamentaux ont été définis, à savoir la compréhension des mécanismes d'échange de chaleur et de matière dans l'environnement d'un couvert végétal, plus particulièrement d'une feuille de plante supérieure et plus exactement encore dans l'environnement d'une feuille artificielle aux propriétés bien définies et fixées. La raison est simple : comme il s'agit de comprendre les phénomènes avec une vision mécanistique et dans des conditions non classiques (gravité réduite ou nulle), il est nécessaire d'aller à la racine des phénomènes en développant les approches physiques. Plus spécifiquement, les travaux réalisés dans le cadre de ce travail de thèse ont visé les objectifs suivants :

1. Concevoir et mettre en œuvre un dispositif expérimental pour étudier les processus de transfert de chaleur et de masse entre une réplique de feuille et son environnement dans des conditions gravitationnelles variables.
2. Valider les performances du système expérimental par des expériences de référence au sol.

3. Quantifier les effets des paramètres environnementaux qui pouvaient être manipulés, à savoir la vitesse du flux d'air autour de la feuille, et l'angle d'inclinaison de la feuille par rapport au flux d'air et à la verticale et des conditions gravitationnelles sur la température de surface et le transfert de masse des répliques de feuilles.
4. Étudier les différences de températures entre des surfaces évaporatives et non évaporatives dans des conditions expérimentales contrôlées.
5. Apporter un éclairage sur la dynamique des échanges thermiques et massiques qui régissent la réponse des plantes en microgravité, contribuant ainsi à la conception de systèmes BLSS performants pour les missions spatiales dans des conditions de vols paraboliques qui permettent d'avoir une vingtaine de secondes en gravité nulle.
6. Développer une approche physique complète pour la modélisation des transferts de chaleur et de masse en gravité non standard et évaluer l'impact de la gravité sur la résistance stomatique.

Les travaux de recherche présentés ici contribuent à la compréhension des processus de transfert de chaleur et de masse en microgravité. Cette étude s'inscrit dans les domaines suivants :

- La caractérisation des processus de transfert de chaleur et de masse en microgravité, pour différentes valeurs de convection forcée et différentes inclinaisons de la réplique foliaire.
- Le découplage des processus physiques et biologiques impliqués dans les échanges gazeux des plantes. L'utilisation de répliques foliaires permet d'étudier les mécanismes physiques qui conduisent à la régulation thermique et l'utilisation de l'eau par les plantes sans introduire de variabilité biologique.

En modélisant les transferts de chaleur et de masse avec des conditions de gravité modifiées et en caractérisant la conductance stomatique, plus exactement la conductance des pores artificielles, en relation avec le transfert d'énergie par évaporation de l'eau dans des configurations contrôlées, l'étude permet une extrapolation aux systèmes végétaux réels, rendant les résultats applicables non seulement aux environnements spatiaux, mais aussi à l'agriculture terrestre en conditions contrôlées. Cette étude pose les bases du développement de systèmes agricoles durables dans l'espace et contribue à des applications plus larges en

contrôle et ingénierie environnementaux. Outre une introduction générale et un rappel des objectifs de l'étude, cette étude est divisée en cinq chapitres principaux.

Chapitre 3 : État de l'art

La première partie de ce chapitre analyse les méthodologies de modélisation végétale et leur importance pour les systèmes de support vie dans les applications spatiales. Elle analyse différents modèles végétaux – empiriques, basés sur les processus et fonctionnels-structurels – et évalue leurs capacités à simuler la croissance végétale, les échanges gazeux et la production de biomasse. Ce chapitre se concentre sur leurs limites pour prédire la réponse des plantes en microgravité et plus généralement dans des conditions non terrestres. Il montre également les étapes nécessaires pour simuler et optimiser avec précision les systèmes de survie régénératifs à base de plantes pour les prochaines missions spatiales. Ce chapitre souligne la nécessité de prendre en compte la gravité, le rayonnement et les variations des conditions atmosphériques.

La deuxième partie de ce chapitre décrit les processus physiques et biologiques régissant les échanges de chaleur et de masse chez les plantes, en se concentrant plus particulièrement sur les applications en environnement spatial. Cette partie aborde la dépendance entre la transpiration, le rayonnement, la convection et le bilan énergétique dans les interactions plante-environnement. Elle montre également les avantages de l'utilisation de répliques de feuilles pour découpler les processus biologiques et physiques chez les plantes, ce qui permet des études plus précises. Ce chapitre examine également l'impact de la microgravité sur les mécanismes de transfert de chaleur et de masse, et comment la modélisation de ces processus contribuera à la conception de systèmes de production végétale efficaces pour les missions spatiales de longue durée.

Chapitre 4 : Conception, développement et protocoles expérimentaux du système de test de répliques de feuilles

Ce chapitre décrit le dispositif expérimental, le matériel et les méthodologies utilisés pour étudier le transfert de chaleur et de masse dans différentes conditions de gravité. Il décrit la conception et les composants des unités expérimentales, notamment les systèmes mécaniques, électriques et logiciels, ainsi que les différences de configuration entre la

première et la deuxième campagne de vols paraboliques, ainsi que l'expérience de référence au sol. Ce chapitre présente également le protocole de collecte des données et la méthode d'analyse de ces données. Enfin, il décrit les analyses statistiques utilisées pour évaluer les données.

Chapitre 5 : Résultats expérimentaux et analyse statistique des expériences au sol et des conditions de vol parabolique

Ce chapitre présente l'analyse des données expérimentales recueillies lors de l'expérience de référence au sol et des campagnes de vols paraboliques. Il décrit les conditions environnementales à l'intérieur des unités expérimentales pendant les essais et analyse les tendances générales pour tous les cas étudiés pour les répliques de feuilles évaporatives et non évaporatives. De plus, des méthodes statistiques, notamment l'ANOVA et des tests de normalité, ont été utilisées pour évaluer l'importance de facteurs tels que l'orientation de la réplique de feuille, la vitesse d'écoulement de l'air, la température globale, l'humidité et l'accélération gravitationnelle. Les résultats sont comparés entre les unités, les campagnes de vol et les conditions testées.

Chapitre 6 : Interprétation et modélisation des résultats expérimentaux

Ce chapitre introduit une approche de modélisation mécaniste pour décrire les phénomènes de transfert de chaleur et de masse observés lors des expériences. Il commence par un aperçu global des objectifs de modélisation et de la sélection d'ensembles de données représentatifs. Un modèle stationnaire est développé pour estimer les distributions de température au sein de la réplique de feuille, et les coefficients de transfert de chaleur sont identifiés par comparaison avec les données expérimentales. Une description détaillée des modèles de couches limites est réalisée, ce qui permet de continuer à voir des modèles agrégés simples de caractérisation des transferts de chaleur et de matière. Un point important concerne la caractérisation et la modélisation de la conductance des pores de la réplique de feuille, qui est l’équivalent biologique étant la conductance stomatique chez les plantes supérieures. Un modèle qui prend en compte les forces de tension superficielle est proposé. Ce modèle représente de façon très satisfaisante les résultats expérimentaux obtenus dans le cadre de

cette étude. Le cadre de modélisation est ensuite étendu aux conditions transitoires, intégrant les effets des régimes de convection et du développement de la couche limite sous différentes conditions gravitationnelles en vols paraboliques. Un modèle prédictif des coefficients de transfert de chaleur est proposé et validé. Parallèlement, un modèle de transfert de masse est établi, incluant les effets de résistance interne et de capillarité. Les prédictions du modèle sont comparées aux résultats expérimentaux.

Chapitre 7 : Conclusions

Les principaux résultats de l'étude sont passés en revue dans un dernier chapitre. Les résultats obtenus sont comparés à certaines données disponibles dans la littérature. Il est démontré que les principales tendances sont similaires à celles obtenues précédemment, tant sur des répliques de feuilles artificielles que sur des plantes supérieures. Ces tendances sont cohérentes avec les prédictions du modèle développé. Une analyse critique du dispositif expérimental utilisé est ensuite réalisée, envisageant les possibilités d'améliorations futures concernant les expériences en conditions terrestres et en vol parabolique. Les perspectives d'amélioration du modèle de transfert de chaleur et de matière et la compréhension de la conductance des répliques de feuilles sont décrites. Le manuscrit se termine par une conclusion générale ouvrant les perspectives d'extension et d'application de ces travaux, tant sur la compréhension des mécanismes d'échange de masse et de chaleur entre une feuille et son environnement terrestre que sur les capacités de prédiction en conditions de gravité non terrestre pour le développement, la conception et le contrôle du pilotage de serres dans des conditions de bases extraterrestres.

L'ensemble de ce travail a conduit à la publication de deux articles parus dans des revues à comité de lecture. Ces articles servent de support au déroulé du premier chapitre sur l'état de l'art.

En outre, ce travail a permis de présenter 5 communications dans des congrès internationaux. 1 communication est en cours d'expertise.

Les références de ces travaux publiés sont fournies en Appendix F.

1. Introduction

1.1 History of Human Space Exploration

Humans have always looked up into the night sky and dreamed about the cosmos. The History of space exploration started not in high-tech modern laboratories, but in the minds of individuals who, with their naked eyes, stared into the sky and contemplated the mysteries beyond.

Long before the era of advanced telescopes and spacecraft, ancient civilizations such as the Babylonians, the Egyptians or the Greeks started to study the sky and observe the movements of celestial bodies. Their motivations varied between religious beliefs and agricultural concerns since, among other things, they were trying to understand the movement of planets and stars to predict season changes and the future (DeYoung, 2000; Hannah, 2015; Steele, 2015).

Hundreds of years later, during the Renaissance, Nicolaus Copernicus and Johannes Kepler questioned the geocentric model, proposing a heliocentric system that placed the Sun at the centre (Gingerich, 1974). Later on Galileo Galilei, with his first telescopes, made ground-breaking observations of the Moon, Jupiter's moons, and the phases of Venus which were indisputable proof for the heliocentric theory and these completely changed our understanding of the universe (Brown, 1985).

In the mid-20th century, humans' space fascination changed from theoretical consideration to actual exploration. The Cold War competition between the United States and the Soviet Union powered the Space Race. In 1957, the Soviet Union launched Sputnik 1, the first artificial satellite into orbit, thus marking the beginning of the space age (McDougall, 1985).

In the 1960s a series of milestones were achieved when space exploration advanced in both robotic and human missions. At that time Yuri Gagarin became the first human in space in 1961, and eight years later, Neil Armstrong and Buzz Aldrin set foot on the lunar surface during the National Aeronautics and Space Administration (NASA) Apollo 11 mission, achieving the historic feat of a crewed Moon landing (Crouch, 2002).

Introduction

At the end of the 20th century, human space exploration entered a new era characterized by international collaborations. First of all, the International Space Station (ISS) became a symbol of peaceful cooperation between former rivals (Jenks, 2022), and second, the Space Shuttle enabled easy access to low-Earth orbit. As the initial excitement of reaching the Moon faded, public interest in human space exploration decreased, and funding for space missions became limited (Neufeld, 2023). Reduced funding made it challenging to undertake ambitious and costly missions, and as a consequence, human space exploration has slowed down, being now mainly limited to missions to the ISS.

At the beginning of the 21st century, human space exploration is characterized by a global collaboration of both governmental and private space entities. The big goals of this shared vision are the Lunar Gateway station, a Moon base, and eventually, human missions to Mars which have been highlighted in the European Space Agency (ESA) and NASA's roadmaps (ESA, 2022; Smith et al., 2020). NASA has outlined its roadmap through the Artemis program and the ESA's strategy follows the same pattern. This initiative focuses on lunar missions as a mid-step for future human space exploration of Mars (Smith et al., 2020). Following the successful uncrewed Artemis I mission, Artemis II, a lunar flyby mission, is in preparation with a launch scheduled for 2026. This mission will orbit the Moon, testing spacecraft capabilities and ensuring the safety of human spaceflight on their mission to the Moon (Creech et al., 2022). The goal of Artemis III is to land humans on the lunar surface. This will lay the foundation for future missions to Mars (Smith et al., 2020).

In the meantime, China has emerged as a major player in human space exploration, with significant advancements in lunar and Martian missions. After the success of the Chang'e lunar missions (Wang et al., 2024), China aims to send astronauts to the Moon. Specific timelines for crewed lunar landings have not been revealed, however, the China National Space Administration (CNSA) has outlined plans for advancing lunar exploration (Xu et al., 2018). Additionally, their potential road to human space exploration of Mars has been marked by a soft landing during the Tianwen-1 mission (Zou et al., 2021) and the successful deployment of the Zhurong rover on the Martian surface (Tian et al., 2021).

With all these plans, space exploration is entering a new era with many new challenges that will have to be overcome. Going beyond LEO will demand a deep fusion of knowledge and advancement in various fields. Among others, it requires advancements in propulsion systems,

rocketry, landing methods, and innovative architectural designs suitable for extra-terrestrial living coupled with the development of a safe and reliable Environmental Control and Life-Support System (ECLSS).

1.2 Environmental Control and Life-Support System

ECLSS is a comprehensive system that provides life support essentials (oxygen, water, waste management) while controlling the overall habitat environment. Essential ECLSS functions encompass:

- control and supply of the atmosphere,
- atmosphere revitalization,
- regulation of temperature and relative humidity,
- water recovery and management,
- waste management,
- detection and suppression of fires.

Additional components that might be included in an ECLSS setup are facilities for food storage and preparation, plant cultivation areas, protection against radiation, removal of external dust, storage that is temperature-controlled, and facilities such as airlocks (NASA, 2018, p. 5).

Life-support systems (LSS) depending on the flow of resources, can be divided into open-loop and closed-loop systems. An open-loop LSS delivers all required supplies, such as water, oxygen, and food, from storage or resupply, and stores waste materials for disposal or return to the Earth. In an open-loop system, the quantity of required resource is proportional to the mission duration and crew size. Closed-loop LSSs require an initial supply of resources, and then convert waste products such as carbon dioxide, urine and wastewater to restore useful resources such as oxygen or water, thus lowering reliance on resupply. Closed-loop systems offer a significant benefit through a singular mass transport operation to carry hardware and initial resources into the orbit, followed by minimal subsequent resupply for non-recoverable losses and expendables (Eckart, 1996a).

Technologies for closed-loop systems, utilize either physicochemical or biological methods, or a combination of both, known as a hybrid LSS. Physicochemical methods involve the use of

fans, filters, and techniques for physical or chemical separation and concentration. Biological or bioregenerative methods use living organisms, such as plants or microorganisms, to create or decompose organic compounds. Traditionally, LSSs have relied on physicochemical processes because they are compact, require low maintenance, and respond quickly. However, these processes are energy-intensive, and they cannot regenerate food supplies, necessitating regular resupply. In contrast, biological processes, while requiring more space, power, and maintenance, as well as having slower response times, offer the possibility to produce food and deal with organic wastes (NASA, 2018). The main challenge with biological systems is not the biology itself, but the engineering required to support and optimize these systems in closed-loop environments.

According to the Life Support Baseline Values and Assumptions Document of NASA (Ewert et al., 2022) each mission longer than 10 months should produce at least 15% of the food on -board and should be equipped with a biological oxygen production unit. The general tendency for choosing a proper life-support system according to the mission duration can be seen in Figure 1-1.

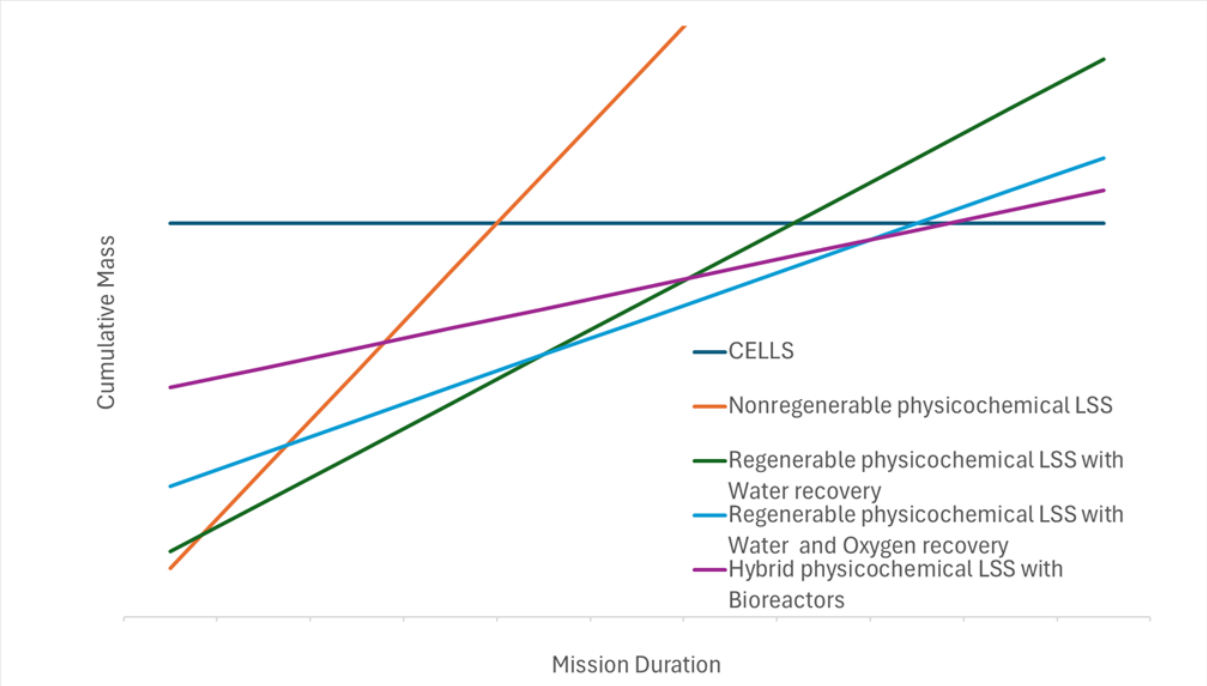

Figure 1-1 *Schematic diagram representing the dependence of LSS mass on time for different types of system types. Graph reproduced from (NASA, 1994)*

For missions lasting years, achieving maximum closure of mass loops becomes crucial, making the recycling of solid waste and the cultivation of food using organic waste a must. Because of that, plants will play a big role in the ECLS systems of future habitats on the Moon, the Mars, and beyond, potentially leading to systems that mirror the complexity of Earth's biosphere.

1.2.1 The evolution of Life-Support Systems for space applications

The design of Environmental Control and Life-Support Systems (ECLSS) is determined by the mission scenario meaning that the LSS had to evolve with an increase in mission duration and complexity.

1.2.1.1 Early Missions and Basic LSS (Vostok and Mercury)

In an early phase of human space exploration, when missions were rather short, LSSs were focused on providing oxygen and maintaining safe atmosphere, with minimal attention to problems like water production, storage, or waste management. However, as missions extended, the LSS had to evolve and incorporate more advanced technologies for air revitalization, water production, waste handling, and food storage.

1.2.1.1.1 Vostok Program (1961–1963)

The Vostok program was the Soviet Union’s first crewed spaceflight program, which launched the first human, Yuri Gagarin, into space in 1961. This series of six missions focused on short-duration flights to test capabilities in space.

To produce oxygen, non-regenerative chemical cartridges of potassium dioxide (KO_2) were used. KO_2 was reacted with water to produce O_2 and potassium hydroxide (KOH). Later on, CO_2 was removed through a reaction with KOH in oxygen regenerator (Eckart, 1996a, p. 135). There was an on-board monitoring of O_2 and CO_2 concentration (NASA, 2018, p. 286). To remove respiratory contaminants, activated charcoal filters were used. Temperature and relative humidity were automatically controlled via a heat exchanger (Stoiko, 1971, p. 177). Silica gel and drying agent impregnated with lithium chloride and activated carbon were used to control relative humidity (Daues, 2006). Water was sterilized before the mission and stored in tanks

with no recycling (NASA, 2018, p. 286). Urine and faeces were only collected and stored (Eckart, 1996a, p. 139).

1.2.1.1.2 Mercury Program (1958–1963)

The Mercury Program was the first human spaceflight program of the US, initiated by NASA. It successfully launched six crewed missions, starting with Alan Shepard's suborbital flight in 1961, 23 days after Yuri Gagarin's orbital flight.

The LSS of the Mercury program showed a few similarities to the Vostok system – automatic control of temperature and pressure of capsule, potable water was provided from a tank, there was no on-orbit monitoring of water and no wastewater processing (Williamson, 2006, p. 243). Like in the Soviet missions, urine and faeces were only stored (NASA, 2018, p. 283). One of the main differences between the Soviet and American spacecraft designs was the adoption of a pure oxygen atmosphere. The oxygen was additionally stored in tanks so unlike in the Soviet missions, there was no on-board production (LePage, 1999). A filter, activated charcoal, and LiOH were used to eliminate odours and CO_2. Condensate was stored in a tank (Williamson, 2006, p. 243).

1.2.1.2 Scaling Up for Extended Missions (Voskhod, Gemini, Soyuz, and Apollo)

After gaining the first experience in space, missions became longer, and more complex with more ambitious goals starting with multi-crew missions. This created a need to improve oxygen production, CO_2 removal, water management, waste handling, and temperature and humidity control systems.

1.2.1.2.1 Voskhod Program (1964–1965)

The Voskhod program was a follow-up to the Vostok program. The objectives were to fly the multi-crew mission and to perform the first spacewalk which was done by Alexei Leonov in 1965.

The Voskhod introduced the first airlock for spacewalks, allowing for depressurization of the cabin during an EVA which consequently created a need for the LSS to handle depressurization of the cabin. According to the literature, all other systems were re-scaled versions of the Vostok program (NASA, 2018, p. 284; Stoiko, 1971, p. 177; Williamson, 2006, p. 240).

1.2.1.2.2 Gemini Program (1961–1966)

The Gemini Program was launched by NASA between 1961 and 1966. It was made to fill gaps in knowledge to allow the landing of astronauts on the Moon. It was designed to test and refine the spaceflight techniques required for Apollo's lunar missions.

The program introduced modifications to the LSS, such as using cryogenic liquid oxygen, to reduce volume and mass of the tanks, and a dual oxygen supply system for redundancy. To manage significantly higher amounts of heat, radiators and regenerative heat exchangers were introduced (Jones, 2006). Wastewater management, the composition of the atmosphere and pressure, waste management, and lack of water monitoring remained unchanged (Diamant and Humphries, 1990; Grimwood et al., 1969, p. 141). However, to keep the water clean, chlorine was added to the tank before the flight (NASA, 2018, p. 287).

1.2.1.2.3 Apollo Program (1961–1972)

The Apollo program by NASA aimed to land the first humans on the Moon and bring them back. It successfully landed on the Moon during the Apollo 11 mission in 1969. In total, six of the program's missions successfully landed 12 people on the Moon. It marked some big improvements in ECLSS technology.

Unlike before, the Apollo program employed a modular approach, incorporating the Command Module (CM), Service Module (SM), and Lunar Module (LM) (Jones and Kliss, 2010) with independent LSS systems for each one. The CM's system was responsible for most of the trip to the Moon, while the LM's system supported astronauts during the lunar descent, surface activities, and ascent (Jones, 2006). The CO_2 removal system and trace contamination control system of the CM and LM of the Apollo program were scaled versions of the Gemini. There was still no atmospheric control (NASA, 2018, p. 283). Instead of simple heat exchangers, the Apollo program used a more advanced sublimation system. Oxygen was still stored in the tanks, serving both as a life support and power systems. The atmosphere inside the CM during launch consisted of 60 % O_2 and 40% N_2. After that, it was kept like in the Gemini and Mercury program. The Apollo program was the first program where water was produced on board. For the CM module, primary source of drinkable water came as a byproduct of fuel cells.A separator made of silver palladium was used to remove both dissolved and free hydrogen from the water r (NASA, 2018, p. 104). To ensure drinkability, sodium hypochlorite solution was added every 24h for CM and for LM, iodine was added before launch (Sauer et al., 1973).

Additionally, the CM managed condensate water by retaining it for use (NASA, 2018, p. 284). Waste management in Apollo also improved. Bactericides were introduced, to stabilize faecal matter. Additionally, a urine receptacle assembly was added (Anderson and Martin, 2005).

1.2.1.2.4 The Space Shuttle Program (1981–2011)

The Space Shuttle program was the first reusable orbiter vehicle. The Shuttle was used to conduct scientific experiments, for satellite deployments, and later to service space stations like *Mir* and the *ISS,* with 135 missions in total.

For shorter missions, like before, the Space Shuttle employed lithium hydroxide (LiOH) for CO_2 removal and activated charcoal to filter out other atmospheric contaminants. However, for extended missions, the Shuttle incorporated an amine-based regenerable CO_2 removal system that also eliminated moisture. Additionally, the Shuttle's air-cleaning system utilized catalytic oxidizers to convert carbon monoxide to CO_2. Ammonia was absorbed by condensate within a condensing heat exchanger (Diamant and Humphries, 1990). The Space Shuttle was the first U.S. spacecraft to replicate a standard sea-level atmosphere onboard. To keep water safe for drinking, the automatic adjustment of the iodine level was introduced (Diamant and Humphries, 1990). Water production was based on the technology used in the Apollo missions (Winkler et al., 1996). Temperature control involved a centralized liquid/air condensing heat exchanger that used water as a coolant. The shuttle has introduced a commode for the collection and storage of faecal matter, moving away from the bag collection method used previously (Diamant and Humphries, 1990).

1.2.1.2.5 Soyuz Program (1967s-present)

The Soyuz program was started by the Soviet Union and continued by Russia. The program holds a few records and milestones, including the longest human spaceflight duration and the first docking between two crewed spacecrafts. The Soyuz spacecraft was designed for missions lasting up to seven days, for a crew of up to three astronauts.

The LSS system of the Soyuz was based on the ones used in earlier *Vostok* and *Voskhod* missions. While retaining a KO_2-based oxygen production, the *Soyuz* introduced larger and more efficient lithium hydroxide (LiOH) beds, which improved efficiency of CO_2 removal. Activated charcoal filters were used for the first time to improve removal of trace contaminants from the air (Daues, 2006). The humidity management system was upgraded through

implementation of a water/glycol mixture and advanced condensation capture. The main function of chemical water absorbents shifted to regulating oxygen generation rate in the O_2 regenerator (NASA, 2018, p. 281). Potable water was still stored and not processed for reuse in the same tanks, as in previous Russian programs. There was still no microbial control of water. There was also no improvement in the waste management regenerator (NASA, 2018, p. 283).

1.2.1.3 Long-Duration Space Stations (Salyut, Skylab, Mir, and ISS)

1.2.1.3.1 Salyut Program (1971–1986)

The Salyut program was a series of Soviet space stations aimed at testing long-duration spaceflight capabilities and conducting scientific research. It was the first space station program, with missions lasting weeks to months, paving the way for future space stations.

One of the most important advancements in LSSs technology was the transition from a chemical-based oxygen production to oxygen generation through water electrolysis. Additionally, CO_2 was removed using regenerable LiOH canisters. The Salyut introduced water recovery from humidity condensate, and later on, expanded this capability to include water recovery from urine (Bobe et al., 2007).

Temperature was controlled by a liquid cooling system, and relative humidity was managed through condensation on heat exchangers (NASA, 2018, p. 281). Though the stations relied heavily on resupply for food and water, they marked the first steps toward more regenerative systems.

1.2.1.3.2 Skylab (1973 - 1974)

Skylab was the first US space station with the goal of performing long-term scientific experiments - up to 84 days.

The station introduced a mixed O_2/N_2 atmosphere, and CO_2 removal was achieved using molecular sieves instead of LiOH (Belew and Stuhlinger, 1973, p. 98). Temperature control relied on air ducts with heaters and a glycol cooling system. Relative humidity was managed through condensing heat exchangers (NASA, 2018, p. 282). There was an iodine level monitoring in the water. Waste management focused on storing urine and venting liquids into

space, with solid waste vacuum-dried and stored. Trace contaminants were removed by a temporary depressurization.

1.2.1.3.3 Mir Station (1986–2001)

The Mir space station was an orbital research facility developed by the Soviet Union and later operated by Russia from 1986 until its deorbiting in 2001. Mir served as a microgravity research laboratory. It was the first modular space station, it consisted of 7 modules, assembled in orbit from 1986 to 1996. It was designed for long-duration missions, lasting from a few months up to over a year. The station could accommodate up to six people for short periods and crew of three for a long-duration mission.

The Mir space station had the first fully integrated a physical-chemical LSS, apart from the carbon dioxide concentration and reduction systems. The system enabled water recovery and oxygen generation (Bobe et al., 2007). The water supply system included systems for water recovery from humidity condensate, urine, hygiene greywater, and a system to store and distribute the water (Pierre et al., 1996). There were separate systems for potable water, service water and for hygiene water. Atmospheric condensate was collected and turned into drinking water after cleaning, adding biocide and minerals, and pasteurization. A conductivity sensor determined the quality of the water (Samsonov et al., 2000). Water for hygiene and kitchen use was reclaimed through a filtration system that utilized fragmented dolomite, artificial silicates, salts, activated charcoal, and ion exchange resins. After filtration, essential minerals were added. Water for electrolysis which was a primary source of O_2 was obtained from urine using a vapor-diffusion distillation process (Daues, 2006). Additionally, Mir was equipped with Solid Fuel Oxygen Generator system as a backup for oxygen generation. Nitrogen was stored as a gas in high-pressure tanks (NASA, 2018, p. 283). The atmosphere kept sea-level pressure with the concentration of O_2 between 21 - 40%, and N_2 up to 78% (Eckart, 1996b, p. 138). CO_2 was removed using sorbent beds and desiccants (Mitchell, 1994, p. 30). Filters, regenerable charcoal beds, and catalytic oxidizers were used to remove carbon monoxide, ammonia, and methane (NASA, 2018, p. 283). A commode was used for the collection of urine and faeces. Urine was directed to the recovery processor. Waste generated from food and water was sent to a waste collection unit (Daues, 2006).

1.2.1.3.4 International Space Station (ISS) (1998-present)

The International Space Station currently represents the most advanced LSS tested in space. It is equipped with advanced regenerative systems for air and water recycling. While the ISS is a collaborative effort involving multiple countries and space agencies (NASA, Roscosmos, ESA, JAXA, CSA), the US and Russian segments operate independently. Their LSSs are based on their respective technological advancements and previous achievements.

For atmosphere management, the US segment utilized two regenerative desiccant beds for water removal and two regenerative molecular sieve beds for CO_2 removal. Later on, CO_2 was heat vacuum desorbed from the beds. It was used in a Sabatier reactor, which was converting CO_2 and H_2 into CH_4 and H_2O, but the reactor was decommissioned. There were 2 attempts to include the Sabatier reactor (one, ESA, one NASA). Currently, CO_2 and H_2 are vented out. Activated charcoal and catalytic oxidizer are employed for trace contaminant control. Other particulates are removed by filters. There is on-board monitoring of N_2, O_2, H_2, CH_4, H_2O, and CO_2. Water electrolysis is done by the Oxygen Generation Assembly it is used to provide oxygen for the crew, and remining H_2 used to be used in Sabatier recator.This system is equipped with a polymer electrolyte membrane. The atmosphere is composed of O_2/N_2 and is kept at 101 kPa. Temperature control features air and water heat exchangers to cool and dehumidify the air, with condensate collected and stored in tanks. Potable and hygienic water is recycled utilizing multifiltration and ion exchange sorbent beds, and catalytic oxidation. The system allows water recycling from condensate, greywater, and urine. Urine is processed in the Urine Processor Assembly, which includes the Vapor Phase Catalytic Ammonia Removal subsystem. This system thermally removes volatile carbon and nitrogen compounds. The treated water from the Urine Processor Assembly is later mixed with water recovered from other sources and sent to the Water Processor Assembly, where it is further purified to potable standards. To sterilize water, iodine is added, and heat sterilization is used. Additionally, there is online conductivity and free-gas monitoring. Off-line monitoring of total organic carbon and microbial contamination can also be performed. Waste management incorporates a commode/urinal system for the collection of human waste. Faeces are collected in bags and stored.

The Russian Segment's CO_2 removal system, water processing system, and temperature control systems are analogous to those of Mir, with automatic adjustment of the CO_2 removal rate. Oxygen generation, trace contaminant control, and ventilation systems bear similarities

to those on Mir as well. There is N_2, O_2, H_2, H_2O, and CO_2 concentration monitoring. The Russian segment mirrors Mir's atmosphere, with O_2 levels between 21-40% and a similar pressure. Water quality monitoring is limited to pH, salinity, and conductivity monitoring. For microbial control like before on the Mir station, water was heated, and ionic silver was added. It employs a commode system for the collection of urine and faeces. Urine is being processed for recovery. Remaining concentrate is stored in tanks until it can be disposed of. All waste, including that from food and water, is directed to a waste collection unit.

1.2.1.4 U.S. vs. Soviet Approaches

The Soviet approach emphasized reliable, robust systems with constant improvements for longer missions, relying on frequent resupply and gradual adoption of recycling. The US approach evolved from simple expendable systems to highly regenerative, modular systems on the ISS, aiming for greater sustainability and less dependence on resupply (Munns and Nickelsen, 2021).

One of the key achievements in LSS technology was the development of onboard water and oxygen production technologies. It drastically reduced the mass of missions and laid the ground for sustainability in long-duration space missions. Onboard water production introduced with the Apollo program reduced reliance on resupply and lowered the mass, enabling more extended missions. For oxygen production, the pioneers were the Soviet Union/Russia, first by using chemical cartridges and later by using water electrolysis to produce oxygen like the one used during the *Mir* space station era. This system significantly reduced dependence on stored oxygen and was another step towards a regenerative LSS.

These differences between Soviet/Russian and US approaches together with key features of all of the LSS described above can be seen in Table 1-1.

Table 1-1 Comparison of LSS used in specific space programs

Feature	Vostok Program	Mercury Program	Voskhod Program	Gemini Program	Apollo Program	Space Shuttle Program	Soyuz Program	Salyut Program	Skylab Program	Mir Space Station	ISS US segment	ISS Russian Segment
Years	1961-1963	1958-1963	1964-1965	1961-1966	1961-1972	1981-2011	1967-present	1971-1986	1973-1974	1986-2001	1998-present	1998-present
Mission duration	1 - 5 days	15 min - 24 h	1 day	5 h - 14 days	8 - 13 days	2 - 18 days	1 - 18 days	12 - 237 days	28 - 84 days	1 - 14 months	typically 6 months, the longest 371 days	
Crew Size	1	1 astronaut	Up to 3	2	3	Up to 7	Up to 3	Up to 3	3	2-6	up to 4	up to 3
Mission Type	Short orbital missions	Suborbital and orbital flights	EVA capable, multi-crew	Extended missions, spacewalks, rendezvous	Moon landing missions	Reusable orbiter for various missions	Long-duration orbital missions	Long-duration space station	Long-duration space station	Long-duration space station	Long-term multinational space station	
Atmosphere Composition	Mixed O_2 and N_2	Pure O_2	Mixed O_2 and N_2	Pure O_2	60% O_2 and 40% N_2 at launch, then 100% O_2	Sea-level equivalent (22% O_2, 78% N_2)	Mixed O_2/N_2	Mixed O_2/N_2	Mixed O_2/N_2	Mixed O_2/N_2	Mixed O_2/N_2	
O_2 Supply	Chemical cartridges (KO_2) reacting with water	Stored in tanks; no onboard production	Similar to Vostok with increased capacity	Cryogenic liquid O_2	O_2 in tanks for life support and power systems	O_2 tanks and environmental control systems	Chemical O_2 generators and onboard regeneration	Electrolysis of water	O_2 in tanks	Electrolysis of water; Solid Fuel Oxygen Generator backup	Electrolysis and pressurized tanks	Similar to Mirm but no urine processor
CO_2 Removal	Chemical reaction (KO_2 and KOH)	LiOH canisters and activated charcoal	Improved capacity for more crew	Similar to Mercury with enhancements for longer missions	LiOH canisters in CM and LM, sized for mission requirements	LiOH canisters for short missions; regenerable amine system for long missions	Lithium hydroxide (LiOH) beds	Regenerable filters (sorbent beds, desiccant beds)	Molecular sieves (zeolite)	Desiccant beds, sorbent beds, catalytic oxidizers	Zeolite molecular sieves with vacuum desorption	Similar to Mir with better control
Temperature and Humidity Control	Heat exchanger with liquid circuit	Manual and automatic controls	Enhanced for airlock operations	Advanced radiators and heat exchangers	Sublimation cooling in LM, radiative and convective in CM	Advanced air/liquid heat exchangers with humidity control	Heat exchanger with condensing system	Heat exchanger with condensing system	Combination of air duct heaters and Coolanol cooling	Liquid-air condensing heat exchanger	Integrated air/liquid systems and thermal radiators	Two internal cooling loops and one external
Water Supply	Sterilized and stored, no recycling	From tanks, no recycling	Similar to Vostok	Chlorinated before flight, no recycling	Produced by fuel cells, iodine or sodium hypochlorite added	Produced by fuel cells, some recycling	Stored in tanks, no active recycling	Recovery from humidity condensate, urine	Stored in tanks, treated for microbial control	Recovery from humidity condensate, urine, and greywater	Advanced recycling from urine, condensate, and other sources	Similar to Mir but no recovery from urine
Contaminant Removal	Activated charcoal filters	Activated charcoal and LiOH for odour and CO_2	Similar to Vostok but with scaling up for more crew	Similar to Mercury with enhancements for duration and crew	Similar technologies in both CM and LM	Activated charcoal, catalytic oxidizers, particulate filters	Activated charcoal filters	Regenerable charcoal beds, other filters	Draeger tubes and other monitoring systems	Regenerable charcoal beds and other filters	High-temperature catalytic oxidizers, filters	High-temperature catalytic oxidizers, filters
Waste Management	Collected and stored	Collected and stored	Similar to Vostok	Collected, no advanced processing	Advanced with bactericides, venting systems, and urine receptacle assembly	Advanced collection and storage systems, recycling in later missions	Collected and stored, minimal processing	Collection systems, re-entry disposal for solids	Collected and stored, advanced treatments for long durations	Collection systems, re-entry disposal for solids	Advanced systems for collection, recycling, and disposal	Advanced systems for collection, recycling, and disposal

1.2.2 Bioregenerative Life-Support Systems

The requirements for ECLSS change according to the mission scenarios. Analysis of these systems started already in the 1960s (Neufeld, 2023) and as it can be seen in the previous subchapters, it has been calculated that short-duration missions like those of Mercury, Vostok, Voskhod, or Apollo could rely on an open-loop ECLSS since carrying the necessary supplies was feasible. In contrast, for longer missions, the increasing distance makes frequent resupply impractical and too expensive. As a result, these missions require more advanced systems to minimize costs and logistical challenges associated with resupply, storage, and waste management.

Regeneration can be done either by physicochemical or biological processes. If the system relies only on biological processes, it is called a bioregenerative (BLSS) or controlled ecological life-support system (CELSS). The system that combines both processes is called a hybrid LSS (Eckart, 1996b, p. 125).

To achieve long-term survival in space, it will be essential to minimize reliance on Earth by developing in situ circular systems for oxygen, water, and food production while ensuring efficient waste recycling to sustain resource availability. In this context, a BLSS will be a must.

A BLSS can be described as an artificial closed ecosystem, guided by ecological principles, composed of humans, plants, animals, and microorganisms. A BLSS mimics the ecosystems from Earth and has the same structure of producer (plants), consumer (humans/animals), and decomposer (microorganisms) (Liu et al., 2021).

A BLSS can regenerate oxygen and water, produce food and other substances essential to astronauts' survival, and provide humans with comfortable environments like Earth’s ecosystem.

1.2.2.1 Research on Bioregenerative Life-Support Systems

The design of LSSs for missions beyond LEO should be built on the knowledge from past and present designs. This knowledge should come from the human spaceflight programs as well as from the terrestrial analogues. BLSS terrestrial analogues have been studied across the globe

since a few years after the first human mission, with significant research and experimental milestones achieved by various countries (Liu et al., 2021):

1.2.2.1.1 USSR/Russia

Research in BLSS was started by the Institute of Biomedical Problems, where an experiment involving a 5 m^3 sealed chamber containing three 15L bioreactors for algae cultivations to produce oxygen was conducted. It proved that algae could regenerate 90% of the air required by humans (Liu et al., 2021).

In the 1960s, the BIOS system was created. It was the first large-scale Earth-based experimental BLSS facility. Initially, the system consisted of a 12 m^3 chamber with an 18 L microalgae reactor for gas circulation and regeneration. The main goal of this project was to test gas circulation only, with no water and no food provision. They could provide up to 20% of a person's material need, so the system improved by adding a 2.5 × 2.0 × 1.7 m plant chamber, transforming the system into BIOS-2.

After four years of adjustments, a 90-day test showed that the gas cycle could be fully closed, with 25% of oxygen regenerated by plants and the rest by microalgae. The water cycle achieved 80–85% closure (Salisbury et al., 1997).

In 1972, building on the BIOS-2 foundation, researchers expanded the system to BIOS-3, a 315 m^3 facility aimed at complete material cycle closure (Liu et al., 2021).

The BIOS-3 project started to operate in 1972 and was the first artificial ecosystem tested with humans. The facility consisted of a human habitat, crop production areas, and a bioreactor with algae. The facility achieved more than 90% closure in gas and water circulation (Gitelson et al., 1997). Water used for sanitary and general purposes was recycled through plant cultivation areas and algae tanks. Water vapor released by plants and algae was used as drinking water. Additionally, water from faeces was extracted and reused and urine was added to the algae. Solid wastes were not recycled. The atmosphere in BIOS-3 was close to being self-sustaining, there was however a problem with the build-up of potentially toxic trace gases (Nelson et al., 2008). 4 to 6 months experiments were conducted between 1972 and 1983. BIOS-3 could achieve over 90% closure for gas and water circulation while providing 40–45% of the food for three people or 70% for two (Gitelson et al., 1989; Gribovskaya et al., 1997). The system also featured automatic regulation of plant photosynthesis in response to internal

environmental changes (Liu et al., 2021). In some of the experiments, BIOS-3 was able to achieve up to 95% closure. This record stood for more than 30 years (Salisbury et al., 1997).

1.2.2.1.2 United States

BLSS studies in the United States started in the 1950s and were initiated by the U.S. Air Force. The focus was on using algae (Chlorella), for atmospheric regeneration. In parallel, NASA began investigating the use of chemoautotrophic organisms, (Hydrogenomonas), in combination with physicochemical methods, to regenerate the atmosphere and produce biomass (Wheeler et al., 2003).

NASA's research into bioregenerative life-support systems started in the early 1960s, with discussions on crop selection for space habitats. As a consequence, a preliminary list of potential space crops was presented in 1962 (Wheeler, 2009). It was followed by studies that refined the list of selected crops based on yield, nutritional value, and environmental requirements (Wheeler et al., 2003). By the late 1960s, NASA's interest in BLSS grew, fuelled by the advancements made by the Soviet Union in the BIOS project (Gitelson et al., 1989). This led NASA to start in the late 1970s, the Controlled Ecological Life-Support System (CELSS) program. In this project they were testing the possibility of using higher plants in controlled environments to produce oxygen, purify water, remove carbon dioxide, and produce food (Galston, 1992; MacElroy and Bredt, 1984).

During the 1980s and early 1990s, NASA, in collaboration with universities and corporations, conducted a series of studies focused on optimizing plant growth in controlled environments and selecting crop species for future space habitat (Johnson et al., 2021).

In the late 1980s, the Biomass Production Chamber was built at NASA's Kennedy Space Center. The chamber had 20 m^2 of arable area and was designed to demonstrate the potential for food production, water recycling, and atmospheric control in space. Experiments tested how plants respond to closed systems (Wheeler et al., 1996).

Meanwhile, the Biosphere 2 initiative, was constructed in the Arizona desert between 1987 and 1991. Biosphere 2 was the largest closed ecological system ever built. It aimed to create a self-sufficient environment to support human life through complete recycling of air, water, and human/animal waste. Biosphere 2 covered different ecosystems, such as a rainforest, an ocean, a mangrove wetland, a savannah, a desert, an agricultural system and a human habitat

(Marino and Odum, 1999). Two major experiments were conducted. The first one lasted 24 months with a crew of eight people. It faced issues with oxygen depletion due to rapid soil respiration by microbes and the unexpected absorption of CO_2 by the concrete structure, which prevented the normal recycling of oxygen via plant photosynthesis. Additionally, low light penetration through the glass structure further limited photosynthetic activity, reducing oxygen production. As a consequence the facility required external oxygen injections. The crew however has managed to produce enough food. Despite that, they experienced significant weight loss due to a low-calorie diet.

Improvements in Mission 2, which lasted 6.5 months, included better crop selection and sealing of the concrete, resulting in more stable oxygen levels (Nelson, 2021, p. 2).

In the mid-1990s, NASA's CELSS program merged with its physicochemical life support research into the Advanced Life Support (ALS) Program. The focus was on increasing the efficiency of life-support systems for long-duration space missions (Berry et al., 1994). By the early 2000s, funding for ALS research had declined due to overall budget cuts. As a consequence, the program was dismantled.

More recently, the Prototype Lunar Greenhouse (LGH) was developed through a collaboration between NASA and researchers at the University of Arizona's Controlled Environment Agriculture Center. The LGH was focusing on plant growth in controlled environments, water and waste recycling, and air revitalization. It successfully grew crops with an average biomass of 60 grams per square meter per day. Water recycling experiments demonstrated that one person's daily needs (27-30 L) could be met through condensation and recycling. The introduction of LED systems resulted in up to 56% energy savings without reducing crop yields (Furfaro et al., 2017).

In 2014, NASA launched the Veggie Plant Growth System, to the International Space Station to test the possibility of growing edible plants in microgravity. Veggie was designed for applied research in food production. It useshydroponic system with LED lighting to grow crops like lettuce, radishes, and zinnias (Massa et al., 2015).

The Advanced Plant Habitat (APH), deployed on the ISS in 2018, is a more complex plant growth chamber focused on fundamental plant biology research. APH provides more controlled environment to study plant growth. The system controls temperature, relative

humidity, oxygen, and CO_2 concentration, as well as light spectrum and intensity ventilation and watering regime (Monje et al., 2020).

1.2.2.1.3 Japan

The construction of the Closed Ecology Experiment Facility (CEEF) in Japan started in 1994 (Nitta et al. 2000). The experiment took into consideration problems that appeared in Biosphere 2 and eliminated all building materials that could absorb oxygen (Nitta 1999).

From 2005 to 2007, the Closed Ecology Experiment Facilities in Japan conducted experiments on closed ecological systems. Their focus was on the circulation of air, water, and materials. The setup included a hydroponic Plant Cultivation Module where 23 crop species were grown. The system also included two humans and two goats in the ecosystem. The conducted experiments duration, ranged from one to four weeks, demonstrated that the Plants Cultivation Module was able to produce between 92 and 95% of the food consumed by humans and 79% of the goat's food. The experiments showed effective recycling of oxygen and carbon dioxide between the plant area and the habitation module. A water circulation loop tested in 2006 indicated a balance between water input and output, closely matching the water content of harvested crops. In 2007, a waste processing system was added, converting organic waste into carbon dioxide which was used in the Plant Cultivation Module. The ability to maintain air quality was confirmed by analysing the trace-contaminant gases concentration which stayed below harmful levels (Tako et al., 2010).

1.2.2.1.4 China

China started their studies on BLSS in the 1990s, in the China Astronaut Research and Training Center. Their primary focus was on plant cultivation, microalgae, and waste. In 2004 the research was expanded to higher plant and microalgae cultivation, water cycling, and animal selection (Liu et al., 2021).

In October 2013, China launched Lunar Palace 1 - its first large-scale, crewed BLSS experiment, which included plant cultivation areas. The experiment lasted 105 days and included 3 people. The experiment involved cultivating 21 types of crops and using yellow mealworms to degrade waste. The experiment achieved 100% oxygen and water regeneration, 55% food regeneration, and 97% overall material closure with a "human-plant-animal-microbe" system (Fu et al., 2016).

Following an upgrade in 2016, Lunar Palace 1 underwent the Lunar Palace 365 experiment, lasting 370 days. The system achieved 100% oxygen and water regeneration, 83% food regeneration, and 98.2% material closure rate (Fu et al., 2021).

In 2016, the Astronaut Center of China conducted the Space 180 experiment, where four crew members lived in a fully enclosed Controlled Ecological Life-Support System (CELSS) for 180 days. The CELSS consisted of six interconnected modules, including four greenhouses. This experiment achieved 100% oxygen regeneration, 99% water regeneration, and 70% food regeneration (Yuan et al., 2019).

1.2.2.1.5 Europe

The MELiSSA (Micro-Ecological Life-Support System Alternative) project was initiated in 1987 by the European Space Agency (ESA). It aims to develop a closed-loop system for long-term crewed space missions. Its research is focused on modelling and the integration of different biological processes for water, air, and food regeneration (Mergeay et al., 1988).

1.2.2.2 MELiSSA project

MELiSSA is a project led by ESA. It is inspired by the ecological processes of lake ecosystems (Hendrickx et al., 2006). The concept of the project can be seen in Figure 1-2.

In the MELiSSA system, waste products generated by the crew are reduced by microorganisms, and the products of this degradation are supplied to algae and plants. These organisms, in turn, use light as an energy source to drive photosynthesis, convert CO_2 into oxygen and produce food and clean water for the crew (ESA, 2023). The concept targets the complete conversion of waste materials into life-sustaining resources.

Figure 1-2 *MELiSSA loop inspiration from a lake ecosystem. Credits: ESA, MELiSSA.*

The MELiSSA concept is structured into five compartments (C1 to C5), each representing a step in the waste processing and resources regeneration cycle. Below are the roles of each compartment:

- **compartment C1** – the Liquefying Compartment – it processes organic waste such as leftover food, urine, paper, inedible parts of plants, and faeces, using a thermophilic anaerobic digestion. This process breaks down these materials to generate volatile fatty acids, CO_2, minerals, and ammonium.
- **compartment C2** – the Microbial Electrolysis Cells Compartment – the role of this compartment is to transform organic carbon into inorganic carbon sources and process volatile fatty acids produced during anaerobic fermentation in C1
- **compartment C3** – the Ureolysis and Nitrification Compartment – it is responsible for converting ammonia into nitrates through the nitrification process, facilitating urea hydrolysis, and removing COD from the crew's urine. For the nitrification, it uses two strains of nitrifying bacteria: *Nitrosomonas europaea*, which oxidizes ammonium into nitrite, and *Nitrobacter winogradskyi*, which further converts nitrite into nitrate. The compartment operates in axenic conditions to ensure that only the intended bacterial strains are active. Heterotrophic bacteria (*Pseudomonas fluorescens*, *Comamonas*

testosteroni, *Acidovorax delafieldii* and *Cupriavidus necator*) are used for urea hydrolysis and COD removal.

- **compartment C4a** – the Photosynthetic Compartment – it is responsible for converting CO_2, minerals and nitrate to food and oxygen. The main organism used in this compartment is *Limnospira indica.*
- **compartment C4b -** the Higher Plant Compartment – it is responsible for food production, oxygen generation, water recovery, and CO_2 removal. In this compartment a variety of crops are grown, to provide a balanced diet for the crew. While the final crop selection is still under consideration, the project has studied 32 potential crop sources. These crops are chosen for their nutritional value and ability to survive. Research in C4b focuses on biomass production rates, plant nutrient composition, and the environmental factors that affect plant growth.
- **compartment C5** – the Crew Compartment – it represents the human component of the loop

The graphical representation of the loop concept can be seen on Figure 1-3.

Figure 1-3 *Schematic representation of the MELiSSA project compartments. Credits: ESA, MELiSSA*

The MELiSSA integration strategy was divided into steps. The goal is to ensure that each compartment operates effectively both individually and as part of the whole system. In the

first step, each compartment is developed and tested on a laboratory scale. Afterward, they are scaled up and further characterized in the MELiSSA Pilot Plant (MPP). The integration strategy is to integrate the gas loop first, then the liquid loop, and then the solid loop.

Currently, compartments C3, C4a, and C5 have been successfully integrated, with the crew being simulated by 3 Wistar female rats. C3, C4a, C5 are connected through the liquid and gas phase (Garcia-Gragera et al., 2021). Additionally, Compartment C4b has been integrated in gas-phase connection with the C5. The integration has been tested over long-time in continuous operation. Both photosynthetic compartments - C4a and C4b were simultaneously connected to C5. It demonstrated the capability of the system to control oxygen concentrations in C5 through regulation of gas flow and illumination in C4b, which was cultivated with staggered hydroponic lettuce crops. The control system showed the capability to managed oxygen demands that changes over the time due to the C5 day/night respiration cycle and the plants' photoperiod (Arnau et al., 2024). Rats provide a model for adjusting respiratory needs depending on the time of the day (Alemany et al., 2019).

MELiSSA's objective is to achieve the highest possible recycling rate within a closed-loop system while not compromising the safety of astronauts. Therefore, it is crucial to improve the efficiency, reliability and robustness of these processes, and compatibility between the compartments. Considering that MELiSSA is formed by several subsystems with different dynamics, working in a coordinated manner in continuous mode, it is essential to provide the system with a sophisticated control system based on mathematical models describing the operation of each one of the compartments and the entire loop. From inception, the MELiSSA project embraced the development of knowledge-based and mechanistic models to describe the mechanisms driving the physical, chemical, and biological processes in all compartments of the loop. All of these models need to be validated with experimental data before being implemented in a global model for the control system of the loop (Poughon et al., 2009).

A mechanistic model requires a comprehensive understanding of all underlying mechanisms, enabling operation across wide range of parameters with accurate predictions of the behaviour of various processes within the system. For LSS technologies, it is especially important because it will allow the control of the system to ensure its operation in nominal conditions and mitigate the potential consequences of system failure.

The main complexity of modelling the entire loop, or its individual compartments operating independently comes from their biological nature and the different time and size scales of the processes. These processes need to be described, and their models should predict how the system evolves over time, for a wide range of parameters. This approach will facilitate the planning of maintenance for equipment and aid in the establishment of predictive control mechanisms (Ciurans Molist et all., 2023)

To create a detailed mechanistic model of the loop it is essential to determine the mass and energy flows, establish precise stoichiometry, and identify the limitations of the system. This process has already been described in detail for C4a (Poughon et al., 2009). The current focus is on modelling the Higher Plant Compartment - C4b, with a specific emphasis on mechanistic models of plant growth in reduced gravity environments (Poulet, 2018, p. 23).

Plants require a model that takes into account their complexity, like various organs and growth stages. Plants should be modelled considering the diversity in morphology and the need for different environmental conditions for different stages of development. This leads to a multifaceted model that includes descriptions of gas exchange at the leaf surface, the absorption of water and solutes by the roots, transport through the stem, and the interception of light. Therefore, the modelling starts with plants as individuals, focusing on the local scale, and then integrates these individual models to represent the entire canopy (Hezard, 2012, p. 14; Sasidharan L., 2012a).

1.3 Gaps to be filled

The development of BLSS is essential for long-term human space missions. Because of that, LSSs need to be more efficient, reliable, and cost-effective. This can be done by minimizing resource use, size, and energy requirements while maintaining safety (Williamson, 2006).

1. **Biological Process Modelling for BLSS**

For BLSS, it is important to understand the biological processes within the system, how they interact with the environment and what are their limitations. Accurate and dynamic models are needed to predict system behaviour, optimize performance, and prevent or manage potential failures. The complexity of biological systems requires the development of precise models that consider gas exchange, nutrient cycling, and plant growth under space conditions.

Key challenges in this context include:

- Current models do not incorporate the effects of gravity, radiation, and change in atmospheric conditions.
- Most plant growth models are designed for terrestrial applications and require modifications to incorporate extra-terrestrial conditions.
- The complexity of plant-environment interactions demands multi-scale modelling approaches that integrate different physiological processes, like transpiration, photosynthesis, or nutrient uptake.

2. **Experimental Validation in Space Conditions**

A lot of data have been collected through Earth-based BLSS experiments. However, unique space conditions, such as gravity, magnetic fields, and radiation, imply that terrestrial results cannot be directly used for the prediction of the behaviour of these systems in space (Liu et al., 2021).

Current gaps in this area include:

- Limited experimental validation of BLSS in space conditions.

- A lack of data to compare the results from Earth-based experiments and space missions.

To address these challenges, future efforts should focus on:

- Conducting controlled BLSS experiments in LEO, on the Moon, and on Mars to compare space data with terrestrial data.
- Calibrating Earth-derived models with spaceflight data to improve predictive accuracy.

3. Thermal and Mass Transfer Challenges in Microgravity

Heat and mass transfer processes are different in microgravity than on Earth.

Key research areas in this context include:

- Studying the impact of altered gravity on plant transpiration and heat dissipation.
- Developing more efficient cooling and ventilation strategies for plant growth chambers in space.

Filling these gaps is mandatory to ensure that BLSS can support a sustainable human presence in space. By experimental validation, refining mathematical models, and improving resource recycling efficiency, long-term missions beyond Earth orbit will become possible.

2 Objectives

To make a sustainable human presence in space possible, it requires the development of efficient BLSS that integrates higher plants. Plants produce oxygen, remove carbon dioxide, purify water, and contribute to food production, and those are functions that cannot be fully achieved by physicochemical systems alone. However, one of the main challenges of these systems is understanding the heat and mass transfer processes that govern plant-environment interactions under different than Earth gravitational conditions.

To achieve this, the current thesis addresses the following objectives:

1. Design and implement of an experimental setup to study heat and mass transfer processes between a leaf replica and its environment under varying gravity conditions.
2. Validate the experimental system's performance through ground reference experiments.
3. Quantify the effects of airflow velocity, inclination angle, and gravitational conditions on the surface temperature and mass transfer of leaf replicas.
4. Investigate differences between evaporative and non-evaporative surfaces under controlled experimental conditions.
5. Provide insights into the thermal and mass exchange dynamics that govern plant response in microgravity, supporting the design of efficient BLSS for space missions.
6. Develop a comprehensive physical approach for modeling heat and mass transfer with non-standard gravity and evaluate how boundary layer is affected by gravity.

2.1 Contribution to the understanding of heat and mass transfer phenomena between plants and the environment

This research contributes to the understanding of heat and mass transfer processes in microgravity. This study contributes to the following areas:

- Heat and mass transfer process characterization in microgravity, for different forced convection values and different inclinations of the leaf replica.

- Decoupling physical and biological processes involved in plant gas exchange. Using leaf replicas allows to study plant thermal regulation and water use without introducing biological variability.
- By modelling heat and mass transfers with altered gravity conditions and stomatal conductance in relation to energy transfer by evaporation of water in controlled setups, the study enables extrapolation to real plant systems, making findings applicable not only to space environments but also to terrestrial agriculture in controlled settings.

This study lays the groundwork for developing sustainable agricultural systems in space and contributes to broader applications in environmental control and engineering.

2.2 Description of the following chapters

Chapter 3: State of the Art

The first part of this chapter analyses plant modelling methodologies and their significance for life-support systems in space applications. It analyses different plant models – empirical, process-based and functional-structural models, assessing their capabilities in simulating plant growth, gas exchange, and biomass production. The chapter focuses on their limitations in predicting plant response under microgravity and extra-terrestrial conditions. It also shows what needs to be done to accurately simulate and optimize plant-based regenerative life-support systems for upcoming space missions It emphasizes the need to take gravity, radiation, and variations in atmospheric conditions into account.

The second part of this chapter describes physical and biological processes governing heat and mass exchange in plants, with a specific focus on applications in space environments. It discusses the dependence between transpiration, radiation, convection, and energy balance in plant-environment interactions. It also shows the advantages of using leaf replica in decoupling the biological and physical processes in plants which allows their more accurate studies. The chapter also examines how microgravity affects the heat and mass transfer mechanisms and how modelling these processes will contribute to the design of efficient plant production systems for long-duration space missions.

Objectives

Chapter 4: Conceptual design, development, and experimental protocols of the leaf replica test system

This chapter describes the experimental setup, hardware, and methodologies used to investigate heat and mass transfer under varying gravity conditions. It describes the design and components of the experimental units, including the mechanical, electrical, and software systems and the difference in the configuration between 1st and 2nd Parabolic Flight Campaign as well as Ground Reference Experiment. Additionally, the chapter presents the data collection protocol and the approach to analyse these data. Finally, the chapter describes the statistical analysis used to evaluate the data.

Chapter 5: Experimental results and statistical analysis for ground experiments and parabolic flight conditions

This chapter presents the analysis of the experimental data collected during the ground reference experiment and the parabolic flight campaigns. The chapter describes the environmental conditions inside the experimental units during the tests and analyses general trends for all studied cases for the evaporative and non-evaporative leaf replica. Additionally, statistical methods, including ANOVA and normality tests, were used to assess the significance of factors such as orientation, airflow velocity, bulk temperature, humidity, and gravitational acceleration. Results are compared across units, flight campaigns, and tested conditions.

Chapter 6: Interpretation and modelling of experimental results

This chapter introduces a mechanistic modelling approach to describe the heat and mass transfer phenomena observed in the experiments. The chapter begins with a global overview of the modelling objectives and the selection of representative datasets. A steady-state model is developed to estimate temperature distributions within the leaf replica, and heat transfer coefficients are identified through comparison with experimental data. The modelling framework is later extended to transient conditions, incorporating the effects of convection regimes and boundary layer development under varying gravitational conditions. A predictive model for heat transfer coefficients is proposed and validated. In parallel, a mass transfer model is established, including internal resistance and capillarity effects. Model predictions are compared to experimental results.

Chapter 7: Conclusions

The main outcomes of the study are reviewed. The obtained results are compared with some available data. It is shown that the main trends are similar to those previously obtained, both on leaf replicas and higher plants. These trends are consistent with the developed model predictions. A critical analysis of the experimental setup used is then carried out, considering possibilities for future improvements concerning both experiments in terrestrial conditions and experiments in parabolic flight. The prospects for improving the heat transfer model and the understanding of the leaf replica's conductance are described. The manuscript ends with a general conclusion opening the possibilities for extension and applications of this work, both on the understanding of the mechanisms of mass and heat exchange between a leaf and its terrestrial environment and on the prediction capabilities in non-terrestrial gravity conditions for the development, the design and the control of greenhouse piloting in extra-terrestrial base conditions.

3 State of the art

3.1 Existing plant models

Plant modelling started in the 1960s and was first focused on estimating light interception and photosynthesis in crop canopies. Over the decades, plant growth modelling has become a major issue in environmental science, forestry, and agriculture.

Primarily developed for terrestrial applications, with the upcoming space era the plant growth models have gained a significant role in future LSS development, as space agencies like NASA and ESA have targeted long-duration missions. The space environment, however, introduces many challenges, such as microgravity, high radiation levels, and fluctuations of temperature and pressure, all of which have a significant impact on plant physiology and development. The complexity of interactions between the plants and their environment as well as the processes occurring within plants requires detailed modelling that goes further than the traditional terrestrial models.

Terrestrial plant growth models can be categorized into 3 groups:

- **Empirical models** depend on the data to predict plant growth. These models are simple and efficient for predicting outcomes within primarily tested range of parameters, but they require a large amount of data to tune their accuracy and they cannot operate outside their tested ranges.
- **Process-based (PB) models** include environmental factors like light, temperature, or water availability as parameters within the model. They are used to predict a yield and as a support in decision-making but simplify plant architecture and focus on biomass production, ignoring the processes within the plant.
- **Functional-structural (FS) models** describe in detail the structure of the plants and they include plant architecture. It allows more accurate simulation of processes, like light interception and resource allocation across different plant organs. However, because of that they require a lot of computational resources and detailed environmental information. It makes them difficult to apply at a larger scale or in real-time scenarios.

In terrestrial crop modelling, final yield is most often predicted using empirical approaches. They are widely used in agronomy because they are computationally efficient and can be calibrated against large terrestrial datasets. It makes them practical for field-scale yield prediction. However, their empirical nature limits their validity outside of the calibration range, and they cannot reliably capture plant responses under novel or extreme environments. For this reason, in the present work we do not focus on empirical yield models. Instead, the emphasis is placed on process-based and functional-structural models, which describe underlying physical and physiological mechanisms.

To understand plant growth the processes on three different levels need to be studied:

- Structural processes that control morphology and development;
- Physical processes like light interception, water circulation, and nutrient movement;
- Biochemical processes such as biomass composition and chemical energy conversion.

PB and FS models use a mechanistic approach to simulate these processes - they follow mass and energy balance principles. However, currently, most of the existing models rely on empirical simplification, so there are no models that accurately account for all these processes.

A major gap in current plant models, except for the MELiSSA Plant model, is lack of gravity as a parameter. Gravity limits heat and mass exchange processes within plants, especially when ventilation is limited. For the detailed description of the MELiSSA Plant model please refer to (Hezard, 2012; Poulet, 2018; Sasidharan L., 2012b).

Developing models that can dynamically respond to changes in plant responses to environmental conditions in real time will be a must to make BLSS reliable.

Future research should focus on improving current models by including gravity, radiation, and varying atmospheric conditions as parameters. Nowadays, black-box models, including AI and data-driven techniques, are becoming more popular. However, they are not transparent and often are not accurate under conditions not represented in their training data as it was shown in (Amitrano et al., 2020). Models based on first principles are not easy to create but they can become more reliable in the environment that is significantly different from the one where the data were collected (like in space compare to terrestrial data), which is critical for life-support applications in space. Future solutions for BLSS may involve hybrid approaches that

combine mechanistic understanding with data-driven adaptability, yet strong physical foundation remains essential for ensuring safe and robust system design.

3.1.1 Main focuses on the use of higher plant growth models for life-support systems

This part is an article that was published in the proceedings of the 51st International Conference on Environmental Systems in July 2022.

51st International Conference on Environmental Systems
10-14 July 2022, St. Paul, Minnesota

ICES-2022-255

Main focuses on the use of higher plant growth models for life support systems

Joanna Kuzma[1], Jean-Pierre Fontaine[2], Lucie Poulet[3] and Claude-Gilles Dussap[4]

Université Clermont Auvergne, Clermont Auvergne INP, CNRS, Institut Pascal, F-63000, Clermont-Ferrand, 63000, France

In long-term plans for space exploration investigated by major space agencies, the exploration of the Moon or Mars involves solving many technological problems. One of them is the development of an efficient and robust life-support system. A one-way trip to Mars will take between 6 to 8 months with current technology. According to NASA's economic calculations, for each trip over 10 months, at least 15% of the food for astronauts should be produced onboard. To make this possible it is necessary to switch from physicochemical (PC) systems in charge of recycling water and oxygen and stabilization of waste - such as the one on the International Space Station - to hybrid ones where part of the system can be based on similar PC technology and part of it is based on biological processes in order to produce edible biomass, e.g. to grow plants. The European Space Agency MELiSSA (Micro-Ecological Life-Support System Alternative) project mimics a lake ecosystem. It consists of a closed-loop bio-regenerative system based on microorganisms and higher plants and provides circular cycling of mass, including food and O_2 production, CO_2 capture and water recycling. As the growth and development of higher plants are strongly influenced by the environmental conditions (gravity, pressure, temperature, humidity, partial pressure of O_2 and CO_2), bio-regenerative life-support systems require a high level of control and management. In systems that include plants, it is possible to use transpiring water as a source of potable water for astronauts, which in turn can reduce the need for physical purification systems. For this to be possible, it is necessary to understand in depth how the various parameters affect the plant growth and transpiration process - especially in closed systems. Most of the existing plant growth models do not consider gravity, radiation, or CO_2 concentration as a variable parameters. However, over the last years, new models of plant growth are being developed in controlled environments. This article presents general overview of the existing models with a focus on the ones that include external parameters to analyze the influence of each one on the global system in space applications. The article also highlights the work that still needs to be done to understand the impact of certain parameters on plant growth for a closed-systems application.

Nomenclature

CELSS	=	Closed Ecological Life-Support Systems
DD	=	Data-Driven
EC	=	Energy Cascade
FS	=	Functional Structural
KDDM	=	Knowledge-and-Data-Driven Modelling
LAI	=	Leaf Area Index
MEC	=	Modified Energy Cascade
MELiSSA	=	Micro-Ecological Life-Support System Alternative
PB	=	Process-Based
PPFD	=	Photosynthetic Photon Flux Density

[1]Ph.D. student, Institut Pascal, joanna.kuzmaa@gmail.com
[2]Professor, Polytech Clermont, j-pierre.fontaine@uca.fr.
[3] Research scientist, Institut Pascal, luciepoulet@yahoo.fr
[4] Professor, Polytech Clermont, c-gilles.dussap@uca.fr

I. Introduction

The very first steps to create crop models were taken in the early 60s. The models were developed to estimate light interception and photosynthesis effect in crop canopies.[1] Since then, plant growth modelling has become one of the most important parts of research activity in the field of environmental science, forestry and agriculture. The improvements in modelling related to the development in the field of science, computer technology as well as measurement techniques and devices.[2]

Current models differ in their level of complexity and precision, and this difference is mainly due to their application. The simplest ones use empirical models which are able to predict plant growth or their behaviour according to previously collected data. Such models can predict yields for specific plant varieties under specific conditions; thus, it is not possible to apply them to a global scale.[3] Hence, different approaches, based on the understanding of the processes within the plants and their interactions with abiotic factors, need to be applied. Because of that, empirical models are being gradually replaced by process-based models with varying degrees of complexity.

In order to understand plant growth and their interactions with the environment, three different levels have to be studied: morphological level, which includes structural changes at the plant scale; physical level to describe rate-limiting processes at the organ scale, and biochemical level to describe the processes at the cell scale.[4]

At the macroscopic level, the architecture and morphology of the plants are regulated at the plant or population level, and they depend on the environmental conditions. These processes, at the organ level, control the matter and energy exchange processes - root absorption, gas exchange, light interception, heat transfer, and nutrient movements. The fluxes of mass and heat exchange are further connected to the metabolic processes at the biochemical level. At the biomass production level, respiration and photosynthesis play a key role and define the mass and the composition of new organs.[5]

All of these processes are known, and global plant growth models have already been developed. Two main types can be seen; the models which are based on mechanistic equations, called process-based (PB), and the functional-structural (FS) models. The first ones were developed to provide support for agricultural industry with a primary focus on the prediction of biomass production for various environmental conditions. FS models take into consideration single plants in order to simulate them in a more accurate way compared to PB models. FS models were developed for a better understanding of single plant behaviour.

While in agronomy existing models are effective enough, in the context of closed systems and life-support systems (LSS) such a description is not sufficient. In the field of agronomy, for example, CO_2 and O_2 availability are not considered as a control variable which means that these models do not follow the Lavoisier principle and because of that they cannot be used without any modification for LSS development where CO_2 and O_2 are limited. This publication contains a review of existing models used in agronomy, their modifications and of models created for the simulation of closed systems like greenhouses and cultivations which are a part of LSS, and a description of what still needs to be done in the context of simulating closed systems for long term space exploration.

II. Existing Models

A. Empirical Models

Empirical (statistical) models are the simplest ones to predict the biomass growth of plants. Therefore, they are frequently used in agriculture, horticulture and forestry to predict the yield of monocultures.[6] Empirical models do not contain any mechanistic equations. These models directly relate biomass production to collected data at certain geographical locations or climate zone or in specific conditions – for example, type of soil. Such models are easy to use and fast to calculate, however, they are not able to predict the yield properly if the conditions are outside the boundaries within which the data were collected.[7] Empirical models also require a large amount of collected data as a starting point, to be able to predict the yield with sufficient precision. Consequently, their use for simulating plant growth in space is strongly limited.

B. Process-Based Models

According to Ref. 8, unlike empirical models, PB models "integrate environmental factors (light, temperature, CO_2, soil conditions, water and nutrient availability, etc.), by using compartment data, such as total leaf surface and harvest index". In those models, the main focus is usually on describing the carbon and nitrogen balance. PB models assume that plant growth depends on the exchange of matter between the individual plant parts based on nutrient uptake. The architectural model of the plants is usually not considered, or its simplified version is included. It is justified by the fact that PB models predict the yield per unit area, and they do not consider every single plant separately.[9] According to Ref. 10, "even if it contains empirical simplifications for some processes, the approach and results are mainly based on extensive experimental knowledge from agriculture results. Also,

soil and atmosphere dynamics can be included in an accurate mechanistic way, and the aim of guiding agricultural practices corresponds to the objective of the life-support system control."
Thanks to their specifications, PB models usually do not require computational power to calculate water or nutrient stress.[10] Compared to FS models (described in the next section) PB models are relatively simple for modelling plant growth which means[8]:

- PB models do not require detailed specifications of plant architecture.
- Light interception calculations are based in most of the cases on the Beer-Lambert law.
- The photosynthetic surface of plants is simplified to the Leaf Area Index (LAI) parameter instead of a model of the whole plant.
- The amount of biomass produced depends on the light use efficiency.
- The influence of environmental conditions is usually determined by empirical functions.
- Biomass allocation to organs depends on their sink strength.

These simplifications imply that the PB model has its limitations:

- Leaf weight cannot be predicted in different climate conditions, which leads to not accurate prediction of the leaf area.
- Organ abortion in vegetable plants and their harvest index are not well predicted.
- Stochastic yield changes are not considered, so the quality of the simulated results cannot be assessed.

Most of the existing PB models used in agriculture make biomass growth dependent on climatic and soil parameters and plant types. Few of them take into consideration pests - like for example InfoCrop model,[11] fertilization and sowing time for example - CROPSyst model.[12] Some models were calibrated to simulate the plant growth in different climate zones like the Sirius model,[13] and others are designed to accurately simulate plant growth in a specific climate zone, for example ORYZA model.[14] For this reason, existing models vary in the degree of accuracy and the number of simulated parameters and inputs. A summary of the main models is given in Table 1.

As it can be seen in Table 1, the development of the plants and the switch between the plant growth stages is a function of thermal time or physiological time sometimes connected with temperature and photoperiod. Light interception is calculated using the Beer-Lambert law (CERES,[15] CROPGRO,[16] Sirius and STICS[17]) or in more detailed ways using multilayer equations like in ORYZA, InfoCrop and CROPSyst models. Water uptake for CERES,[18] CROPGRO and STICS models is calculated based on the soil water content and roots density or/and soil depth, whereas the soil is simulated in a complex and detailed way. They all follow the mass and energy balance principle for simulating evapotranspiration. Evapotranspiration in PB models is calculated using the Penman-Monteith model or a modified version of this model, the Priestley-Taylor model or a simplified implementation that only requires air temperature as an entry parameter. The exception is the ORYZA model where evapotranspiration is not described in the analyzed publications.[14,19] None of these models simulates water accumulation in the plants. The driving force for biomass production is the light or radiation use efficiency. In most of the models, partitioning depends on plant development and assigns a specific percentage of the biomass to every organ. In CERES, CROPGRO, STICS and InfoCrop models, partitioning can also vary with the physiological or thermal time or stress. The CROPSyst model is the only one between the analyzed models, where partitioning has predefined coefficients which do not change during plant growth. Almost all of the models consider H_2O and N availability as a stress factor (exception is ORYZA model where only N is considered as a limiting factor). STICS, InfoCrop and CROPSyst additionally consider factors like temperature frost, flood or light.

This short review presents a general overview of the trends in process-based models. Such models are based on mechanistic equations; however, to make them easier to calculate, the global model is simplified with many empirical principles or more hypotheses. Additionally, these models do not totally satisfy the carbon and water mass balances and do not consider O_2 and CO_2 availability as a limiting factor, which is a proper approach for a terrestrial application (as the atmosphere acts like a buffer) but cannot be used in Closed Systems, where O_2 and CO_2 will be limited. Hence, those models are not suitable for future space LSS without some modification.

model [reference]	parameter							
	development - stage switch	**leaf area index**	**light**	**H2O uptake**	**evapo-transpiration**	**dry mass production**	**partitioning**	**stress**
CERES [15,18,20]	function of thermal time and photoperiod	expotential then linear with thermal time	Beer's law with constant radiation use efficiency	function of roots density, soil water content and soil depth	Priestley-Taylor	linear with light	function of development, thermal time	H2O, N
CROPGRO [16,21]	function of physiological time depending on temperature	function of plant height	Beer's law with variable radiation use efficiency or adapted two leaf	function of roots density, soil water content and soil depth	Priestley-Taylor or FAO-Penman	concentration of C containing compounds, conversion of CO2 uptaken with light	function of development, physiologicla time, and temperature for seeds	H2O, N
ORYZA [14,19]	function of physiological time depending on temperature and photoperiod	expotential then linear with thermal time	Mulitlayer integration with Leaf Area Index and temperature	function of soil water content	not described	function of light, temperature physiological time and CO2 conversion	function of development	N
Sirius [13,22]	function of thermal time and photoperiod	expotential then linear with thermal time	Beer's law with constant radiation use efficiency	function of soil water content and soil depth	Penman-Monteith and Beer's law	linear with light	function of development	H2O, N
STICS [17,23]	function of physiological time depending on temperature, daylength and vernalisation requirements	function of physiological time, temperature, and density	Beer's law with variable radiation use efficiency	function of rood density, soil water content and evapotranspiration	Priestley-Taylor and Beer's or resistance-based	function of the radiation use efficiency	function of development, physiologicla time, and temperature for seeds	H2O, N, T
InfoCrop [11,24]	function of physiological time depending on temperature and photoperiod	thermal time-dependent relative growth rate of LAI	Mulitlayer integration with Leaf Area Index and temperature	function of soil water content and soil depth	Priestley-Taylor or Penman-Monteith	function of the radiation use efficiency	function of development stage and stress	H2O, N, flooding, frost
CROPSyst [12,25]	function of thermal time, daylength and vernalisation requirements	function of biomass accumulation, specific leaf area, and a partitioning coefficient	Mulitlayer integration with Leaf Area Index and temperature	function of water distribution in the soil profile, crop transpiration, and evaporation	Priestley-Taylor or Penman-Monteith	function of intercepted radiation, water availability, air temperature and nitrogen availability	specific coefficient	H2O, N, T and light

Table 1: Parameter and processes included in chosen process-based models

C. Functional-Structural Models

FS models are a combination of structural and functional approaches, which were created to better understand plant physiology.[26] In FS models, the plant structure is always explicitly represented in terms of a network of elementary units in relation to the environment, and as mentioned before their physiology is simulated with a mechanistic approach.[27]

Unlike PB models, this type of model cannot be easily extended to the stand scale. FS models can simulate:

- The development of the plants and their structure by using for example L-System grammar,[28] one of the existing extensions of this formalism or other models.
- Plant growth, based on intercepted light and biomass production at the level of every leaf.
- Transport and partitioning of biomass in the plant at the level of individual organs.

However, the integration of the structure of the plants with physiological knowledge remains a serious challenge. The complexity of the model makes the simulations computationally costly - for example light interception needs to be calculated for every leaf, as well as the production, transport and partitioning of the assimilates.[8] This complexity also causes difficulties in rigorously applying statistical methods for parameter estimation and model evaluation using experimental measurements.

In the FS models, plants are considered as connected to each-other elementary units (phytomers or metamers). Plants respond to the surrounding environment by adapting the structure and functions – like the shape of organs and orientation, N allocation, transpiration, or photosynthesis.[29] This in turn might influence the conditions in which specific parts of the plants operate creating a feedback loop. The feedback loop also exists between the single organs and the whole plant.

In Table 2 the comparison of four commonly used FS models is shown. In FS models, stage switch during plant growth is usually connected to the architectural description of the plants, the dynamics of the production of organs and maturation, which depends on biomass availability in L-PEACH[30] or thermal time in GREENLAB[26] and GRAAL-CN[31] models and thermal time connected with photoperiod in ADEL model[32].
Light interception is simulated differently compared to PB models - using light scattering equations for L-PEACH and ADEL model, and similar to PB models using multilayer equations for GRAAL-CN model or Beer-Lambert law for GREENLAB model. Transpiration depends on the light availability at the specific level of the plant for ADEL model or following Penman-Monteith equations coupled with Beer's equation. Unlike PB models, in FS models the accumulation of water in the plants is simulated by a fixed value between water uptake and transpiration. Biomass production is mainly linked to the light intensity. Partitioning depends on the sink strength of the organs in GREENLAB and L-PEACH models. This parameter is simulated in more detail compared to the PB models. For GRAAL-CN model partitioning is based on empirical coefficients and the ADEL model accounts for the partitioning of nitrogen into structural and photosynthetic parts of the leaves. The stress factors are introduced gradually with the plant growth rate response and architectural adaptation, like light adaptation in ADEL and GREENLAB models and water stress in L-PEACH model.

model [reference]	**parameter**									
	development		**Architecture**		**Light**	**Evapo-transpiration**	**H2O uptake**	**biomass production**	**partitioning**	**stress**
	stage switch	**organ formation**	**upper part of the plants**	**roots**						
GREENLAB [5,26,33-34]	predefined	function of the thermal time	based on AMAP model	Roots included as a single organ	Beer-Lambert law, assuming that light propagates into a turbid medium	Penman-Monteith and Beer's	function of soil water content not described	depends on photosynthetically active radiation based on the Beer Lambert Law and leaf area index	proportionately distributed to each growing organ according to its sink strength and maturity	Light - growth rate and architectural adaptations
GRAAL-CN [31,35]	predefined	function of thermal time	own model	depends on carbon availability	Mulitlayer integration with Leaf Area Index	not included	not included	function of light and available carbohydrates	growth of each organ is derived from field experiments carried out under low limiting conditions of growth as regards light, nutrients and water	not included
L-PEACH [30,36]	predefined	function of available biomass	L-systems for each organ, its shape and size	Roots included with simplified architecture	Light scattering at a local scale with quasi-Monte-Carlo method with constant radiation use	transpiration demand depending on light at the local level	function of root biomass, soil volume, soil water content	function of light and available carbohydrates	depends on sink strength for each organ depending on development, resistance to sap flow	H2O
ADEL [32,37-38]	function of temperature and photoperioid	function of the thermal time	L-systems for each organ, its shape and size	Roots included as a single organ	Light scattering simulation at the leaf level with constant radiation use efficiency and morphogenetic	not included	not included	proportional to leaf area with constant SLA or proportional to light withconstant radiation use efficiency	%biomass leaf - function of leaf surface, other organs not included	Light - architectural adaptations

Table 2: Parameter and processes included in functional-structural models

III. Closed Life-Support Systems

Closed Ecological Life-Support Systems (CELSS) are self-supporting systems for space stations and colonies, typically using controlled closed ecological systems.[39] CELSS will play a crucial role in the long-term human space exploration or space colonization as part of future regenerative life-support systems. Therefore, they were and are being studied by national space agencies and universities,[40] in projects like Biosphere 2 in the USA, BIOS-3 in Russia, Yuegong-1 in China and MELiSSA (Micro-Ecological Life-support System Alternative) by the European Space Agency. One of the key elements in such systems is the higher plants that grow in controlled environments to provide food, oxygen and potable water.[41] However, CELSS experiments have to be deeply understood at different scales to be able to sustain life in the long term, thus a complex model of mass and energy balance for the system needs to be developed. The models need to predict the main fluxes (water, biomass, temperature, CO_2 and O_2 concentration) and provide environmental control for the plants and humans compartments.[42]
Most of the existing plant growth models follow a mass and energy balance approach and simulate specific processes with a different accuracy. However, none of them describes all of the processes involved with the same precision, due to the use of empirical simplifications, without understanding the principle behind. Additionally, models like this are adapted to the natural environment, where limited quantity of the external (for example

environmental) parameters is measured.[10] Moreover, plants in space will have to deal with parameters like gravity or cosmic radiation, which have not been considered in the current terrestrial models. In LSS, environmental factors like for example concentration of CO_2, O_2, water and nutrients availability should be fully controlled. Additionally, it should be remembered that the response of the plants is closely linked to the environmental factors – a change in the microclimate (air flow velocity, humidity level, air temperature) may result in modifications in the plant on the physiological or morphological levels. This can affect the transpiration and the gas exchange of the plants which in return can influence the surrounding environment.[43]
As a summary, the equations defined in the model need to operate for a large range of parameters with required precision which leads to the use of knowledge-based models. Over the years, several models have been developed or adapted for closed systems. The following section provides a focus on three of them.

A. Modified Energy Cascade Model

The Energy Cascade (EC) model was initially conceived to simulate wheat growth,[44] and was later modified for use in Advanced Life-Support system studies,[45] with the model calibrations to other crops such as dry bean, lettuce, peanut, white potato, rice, soybean, sweet potato, tomato, and wheat.[46] The modified energy cascade (MEC) model is an extended version of the EC model.[44] Because of that, only the MEC model is described here. This model calculates the daily carbon gain, which expresses the carbon fixation rate of plants. It consists of 3 stages simulating processes between the capture of light and the carbon fixation[47]:

- the absorption of PPF by the canopy,
- the absorbed energy use in the photosynthetic process to convert carbon into sucrose,
- the conversion of sucrose into biomass.

This model requires three empirical crop parameters: the time of canopy closure, the time of senescence onset, the time of harvesting. This model also requires information about environmental parameters like: PPFD, temperature, humidity, pressure, CO_2 concentration and dark period duration.[48] The outputs of the models are biomass production, water transpiration (or evapotranspiration), and water, CO_2 and dry salt consumptions.[46] One of the advantages of this model is that it allows simulating multi-crop cultivars. The MEC model calculates the growth of plants as a function of biomass production using the daily carbon gain dependent on the canopy light absorption, the canopy quantum yield, and the carbon use efficiency.
As described in Ref. 49, "The atmospheric temperatures, one for light periods and a second for dark periods, and the photoperiod are constant, and the plant growth is not limited by water or nutrients."
Based on these, the following parameters are calculated[46]: canopy light absorption increases from emergence through canopy closure, light absorption after canopy closure and a canopy quantum yield.
The MEC model uses a multi-layer plant canopy photosynthesis model to generate multivariable polynomial regression equations for the calculation of the maximum canopy quantum yield as a function of the irradiance and CO_2 concentrations. Transpiration depends on temperature, photoperiod, relative humidity, carbon dioxide level and crop growth and uses the relationships linking canopy stomatal conductance to canopy net photosynthesis.[46] During the dark period, transpiration is neglected. The model also distinguishes between different stages of plant maturity.[47] The model was validated on a Lunar greenhouse prototype study.[46,49]
In general, MEC model can be applied for PPFD from 200 to 1000 $\mu mol \cdot m^{-2} \cdot s^{-1}$ and in a range of CO_2 concentration from 330 to 1300 ppm. With a bigger PPFD range for rice and wheat (up to 2000 $\mu mol \cdot m^{-2} \cdot s^{-1}$) and smaller for lettuce (200 to 500 $\mu mol \cdot m^{-2} \cdot s^{-1}$).[49] These limitations come from the empirical nature of the model. As it was mentioned before, empirical models work well only within the range of the parameters where they were tested. Since in space plants will deal with for example different gravity or radiation this model might not predict the yield properly

B. GREENLAB+ model

GREENLAB+ uses a knowledge-and-data-driven modelling (KDDM) approach to simulate the growth of plants and the dynamics of CO_2/O_2 concentrations in a CELSS with humans and plants inside. The model is a synthesis of a TomSim process-based model, a GREENLAB structural model and a Data driven (DD) model for the CO_2 production and O_2 consumption by the crew members. The TomSim model is a dynamic simulation model developed for tomato crop growth and development.[50] This model calculates a potential crop growth, and a daily crop gross assimilation rate by integration of the leaf assimilation rates and total crop leaf area within the 24h period.[51] The model assumes that all plants are monolithic and that the photosynthetic characteristics of the individual leaves are identical for all leaves of the crop. The reflection of radiation from the substrate is also taken into account. Crop growth is calculated using the: gross assimilation rate, the respiration rate and the conversion efficiency. Partitioning calculations are based on the sink strength of the plant organs. The model distinguishes individual fruit trusses and vegetative units within the plant. Sink strength of every organ is defined as a function

of the developmental stage of the plant.[50] The DD sub-model is a linear model of the CO_2 production and O_2 consumption by the crew member. The two sub-models were integrated through a mass balance model with metabolic stoichiometries, which were derived for CO_2/O_2 concentrations in a closed system. A three-step parameter estimation method was developed to identify the proposed model parameters.

The model simulates the dynamics of plant organogenesis, biomass production and allocation[52] and it provides source and sink parameters with an inverse method using the GREENLAB model. The biomass production is simulated using TomSim model – which has described it in a more detailed way. As input parameters, the model needs information about CO_2 concentration, radiation, temperature, and initial LAI. Those parameters are used to calculate successively the leaf photosynthesis, crop photosynthesis, dry mass production which depends also on respiration. This generates the growth of the specific organs of the plants in the model. This finally affects the leaf area index and respiration. In GREENLAB+, the produced biomass is proportionately distributed to each growing organ according to its sink strength. The time step for calculating crop photosynthesis and maintenance respiration can vary within the model. Biomass allocation and organ expansion are computed daily, with an implicit assumption that plant morphology is stable during a one-day period. To calculate CO_2 production and O_2 consumption by the crew, empirical equations were introduced. However, the model was developed mainly for terrestrial crop cultivations in closed or semi-closed systems, where CO_2 and O_2 concentrations can vary over time. The model does not take into account the effects of gravity or radiation on plant growth.

C. MELiSSA_Plant

The model developed within the MELiSSA project[10,44] is divided into modules: morphological, physical biochemical, energy balance and the last one linking the environment surrounding the plants to the plant modules. This model uses a single leaf approach and simulates plants architecture using empirical parameters connected to a specific cultivar of crops. The morphological module is also described with empirical equations, considering the canopy surface and the total biomass synthesis. However, for the moment, the morphological module does not take into account the ratio of the volume (or wet mass of plants synthesized) over the exchange areas, either of the leaves exchange areas or the roots' exchange surface.

The intercepted light flux is simulated using the Beer-Lambert law and depends on the incident light flux, the LAI, and culture-specific coefficients. CO_2 uptake from the gas phase to the plant is calculated using the first law of diffusion across a gas boundary layer, depending on air velocity in the aerial part of the culture chamber. It depends on CO_2 partial pressure, the leaf area, the CO_2 diffusion coefficient, and the thickness of the mass boundary layer surrounding the leaf. The thickness of the gas boundary layer and the CO_2 partial pressure gradient between the leaf surface and bulk air influence transpiration and CO_2 uptake, and thus biomass production. Because of this dependence and the fact that future crop cultivation may take place under different gravitational conditions, the influence of gravity and air velocity on the thickness of the boundary layer was included in the model as well. The quantum yield depends on available incident light flux and CO_2 used for photosynthesis. Respiration rate is not included in the physical module because O_2 is not considered as a limiting factor. Water transpiration is a function of the water gradient, conductance, the saturating vapor pressure, the relative humidity in the vapour phase and the leaf area. The water migration from the roots part to the leaves is derived from the Hagen-Poiseuille model. Water absorption is calculated using the water potential gradient (between the roots and the nutrient solution in the root zone) and resistance to water flow, calculated with the radius of the sap vessel, the xylem sap dynamic viscosity, and the stem length, multiplied by the sap vessel number. Water lost by transpiration is a fixed percentage of total water uptake. The difference between the water uptake and transpiration represents water accumulation which is considered as the water content in biomass.

All of these processes are limited by the metabolic reactions, which are related to the main biochemical routes accounting for carbon uptake, O_2 production by photosynthesis, carbon backbones synthesis and respiration mechanisms operating in dark conditions.

.

IV. Comparison of closed system models

The comparison of the different models is given in Tables 3 and 4. It is shown that the complete modelling of higher plant growth including all parameters and environmental variables remains to be done.

One important point is to account for all conservation balances during the different phases of growth. This entails accounting of elements conservation (at least carbon, oxygen, hydrogen and nitrogen) by example of stoichiometric equations including the light energy requirements. On the other hand, the knowledge and modelling of exchange surfaces is the unique link to provide relationships between the growth rates and the environment variables, including the influence of gravity that plays a role in the transfer rates. At the present stage, this remains

to be done and at least formulated, including the determination of morphology variables enabling the constraints of the compounds migration between the different parts of the plant to be understood and represented.

parameters /model	O2	CO2	PPFD	T	RH	pressure	day/ night	air velocity	multicrop	gravity	plants development	partitioning	leaf conductance
MEC	+	+	+	+	+	+	+		+		+		
MELiSSA	+	+	+	+	+	+		+		+	+		+
GREENLAB+	+	+	+	+	+				+		+	+	

Table 3. Comparison of the parameters included in the analyzed closed system models

outputs /model	biomass production	transpiration	water uptake	CO2 consumption	nutrients consumption	LAI	energy balance	boundary layer
MEC	+	+	+	+	+			
MELiSSA	+	+	+	+		+	+	+
GREENLAB+	+			+		+		

Table 4. Comparison of the outputs of the analyzed closed system models

V. Conclusion

In the GREENLAB+ model it was shown that plants can adapt to their environment, according to their needs and change their photosynthetic rate, according to the crew activity. So, it shows the need to simulate plant behaviour according to dynamic changes of the gas atmospheric composition in the culture chamber. Additionally, future LSS plant growth models will need to describe root development and water and nutrient uptake and how these processes are affected in different gravity conditions. It was proven that in microgravity conditions, the roots grow more randomly, and especially lateral roots tend to develop much more, instead of having a large primary root. Another problem is the lack of convection in microgravity conditions. Without proper ventilation, the boundary layer around the leaves gets thicker, which increases the transportation resistance in the diffusion process and this, in turn, reduces gas exchange at the leaf surface. Thicker boundary layers also slow down the transpiration process and it leads to an increase in the leaf temperature. Consequently, the lack of convection causes the accumulation of gases and volatile organic compounds. Because of that, a more detailed study of the boundary layer in the microgravity conditions has to be done.

This comparison between the different models of higher plant growth permits selection of the main requirements of a model usable for a representation for LSS applications, including design, monitoring and control of higher plant chambers. This is summarized as follows:

- Representation of the different growth phases by sets of stoichiometric equations ensuring structural conservation of elements.
- Assessment of the main metabolic routes responsible for biomass synthesis as building blocks for deriving the previous global stoichiometric approach.
- Description of light energy transfer at the canopy surface, including thermal and radiative balances.
- Description of transfer fluxes between the environment and the different parts of the plant. This includes transpiration, mass transfer at the leaf surface, mass transfer at the root exchange surface, heat transfer at the leaf surface and internal migration of water and solutes between roots and leaves.
- Morphology description for deriving a representation of the exchange areas and of the geometry of the internal ducts.

All these elements would provide the way to assemble a complete model for higher plant growth, defining the path to understand, predict and model the influence of non-terrestrial gravity conditions that is mandatory for defining a rationale reasoning for the design and control of higher plant chambers for LSS purpose adapted to space conditions.

Acknowledgments

The authors would like to acknowledge CNES and the MELiSSA Foundation for funding JK's PhD, in the frame of which this study was done.

References

[1]Sinclair, T. R., and Seligman, N. G., "Crop modeling: from infancy to maturity", *Agronomy Journal*, Vol. 88, No. 5, 1996, pp. 698-704
[2]Ilse, V., and Lenz, S., "A process-based crop growth model for assessing Global Change effects on biomass production and water demand - A component of the integrative Global Change decision support system DANUBIA.", PhD thesis, Universität zu Köln, 2007, pp.8-10
[3]Kang, F., "Plant growth models and methodologies adapted to their parameterization for the analysis of phenotypes", Other. Ecole Centrale Paris, 2013. English. ffNNT: 2013ECAP0035f s.38-40
[4]Poulet, L., Dussap C. G., Fontaine, J.P., "Development of a mechanistic model of leaf surface gas exchange coupling mass and energy balances for life-support systems applications", *Acta Astronautica*, Vol. 175, 2020, pp. 517–530
[5]Fan, X. R., Wang, X., Kang, M., Hua, J., Guo, S., de Reffye, P., and Hu, B. G., "A knowledge-and-data-driven modeling approach for simulating plant growth and the dynamics of CO2/O2 concentrations in a closed system of plants and humans by integrating mechanistic and empirical models", *Computers and Electronics in Agriculture*, Vol. 148, No. 4, 2018, pp. 280–290
[6]Poorter, H., Anten, N. P. R., and Marcelis, L. F. M., "Physiological mechanisms in plant growth models: Do we need a supra-cellular systems biology approach?", *Plant, Cell and Environment*, Vol. 36, No. 9, 2018, pp. 1673–1690
[7]Dourado-Neto, D., Teruel, D. A., Reichardt, K., Nielsen, D. R., Frizzone, J. A. and Bacchi, O.O.S., "Principles of crop modeling and simulation: I. Uses of mathematical models in agricultural science", *Scientia Agricola,* Vol. 55, No. Special, 1998, pp. 46–50
[8]de Reffye, P., Heuvelink, E., Guo, Y., Hu, B.-G., and Zhang, B.-G., "Coupling Process-Based Models and Plant Architectural Models: A Key Issue for Simulating Crop Production", *Crop Modeling and Decision Support,* Crop Modeling and Decision Support. Springer, Berlin, Heidelberg, 2009, pp. 130–147
[9]Fourcaud, T., Zhang, X., Stokes, A., Lambers, H., and Körner, C., "Plant growth modelling and applications: The increasing importance of plant architecture in growth models", *Annals of Botany*, Vol. 101, No. 8, 2008, pp. 1053–1063
[10]Hezard, P., "Higher plant growth modelling for life-support systems: global model design and simulation of mass and energy transfers at the plant level", Chemical and Process Engineering. Université Blaise Pascal - Clermont-Ferrand II, 2012. English.
[11]Aggarwal, P. K., Kalra, N., Chander, S., and Pathak, H., "InfoCrop: A dynamic simulation model for the assessment of crop yields, losses due to pests, and environmental impact of agro-ecosystems in tropical environments", *Agricultural Systems*, Vol. 89, No. 1, 2006, pp. 1–25
[12]Stockle, C.O., The CropSyst Model: A brief description,
http://sites.bsyse.wsu.edu/cs_suite/cropsyst/documentation/articles/description.htm
[13]Jamieson, P. D., Semenov, M. A., Brooking, I. R., and Francis, G. S., "Sirius: a mechanistic model of the wheat response to environmental variation", In *European Journal of Agronomy*, Vol. 8, No. 3–4, 1998, pp. 161–179
[14]Radanielson, A. M., Gaydon, D. S., Li, T., Angeles, O., and Roth, C. H., "Modeling salinity effect on rice growth and grain yield with ORYZA v3 and APSIM-Oryza", *European Journal of Agronomy*, Vol. 100, 2018, pp. 44–55
[15]Nain, A. S., and Kersebaum, K. C., "Calibration and validation of CERES model for simulating. Modelling Water and Nutrient Dynamics in Soil–crop Systems", Modelling water and nutrient dynamics in soil–crop systems. Springer, Dordrecht, 2007, pp. 161–181
[16]Boote, K. J., Jones, J. W., Hoogenboom, G., Pickering, N. B., "The CROPGRO model for grain legumes". In: Tsuji G. Y., Hoogenboom G., Thornton P. K. Understanding Options for Agricultural Production. Systems Approaches for Sustainable Agricultural Development, Vol. 7, Springer, Dordrecht. 1998
[17]Brisson, N., Gary, C., Justes, E., Roche, R., Mary, B., Ripoche, D., et all., "An overview of the crop model stics", *European Journal of Agronomy*, Vol. 18, No. 3–4, 2003, pp. 309–332
[18]Gabrielle, B., Denoroy, P., Gosse, G., Justes, E., Andersen, M. N., "Development and evaluation of a CERES-type model for winter oilseed rape", *Field Crops Research*, Vol. 57, No.1, 1998, 95–111
[19]Bouman, B. A. M., Keulen, H. van, Laar, H. H. van, and Rabbinge, R., "The 'School of de Wit' Crop Growth Simulation Models: A Pedigree and Historical Overview", *Agricultural Systems*, Vol. 52, No. 213, 1996, pp. 171–198
[20]Castrignanò, A., Katerji, N., Karam, F., Mastrorilli, M., and Hamdy, A., "A modified version of CERES-Maize model for predicting crop response to salinity stress", In *Ecological Modelling*, Vol. 111, No. 2–3, 1998, pp. 107-120
[21]Boote, K. J., Scholberg, J. M. S., and Jones, J. W., "Improving the CROPGRO-Tomato Model for Predicting Growth and Yield Response to Temperature", *HortScience,* Vol. 47, No. 8, 2012, pp. 1038-1049
[22]Semenov, M. A., Jamieson, P. D., and Martre, P., "Deconvoluting nitrogen use efficiency in wheat: A simulation study", *European Journal of Agronomy*, Vol. *26*, No. 3, 2007, 283–294
[23]Strullu, L., Beaudoin, N., Thiébeau, P., Julier, B., Mary, B., Ruget, et all., "Simulation using the STICS model of C&N dynamics in alfalfa from sowing to crop destruction", *European Journal of Agronomy*, Vol. 112, 2020, pp. 1–14
[24]Singh, J. P., Govindakrishnan, P. M., Lal, S. S., and Aggarwal, P. K., "Increasing the efficiency of agronomy experiments in potato using INFOCROP-POTATO model", *Potato Research,* Vol. 48, No. 3–4, 2005, pp. 131–152
[25]Confalonieri, R., and Bechini, L., "A preliminary evaluation of the simulation model CropSyst for alfalfa", *European Journal of Agronomy*, Vol. 21, No. 2, 2004, pp. 223–237
[26]de Reffye, P., Hu, B., Kang, M., Letort, V., and Jaeger, M., "Two decades of research with the GreenLab model in agronomy", *Annals of Botany*, Vol. 127, No. 3, 2021, pp. 281–295
[27]Vos, J., Evers, J. B., Buck-Sorlin, G. H., Andrieu, B., Chelle, M., and de Visser, P. H. B., "Functional-structural plant modeling: A new versatile tool in crop science", *Journal of Experimental Botany*, Vol. 61, No. 8, 2010, pp. 2101–2115

[28]Soualiou, S., Wang, Z., Sun, W., de Reffye, P., Collins, B., Louarn, G., and Song, Y., "Functional–Structural Plant Models Mission in Advancing Crop Science: Opportunities and Prospects", *Frontiers in Plant Science*, Vol. 12, 2021,
[29]Vos, J., Evers, J. B., Buck-Sorlin, G. H., Andrieu, B., Chelle, M., and de Visser, P. H. B., "Functional-structural plant modelling: A new versatile tool in crop science", *Journal of Experimental Botany,* Vol. 61, No. 8, 2010, pp. 2101–2115
[30]Lopez, G., Favreau, R. R., Smith, C., and Dejong, T. M., "L-PEACH: A computer-based model to understand how peach trees grow", *HortTechnology*, Vol. *20*, No. 6, 2010, pp. 983–990
[31]Drouet, J. L., and Pagès, L., "GRAAL-CN: A model of GRowth, Architecture and ALlocation for Carbon and Nitrogen dynamics within whole plants formalised at the organ level", *Ecological Modelling*, Vol. 206, No. 3–4, 2007, pp. 231–249
[32]Fournier, C., and Andrieu, B., "ADEL-maize: An L-system based model for the integration of growth processes from the organ to the canopy. Application to regulation of morphogenesis by light availability", *Agronomie*, Vol. 19, No. 3–4, 1999, pp. 313–327
[33]Yan, H.-P., Kang, M.Z., de Reffye, P. and Dingkuhn, M., "A Dynamic, Architectural Plant Model Simulating Resource-dependent Growth", *Annals of Botany,* Vol. 93, No. 5, 2004, pp. 591–602
[34]Cournède, P.-H., Mathieu, A., Houllie, R. F., Barthélémy, D. and de Reffye, P., "Computing Competition for Light in the GREENLAB Model of Plant Growth: A Contribution to the Study of the Effects of Density on Resource Acquisition and Architectural Development", *Annals of Botany,* Vol. 101, No. 8, 2008, pp. 1207–1219
[35]Drouet, J. L., and Pagès, L., "GRAAL: A model of GRowth, Architecture and carbonALlocationduring the vegetative phase of the whole maize plant Model description and parameterisation", *Ecological Modelling*, Vol. 165, No. 2–3, 2003, pp. 147–173
[36]Allen, M. T., Prusinkiewicz, P., and DeJong T. M., "Using L-systems for modeling source-sink interactions, architecture and physiology of growing trees: the L-PEACH model", *New Phytologist*, Vol. 166, No. 3, 2005, pp. 869–880
[37]Maddonni, G. A., Otegui, M. E., Andrieu, B., Chelle, M., and Casal, J. J., "Maize Leaves Turn Away from Neighbors", *Plant Physiology,* Vol. 130, No. 3, 2002, pp. 1181–118
[38]Bertheloot, J., Andrieu, B., Fournier, C., and Martre, P., "A process-based model to simulate nitrogen distribution in wheat (Triticum aestivum) during grain-filling", *Functional Plant Biology,* Vol. 35, No. 10, 2008, pp. 781–796
[39]https://en.wikipedia.org/wiki/Controlled_ecological_life-support_system
[40]Poulet, L., "Developing physical models to understand the growth of plants in reduced gravity environments for applications in life-support systems", Chemical and Process Engineering. Université Blaise Pascal - Clermont-Ferrand II, 2018. English
[41]Wheeler, R. M., 2015, "NASA's controlled environment agriculture testing for space habitats", New Space 3, pp. 154–164
[42]Lasseur, C., Brunet, J., Weever, H. de, Dixon, M., Dussap, G., Godia, et all., "Melissa: The European project of closed life support system", *Gravitational and Space Biology*, Vol. 23, No. 2, 2010, pp. 3–12
[43]Amitrano, C., Arena, C., Rouphael, Y., De Pascale, S., De Micco, V., "Vapour pressure deficit: The hidden driver behind plant morpho functional traits in controlled environments", *Annals of Applied Biology*, Vol. 175, No. 1, 2019, pp. 313–325
[44]Volk, T., Bugbee, B., Wheeler, R. M., "An approach to crop modeling with the energy cascade", *International Journal of Earth Space,* Vol. 1, No. 3–4, 1995, pp. 119–127
[45]Cavazzoni, J., "Using explanatory crop models to develop simple tools for Advanced Life Support system studies", *Advances in Space Research*, Vol. 34, No. 7 spec, 2004, pp. 1528–1538
[46]Boscheri, G., Kacira, M., Patterson, L., Giacomelli, G., Sadler, P., Furfaro, R., et. all., "Modified energy cascade model adapted for a multicrop Lunar greenhouse prototype", *Advances in Space Research*, Vol. 50, No. 7, 2012, pp. 941–951
[47]Jones, H., Cavazzoni, J., "Top-Level Crop Models for Advanced Life Support Analysis", SAE Tech. Pap., 1999
[48]Bisbis, M. B., Gruda, N., Blanke, M., "Potential impacts of climate change on vegetable production and product quality–A review", *Journal of CleanerProduction*, Vol. 170, No. 1, 2018, pp. 1602–1620
[49]Anderson, M. S., Ewert, M. K., Keener, J. F., Wagner, S. A., "Life Support Baseline Values and Assumptions Document", Nasa/Tp-2015-218570, 2022, pp. 179–192
[50]Heuvelink, E., "Dry matter production in a tomato crop: measurements and simulation", *Annals of Botany,* Vol. 75, No. 4, 1995, pp. 369–379
[51]Heuvelink, E., "Evaluation of a Dynamic Simulation Model for Tomato Crop Growth and Development", *Annals of Botany*, Vol. 83, No. 4, 1999, pp. 413–422
[52]Guo, Y., Ma, Y., Zhan, Z., Li, B., Dingkuhn, M., Luquet, D., and de Reffye, P., "Parameter optimization and field validation of the functional-structural model GREENLAB for maize", *Annals of Botany*, Vol. 97, No. 2, 2006, pp. 217–230

3.1.2 Main outcomes of the article

- Plants need to be grown in hybrid LSSs for long-term space missions as physicochemical systems are too costly and insufficient for long-duration space missions.
- Existing empirical, process-based, and functional-structural models have limitations, they do not include space-specific factors such as altered gravity, exposure to cosmic/ionizing radiation (filtered out by Earth's atmosphere), and actively controlled atmospheric conditions (e.g., dynamic adjustment of humidity, CO_2, O_2, and light intensity to balance gas exchange). Because of that new type of model is needed.
- Future research should focus on improving model adaptability to include space-specific factors like gravity, radiation, and varying atmospheric conditions. This will allow the LSS to respond to changes in plant responses to environmental conditions in real time.

3.2 Heat and mass transfer

3.2.1 Physical vs. biological processes in plants

The interactions between physical processes, e.g., the movement of water and nutrients or heat and mass exchange, and biological processes in plants, like respiration, photosynthesis, and hormonal regulation, are essential for their growth, development, and adaptation to environmental changes. Physical processes are essential for immediate survival, biological processes enable long-term adaptation and evolution, showcasing the intricate balance between these two aspects in plant life.

Photosynthesis and transpiration stand out as the primary physiological processes driving gas and mass exchange between plants and the environment (Albrecht et al., 2020). Therefore, the exchange of heat and mass between plants and their surroundings strongly influences plant productivity, water consumption, and water use efficiency (Schymanski and Or, 2016).

Heat and mass transfer components are affected both by physiological (photosynthesis, transpiration, and respiration) and non-physiological processes (radiative and convective heat transfer). The close link between these processes means that changes in environmental conditions affect not just plant growth but also the overall heat exchange system within the plant.

The most important components of the heat balance are the convective and latent heat transfer, and the energy related to the short- and long-term radiation (see Figure 3-1).

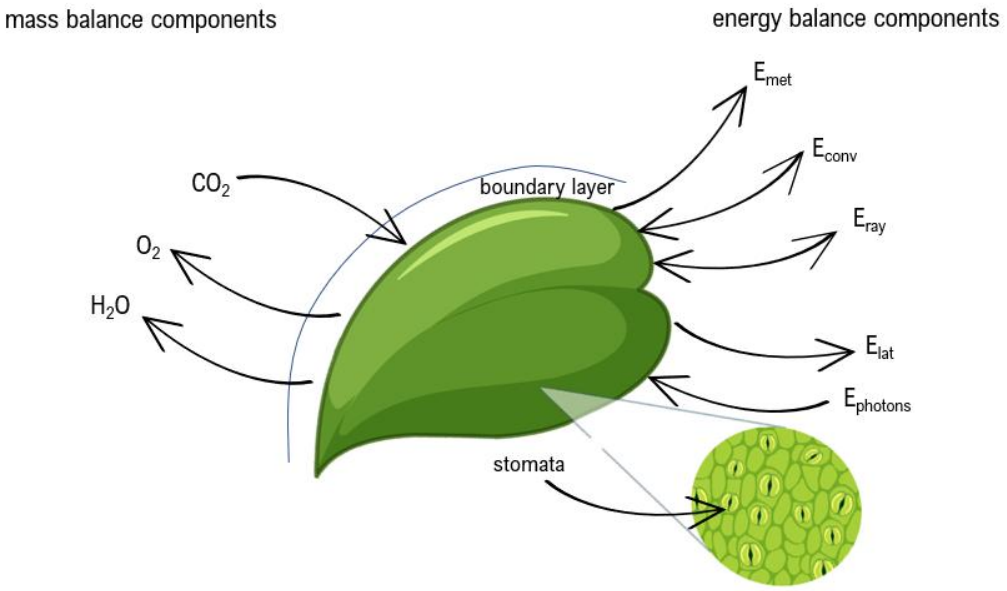

Figure 3-1 *Energy and mass balance components on the leaf level. $E_{photons}$ – Short-wave radiation Energy – [W], E_{ray} – Net longwave radiation Energy – [W], E_{conv} – Convection Energy – [W], E_{lat} – Latent Energy – [W], E_{met} – Metabolic Energy –[W]*

Convection is one of the main components of heat transfer in plants. There are two types of convection: forced and free convection. Forced convection is caused by wind or air movement, and it drives the heat transfer process. Free convection occurs due to differences in air density between the plant surface and the surrounding air. Both forced and free convection are driving forces for the exchange of heat between the plant and its environment. The efficiency of heat transfer by convection depends largely on the air velocity and temperature gradients, both of which impact the heat balance in plant tissues.

Transpiration, which involves heat loss through water evaporation, influences the leaf temperature, which in turn impacts convective heat transfer. Furthermore, the efficiency of transpiration is limited by the conductance of the boundary layer which is determined by the temperature, gas concentration gradients, and air velocities (Poulet et al., 2020). The boundary layer conductance is estimated by the use of heat transfer coefficients since direct measurements are not possible. These coefficients link the heat flux densities per unit area of the leaf to the temperature difference between the leaf and the surrounding air. The heat transfer coefficient strongly depends on the air velocity (forced convection), and the density

difference between the leaf surface and the environment (free convection), this values can be described using dimensionless numbers, like the Reynolds, or Nusselt (Defraeye et al., 2013).

Air movement impacts latent heat transfer by reducing the boundary layer resistance and preventing humidity build-up near the leaf. This maintains the vapor pressure gradient between the leaf and the ambient air, increasing transpiration and potentially inducing stomatal closure (Albrecht et al., 2020). Stomatal response is also affected by other environmental conditions like CO_2 concentration (Xu et al., 2016), incoming radiation, or the thermal conductivity of the leaves.

The thermal conductivity of plant leaves is high, as a result of a high-water content – for most of the terrestrial plants it is between 55%-85% of their fresh mass (Su et al., 2010). Therefore, the leaf water content affects the dynamics of the leaf surface temperature change.

3.2.2 Justification for using a leaf replica

Section 4.1 discusses the significance of heat and mass transfer in the interactions between plants and their surrounding environment. These interactions, which are significantly influenced by photosynthesis, transpiration and respiration, highlight the complexity of the processes taking place within plants to maintain an energy balance and respond to environmental stimuli. Although the focus of this PhD thesis lies on the physical processes occurring within plants, such as radiation absorption, heat convection, and mass transfer, it becomes increasingly clear that these cannot be entirely isolated from the biological processes occurring in the plants.

Physiological processes like for example transpiration and photosynthesis not only contribute to, but also regulate, the physical aspects of heat and mass transfer between the plants and the environment. Similarly, photosynthesis, plays a key regulatory role in the energy dynamics of the plant despite its minimal contribution to the overall energy budget,

Plants require essential elements like light (energy), water, carbon, and nutrients. When these factors deviate significantly from the optimal conditions, they can cause an abiotic stress (Cramer et al., 2011). Another source of stress can be rapid environmental fluctuations, such as temperature, light, or relative humidity.

According to (Zhang et al., 2020) the active suppression of growth is part of a plant survival strategies in response to adverse environments. The exact mechanisms, however, remain unknown, making it hard to incorporate stress factors into an energy balance or transpiration rate models. Current transpiration models do not simulate stomata real-time responses and because of that often underestimate water loss during high-temperature stress(Liu et al., 2024; Raghav et al., 2024), in order to simulate it more accurately it is necessary to create non-steady-state stomatal conductance models (Liu et al., 2024).

Another factor affecting the accuracy of modelling is the plant morphology. The size and density of stomata can vary not only within the same plant species but also within the same plant if the environmental conditions vary. For example, light or wind gradients can result in different stomatal densities and sizes between the leaves of a single plant.

Research on monocotyledonous plants (Sunarseh and Daningsih, 2019) shows that stomatal density decreases by ca. 20-25% while stomatal size increases by ca. 23-24% from the top to the bottom leaves of the plant, due to differences in light exposure and leaf developmental stage (earlier vs later-emerging leaves). Similarly, in lettuce (*Lactuca sativa*), studies have found that stomatal size and conductance vary significantly depending on light direction, with bottom-lit leaves developing stomata that are ca. 30-35% larger but ca. 40% lower in density compared to top-lit leaves (Wang et al., 2021).

Moreover, the opening and closing of stomata are closely related to the time of day and weather conditions (Monje and Bugbee, 2019; Wheeler et al., 2019). Stomatal movement participate in regulating transpiration, affecting leaf cooling, and modifying mass exchange rates in response to environmental conditions.

Leaves can also modify the magnitude of absorbed solar radiation – incident, reflected, and transmitted – by adjusting their orientation towards or against the sun and the wind (Lambers et al., 2008).

Biological responses to environmental stresses, nutrient availability and metabolic changes affect the physical processes of energy and mass transfer. Consequently, it is hard to study purely physical phenomena when working with real plants.

To decouple biological processes from physical ones, leaf replicas were introduced as a model to understand heat and mass transfer. Using leaf replicas in research focused on physical processes offers several advantages, including:

- They allow the study physical phenomena independently of biological and genetic variations.
- With replicas, it is easier to control and vary specific conditions to study their effects on heat and mass transfer.
- Experiments using replicas can be easily repeated to verify the results, which is more difficult with real plants due to their morphological variability.
- It eliminates the risks associated with the potential failure of biological systems under experimental conditions.
- In microgravity and parabolic flight studies, replicas provide a stable, consistent model without the biological changes that real plants would undergo in such environments.
- By understanding how various physical factors influence plant-like structures, more accurate models of heat and mass exchange can be developed.

Leaf replicas are useful tools for gaining new information in environments characterized by rapidly changing conditions, such as for example during parabolic flights which were used in these studies and are described in the chapter 5. The advantages include:

- Rapid changes in gravitational forces during the parabolic flight do not affects the behaviour of leaf replica, unlike real plants, which might suffer from physical stress under such conditions.
- Leaf replicas ensure consistent experimental conditions during the duration of the experiment, enabling more reliable data collection.
- Leaf replicas can be equipped with sensors and instrumentation that might be too invasive or damaging for live plants.
- Leaf replicas facilitate statistical analysis, ensuring consistent and reproducible conditions.

3.2.3 Modelling physical processes in higher plants using leaf replicas for space applications

This part is an article that was published in Comptes Rendus Mécanique, Volume 351, Special Issue S2 (2023), p. 97-113

INSTITUT DE FRANCE
Académie des sciences

Comptes Rendus
Mécanique

Joanna Kuzma, Lucie Poulet, Jean-Pierre Fontaine and Claude-Gilles Dussap

Modelling physical processes in higher plants using leaf replicas for space applications

Published online: 6 March 2023

https://doi.org/10.5802/crmeca.152

Part of Special Issue: Physical Science in Microgravity within the Thematic Group Fundamental and Applied Microgravity

Guest editors: Olga Budenkova (CNRS, Université Grenoble Alpes,Grenoble INP, SIMaP, 38000 Grenoble, France), Catherine Colin (IMFT, Université de Toulouse, CNRS, INPT, UPS et GDR 2799 Micropesanteur Fondamentale et Appliquée) and Guillaume Legros (ICARE, CNRS UPR 3021, Univ. Orléans et GDR 2799 Micropesanteur Fondamentale et Appliquée)

Les Comptes Rendus. Mécanique *sont membres du Centre Mersenne pour l'édition scientifique ouverte*
www.centre-mersenne.org
e-ISSN : 1873-7234

State of the art

Comptes Rendus
Mécanique
Published online: 6 March 2023
https://doi.org/10.5802/crmeca.152

Physical Science in Microgravity within the Thematic Group Fundamental and Applied Microgravity / *Sciences physiques en microgravité au sein du GDR Micropesanteur Fondamentale et Appliquée*

Modelling physical processes in higher plants using leaf replicas for space applications

Modélisation de processus physiques de plantes supérieures à l'aide de répliques de feuilles pour des applications spatiales

Joanna Kuzma [a, b], **Lucie Poulet** [a], **Jean-Pierre Fontaine*** [a] **and Claude-Gilles Dussap** [a]

[a] Université Clermont Auvergne, Clermont Auvergne INP, CNRS, Institut Pascal, F-63000, Clermont-Ferrand, 63000, France

[b] Centre National d'Etudes Spatiales (CNES), 31400 Toulouse, France

E-mails: joanna.kuzma@doctorant.uca.fr (J. Kuzma), Lucie.POULET@uca.fr (L. Poulet), j-pierre.fontaine@uca.fr (J.-P. Fontaine), C-Gilles.DUSSAP@uca.fr (C.-G. Dussap)

Abstract. In the future, higher plant cultivation will be a key component of Bioregenerative Life-Support Systems. This will require a deep understanding of phenomena that play an important role at the core of plant metabolism and of their interaction with the environment. Plants are complex organisms that must be studied with the use of leaf replicas. This enables the study of physical phenomena at the leaf surface, without biochemical or biological interactions nor genetic variability. To assess the influence of gravity, it is a necessary step to develop precise mechanistic models of plant behaviour in space. This review article presents the state-of-the-art of leaf replicas and concomitant phenomena, with a space gaze.

Résumé. À l'avenir, la culture de plantes supérieures sera un élément clé des systèmes de support de vie biorégénératifs. Cela nécessitera une compréhension approfondie des phénomènes qui jouent un rôle important au cœur du métabolisme des plantes et de leur interaction avec l'environnement. Les plantes sont des organismes complexes qui doivent être étudiés à l'aide de répliques de feuilles. Ceci permet l'étude des phénomènes physiques à la surface des feuilles, sans interactions biochimiques ou biologiques, ni variabilité génétique. Pour évaluer l'influence de la gravité, il est nécessaire de développer des modèles mécanistes précis du comportement des plantes dans l'espace. Cet article de synthèse présente l'état de l'art des répliques foliaires et des phénomènes concomitants, pour une application spatiale.

* Corresponding author.

Keywords. Leaf replica, Transpiration, Energy balance, Life-support systems, Heat exchange, Biophysical phenomenon, Mechanistic modelling.

Mots-clés. Réplique foliaire, Transpiration, Bilan énergétique, Systèmes de support de vie, Échange de chaleur, Phénomène biophysique, Modélisation mécaniste.

Published online: 6 March 2023

1. Introduction

The four pillars of life-support systems (LSS) are the provision of air, water, and food, as well as waste treatment [1, 2]. For long-duration space exploration missions, it will be necessary to recycle as much resources as possible and to grow food *in situ* [3]. Plants allow the supply of fresh vitamins and nutrients which will be lacking after many months in space [4, 5]. They also enable the recycling of oxygen and carbon into fresh nutrients and water sanitation through photosynthesis [6]. Moreover, it is well accepted that they contribute to the crew well-being [7].

Plants have grown in low Earth orbit [8, 9] for decades, but many challenges still remain before it will be possible to grow them sustainably for food production [10–13]. Since plants are reactive biological organisms, the elementary processes that govern their growth and development need to be thoroughly understood before they can reliably be grown on a larger scale in space and integrated within a bioregenerative LSS (BLSS) [12, 14]. This can be achieved with a mechanistic, multi-layer, and multi-scale (in space and time) approach to allow the development of knowledge-based models, which are prerequisites for implementing predictive models and run simulations out of the standard parametric range (e.g., in reduced gravity). For example, buoyancy-driven gas exchange at the leaf surface is altered in microgravity [15–18] and since it drives biomass and oxygen production [19], its understanding is crucial for plant growth in space.

Gas and heat exchange is largely dependent on leaf and plant canopy boundary layer thickness, which is a physical phenomenon linked to convective properties of the growth environment [17, 18, 20–22], which can be modelled independently of biological processes [23, 24]. It is influenced by airflow movements, which depend on forced and free convection—a result of buoyancy forces which therefore depends on gravity [17, 18]. Gas and heat exchange also depends on the plant stomata size and density, which are dependent on plant species and their growth environment [25–27].

The fact that plants present a genetic variability and are reactive systems [23,28,29] makes hard to study a given phenomenon independently from the others, in a controlled way. Therefore, leaf replicas have been developed and used to study strictly physical processes without influence of plant biological processes, particularly in the context of heat and mass exchange [21, 22, 30–45]. Most of the studied leaf replicas are made of metal and/or felt sheets and can incorporate pores to simulate stomata or resistors to study heat exchange. Their design depends on the hypotheses and research questions of the study.

The objective of this review is to provide an overview of the state-of-the-art of existing leaf replicas and their use to answer various questions pertaining to heat exchange and water transport across plants. A focus will be on the specific context of developing mechanistic models of plant gas exchange for applications in BLSS.

2. Challenges in using real plants

The high sensitivity of plants to their environment and their genetic variability makes it challenging to study their biophysical processes in spaceflight conditions, where volume and experiment opportunities are limited.

2.1. *Plants are reactive systems*

Plants need light (energy), water, carbon and nutrients and if these parameters are too far from optimal conditions, abiotic stress can appear [46]. Another source of stress can be the rapid changes in environmental physical parameters, such as temperature, light, or relative air humidity. The stress associated with these factors occurs within seconds to minutes of the parameter change and affects the metabolic processes of the plant which in consequence can lead to reduced yield [47].

According to [48] active suppression of growth is part of the plant survival strategies in response to adverse environments. The exact mechanisms, however, remain unknown, making it hard to take stress factors into consideration while modelling the growth or while computing for example the energy balance or transpiration rate.

Another factor which can affect the accuracy of the modelling is the plant morphology description. As it was highlighted in [49], the size and density of stomata can vary not only within the same plant species but also within the same plant if the environment conditions slightly vary. For example, small light or wind gradient can result in different stomatal densities between the leaves of a single plant. Moreover, the opening and closing of stomata is closely related to the time of day and to weather conditions [25, 50].

According to the plant needs, leaves can also modify the magnitude of absorbed solar radiation—incident, reflected, and transmitted—by orientating the leaves towards or against the sun and the wind [51]. As a consequence, untangling the biological and physical parameters is not simple.

2.2. *Sample size*

The estimation precision of the energy components or mass exchange between the environment and plants can also be affected by the variability of the collected samples, the variability of the process and the heterogeneity of environmental conditions. It was proven that light gradients across a growth chamber can cause significant differences in structure and physiology of the leaves [52]. These results highlight the fact that sample size may significantly affect the accuracy of ecophysiological trait estimates. To receive meaningful results, the sample size should be adjusted to the required confidence level and margin of error, as well as to the expected variation between individual results [53]. Taking all those factors into consideration, finding the optimal plant size sample is a challenge in spaceflight conditions where mass and volume are limited. Moreover, sample size might be limited by external factors like time, funding, or human capital.

One of the examples of a limited space and time are studies done in microgravity conditions—parabolic flights or outer space studies. Parabolic flight is one of the main sources of data on heat and mass exchange and boundary layer in microgravity, mainly because of its relatively low cost and availability, compared to studies in low Earth orbit. Additionally, most of the systems which were tested in space did not have the possibility to measure all of the previously mentioned parameters and phenomena on plants or leaf replicas because of the lack of humidity and/or temperature control [54]. In parabolic flight studies, the periodic evolution of the gravity level induces extra stresses to the plants. As described in the previous section, the influence of these stresses is not yet fully detailed and understood, and this might introduce confounded factors to the measurements.

Leaf replicas have been introduced in order to study physical processes occurring at the leaf level in steady and transient states, without the bias caused by environmental stress factors or genetic variability occurring on limited sample size. The collected data can be used for primary validation of predictive models describing these processes without biochemical interaction.

A model, which can accurately simulate physical processes, can later be extended or scaled to the whole canopy level [51].

3. Leaf replicas used in recent literature

Different types of replicas have been used to study physical processes within plants. Depending on the purpose, we identified three groups of replicas:

- Simple replicas made of one material (dry and wet),
- Complex replicas with simulated stomata,
- Replicas with internal heating.

The major topics analysed with replicas concerned the energy balance and transpiration rate and the boundary layer conductance. The symbols and notations, used later in this section, to present how leaf replicas can simplify the equations, are summarized in Table 1.

3.1. *Energy balance*

3.1.1. *Description of the biophysical phenomena*

The temperature of the environment is one of the major factors affecting almost all plant processes like photosynthesis, respiration, biosynthesis, membrane transport, transpiration and the volatilization of specific compounds [51]. Consequently, it is crucial to precisely understand its role in all processes.

Leaves absorb most of the short-wave radiation emitted by the sun (E_{photons}), from which small fractions are reflected, transmitted, or used in metabolic processes. As a result, plants developed mechanisms to dissipate the induced heat, to avoid getting overheated, so that these heat loss mechanisms are crucial for their survival. Heat is also given off as a side effect of photosynthesis through transpiration. The main components of plant energy balance are [55]:

- Emitting long-wave infrared radiation (E_{ray}),
- Convection heat transfer (E_{conv}),
- Latent heat transfer (E_{lat}).

All of the energy balance components are presented on the Figure 1.

During metabolic processes plants also produce some energy and during photosynthesis a certain amount of energy is consumed, however the amount of heat involved during these processes is relatively small compared to the processes mentioned above and is usually neglected in the calculations [51]. At steady state the conservation of energy implies that the sum of all these energy components is equal to zero, but even a small change in one of the components of the energy balance will cause a change in the leaf temperature. Mechanistic approaches to plant energy balance models have been described in [20, 24]. In general, the energy balance can be described using the following equation:

$$\frac{\mathrm{d}T_{\text{leaf}}}{\mathrm{d}t} = \frac{E_{\text{photons}} - E_{\text{ray}} - E_{\text{conv}} - E_{\text{lat}}}{Cp_{\text{leaf}}} \tag{3.1.1}$$

where Cp_{leaf}—the leaf specific heat capacity in $\mathrm{J{\cdot}K^{-1}}$.

For discrete light spectrum (like the ones in use on ISS), the amount of energy absorbed by the plants can be calculated using the equations described in [24]:

$$E_{\text{photons}} = I^{\max} N_A hc \sum_{i=\lambda_{\min}}^{\lambda_{\max}} \frac{\gamma_i}{\lambda_i} \tag{3.1.2}$$

Table 1. Summary of the symbols and notations

Name	Symbol	Unit
Light velocity	c	$\mathrm{m{\cdot}s^{-1}}$
Molar air specific heat capacity at constant pressure	C_p	$\mathrm{J{\cdot}mol^{-1}{\cdot}K^{-1}}$
Liquid water specific heat capacity at constant pressure	$Cp_{\mathrm{H_2O}}$	$\mathrm{J{\cdot}kg^{-1}{\cdot}K^{-1}}$
Specific heat capacity of humid air	C_s	$\mathrm{J{\cdot}kg^{-1}{\cdot}K^{-1}}$
Specific heat capacity of i component	C_p^i	$\mathrm{J{\cdot}K^{-1}}$
Diffusion coefficient for water	$D_{\mathrm{H_2O}}$	$\mathrm{m^2{\cdot}s^{-1}}$
Heat diffusion coefficient	D_t	$\mathrm{m^2{\cdot}s^{-1}}$
Convection energy	E_{conv}	W
Latent energy	E_{lat}	W
Short-wave radiation energy	E_{photons}	W
Net longwave energy	E_{ray}	W
Gravitational acceleration	g	$\mathrm{m{\cdot}s^{-2}}$
Leaf conductance for water vapour	$G^{\mathrm{H_2O}}$	$\mathrm{mol{\cdot}m^{-2}{\cdot}s^{-1}}$
Boundary layer conductance for water	$g_{\mathrm{BL}}^{\mathrm{H_2O}}$	$\mathrm{mol{\cdot}m^{-2}{\cdot}s^{-1}}$
Stomatal conductance for water	$g_s^{\mathrm{H_2O}}$	$\mathrm{mol{\cdot}m^{-2}{\cdot}s^{-1}}$
Boundary layer conductance for heat transfer	$g_{\mathrm{BL}}^{\mathrm{heat}}$	$\mathrm{m{\cdot}s^{-1}}$
Planck constant	h	J·s
Height of plant chamber	H	m
Maximum light absorption rate	I^{max}	$\mathrm{mol{\cdot}s^{-1}}$
Incident shortwave radiation	I_s	$\mathrm{W{\cdot}m^{-2}}$
Heat capacity	k	$\mathrm{J{\cdot}m^{-2}{\cdot}K^{-1}}$
Heat transfer coefficient	k_t	$\mathrm{m{\cdot}s^{-1}}$
Leaf characteristic length	L	m
Leaf area	LA	$\mathrm{m^2}$
Water mass in the leaf	$m_{\mathrm{H_2O}}$	kg
Avogadro number	N_A	$\mathrm{mol^{-1}}$
Atmospheric pressure of the bulk air	P_{bulk}	Pa
Water partial pressure in bulk air	$p_{\mathrm{bulk}}^{\mathrm{H_2O}}$	Pa
Water partial pressure at the leaf surface	$p_{\mathrm{leaf}}^{\mathrm{H_2O}}$	Pa
Ideal gas constant	R	$\mathrm{J{\cdot}mol^{-1}{\cdot}K^{-1}}$
Temperature	T	K
Bulk air temperature	T_{bulk}	K
Bulk air velocity	V_{bulk}	$\mathrm{m{\cdot}s^{-1}}$
Forced convection velocity	V_{forced}	$\mathrm{m{\cdot}s^{-1}}$
Free convection velocity	V_{free}	$\mathrm{m{\cdot}s^{-1}}$
Short wave absorbance	α	-
Percentage of the wavelength	γ_i	-
Boundary layer thickness	δ	m
Emissivity	ε	-
Incident photon wavelength	λ_i	m
Air density	ρ	$\mathrm{kg{\cdot}m^{-3}}$
Water vapor molar density	$\rho_{\mathrm{mol,H_2O}}$	$\mathrm{mol{\cdot}m^{-3}}$
Stefan–Boltzmann constant	σ	$\mathrm{W{\cdot}m^{-2}{\cdot}K^{-4}}$
Water transpiration rate	$\varphi_{\mathrm{H_2O}}$	$\mathrm{mol{\cdot}s^{-1}}$
Water latent heat of vaporisation	Λ_{mol}	$\mathrm{J{\cdot}mol^{-1}}$
Subscript i refers to leaf, replica, black replica, white replica, dry replica, wet replica, heated replica respectively	i_{leaf}, i_{rep}, i_{black}, i_{white}, i_{dry}, i_{wet}, i_{heated}	-

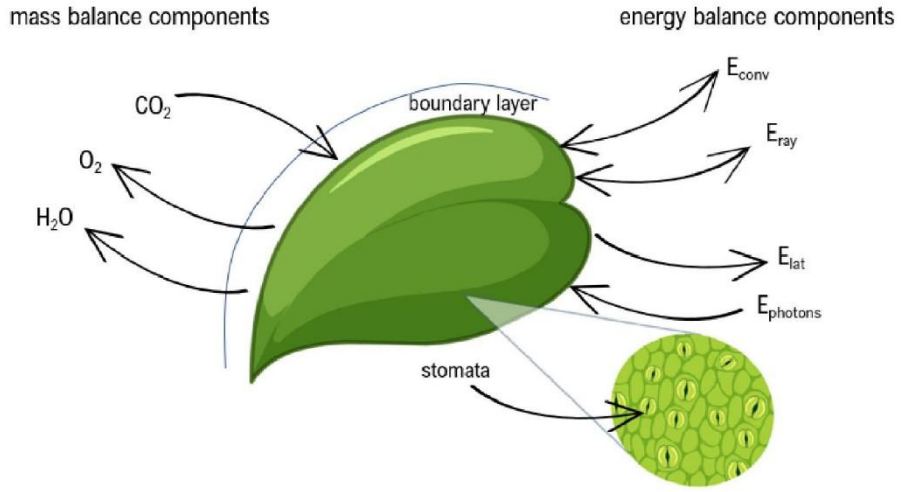

Figure 1. Leaf energy balance components.

where $I^{\max}$—maximum light absorption rate, N_A—Avogadro number, h—Planck constant, c—light velocity, $\lambda_{\min/\max}$—respectively the lowest and highest wavelengths of the light source, γ_i—percentage of the wavelength λ_i.

For continuous light spectrum (like the sun), the absorbed energy can be described as:

$$E_{\text{photons}} = \int_{\lambda_{\min}}^{\lambda_{\max}} \frac{I \cdot N_A h c}{\lambda} \, \mathrm{d}\lambda. \tag{3.1.3}$$

By assuming the plant canopy and the surroundings have similar emissivity, and according to the Stefan–Boltzmann law, the net radiation energy for the leaf can be calculated using following equation:

$$E_{\text{ray}} = \varepsilon\sigma(T_{\text{leaf}}^4 - T_{\text{bulk}}^4)LA \tag{3.1.4}$$

where ε—emissivity coefficient value usually between 0.94 and 0.99 for plants, σ—Stefan–Boltzmann constant, T_{leaf}—leaf temperature, T_{bulk}—bulk air temperature and LA—leaf area.

Although heat exchanged via transpiration is one of the main components of the energy balance, subsequent leaf cooling is a consequence of the stomatal opening required to sustain photosynthesis and leading to water evaporation through them, rather than a mechanism to control leaf temperature. Without latent energy loss however, the leaf temperature could rapidly rise to lethal level [56].

The latent heat flux can be calculated using the following equation:

$$E_{\text{lat}} = \Lambda_{\text{mol}} \varphi_{\text{H}_2\text{O}} \tag{3.1.5}$$

where Λ_{mol}—water latent heat of vaporisation and $\varphi_{\text{H}_2\text{O}}$—water transpiration rate.

Another component of plant heat balance is the convective heat transfer which is related to the air flow around the leaf. Heat and mass diffuse through the leaf boundary layers and are modelled by the boundary layer conductance [52]. It can be described with the following equation [24]:

$$E_{\text{conv}} = C_p k_t \frac{P_{\text{bulk}}}{R T_{\text{bulk}}} (T_{\text{leaf}} - T_{\text{bulk}}) LA \tag{3.1.6}$$

where C_p—molar air specific heat capacity at constant pressure, P_{bulk}—atmospheric pressure of the bulk air, T_{leaf}—leaf surface temperature, LA—leaf area, k_t—heat transfer coefficient defined as a function of heat boundary layer thickness and heat diffusion coefficient:

$$k_t = \frac{D_t}{\delta} \tag{3.1.7}$$

where δ—boundary layer thickness D_t—heat diffusion coefficient.

Because of the phenomena described in this article appear in a gas phase—the Prandtl and Schmidt numbers are close to unity, the heat and mass boundary layers described here later, are assumed to be equal and named δ hereafter.

The boundary layer thickness can be calculated using following equation:

$$\delta = \frac{2}{\xi}\sqrt{\frac{\upsilon L}{V_{\text{bulk}}}} \tag{3.1.8}$$

where ξ—empirical coefficient, usually varying between 1–1.33, υ—air kinetic viscosity, L—leaf characteristic length, V_{bulk}—bulk air velocity.

Where bulk air velocity is defined in the following way:

$$V_{\text{bulk}} = V_{\text{free}} + V_{\text{forced}} \tag{3.1.9}$$

where V_{free}—free convection velocity, V_{forced}—forced convection velocity.

Free convection velocity is a function of gravity:

$$V_{\text{free}} = \sqrt{2gH\frac{\Delta\rho}{\rho}} \tag{3.1.10}$$

where g—gravitational acceleration, H—height of the chamber $\Delta\rho$—density gradient between the surface of the leaf and bulk air ρ—air density. Detailed description of this model can be found in [24].

For studies conducted in microgravity, the lack of natural convection must be considered, as it significantly affects the energy balance components [56]. The studies in microgravity will allow to understand this phenomenon and test the accuracy of the model.

3.1.2. *Associated replicas*

To study the energy balance of a leaf, many researchers used dry replicas (Table 2). The idea was to use a dry reference surface with properties (radiative and aerodynamic) similar to a real leaf and to place it in the same environment as a real plant or other replicas in order to assess the net energy flux due to light energy exchanges [31, 32]. The source of the energy provided to the replica was an external light source [32–34] or internal heating by using resistors [35,36]. The use of dry replicas eliminates the latent heat term from the energy balance equations and thus enables their simplification; it also allows to remove from the equation most of the effects of the surrounding environment like for example long wave radiation.

Dry replicas were used to estimate the convective heat transfer in normal conditions—for different airflows [32,38], leaf temperatures [35,36], or gravity conditions [32,33] without secondary effects of the stress on other energy balance components.

The shapes of the leaf replicas were usually mimicking the shape of real leaves tested in parallel, such as those of barley wheat, strawberry or sweet potato [31, 32, 36]. Dry replicas were made from copper [32], brass sheet [35], Perspex [36] or aluminium sheet [31,34]. Scientists were searching for materials with optical properties close to the ones of real leaves [32,35,36].

Vialet-Chabrand and Lawson however have highlighted in [31] that the reference materials did not have exactly the same optical and thermal properties as real leaves, and this may introduce a bias in estimating the heat balance parameters. The authors suggested to directly include

Table 2. Summary of the energy balance studies done with replicas

Studied phenomena	Type of replica	Reference	Tested parameters	Used sensors	Environment
Energy balance	Dry replica	[31]	Day/night transition	IR camera, thermocouples, light sensor	Controlled
	Pair of dry/wet replica	[32]	Wind speed, irradiance	Thermocouples	Controlled
		[33]	Gravity, wind speed	IR camera	Controlled
		[34]	Wind speed	Thermocouples, anemometer, scale	Controlled
	Heated replica/non heated replica	[35]	Wind speed	Thermocouples, anemometer	Controlled
		[36]	Wind speed, wind angle	IR camera, thermocouples, radiometer	Controlled
	Replica with stomata	[30]	Wind speed, humidity, irradiance, pores density	IR camera, thermocouples, heat flux sensor	Controlled
		[31]	Day/night transition	IR camera, thermocouples, light sensor	Controlled

differences in thermal and optical properties in the energy balance equations and predict the leaf thermal kinetics from a reference material instead of mimicking leaf properties [35]:

$$\frac{\mathrm{d}T^{\mathrm{leaf}}}{\mathrm{d}t} = \frac{Cp^{\mathrm{rep}}\frac{\mathrm{d}T^{\mathrm{rep}}}{\mathrm{d}t} - (E^{\mathrm{leaf}}_{\mathrm{photons}} - E^{\mathrm{rep}}_{\mathrm{photons}}) + (E^{\mathrm{leaf}}_{\mathrm{ray}} - E^{\mathrm{rep}}_{\mathrm{ray}}) + (E^{\mathrm{leaf}}_{\mathrm{conv}} - E^{\mathrm{rep}}_{\mathrm{conv}}) + E^{\mathrm{leaf}}_{\mathrm{lat}}}{Cp^{\mathrm{leaf}}} \tag{3.1.11}$$

The terms are as explained above. The superscript leaf is of the real leaf, the subscript rep for replica.

Another approach to simplify energy balance is by using dry and wet replicas with similar thermal capacity. Measuring the temperature difference between them in the same environmental conditions enables the computation of the latent heat flux from the wet replica. Indeed:

$$Cp^{\mathrm{rep}}\left(\frac{\mathrm{d}T^{\mathrm{dry}}}{\mathrm{d}t} - \frac{\mathrm{d}T^{\mathrm{wet}}}{\mathrm{d}t}\right) = (E^{\mathrm{dry}}_{\mathrm{photons}} - E^{\mathrm{wet}}_{\mathrm{photons}}) - (E^{\mathrm{dry}}_{\mathrm{ray}} - E^{\mathrm{wet}}_{\mathrm{ray}}) - (E^{\mathrm{dry}}_{\mathrm{conv}} - E^{\mathrm{wet}}_{\mathrm{conv}}) - (E^{\mathrm{dry}}_{\mathrm{lat}} - E^{\mathrm{wet}}_{\mathrm{lat}}) \tag{3.1.12}$$

The terms are as explained above. The superscript dry is of the dry replica, the subscript wet for wet replica.

Since the short-wave incoming radiation energy, the long-wave energy and the convection

energy are the same for both replicas, the equation can be derived only with the modelling of the latent energy flux:

$$Cp^{\text{rep}}\left(\frac{\mathrm{d}T^{\text{dry}}}{\mathrm{d}t}-\frac{\mathrm{d}T^{\text{wet}}}{\mathrm{d}t}\right)=E_{\text{lat}}^{\text{wet}} \tag{3.1.13}$$

By using replica with stomata together with dry replica it is possible to calculate the latent energy flux of the leaves with the specified size of stomata by applying Equation (3.1.13).

Heated replicas combained with not heated ones were used to calculate the convection energy. If the replica did not have an external source of energy (other than the heater in one of them) and if the temperature of the not heated one is equal to the temperature of the environment the Equation (3.1.12) can be simplified to:

$$Cp\frac{\mathrm{d}T^{\text{heated}}}{\mathrm{d}t}=-E_{\text{conv}}^{\text{heated}} \tag{3.1.14}$$

The terms are as explained above. The superscript heated is of the heated replica.

3.2. *Transpiration*

3.2.1. *Description of the biophysical phenomenon*

The transpiration rate (φ_{H_2O}) from the Equation (3.1.5) can be calculated using the following equation:

$$\varphi_{H_2O}=\Lambda_{\text{mol}}\frac{G^{H_2O}}{P_{\text{bulk}}}(p_{\text{leaf}}^{H_2O}-p_{\text{bulk}}^{H_2O})LA \tag{3.2.1}$$

where P_{bulk}—bulk air total pressure, $p_{\text{leaf}}^{H_2O}$—water partial pressure at the leaf surface, $p_{\text{bulk}}^{H_2O}$—water partial pressure in bulk air and LA—leaf area, G^{H_2O}—leaf conductance for water vapour defined as:

$$G^{H_2O}=\frac{g_{\text{BL}}^{H_2O}+g_s^{H_2O}}{g_{\text{BL}}^{H_2O}\cdot g_s^{H_2O}} \tag{3.2.2}$$

where $g_s^{H_2O}$—stomatal conductance for water and $g_{\text{BL}}^{H_2O}$—boundary layer conductance for water vapour, defined as a function of boundary layer thickness, where boundary layer thickness depends on the gravity. For the detailed equations, please refer to [24].

The leaf conductance for diffusion of water vapour depends on the stomatal and boundary layer conductance. The boundary layer conductance depends on their thicknes which depends on the gravity as it was described in Equations (3.1.8)–(3.1.10), so transpiration is another component which is strongly affected by a reduced or the absence of gravity and therefore needs to be studied.

3.2.2. *Associated replicas*

In the studies of transpiration rates, a few types of replicas have been used (see Table 3). The simplest approach was to use a wet replica together with a real leaf to determine the air water vapor resistance [22, 37].

When a wet replica was combined with a dry one, the resistance value could later be used to calculate the transpiration rate of the real leaf [34]. One of the early studies of the transpiration used two aluminium sheets, a bare one and one with a wet filter glued to it [34]. Both replicas had thermocouples sticked to the surface and were placed on a scale to measure the evaporation rate. The goal of the study was to determine the air water vapor resistance. Currently the simple wet replicas were mostly made from wet cloth or paper and placed on a supporting structure.

Table 3. Summary of the transpiration studies done with replicas

Studied phenomena	Type of replica	Reference	Tested parameters	Used sensors	Environment
Transpiration rate	Wet replica combined with real leaf	[22]	Wind speed	IR camera, thermocouples, hygrometer	Controlled
		[37]	Gravity	IR camera, thermocouple, leaf porometer, hygrometer	Controlled
	Wet replica	[38]	Light intensity	IR camera	Controlled
	Pair of dry/wet replica	[34]	Wind speed	Thermocouples, anemometer, scale	Controlled
	Vessel with the perforated structure on the top	[39]	Pores size, pores density	Scale, humidity sensors	Controlled
		[40]	Pores size, pores density, pore geometry	Scale, anemometer, humidity sensor,	Controlled
		[41]	Pores size, pores density, leaf angle	Scale, thermocouples, anemometer, humidity sensor, pressure sensor	Controlled
	Replica with stomata	[30]	Wind speed, humidity, irradiance, pores density	IR camera, thermocouples, heat flux sensor	Controlled
		[31]	Day/night transition	IR camera, thermocouples, light sensor	Controlled

When they were compared with dry replicas it was possible to calculate the transpiration rate by applying equation:

$$\varphi_{H_2O} = \frac{Cp}{\Lambda_{mol}} \left(\frac{dT^{dry}}{dt} - \frac{dT^{wet}}{dt} \right) \tag{3.2.3}$$

The terms are as explained above.

The simple wet replica however, did not have pores, so the evaporation was not limited by them and it was similar to the evaporation from a free surface [34]. Hence, the evaporation energy from such replicas is overestimated compared to the one of a real leaf. To solve this problem another type of replica was developed. In the literature two types of replicas with artificial stomata are described. The first one consists of a petri dish or other small vessel with a micro-perforated foil, or a plate placed on it [39–41]. The main purpose of these studies was to investigate the influence of the size, the density, the shape of pores and the angle of the leaf on the evaporation

rate and relate it to the influence of stomata on leaf transpiration. The replicas were put on a scale or were weighted periodically [39–41] to measure the change in weight over time. This kind of setup allowed an accurate evaluation of the rate of evaporation, but the thermal and buffer properties of this type of replica are significantly different from those of real leaves. This is due to different surface areas, materials and thicknesses, flat shapes, not flexible structures, and greater heat capacities (due to the thick water layer in the vessel with water).

In order to solve this problem Schymanski *et al.* proposed another type of replica, which includes pores that are similar to stomata in terms of size [30]. This replica consists of a capillary filter paper glued onto aluminium tape with a water supplying tube and thermocouples sandwiched between the layers. On one side of the replica, the aluminium foil had artificial stomata with defined dimensions—similar in size to real stomata. The non-transpiring side was covered with black aluminium tape. The studies were conducted in a closed chamber and the evaporation rate was measured based on the parameters of the air coming in and out of the measurements area with the humidity sensor, anemometers, and thermocouples. The replica was tested for various humidity and wind speed conditions and with several pore densities. This setup allowed to study evaporation rate together with the energy balance. The replica was mainly developed to study the energy balance at steady state. This type of replica was slightly modified later by Vialet-Chabrand and Lawson to make measurements in dynamic conditions [31]. This replica was made of an aluminium plate which was covered by black tape with known absorbance and emissivity on non-transpiring side like in the previously described replica. The transpiring side of the leaf was covered with a felt fabric enclosed in a plastic microporous sheet, where pores had a known diameter depth and density. The felt sandwiched between the aluminium layers was saturated with water, so the only factors affecting the transpiration were the size and density of the pores and the environmental conditions (fluctuating light environment, wind speed or humidity). These factors together with the angle of the leaf facing the flow were studied in detail. This replica was studied together with two dry replicas of same absorbance but different emissivity. This allowed the calculation of every component of the leaf energy balance separately by measuring the difference in the temperature between all the replicas. The whole calculation procedure is described in [31].

3.3. *Boundary layer*

The boundary layer is a representation model of the thin layer of air that develops close to a leaf in presence of an air flow and where the physical parameters like velocity, temperature, H_2O and O_2 concentrations are modified by diffusion [57].

3.3.1. *Description of the biophysical phenomenon*

The boundary layer conductance for water ($g_{BL}^{H_2O}$) can be described using the following equation:

$$g_{BL}^{H_2O} = \frac{D_{H_2O}\rho_{mol,H_2O}}{\delta} \tag{3.3.1}$$

where: D_{H_2O}—diffusion coefficient for water, ρ_{mol,H_2O}—water vapor molar density, δ—boundary layer thickness, described with the Equation (3.1.8). For more details please, refer to [24].

It was shown in [22] that increased ventilation causes a reduction in the leaf boundary layer resistance. This phenomenon is quite significant in microgravity, where there is no free convection, and the thickness of the boundary layer goes to infinity if there is no forced convection [24]. A detailed description of the model of the boundary layer with the gravity as a parameter can be found in Poulet *et al.* [24].

3.3.2. *Associated replicas*

The experiments to study the boundary layer conductance can be divided into two groups (Table 4): experiments performed in a controlled, laboratory environment [22,30,31,33,35,36,44] and experiments in a natural environment—like field, forest or a greenhouse [21, 42–44].

Most of the experiments carried out in the field used a similar design for the leaf replica. They were made of highly polished brass sheets [21, 42, 44] or flexible Mylar1 sheet [43]. The shape and size of the replicas were adjusted to the shape and size of the average leaf of the studied plant or tree. In between the sheets or on the bottom part the heaters were glued. The heater was or isolated with enamel coating [21], or double-sided adhesive tape [42, 45] or glued with double-sided adhesive tape with epoxy resin [44], Sellotape [35] or moulded into the leaf replica [36]. The thermocouples were attached to the replica to measure the mean temperature of the replica surface and the dynamic of the temperature change. In the field experiments, replicas were attached to the real plant. In some studies, the replicas were used in pairs and were alternatively heated [42, 43] or one was heated and the other not [21, 44]. Similar replicas have been used to calculate the boundary layer conductance in controlled environment [35, 36, 44, 45]. In these tests, the main goal was to calculate the boundary layer conductance as a function of the leaf temperature and airflow [35, 36, 44, 45] and study the corelation between the boundary layer conductance and the angle of the wind [36]. The thickness and shape of the leaf were similar to the real leaves. In the experiment described by Schymanski *et al.* [30] the replica described in Section 3.2.2 was used, to test the leaf conductance as a function of wind speed and vapour pressure in steady state.

To simulate boundary layer parameters, Vialet-Chabrand and Lawson in [31] has proposed another approach (described as well in the Section 3.2.2). Using two dry replicas at the same time with identical thermal properties but covered with a different colour (black and white to differentiate their optical properties), allows to calculate heat boundary layer conductance in the dynamic conditions by applying equation below:

$$g_{\mathrm{BL}}^{\mathrm{heat}} = \frac{k\left(\frac{\mathrm{d}T^{\mathrm{white}}}{\mathrm{d}t} - \frac{\mathrm{d}T^{\mathrm{black}}}{\mathrm{d}t}\right) + I_s(\alpha^{\mathrm{black}} - \alpha^{\mathrm{white}}) - 2\sigma(\varepsilon^{\mathrm{white}} T^{\mathrm{white}^4} - \varepsilon^{\mathrm{black}} T^{\mathrm{black}^4})}{2\rho C_s(T^{\mathrm{white}} - T^{\mathrm{black}})} \tag{3.3.2}$$

where $g_{\mathrm{BL}}^{\mathrm{heat}}$—boundary layer conductance, I_s—incident shortwave radiation, α—short wave absorbance, ρ—air density, k—heat capacity of the replica, C_s—specific heat capacity of humid air.

The main goal of this experiment was to develop a procedure and model to calculate the stomatal conductance in transient regime by using replicas. A good understanding of the processes at the leaf level can pave the way to scaling up and modelling a whole canopy instead of single leaves by using mechanistic equations. The complexity of this topic is described in the next section.

4. Scaling-up gas exchange from the leaf to the canopy level with an energy balance

For the scaling-up of the physical phenomena from the leaf level to the canopy level, it is fundamental to determine among all the interactions within the plants, especially the ones that are strongly affected by the surroundings, as in most cases changing from one scale to another is not linear. For example, the prediction of canopy transpiration is different from the results which would be obtained by summing up individual leaf responses because each leaf significantly affects the surrounding environment by changing e.g., the wind speed, the irradiance, or the relative humidity. Therefore, the transpiration rate predicted for a canopy from a single leaf model would be overestimated. In addition, the change in irradiance is exponentially decreasing with

Table 4. Summary of the energy balance studies with replicas

Studied phenomena	Type of replica	Reference	Tested parameters	Used sensors	Environment
Boundary layer conductance	Wet replica	[22]	Wind speed	IR camera, thermocouples, hygrometer	Controlled
	Pair of 2 dry replicas	[31]	Day/night transition	IR camera, thermocouples, light sensor	Controlled
	Pair of dry/wet replica	[33]	Gravity, wind speed	IR camera	Controlled
	Heated replica	[21]	Day/night transition, leaf position	IR camera, thermocouples, light sensor	Greenhouse
		[42]	Wind speed	IR camera, thermocouples, light sensor	Greenhouse
		[43]	Wind speed, time of the day	IR camera, thermocouples	Field experiment
		[44]	Wind speed	Thermocouples, humidity sensor, anemometer, scale	Field experiment, controlled
		[35]	Wind speed	Thermocouples, anemometer	Controlled
		[45]	Temperature gradient, wind speed	Thermocouples, cameras	Controlled
		[36]	Wind speed, wind angle	IR camera, thermocouples, radiometer	Controlled
	Replica with stomata	[30]	Wind speed, humidity, irradiance, pores density	IR camera, thermocouples, heat flux sensor	Controlled
		[31]	Day/night transition	IR camera, thermocouples, light sensor	Controlled

the leaf area index, and this significantly reduces the amount of light absorbed by the leaves which are not directly exposed to the sun [51].

The plant canopy generates a resistance to air movements, which in consequence reduces wind speed within the canopy and in turn lowers the boundary layer conductance of certain leaves, as compared to what would be expected based on a single leaf of similar dimension and submitted to the same environmental parameters. Transpiration also affects the local water vapour pressure around the leaf. When stomatal conductance increases, water vapour pressure around the leaves increases as well and therefore reduces transpiration (see Equation (3.2.1)). In consequence transpiration increases less than what would be expected from the increase in stomatal conductance alone [58].

A good model for scaling-up from leaf to the canopy level will be based on mechanistic processes that develop at a lower scale. Hence, it is necessary to determine mechanistic model of a single leaf behaviour under specific environmental conditions, and for that it is necessary to start with a leaf replica.

This approach will help to address the questions which still have not been completely answered, like for example: can we use a big leaf model to calculate gas exchange and energy balance of a whole plant? Or it is necessary to combine individual gas exchange of each leaf and their individual microclimate in the energy balance at the canopy level?

Answering these questions is mandatory for developing safe, reliable, and robust LSS based on plants and to reach a full control of them.

5. Conclusions—how can leaf replicas help us to fill the gap in modelling

Understanding physical processes behind stomatal conductance in space environment, linked to energy and mass balances through mechanistic models, should enable a better comprehension of plant gas exchange in greater details. To achieve this, it is crucial to quantify how the boundary layer thickness varies in changing conditions, like space, or fluctuating conditions associated to parabolic flights. Microgravity strongly affects the physical exchanges at the leaf surface, being the first step of a cascade of biological events that are a consequence of these out-of-range conditions. To achieve a detailed understanding of physical processes at the leaf surface, replicas are necessary. This will allow the development of safe and controllable life-support systems based on living organisms.

The integration of mechanistic models at the leaf level will have to be scaled at the whole canopy in order to use knowledge-based description of mass, heat and energy exchange instead of empirical models, that were not developed for closed or space environments. This is the path for the development of reliable higher plant chambers in space environments.

Conflicts of interest

Authors have no conflict of interest to declare.

Acknowledgements

The authors would like to acknowledge CNES and the MELiSSA Foundation for funding JK's PhD, in the frame of which this study was done.

The authors wish to thank deeply the reviewers for the time they spent on the review and the judicious comments they gave.

References

[1] M. K. Ewert, T. T. Chen, C. D. Powell, *Life Support Baseline Values and Assumptions Document*, 2022, NASA/TP-2015218570/REV2, NASA JSC. (English only) https://ntrs.nasa.gov/citations/20210024855.

[2] P. Eckart, "Fundamentals of life support systems", in *Spaceflight Life Support and Biospherics*, Springer, Netherlands, Dordrecht, 1996, p. 79-173.

[3] R. M. Wheeler, "Agriculture for space: people and places paving the way", *Open Agric.* **2** (2017), p. 14-32.

[4] G. D. Massa, J. T. Richards, L. E. Spencer, M. E. Hummerick, G. W. Stutte, R. M. Wheeler, G. L. Douglas, T. Sirmons, "Selection of leafy green vegetable varieties for a pick-and-eat diet supplement on ISS", in *45th International Conference on Environmental Systems ICES-2015-252, Bellevue, Washington, July*, 2015.

[5] C. M. Johnson, H. O. Boles, L. E. Spencer, L. Poulet, M. Romeyn, J. M. Bunchek, R. Fritsche, G. D. Massa, A. O'Rourke, R. M. Wheeler, "Supplemental food production with plants: a review of NASA research", *Front. Astron. Space Sci.* **8** (2021), article no. 734343.

[6] R. M. Wheeler, "Plants for human life support in space: from Myers to Mars", *Gravitat. Space Res.* **23** (2010), p. 25-36.

[7] R. Odeh, C. L. Guy, "Gardening for therapeutic people-plant interactions during long-duration space missions", *Open Agric.* **2** (2017), p. 1-13.

[8] D. M. Porterfield, G. S. Neichitailo, A. L. Mashinski, M. E. Musgrave, "Spaceflight hardware for conducting plant growth experiments in space: The early years 1960–2000", *Adv. Space Res.* **31** (2003), p. 183-193.

[9] G. D. Massa, R. M. Wheeler, R. C. Morrow, H. G. Levine, "Growth chambers on the International Space Station for large plants", *Acta Hortic.* **2** (2016), no. 1, p. 215-222.

[10] M. S. Anderson, D. Barta, G. Douglas, B. Motil, G. Massa, R. Fritsche, C. Quincy, M. Romeyn, A. Hanford, "Key gaps for enabling plant growth in future missions", in *AIAA SPACE and Astronautics Forum and Exposition*, American Institute of Aeronautics and Astronautics, Orlando, FL, 2017.

[11] E. Kordyum, K. H. Hasenstein, "Plant biology for space exploration – Building on the past, preparing for the future", *Life Sci. Space Res.* **29** (2021), p. 1-7.

[12] F. J. Medina, A. Manzano, A. Villacampa, M. Ciska, R. Herranz, "Understanding reduced gravity effects on early plant development before attempting life-support farming in the Moon and Mars", *Front. Astron. Space Sci.* **8** (2021), article no. 729154.

[13] L. Poulet, K. Engeling, T. Hatch, S. Stahl-Rommel, Y.-A. Velez Justiniano, S. Castro-Wallace, J. Bunchek, O. Monje, M. Hummerick, C. L. M. Khodadad, L. E. Spencer, J. Pechous, C. M. Johnson, R. Fritsche, G. D. Massa, M. W. Romeyn, A. E. O'Rourke, R. W. Wheeler, "Large-scale crop production for the Moon and Mars: current gaps and future perspectives", *Front. Astron. Space Sci.* **8** (2022), article no. 733944.

[14] L. Poulet, J.-P. Fontaine, C.-G. Dussap, "Plant's response to space environment: a comprehensive review including mechanistic modelling for future space gardeners", *Bot. Lett.* **163** (2016), p. 337-347.

[15] Y. Kitaya, M. Kawai, J. Tsuruyama, H. Takahashi, A. Tani, E. Goto, T. Saito, M. Kiyota, "The effect of gravity on surface temperature and net photosynthetic rate of plant leaves", *Adv. Space Res.* **28** (2001), p. 659-664.

[16] Y. Kitaya, H. Hirai, T. Shibuya, "Important role of air convection for plant production in space farming", *Biol. Sci. Space* **24** (2010), p. 121-128.

[17] D. M. Porterfield, "The biophysical limitations in physiological transport and exchange in plants grown in microgravity", *J. Plant Growth Regul.* **21** (2002), p. 177-190.

[18] O. Monje, G. W. Stutte, G. D. Goins, D. M. Porterfield, G. E. Bingham, "Farming in space: Environmental and biophysical concerns", *Adv. Space Res.* **31** (2003), p. 151-167.

[19] E. Peiro, A. Pannico, S. G. Colleoni, L. Bucchieri, Y. Rouphael, S. De Pascale, R. Paradiso, F. Gòdia, "Air distribution in a fully-closed higher plant growth chamber impacts crop performance of hydroponically-grown lettuce", *Front. Plant Sci.* **11** (2020), article no. 537.

[20] S. J. Schymanski, D. Or, "Wind increases leaf water use efficiency", *Plant Cell Environ.* **39** (2016), p. 1448-1459.

[21] K. Kimura, D. Yasutake, A. Yamanami, M. Kitano, "Spatial examination of leaf-boundary-layer conductance using artificial leaves for assessment of light airflow within a plant canopy under different controlled greenhouse conditions", *Agric. For. Meteorol.* **280** (2020), article no. 107773.

[22] Y. Kitaya, J. Tsuruyama, T. Shibuya, M. Yoshida, M. Kiyota, "Effects of air current speed on gas exchange in plant leaves and plant canopies", *Adv. Space Res.* **31** (2003), p. 177-182.

[23] S. J. Schymanski, D. Or, M. Zwieniecki, "Stomatal control and leaf thermal and hydraulic capacitances under rapid environmental fluctuations", *PLoS One* **8** (2013), article no. e54231.

[24] L. Poulet, C.-G. Dussap, J.-P. Fontaine, "Development of a mechanistic model of leaf surface gas exchange coupling mass and energy balances for life-support systems applications", *Acta Astronaut.* **175** (2020), p. 517-530.

[25] O. Monje, B. Bugbee, "Radiometric method for determining canopy stomatal conductance in controlled environments", *Agronomy* **9** (2019), article no. 114.

[26] G. Thakur, S. Schymanski, I. Trebs, K. Mallick, M. Suils, O. Eiff, E. Zehe, "Bridging the gap between leaf surface and

the canopy air space: Leaf size matters for heat transfer resistance at canopy-scale", in *EGU General Assembly 2022, Vienna, Austria, 23–27 May 2022, EGU22-4268*, 2022.

[27] C. Amitrano, Y. Rouphael, A. Pannico, S. De Pascale, V. De Micco, "Reducing the evaporative demand improves photosynthesis and water use efficiency of indoor cultivated lettuce", *Agronomy* **11** (2021), article no. 1396.

[28] F. E. Rockwell, N. M. Holbrook, A. D. Stroock, "The competition between liquid and vapor transport in transpiring leaves", *Plant Physiol.* **164** (2014), p. 1741-1758.

[29] S. Vialet-Chabrand, T. Lawson, "Thermography methods to assess stomatal behaviour in a dynamic environment", *J. Exp. Bot.* **71** (2020), p. 2329-2338.

[30] S. J. Schymanski, D. Breitenstein, D. Or, "Technical note: An experimental set-up to measure latent and sensible heat fluxes from (artificial) plant leaves", *Hydrol. Earth Syst. Sci.* **21** (2017), p. 3377-3400.

[31] S. Vialet-Chabrand, T. Lawson, "Dynamic leaf energy balance: deriving stomatal conductance from thermal imaging in a dynamic environment", *J. Exp. Bot.* **70** (2019), p. 2839-2855.

[32] Y. Kitaya, M. Kawai, J. Tsuruyama, H. Takahashi, A. Tani, E. Goto, T. Saito, M. Kiyota, "The effect of gravity on surface temperatures of plant leaves: Effect of gravity on leaf temperatures", *Plant Cell Environ.* **26** (2003), p. 497-503.

[33] A. Tokuda, Y. Kitaya, H. Hirai, H. Hashimoto, Y. Inatomi, "Effects of gravity on stem sap flow and water and heat exchange in the leaves of sweetpotato", *Int. J. Microgravity Sci. Appl.* **35** (2018), no. 3, p. 350302-1-350302-6.

[34] A. S. Thom, "The exchange of momentum, mass, and heat between an artificial leaf and the airflow in a wind-tunnel", *Q. J. R. Meteorol. Soc.* **94** (1968), p. 44-55.

[35] J. Grace, F. E. Fasehun, M. Dixon, "Boundary layer conductance of the leaves of some tropical timber trees", *Plant Cell Environ.* **3** (1980), p. 443-450.

[36] G. Wigley, J. A. Clark, "Heat transport coefficients for constant energy flux models of broad leaves", *Bound.-Layer Meteorol.* **7** (1974), p. 139-150.

[37] H. Hirai, Y. Kitaya, "Effects of gravity on transpiration of plant leaves", *Ann. N. Y. Acad. Sci.* **1161** (2009), p. 166-172.

[38] A. Tokuda, Y. Kitaya, H. Hirai, "Development of a simple thermal method for measuring sap flow in plants for space experiments", *Biol. Sci. Space* **32** (2018), p. 17-21.

[39] M. A. Zwieniecki, K. S. Haaning, C. K. Boyce, K. H. Jensen, "Stomatal design principles in synthetic and real leaves", *J. R. Soc. Interface* **13** (2016), article no. 20160535.

[40] I. P. Ting, W. E. Loomis, "Diffusion through stomates", *Am. J. Bot.* **50** (1963), p. 866-872.

[41] J. N. Cannon, W. B. Krantz, F. Kreith, D. Naot, "A study of transpiration from porous flat plates simulating plant leaves", *Int. J. Heat Mass Transf.* **22** (1979), p. 469-483.

[42] N. Katsoulas, A. Baille, C. Kittas, "Leaf boundary layer conductance in ventilated greenhouses: An experimental approach", *Agric. For. Meteorol.* **144** (2007), p. 180-192.

[43] V. J. Stokes, M. D. Morecroft, J. I. L. Morison, "Boundary layer conductance for contrasting leaf shapes in a deciduous broadleaved forest canopy", *Agric. For. Meteorol.* **139** (2006), p. 40-54.

[44] A. J. Brenner, P. G. Jarvis, "A heated leaf replica technique for determination of leaf boundary layer conductance in the field", *Agric. For. Meteorol.* **72** (1995), p. 261-275.

[45] M. Kitano, H. Eguchi, "Buoyancy effect on forced convection in the leaf boundary layer", *Plant Cell Environ.* **13** (1990), p. 965-970.

[46] G. R. Cramer, K. Urano, S. Delrot, M. Pezzotti, K. Shinozaki, "Effects of abiotic stress on plants: a systems biology perspective", *BMC Plant Biol.* **11** (2011), article no. 163.

[47] H. Kollist, S. I. Zandalinas, S. Sengupta, M. Nuhkat, J. Kangasjärvi, R. Mittler, "Rapid responses to abiotic stress: priming the landscape for the signal transduction network", *Trends Plant Sci.* **24** (2019), p. 25-37.

[48] H. Zhang, Y. Zhao, J.-K. Zhu, "Thriving under stress: How plants balance growth and the stress response", *Dev. Cell* **55** (2020), p. 529-543.

[49] S. H. Eckerson, "The number and size of the stomata", *Bot. Gaz.* **46** (1908), p. 221-224.

[50] R. M. Wheeler, A. H. Fitzpatrick, T. W. Tibbitts, "Potatoes as a crop for space life support: effect of CO_2, irradiance, and photoperiod on leaf photosynthesis and stomatal conductance", *Front. Plant Sci.* **10** (2019), article no. 1632.

[51] H. Lambers, F. S. Chapin, T. L. Pons, "The plant's energy balance", in *Plant Physiological Ecology*, Springer, New York, NY, 2008, p. 225-236.

[52] F. Valladares, S. J. Wright, E. Lasso, K. Kitajima, R. W. Pearcy, "Plastic phenotypic response to light of 16 congeneric shrubs from a panamanian rainforest", *Ecology* **81** (2000), p. 1925-1936.

[53] M. Pérez-Llorca, E. Fenollosa, R. Salguero-Gómez, S. Munné-Bosch, "What is the minimal optimal sample size for plant ecophysiological studies?", *Plant Physiol.* **178** (2018), p. 953-955.

[54] P. Zabel, M. Bamsey, D. Schubert, M. Tajmar, "Review and analysis of over 40 years of space plant growth systems", *Life Sci. Space Res.* **10** (2016), p. 1-16.

[55] S. L. Ustin, S. Jacquemoud, "How the optical properties of leaves modify the absorption and scattering of energy and enhance leaf functionality", in *Remote Sensing of Plant Biodiversity* (J. Cavender-Bares, J. A. Gamon, P. A. Townsend, eds.), Springer International Publishing, Cham, 2020, p. 349-384.

[56] L. Poulet, J.-P. Fontaine, C.-G. Dussap, "A physical modeling approach for higher plant growth in reduced gravity environments", *Astrobiology* **18** (2018), p. 1093-1100.
[57] H. Schlichting, K. Gersten, "Fundamentals of boundary-layer theory", in *Boundary-Layer Theory*, Springer, Berlin, Heidelberg, 2017, p. 29-49.
[58] P. G. Jarvis, K. G. McNaughton, "Stomatal control of transpiration: scaling up from leaf to region", in *Advances in Ecological Research*, vol. 15, Elsevier, 1986, p. 1-49.

3.2.4 Main outcomes of the article

- Leaf replicas are useful tools for isolating and studying physical processes in plants, such as heat exchange, transpiration, and gas exchange, without the influence of biological variability or stress responses.
- By simplifying complex biophysical phenomena, leaf replicas allow precise measurements and modelling of energy balance components like radiation, convection, and latent heat transfer, leading to a better understanding of plant-environment interactions.
- In microgravity or reduced gravity, where natural convection is altered or absent, leaf replicas provide a controlled environment to study gas and heat exchange.

4 Conceptual design, development, and experimental protocols of the leaf replica test system

This chapter is divided in 3 parts; the conception, the construction, and the characterization of the experimental design; the design of the experimental campaign; and the description of statistical analysis conducted on the collected data.

4.1 Hardware description

This section describes the hardware designed to study heat and mass transfer between the leaf replica and the environment during parabolic flight campaigns. The same hardware was also used for the Ground Reference Experiment.

4.1.1 Mechanical System Overview

The Primary structure used to house the experiment is the CNES R13 Rack. This structure is made from Bosch items - strut profiles, connecting elements, bolts, screws (Bosh Rexroth AG, Lohr, am Main, Germany) and machined aluminium plates (Figure 4-1), with total dimensions of 1167.6 x 730 x 655 mm (with the mounting part) or 845 x 645 x 645 mm if we measure only the frame bounded by the Bosch profiles (see technical drawing of the in Appendix A). The aluminium plates are used as a shelf and a baseplate, ensuring the interface with the aircraft fixation system.

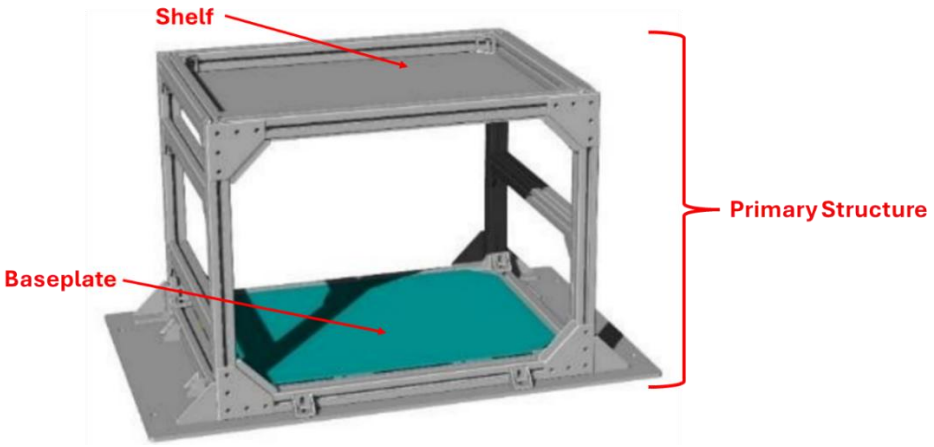

Figure 4-1 *CNES R13 Rack is the primary structure of the experiment in the aircraft (Credits: CNES).*

The top shelf (Figure 4-2) serves as the control part of the experiment. It contains adjustable power suppliers, an LED controller, and an interface device (Laptop) which is used to run and control the experiment. All of the elements are fixed to the plate with Dual lock SJ3550 (3M, Maplewood, Minesota).

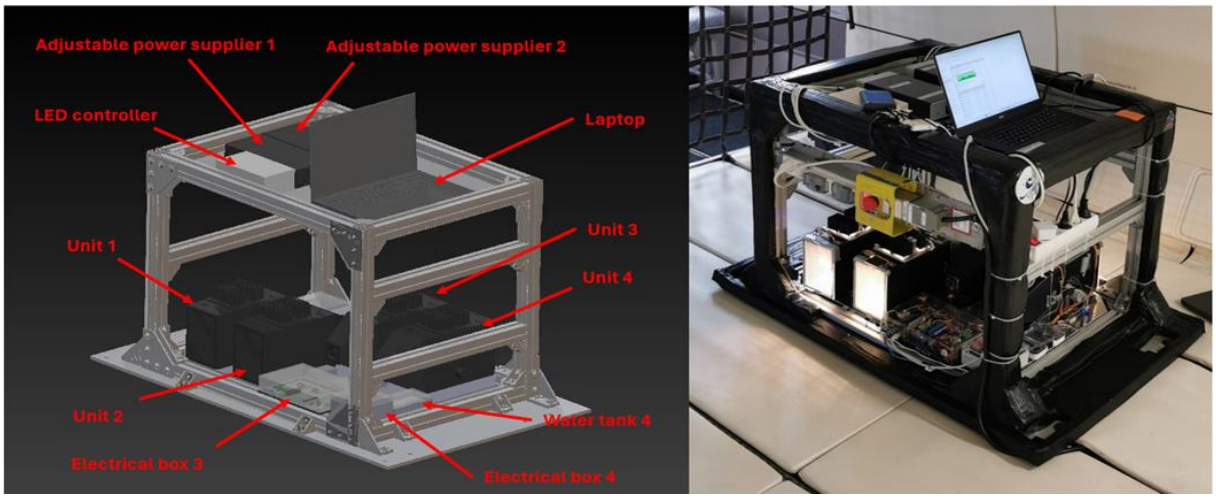

Figure 4-2 *Complete experimental assembly*

The aluminium baseplate (Figure 4-3) contains four experimental units, arranged in two mirrored pairs. Units 1 and 4 are the first pair, while Units 2 and 3 form the second. Its purpose is to provide redundancy, backup functionality, and more measurements for statistical purposes. Units 1 and 2 are linked to electrical boxes 1 and 2, and Units 3 and 4 are connected to electrical boxes 3 and 4. There are four water tanks placed on the baseplate. They are connected to their respective units. On the baseplate, there is an MSR (Multi Sensor Rack) data logger that measures environmental parameters like temperature, relative humidity, pressure, and acceleration across three axes.

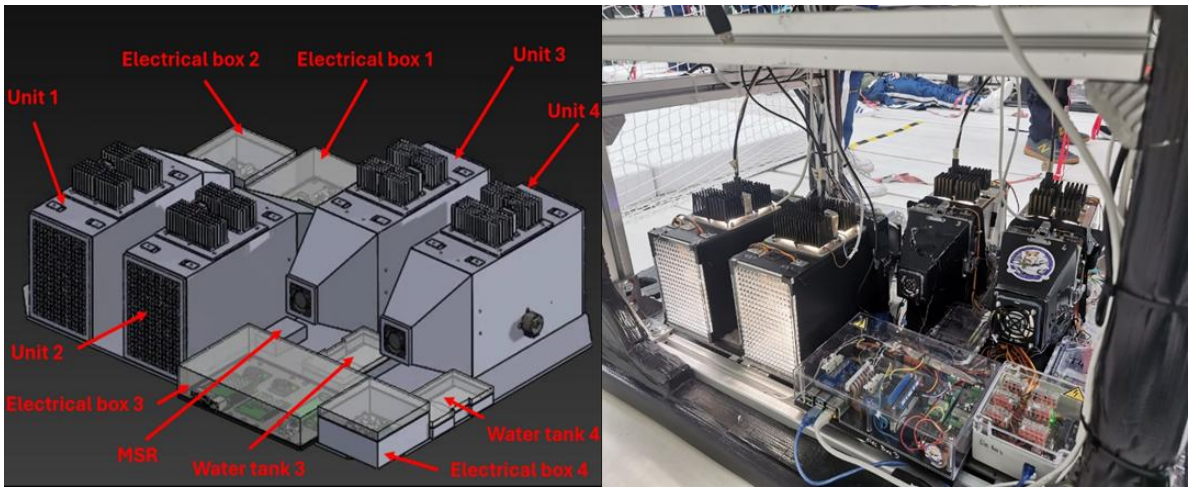

Figure 4-3 *Baseplate with the experimental part*

The total size of each unit is 120 x 160 x 370 mm. At its core is a leaf replica set on a one-degree-of-freedom frame (Figure 4-4). The fan at the unit's end generates an airflow through the wind tunnel, directed over the leaf replica. The fan is linked to an adjustable power supply, allowing for adjustments in air velocity throughout the experiment. There is a hydrophobic filter placed between the nozzle and the main part of the unit, to avoid spreading water via the fan in the aircraft and a hydrophilic filter placed on the bottom of the unit to absorb any water leak. These were requirements from the company operating the parabolic flights (Novespace).

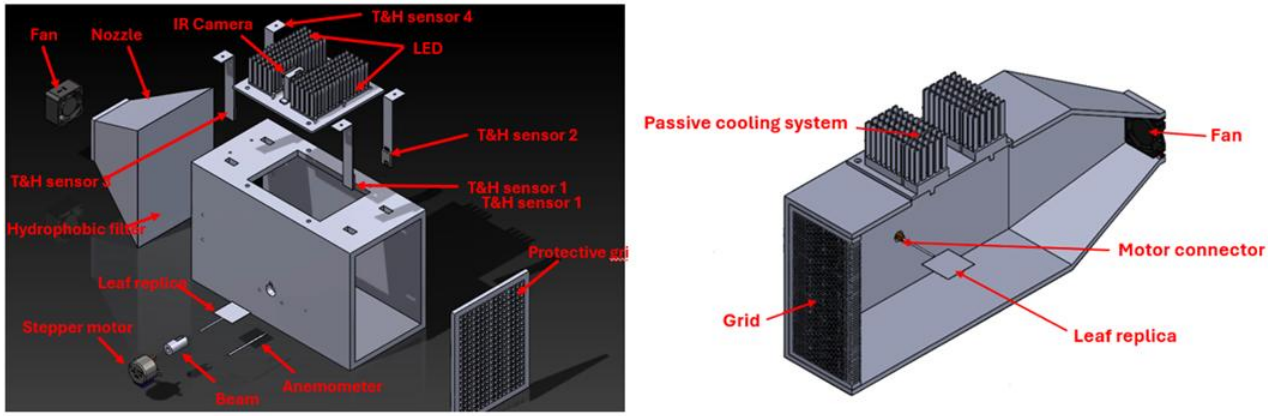

Figure 4-4 *Single Unit design*

A protective plexiglass grid (5 mm thick) is installed at the wind tunnel's input to prevent flying objects from entering the unit during parabolic flight. Additionally, the fans are secured with a second protective grid, to prevent accidental contact with the fan's rotating components. The protective grids can be seen in the Figure 4-5.

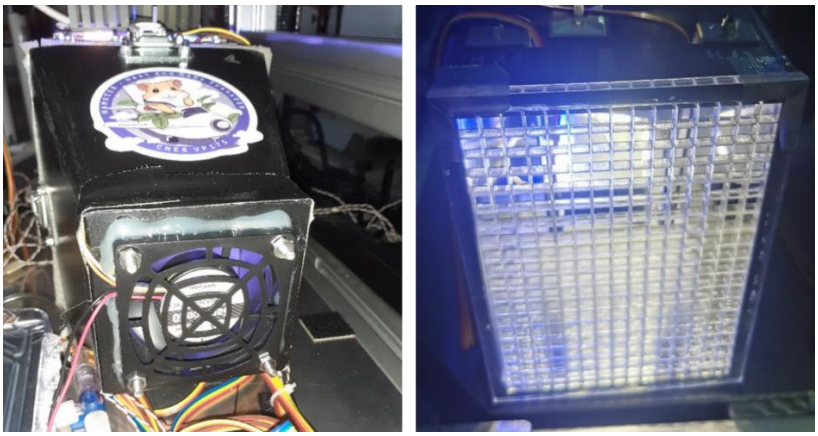

Figure 4-5 *Protective grid for the fan (left) and protective grid at the entrance of the unit (right)*

A dedicated LED system with an integrated IR camera is mounted on the top of the unit. IR cameras and thermocouples measure the leaf replica's temperature, while additional sensors (an anemometer, and relative humidity and temperature sensors) are placed inside the unit to monitor ambient conditions (temperature, relative humidity, and air velocity). A soft water tank with a volume of approximately 25 mL is directly connected to each leaf replica. Each unit is secured to the rack using Dual Lock™ SJ3560 D-rings with M4 screws and straps.

4.1.1.1 Unit Structure

The purpose of the unit's mechanical structure is to securely house the components and provide a suitable environment for the experiment.

The unit structure is made from 8 mm-thick black polyethylene, forming a rectangular main body and a convergent nozzle. The main body of the unit measures 120 x 160 x 250 mm, while the base of the convergent nozzle is 120 x 160 mm with a depth of 100 mm.

These two blocks - the main body and the convergent nozzle - are mechanically connected with steel toggle latches (Figure 4-6). Technical drawings of the components can be found in Appendix B.

Figure 4-6 *Unit Structure visualization and photo*

As mentioned before each unit structure also features sensors, a fan, and a stepper motor to rotate the leaf replica. Units 1 and 4 are equipped with larger fans, and units 2 and 3 with smaller ones. The detailed description of the fans together and their characteristics are described in the Electrica system section.

The stepper motor (Figure 4-7) connects to the replica via a 3D-printed beam (5 mm thick and 5 cm long), ensuring that the motor can adjust the leaf replica's position within a range of ±30°. The resin used to 3D print the beam is Deep Blue (Fun to Do, Kotka, Finland).

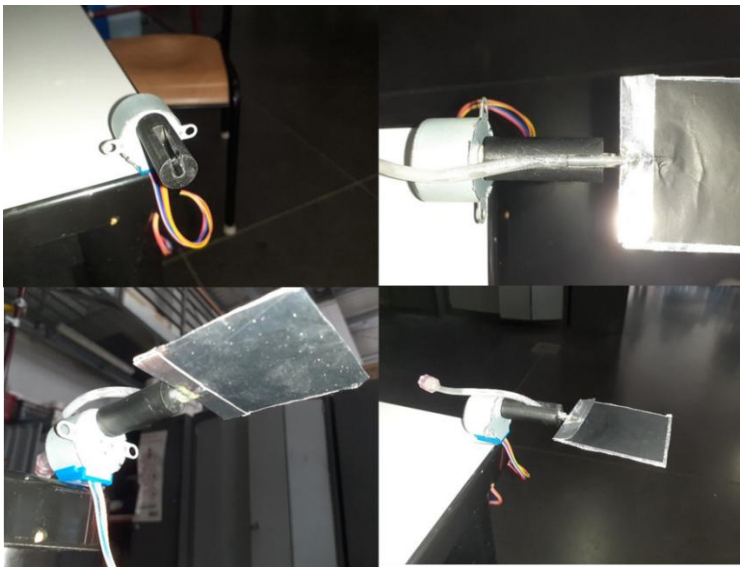

Figure 4-7 *Motor – beam – leaf replica connection*

T&RH (Temperature and relative humidity) sensors are integrated into the unit to measure the environmental conditions (Figure 4-8). Two sensors are placed upstream (before the leaf replica) and two sensors are placed downstream (after the leaf replica) to measure the temperature and relative humidity changes that occur across the unit. These sensors are positioned approximately 1.5 cm above the leaf replica to ensure that they do not disturb the airflow around the leaf replica.

The anemometer is positioned before the leaf replica, 4 cm from the wall and at the same height as the leaf replica.

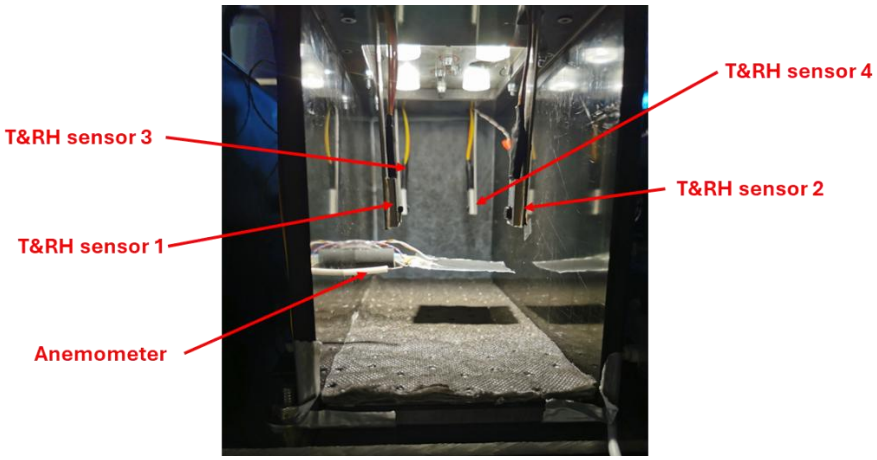

Figure 4-8 *Sensor, actuators and filters placement inside the unit*

A dedicated LEDs system is mounted on the top of the unit (Figure 4-9), directly above the leaf replica to provide light energy to the surface of the leaf replica. Each LED module is connected to a passive cooling system, which dissipates the heat created by LEDs. The IR camera is integrated into the passive cooling system of the LEDs.

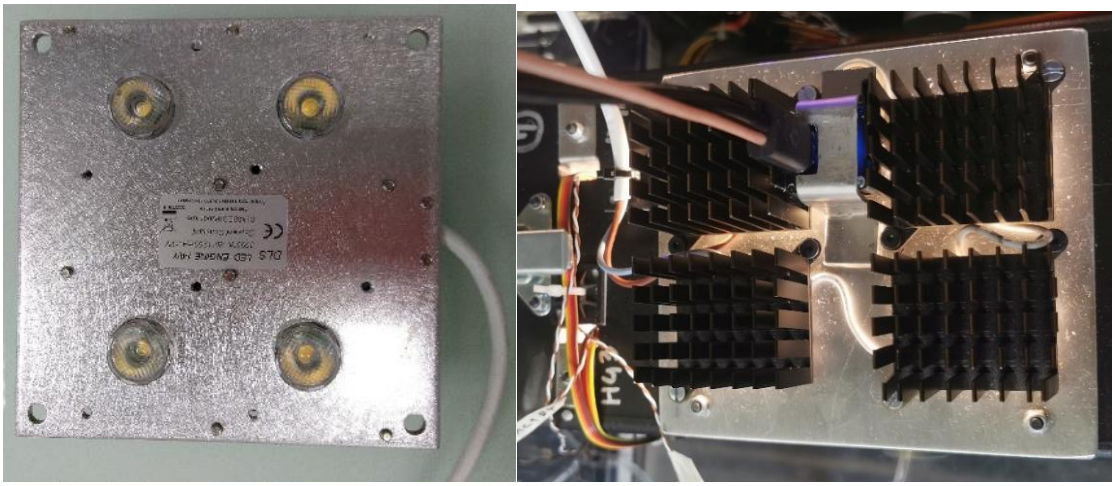

Figure 4-9 *LED module bottom side (left) and upper side with the passive cooling system (right with IR camera integrated to the system)*

This design choice was made because both the LEDs and the camera need to be positioned directly above the leaf replica, it was necessary due to the minimal focal distance of the IR camera, which is 9 cm. In this setup, the camera is located 10 cm above the leaf replica.

4.1.1.2 Evaporative leaf replica

The leaf replica is made of two layers of aluminium foil with a thermocouple and a filter sandwiched between the layers to replicate the thermal properties of a real leaf (Figure 4-10). The bottom layer is made from 30 µm thick untreated aluminium sheet and has laser-perforated holes. The size of the replica is 60 x 50 x 0.65 mm. The filter used to distribute the water inside the replica is Whatman 41 Filter (cat no. 1441-150) with an exchange surface of 45 x 45 mm. The replica is sealed at the edges to prevent unwanted leakage, thereby ensuring that mass transfer occurs only through the perforated pores. The top layer of the leaf is covered with black aluminium tape (produced by axall) to simulate the emissivity of real leaves (typically around 0.98 ±0.01 – the emissivity of the tape is 0.98), allowing for realistic radiative heat transfer similar to natural leaves. Additionally, with a high absorbance, black tape enables precise temperature measurements with an IR camera.

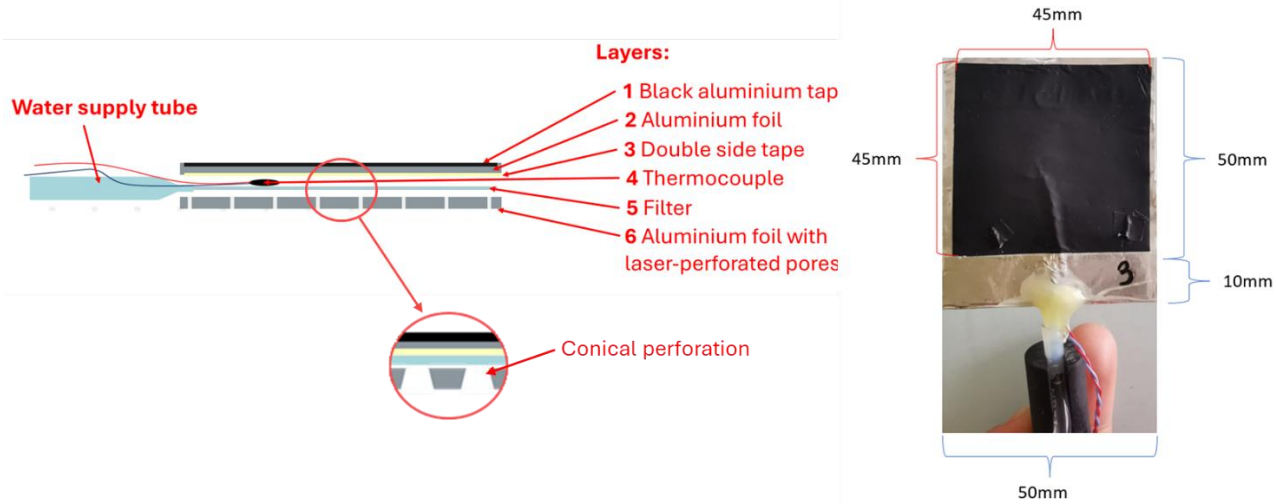

Figure 4-10 *Leaf replica design schematics and a photo with its dimensions*

The size and the mass of all of the components of the evaporative leaf replica can be found in (Table 4-1).

Component		Size [mm]	Mass [g]	Standard deviation
Perforated foil		50 x 50 x 0.03	0.198	7.07E-05
Whatman 41 filter 1441-150		45 x 55 x 0.1	0.217	2.31E-03
Aluminium foil		70 x 50 x 0.03	0.282	7.21E-03
Double side tape	Polypropylene	50 x 57 x 0.03	0.196	1.08E-02
	glue		0.314	
Black aluminium tape	Aluminium foil	46 x 46 x 0.03	0.162	2.71E-03
	glue		0.076	
Aluminium tape	Aluminium foil	25 x 5 x 0.03	0.241	3.08E-03
	glue		0.154	
Water		x	0.880	4.35E-02

Table 4-1 *Thermal capacity of both the individual components of the evaporative leaf replica and the whole replica*

The diameter of the pores on the evaporative side of the leaf replica varies between 50-65 µm, with the center-to-center spacing 380 µm. The size of the pores are summarised in Table 4-2.

Parameter	Symbol	Range or Value
Pore depth	l_0	30 µm
Internal diameter	d_{min}	43–50 µm
External diameter	d_{max}	55–60 µm
Spacing	L	380 µm

Table 4-2 *Spacing and dimensions of the pores in the leaf replica*

In order to get a stomatal conductance for water between 250-500 mmol/m^2/s to match stomatal conductance values seen in real leaves. C3 plants typically exhibit stomatal conductance values ranging from 0.2 to 0.5 mol m^{-2} s^{-1} (Hetherington and Woodward, 2003). Because of laser limitations, the diameter of the pores is larger than that of real stomata, so the density of the pores is smaller to keep the stomatal conductance within the desired range (Figure 4-11). Typically, the sizes of stomata range from 15.65 µm to 74.44 µm in length and 9.71 µm to 42.08 µm in width (Vivin K. and Daningsih, n.d.).

The calculations for the pore conductance for the leaf replicas were done as described in (Schymanski et al., 2017) and the results can be seen in Table 4-3. Used equations can be found in Appendix C.

Internal pores diameter (µm)	External pores diameter (µm)	Pores conductance $g_{sw,mol}$ (mol·m^{-2}·s^{-1})	Pores conductance g_{sw} (m·s^{-1})
43	55	0.280	6.82E-03
43	60	0.304	7.40E-03
50	55	0.313	7.64E-03
50	60	0.338	8.25E-03

Table 4-3 *Pores conductance calculation results*

The perforation was done by Femto Engineering (Besancon, France) using a laser, resulting in pores having two different sides. The pores have a slightly conical geometry, with one side featuring a wider opening and the opposite side having slightly smaller pore openings as can be seen in Figure 4-10. This dual-sided nature of the pores means that the pore geometry is not uniform along the length of the perforation. As a result, the pores may appear larger when viewed from one side and slightly smaller from the other. This characteristic can be seen in Figure 4-11and Figure 4-12. Leaf replicas used in the experiment were made in a way that the wider part was facing outside.

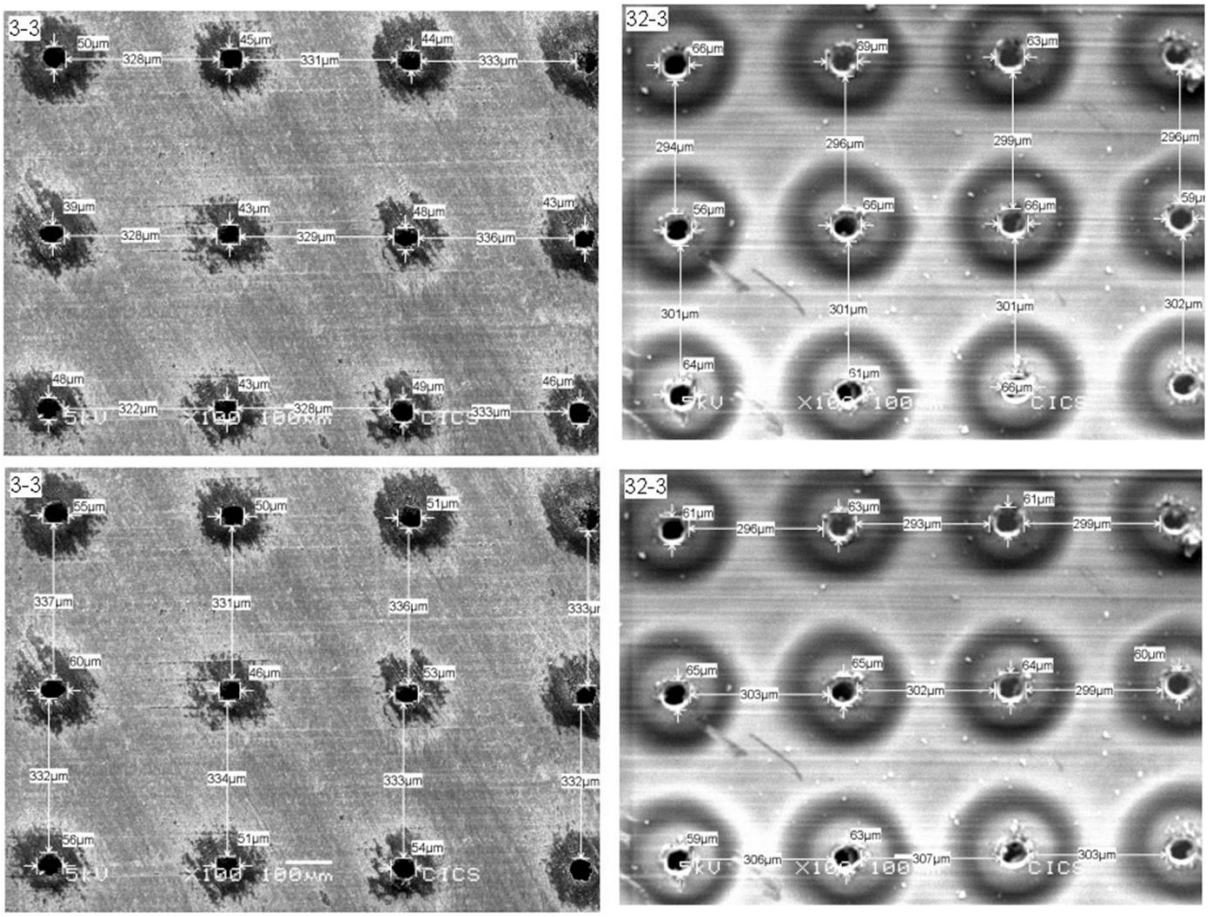

Figure 4-11 *SEM (scanning electron microscope) picture of the evaporative side of the leaf replica showing the two sides characteristic of the laser perforation done for leaf replica – surface. The pictures were done by the Centre Imagerie Cellulaire Santé, UFR Médecine (UCA) using an SEM - JEOL - JSM-6060 microscope.*

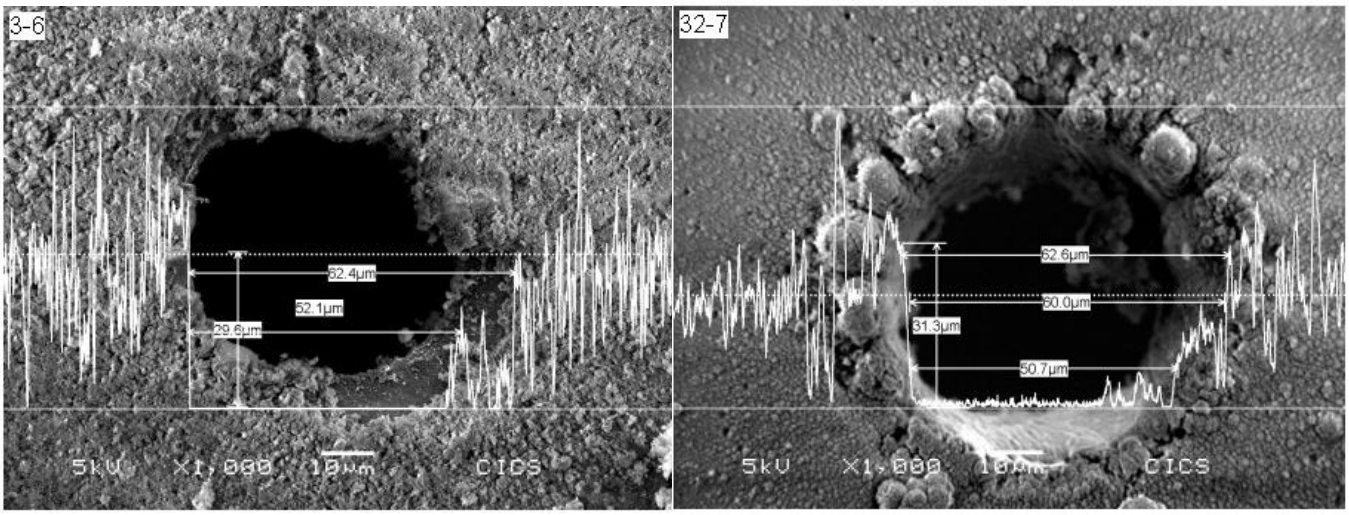

Figure 4-12 *Two sides characteristic of the laser perforation done for leaf replica – single porous*

4.1.1.3 Non-evaporative leaf replica

The non-evaporative leaf replica is made in the same way, with the only difference being that non-perforated aluminium foil is used on the bottom instead of perforated one. The weight of all of the leaf replica's components, is summarised in Table 4-4.

Component		Size [mm]	Mass [g]	Standard deviation
Perforated foil		50 x 50 x 0.03	0.198	7.07E-05
Whatman 41 filter 1441-150		45 x 55 x 0.1	0.217	2.31E-03
Aluminium foil		70 x 50 x 0.03	0.282	7.21E-03
Double side tape	Polypropylene	50 x 57 x 0.03	0.196	1.08E-02
	glue		0.314	
Black aluminium tape	Aluminium foil	46 x 46 x 0.03	0.162	2.71E-03
	glue		0.076	
Aluminium tape	Aluminium foil	25 x 5 x 0.03	0.241	3.08E-03
	glue		0.154	
Water		x	0.630	4.35E-02

Table 4-4 *Thermal capacity of both the individual components of the non-evaporative leaf replica and the whole replica*

4.1.1.4 Water supply

The water transport mechanism is based on capillary force, allowing passive, pressure-free movement of water without the need for any pumping systems (Figure 4-13).

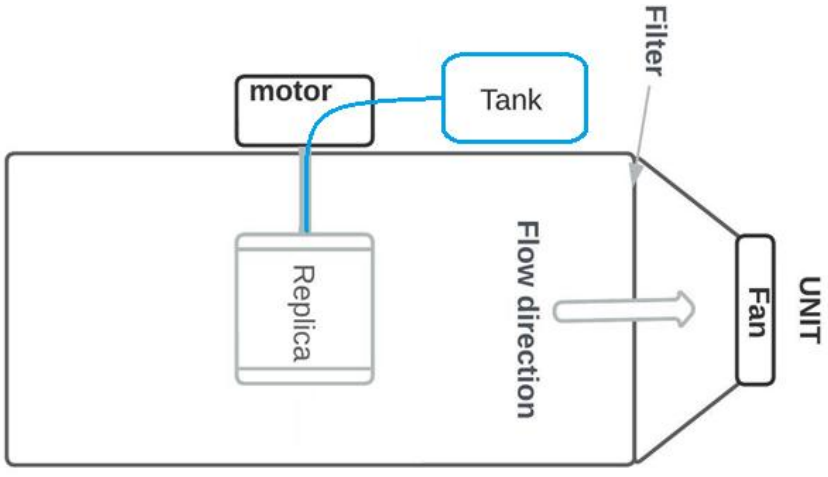

Figure 4-13 *Water supply system diagram*

The water tank selected for this experiment is a 20 mL reagent bag (Figure 4-14), made of PVC/EVA with dimensions of 65 x 105 x 5 mm (Milteny Biotec, Cologne, Germany).

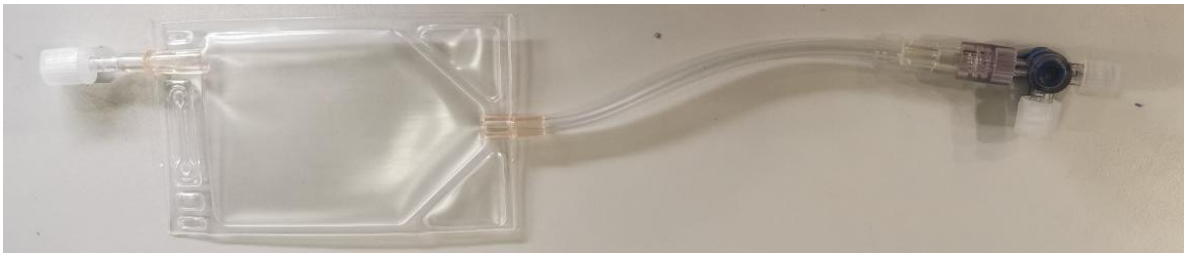

Figure 4-14 *Water tank*

Each connector on the bag is equipped with a luer lock, and the connection to the leaf replica is facilitated by a Discofix-3 three-way stopcock valve (B. Braun, Melsungen, Germany) (Figure 4-15). The tubes used for these connections are B. Braun Perfusor® extension lines.

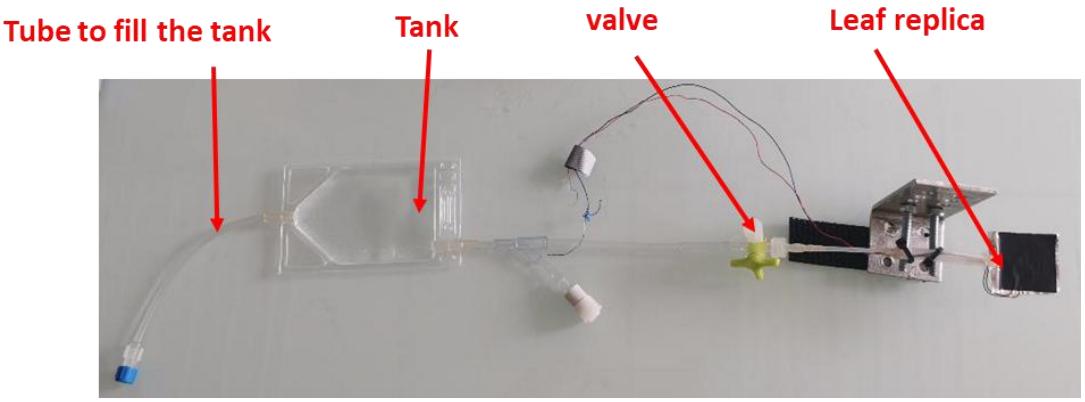

Figure 4-15 *Tank to leaf replica connection*

To evaluate the system's robustness, the following tests were conducted:

1. Compression test - a 180 g weight (flat metal plate) was placed on top of the tank to check whether external pressure would induce leakage. A leak was detected after 5 minutes and 23 seconds.

2. Pressing test - In the tank was manually pressed to determine if increased pressure could lead to leakage at the joint points of the replica. The result was the formation of droplets on the upper and lower sides of the leaf replica at the connection points.

3. Levelling test - it was performed to see if the water flow would remain uninterrupted when the outlet of the tank was positioned 3 cm below the leaf replica. During the test, the setup was similar to the final setup, with controlled airflow and the leaf replica illuminated by the LEDs. The water flow was monitored to see if it would remain uninterrupted. At the beginning of the experiment, the tank was filled with 25 mL of

water. The flow remained uninterrupted until the amount of water in the tank dropped to approximately 5 g.

4. Lower pressure test - to evaluate the system performance under reduced external pressure. The setup involved placing the leaf replica and the connected water tank in a vacuum chamber and reducing the pressure to 0.8 bar. The results demonstrated no observable air intake or leakage during the test.

To mitigate the leakage risk from the tank, each water tank is enclosed within a containment box that provides a double protection. A push-button lock is used to keep the box closed throughout the experiment. Additionally, the tank rests on a layer of black cellulose absorbent paper, which serves as a secondary containment measure to absorb any accidental leaks. The tubing connecting the tank to the leaf replica passes through a hole located on one side of the box (Figure 4-16).

Figure 4-16 *Watering tank on absorbent paper connected to the leaf replica within its enclosure (left) and outlet when closed (right).*

4.1.2 Electrical system

The electrical system of the experiment is responsible for powering and connecting all sensors and actuators of the experiment. The electrical circuit schematic of the experiment is shown in Figure 4-17. It shows all the components, including power distribution, sensor connections, motor controls, and all signals within this system for two units (Table 4-5). The electrical system for two other units is almost identical copy of that system. The only difference is the lack of the MSR in the second electrical loop. The main control interface is a Dell laptop, which

synchronizes the Raspberry Pi units and provides a unified platform for real-time monitoring and adjustment.

Ref.	Item	Model	Qt.	Manufacturer	Dimensions	Power cons.
RP 12,34	Raspberry Pi	4B	2	Raspberry Pi	85 x 56 x 20	5V 2A
	Raspberry Pi Power Supplier	DSA-13PFC-05 FCA	2	Stontronics	-	5V 2.5A
AU 12,34	Elegoo Board	Uno R3	2	Elegoo	69 x 54 x 20	-
DAQ 1-4	Thermocouple DAQ HAT	MCC 134	4	Digilent	65 × 56.5 × 12	-
TC 1.0-4.3	Thermocouple	T-Type	16	RS Pro	-	-
T&RH 1.1-4.4	Temperature and Relative humidity Sensor	Sensor AM2302	16	Asair	25 x 15 x 8	5V 1.2mA
CIR 1-4	IR Camera	Boson	4	FLIR	21 x 21 x 11	3.3V 0.45 A
M1-4	Stepper Motor	28BYJ-48	4	Elegoo	35 x 17 x 19	5V 0.2A
	Driver Board	ULN2003	4	Elegoo	35 x 31 x 2	5V 0.2A
F 2,3	Fan	412fm	2	ebmpapst	40 x 40 x 10	12V 0.045A
F 1,4	Fan	San Ace60	2	Sanyo Denki	60 x 60x 15	12V 0.16A
AF 1-4	Anemometer	SFS07	4	IST	6,9 x 2,4 x 0,2	5V 6mA
	Flow Demo Board FS7	-	4	IST	80 x 31 x 15	9V 0.3A
LED 1-4	LED System	-	4	Tridonic	110 x 110 x 30	12V 1.2A
LED Driver	LED Driver	-	1	Tridonic	65 x 35 x 23	230V AC 1.4A
AC/DC 1	AC/DC Converter	124-2183	1	RoHS	36 x 17 x 35	5V 1.5A
AC/DC 2	AC/DC Converter	FW 7555M/09	1	RSPro	80 x 40 x 40	9V 1,5A
MSR	Environmental Data Logger	MSR 145s	1	MSR	39 x 23 x 72	-
Laptop	Laptop	P56F	1	Dell	378 x 257 x 27.4	19.5V 6.67A
AC/DC Adjustable 1-2	Adjustable Power Supplier	LS-1165	2	Voltcraft	271 x 56 x 136	230V AC 3A

Table 4-5 *Electrical components of the experiment*

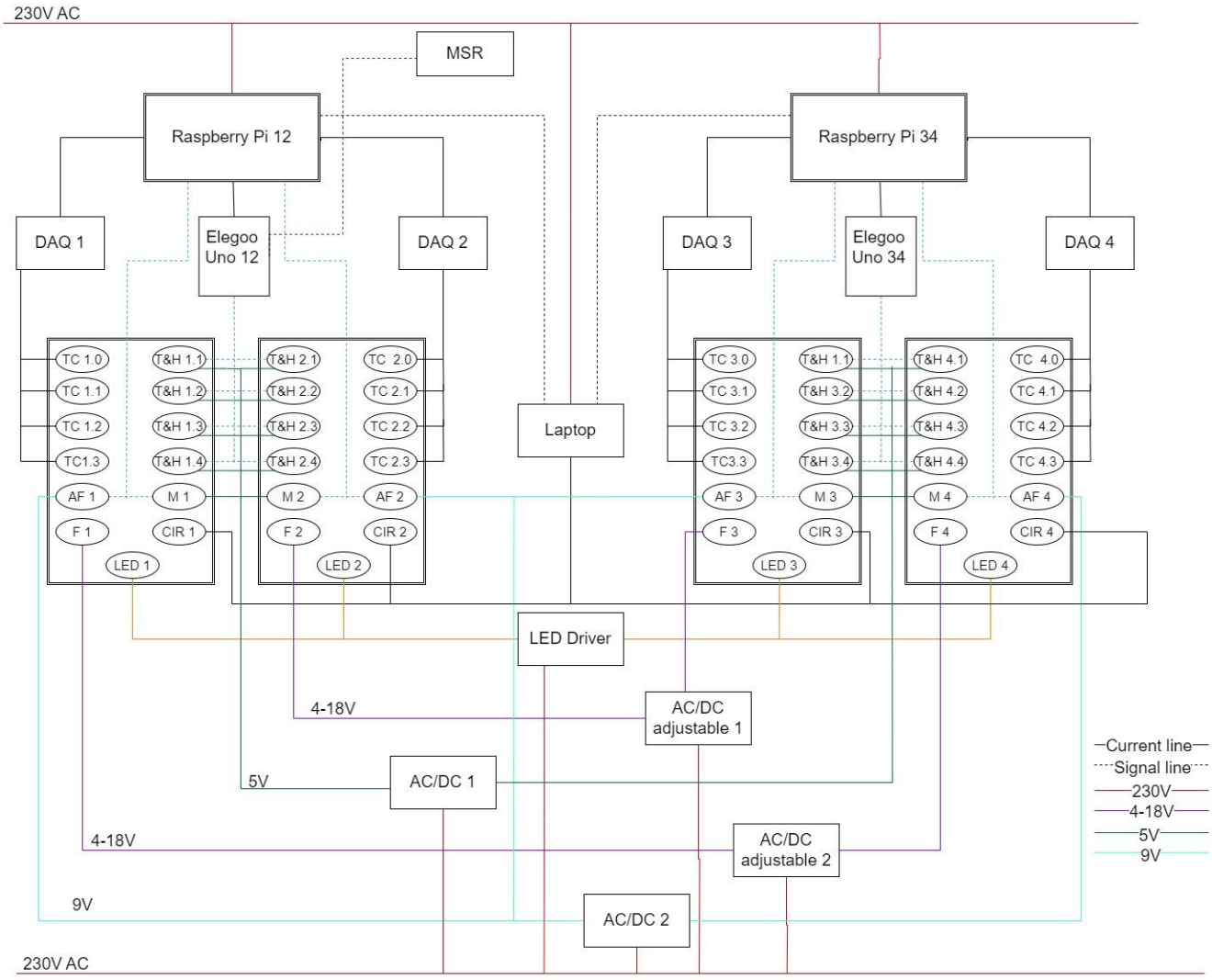

Figure 4-17 *Electrical diagram of the experiment*

4.1.2.1 Power Supply and Distribution

The power supply system is composed of several AC and DC power lines. The main power line, sourced from a 230V AC socket, provides power to:

- The primary control interface, the Dell laptop, which is used for user interaction and synchronization of all connected devices.
- Two Raspberry Pi 4 units, which are responsible for data collection, processing, and control of the experiment.
- The LED driver system, which powers the dedicated LED modules.
- Four AC/DC converters that convert the voltage for use with specific components.

Each AC/DC converter is used to power a different part of the system:

1. A 5V line supplies power to 16 temperature and relative humidity sensors. The maximum power output for this line is 7.5W.
2. A 9V line powers four anemometers and their corresponding flow boards, with a power output of up to 13.5W.
3. Two additional adjustable 0V-18V lines each supply power to two fans.

4.1.2.2 Computers and microcontrollers

The experimental setup is composed of computers and microcontrollers to manage data acquisition, sensor control, and real-time monitoring. This section describes the specifications and role of these components.

4.1.2.2.1 Laptop

The Dell laptop is connected to the Raspberry Pi and IR cameras. Each camera is connected directly to the laptop via a USB cable and Raspberry Pis are connected via ethernet cables.

4.1.2.2.2 Raspberry Pi 4

Two Raspberry Pi 4 computers serve as the primary controllers of the experiment, managing data collection and the interface with sensors and actuators. They are equipped with a 64-bit ARM Cortex-A72 quad-core processor running at 1.5GHz, 8GB LPDDR4 RAM, and possibility to connect via GPIO pins, Ethernet, and USB ports. Each Raspberry Pi is equipped with 2 MCC 134 DAQ HATs (Data Acquisition Hardware Attached on Top) for interfacing with thermocouples, providing 24-bit analog-to-digital conversion and hot junction compensation. Each HAT has 4 isolated thermocouple inputs with cold junction compensation.

4.1.2.2.3 Elegoo Uno Boards

The Elegoo boards handle data acquisition from AM2302 temperature and relative humidity sensors, using serial communication to send the data to the Raspberry Pi units. They are connected to the Raspberry Pi via USB-A to USB-B cables.

4.1.2.2.4 MSR Environmental Logger

An MSR 145S logger is used to collect environmental data, such as temperature, relative humidity, pressure, and acceleration across three axes. The MSR 145S measures temperature

with an accuracy of ±0.1°C, relative humidity with an accuracy of ±2% RH, and pressure from 0 to 2000 hPa with an accuracy of ±1 hPa. This logger is used to monitor the parameters outside the units as well as to record the gravitational acceleration during the parabolic flight.

4.1.2.3 Sensors and Actuators

4.1.2.3.1 Fans

After careful and thorough tests on output linearity and operating range, two types of fans were chosen: San Ace 60 fans in Units 1 and 4, and ebmpapst 412fm fans in Units 2 and 3. These fans provide forced convection to the leaf replicas and are controlled through adjustable power supplies (Figure 4-18).

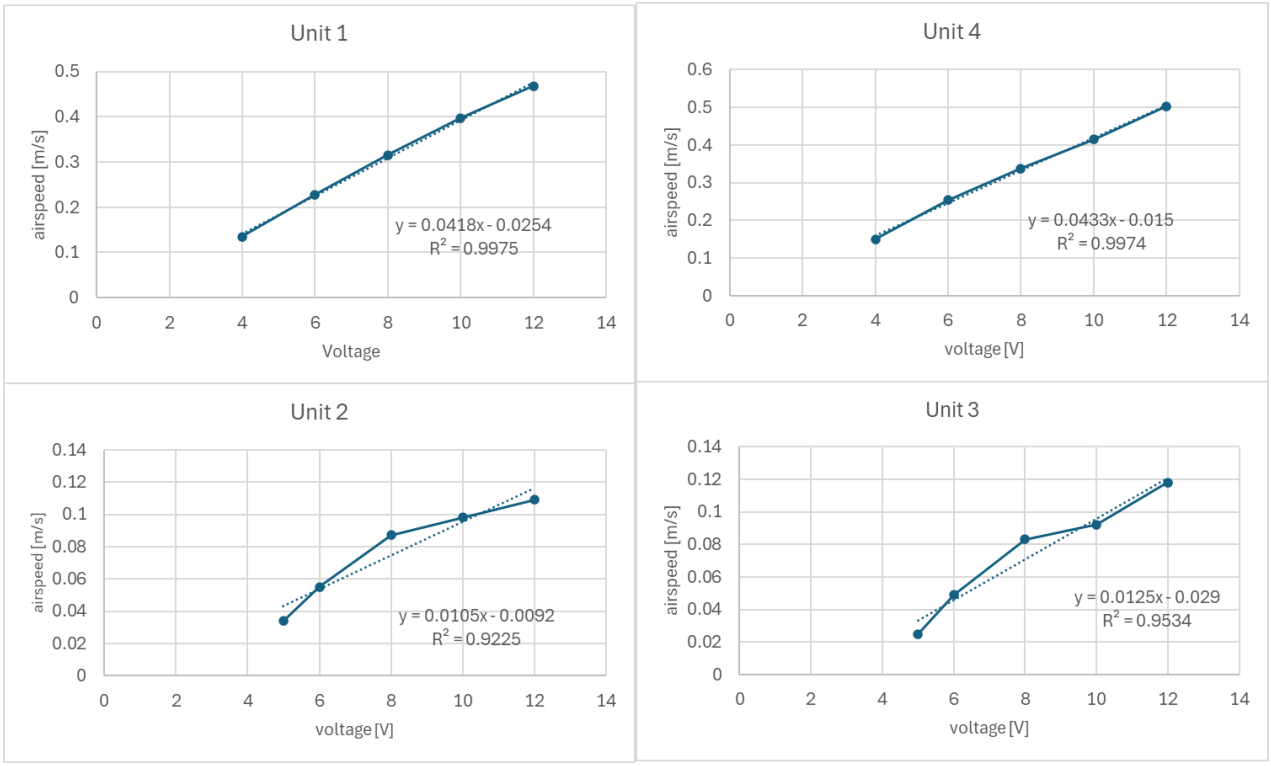

Figure 4-18 *Response curves for air velocity as a function of voltage for fans with the hydrophobic filter inside the units*

4.1.2.3.2 Stepper Motors

Each unit is equipped with a stepper motor (28BYJ-48) that rotates the leaf. The 28BYJ-48 motor operates on 5V DC with a current consumption of approximately 200mA. The motors are controlled via ULN2003 driver boards, which are interfaced with the Raspberry Pi units.

Each motor's position can be adjusted through a GUI. The 28BYJ-48 is a 4-phase, 8-beat motor, with a step angle of 5.625° and a 64:1 gear reduction, which translates to approximately 0.088° per step.

4.1.2.3.3 LED System

The LED modules are custom-built and powered by a Tridonic LED driver (Figure 4-19), with a total power consumption of 14W and a current of 1200mA. The spectral distribution of each LED module can be seen in Figure 4-19. The whole lighting system consists of four modules each one composed of an aluminium plate and 4 white LED lights. Each module is individually connected to the LED driver and is equipped with fins on the back side to evacuate the heat generated by the LEDs. One module measures 11.5 cm x 11.5 cm x 4 cm. The driver measures 18 cm x 10.5 cm x 6 cm.

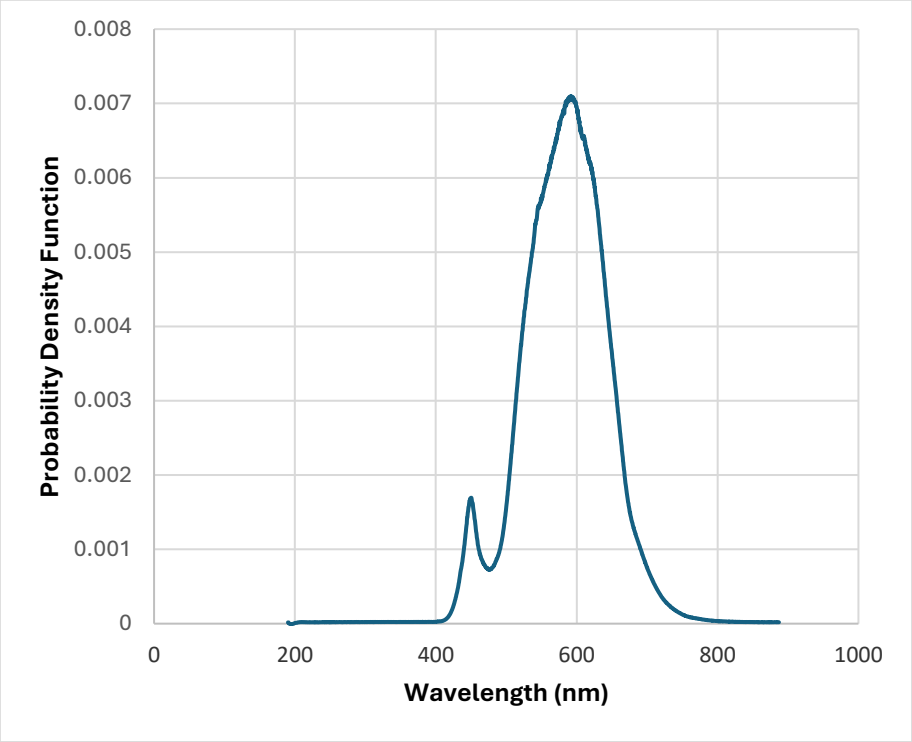

Figure 4-19 *Spectral distribution of chosen lighting system*

In order to calculate the amount of energy delivered to the surface of the leaf replica, the LI-COR LI-250A Light Meter was used together with the LI-COR Quantum Sensors. The value was measured in 9 points that correspond to 9 points on the surface of the leaf replica (Figure 4-20)

Figure 4-20 *Measurement points on the surface of the leaf replica*

At each point, 10 measurements of the PPFD (Photosynthetic Photon Flux Density) were taken. These were then recalculated to provide the value in W/m2. The probability density function of wavelength was scaled using the PPFD to calculate the spectral power distribution in $\frac{W}{m^2}$ based on the distribution presented in **Figure 4-19** Spectral distribution of chosen lighting system. The conversion factor between PPFD to $\frac{W}{m^2}$ was 0.214. Table 4-6 shows the average of these 9 measurements along with the standard deviation.

UNIT 1										
	unit	position								
		1.1	1.2	1.3	2.1	2.2	2.3	3.1	3.2	3.3
Average PPFD	mmol/m2/s	382.51	780.45	699.93	422.84	540.71	585.48	730.89	768.75	907.61
Standard deviation	mmol/m2/s	3.01	7.40	10.16	2.45	2.38	3.97	13.01	9.71	14.53
Irradiance	W/m^2	81.86	167.02	149.78	90.49	115.71	125.29	156.41	164.51	194.23
Standard deviation	W/m^2	0.64	1.58	2.17	0.52	0.51	0.85	2.78	2.08	3.11
UNIT 2										
Average PPFD	mmol/m2/s	860.98	743.51	535.21	616.70	662.73	613.51	856.51	1018.28	1005.39
Standard deviation	mmol/m2/s	5.47	5.74	7.99	4.17	4.33	8.71	16.36	9.07	12.64
Irradiance	W/m^2	184.25	159.11	114.54	131.97	141.82	131.29	183.29	217.91	215.15
Standard deviation	W/m^2	1.17	1.23	1.71	0.89	0.93	1.86	3.50	1.94	2.71
UNIT 3										
Average PPFD	mmol/m2/s	591.04	631.25	613.26	558.75	592.98	585.59	892.65	934.94	916.91
Standard deviation	mmol/m2/s	5.31	5.69	3.89	5.01	7.02	6.33	6.50	18.89	12.96
Irradiance	W/m^2	126.48	135.09	131.24	119.57	126.90	125.32	191.03	200.08	196.22
Standard deviation	W/m^2	1.14	1.22	0.83	1.07	1.50	1.36	1.39	4.04	2.77
UNIT 4										
Average PPFD	mmol/m2/s	641.49	634.66	520.04	567.43	627.76	574.23	787.14	873.98	974.55
Standard deviation	mmol/m2/s	6.54	6.03	8.36	2.12	6.10	9.35	7.58	114.64	8.65
Irradiance	W/m^2	137.28	135.82	111.29	121.43	134.34	122.88	168.45	187.03	208.55
Standard deviation	W/m^2	1.40	1.29	1.79	0.45	1.31	2.00	1.62	24.53	1.85

Table 4-6 *Average PPFD and irradiance measurements with standard deviations for all units*

4.1.2.3.4 IR Camera

Each unit is equipped with a FLIR Boson radiometric IR camera (320x256 resolution, 50° field of view) to monitor the upper surface temperature of the leaf replicas. The Boson camera operates in the longwave infrared spectrum, with a spectral response between 8-14 µm and a thermal sensitivity of less than 40 mK. The camera is integrated directly into the passive cooling system of the LED module and positioned 10 cm above the leaf replica. This placement allows to meet the minimal focal distance constrain which is 9 cm for the chosen camera.

The camera operates with a QVGA sensor array, providing a 320x256 pixel resolution. The FLIR Boson's radiometric output provides temperature data for every pixel, allowing analysis of heat distribution and thermal changes on the leaf replica during varying air velocity, angles and gravity conditions. It is powered via a 3.3V USB connection. The accuracy of the camera is 5K and the thermal sensitivity is 40mK.

4.1.2.3.5 Relative humidity and Temperature Sensors

Four AM2302 sensors (used for monitoring relative humidity and temperature) are placed within each unit. They have an accuracy of ±3% RH and ±0.5°C, with a response time of 2 seconds for relative humidity and 1 second for temperature. Two sensors are placed upstream and two sensors are placed downstream of the leaf replicas, to provide information about relative humidity and temperature distribution along the unit.

4.1.2.3.6 Anemometers

The IST FS7 anemometers are positioned within each unit to measure air velocity. They have a range of 0 to 100 m/s, with the ability to be calibrated for a narrower range suitable for the experimental needs. The anemometers are powered at 9V and have a power consumption of approximately 30 mW. The calibration data of the sensors can be found in Appendix D.

4.1.3 Software system and Data Acquisition

4.1.3.1 Laptop

The laptop acts as a central control unit and time server for synchronizing all devices involved. It is used for:

1. Time synchronization for Raspberry Pis and MSR sensor - it acts as a Network Time Protocol (NTP) server, to ensure that the Raspberry Pis, MSR sensor, and camera use the same time reference while recording the data.
2. Management and control of IR cameras - Four FLIR Boson IR cameras are connected to the laptop (one camera per unit). These cameras capture thermal images of the leaf replica and the surrounding environment. The IR cameras are operated via software provided by the camera manufacturer, which is installed and run on the laptop.
3. User interface display for Raspberry Pis - The laptop also serves as the display hub for the Graphical User Interfaces (GUIs) of both Raspberry Pi units. They are connected to the laptop via an Ethernet cable.

4.1.3.2 MSR Sensor

The MSR 145 sensor is powered by its own battery and communicates with the computer via a USB port. It uses the laptop as its time server, ensuring synchronized data collection with the rest of the system at a frequency of 1 Hz. The sensor pairs with MSR PC software for parameter settings, real-time monitoring, and exporting data to a CSV file.

4.1.3.3 Raspberry Pi

The software for the experiment was developed using Python, with two Raspberry Pi 4 units serving as the central processing units (CPUs). The main task of the software is to control the sensors, actuators, and data acquisition devices while providing real-time data visualization and control through a GUI (see data flow on Figure 4-17- the dashed line), and the data are logged into CSV files.

4.1.3.4 Motor Control

The motor control software is responsible for adjusting the position of the leaf replica during the experiment. The stepper motors are managed by a Motor Class within the software, which handles:

- Moving the motor to defined angles.

- Resetting the motor to its initial position after a sequence of movements.
- Shuffling or randomizing the angles.

The motors are controlled using GPIO pins on the Raspberry Pi. To force the action, a button on the GUI needs to be pressed.

4.1.3.5 Sensor Data Acquisition

The system acquires data from the following sensors:

- Thermocouples - The experiment uses MCC 134 thermocouple HATs mounted on the Raspberry Pi to measure temperature at different points on the leaf replica. Each unit has a dedicated HAT with 4 thermocouples.
- Air velocity sensors - The software reads voltage data from anemometers using the ADS1115 ADC module. Raw voltage readings from the anemometer are logged, and later on they are converted to actual air velocity.
- T&RH sensors - These sensors are connected via Elegoo boards, which communicate with the Raspberry Pi over a serial interface.

The data acquisition loop continuously reads sensor values and updates the GUI. This loop includes error-handling mechanisms to ensure that data collection continues even if sensor failures or data anomalies occur.

4.1.3.6 Graphical User Interface

A Tkinter-based Graphical User Interface (GUI) was developed to monitor the experiment and provide control over the stepper motor. The interface is divided into distinct sections, displaying real-time data from:

- T&RH sensors, measuring the relative humidity and temperature inside the units.
- Thermocouples, measuring temperature across the leaf replica (upper and lower surfaces and the temperature inside the leaf replica).
- Anemometers, capturing air velocity.
- Motor angles, showing the current position of the leaf replica.

Users can interact with the GUI to adjust the motor positions, reset them to their initial state, or shuffle angles.

4.1.3.7 Data Logging and File Management

The system logs data from all sensors into CSV files in real time. Bash script automates the startup of both Raspberry Pis, ensuring that all data are correctly timestamped and aligned. Bash scripts automate the startup of both Raspberry Pis, ensuring that all data are correctly timestamped and aligned. Two separate CSV files are created for each Raspberry Pi board Box 1 and Box 2 for Raspberry Pi 1-2 and Box 3 and Box 4 for Raspberry Pi 3-4, each containing:

- Timestamp and computer time.
- Relative humidity and temperature readings from the T&RH sensors.
- Thermocouple temperature data.
- Air velocity from the anemometers.
- Current motor angles.

These CSV files are generated with filenames based on the current date and time. Data are logged at an approximately 3 Hz frequency. Figure 4-21 shows a CSV file created during one of the days of the measurements.

	A	B	C	D	E	F	G	H	I	J	K	L	M	N	O	P
1	Computer time	Timestamp (s)	Humidity 1 (%)	Temperature 1 (°C)	Humidity 2 (%)	Temperature 2 (°C)	Humidity 3 (%)	Temperature 3 (°C)	Humidity 4 (%)	Temperature 4 (°C)	Thermocouple 1 (°C)	Thermocouple 2 (°C)	Thermocouple 3 (°C)	Thermocouple 4 (°C)	Voltage anemometer (mV)	Current angle motor ()
2	09:24:29	1711527870	24.9	17.8	21.9	16.5	24.4	16.2	27	15.9	15.0932	22.0821	21.9402	22.6849	2129	0
3	09:24:30	1711527870	24.9	17.8	21.9	16.5	24.4	16.2	27	15.9	15.0932	22.0821	21.9402	22.6849	2133	0
4	09:24:30	1711527871	24.9	17.8	21.9	16.5	24.4	16.2	27	15.9	15.0932	22.0821	21.9402	22.6849	2130	0
5	09:24:31	1711527871	24.9	17.8	21.9	16.5	24.4	16.2	27	15.9	15.0932	22.0821	21.9402	22.6849	2134	0
6	09:24:31	1711527871	24.9	17.8	21.9	16.5	24.4	16.2	27	15.9	15.0938	22.101	21.9608	22.7008	2140	0
7	09:24:31	1711527872	24.9	17.8	21.9	16.5	24.4	16.2	27	15.9	15.0938	22.101	21.9608	22.7008	2136	0
8	09:24:31	1711527872	24.9	17.8	21.9	16.5	24.4	16.2	27	15.9	15.0938	22.101	21.9608	22.7008	2139	0
9	09:24:32	1711527872	24.9	17.8	21.9	16.5	24.4	16.2	27	15.9	15.0938	22.101	21.9608	22.7008	2137	0
10	09:24:32	1711527872	24.9	17.8	21.9	16.5	24.4	16.2	27	15.9	15.0938	22.101	21.9608	22.7008	2130	0
11	09:24:32	1711527872	25	17.8	21.9	16.5	24.8	16.3	27.2	15.9	15.0938	22.101	21.9608	22.7008	2133	0
12	09:24:32	1711527873	25	17.8	21.9	16.5	24.8	16.3	27.2	15.9	15.0962	22.1276	21.9886	22.7298	2128	0
13	09:24:32	1711527873	25	17.8	21.9	16.5	24.8	16.3	27.2	15.9	15.0962	22.1276	21.9886	22.7298	2126	0
14	09:24:33	1711527873	25	17.8	21.9	16.5	24.8	16.3	27.2	15.9	15.0962	22.1276	21.9886	22.7298	2125	0
15	09:24:33	1711527873	25	17.8	21.9	16.5	24.8	16.3	27.2	15.9	15.0962	22.1276	21.9886	22.7298	2122	0
16	09:24:33	1711527874	25	17.8	21.9	16.5	24.8	16.3	27.2	15.9	15.0962	22.1276	21.9886	22.7298	2131	0
17	09:24:33	1711527874	25	17.8	21.9	16.5	24.8	16.3	27.2	15.9	15.0962	22.1276	21.9886	22.7298	2136	0
18	09:24:34	1711527874	25	17.8	21.9	16.5	24.8	16.3	27.2	15.9	15.0962	22.1276	21.9886	22.7298	2132	0
19	09:24:34	1711527874	25	17.8	21.9	16.5	24.8	16.3	27.2	15.9	15.0947	22.1511	22.0124	22.7514	2131	0
20	09:24:34	1711527875	24.9	17.8	21.9	16.6	24.8	16.2	27.2	15.9	15.0947	22.1511	22.0124	22.7514	2136	0
21	09:24:34	1711527875	24.9	17.8	21.9	16.6	24.8	16.2	27.2	15.9	15.0947	22.1511	22.0124	22.7514	2136	0
22	09:24:35	1711527875	24.9	17.8	21.9	16.6	24.8	16.2	27.2	15.9	15.0947	22.1511	22.0124	22.7514	2127	0
23	09:24:35	1711527875	24.9	17.8	21.9	16.6	24.8	16.2	27.2	15.9	15.0947	22.1511	22.0124	22.7514	2134	0
24	09:24:35	1711527876	24.9	17.8	21.9	16.6	24.8	16.2	27.2	15.9	15.093	22.1736	22.0353	22.7734	2127	0
25	09:24:35	1711527876	24.9	17.8	21.9	16.6	24.8	16.2	27.2	15.9	15.093	22.1736	22.0353	22.7734	2127	0
26	09:24:36	1711527876	24.9	17.8	21.9	16.6	24.8	16.2	27.2	15.9	15.093	22.1736	22.0353	22.7734	2125	0
27	09:24:36	1711527876	24.9	17.8	21.9	16.6	24.8	16.2	27.2	15.9	15.093	22.1736	22.0353	22.7734	2131	0
28	09:24:36	1711527877	24.9	17.8	21.9	16.6	24.8	16.2	27.2	15.9	15.093	22.1736	22.0353	22.7734	2124	0
29	09:24:36	1711527877	24.9	17.9	21.8	16.6	24.8	16.2	27.1	15.9	15.093	22.1736	22.0353	22.7734	2131	0
30	09:24:37	1711527877	24.9	17.9	21.8	16.6	24.8	16.2	27.1	15.9	15.0967	22.1956	22.0538	22.7955	2131	0
31	09:24:37	1711527877	24.9	17.9	21.8	16.6	24.8	16.2	27.1	15.9	15.0967	22.1956	22.0538	22.7955	2126	0
32	09:24:37	1711527877	24.9	17.9	21.8	16.6	24.8	16.2	27.1	15.9	15.0967	22.1956	22.0538	22.7955	2127	0
33	09:24:37	1711527878	24.9	17.9	21.8	16.6	24.8	16.2	27.1	15.9	15.0967	22.1956	22.0538	22.7955	2127	0
34	09:24:37	1711527878	24.9	17.9	21.8	16.6	24.8	16.2	27.1	15.9	15.0967	22.1956	22.0538	22.7955	2136	0
35	09:24:38	1711527878	24.9	17.9	21.8	16.6	24.8	16.2	27.1	15.9	15.0967	22.1956	22.0538	22.7955	2140	0
36	09:24:38	1711527878	24.9	17.9	21.8	16.6	24.8	16.2	27.1	15.9	15.0967	22.1956	22.0538	22.7955	2131	0
37	09:24:38	1711527879	24.9	17.9	21.8	16.6	24.8	16.2	27.1	15.9	15.1007	22.212	22.0734	22.8099	2136	0
38	09:24:38	1711527879	24.8	17.9	21.8	16.6	24.7	16.2	27.1	15.9	15.1007	22.212	22.0734	22.8099	2126	0
39	09:24:39	1711527879	24.8	17.9	21.8	16.6	24.7	16.2	27.1	15.9	15.1007	22.212	22.0734	22.8099	2131	0

Figure 4-21 *CSV file generated during one of the days of the campaign*

4.1.3.8 Files Needed to Run the Experiment Code

The software for the experiment includes several files and they communicate in a way presented in Figure 4-22:-.

There are 3 main parts of the code that are responsible for the following tasks:

Collection_data_2_Units.py:

This script is responsible for the data collection from two units. It reads data from all connected sensors. The script saves the data to CSV files in real time and implements error-handling mechanisms. It ensures continuous data collection even if an error occurs. It reads sensor values at 3Hz and updates the GUI to provide real-time visualization of readings.

Sensor_HT.ino:

This file contains the Arduino sketch used to manage the T&RH sensors. The Elegoo board reads relative humidity and temperature data from 8 sensors and sends these data to the Raspberry Pi over a serial connection. The script uses a start signal from the Raspberry Pi to trigger the data reading process, after which the Arduino transmits the measured data back to the Raspberry Pi for logging and visualization in the GUI.

UI_HAMSTER.py:

This script is responsible for the GUI and allows the experimenter to interact with the experiment in near real-time. The interface is divided into distinct sections to monitor each unit individually.

The GUI displays relative humidity, temperature, air velocity, and motor position data from the connected sensors and allows control of the motor.

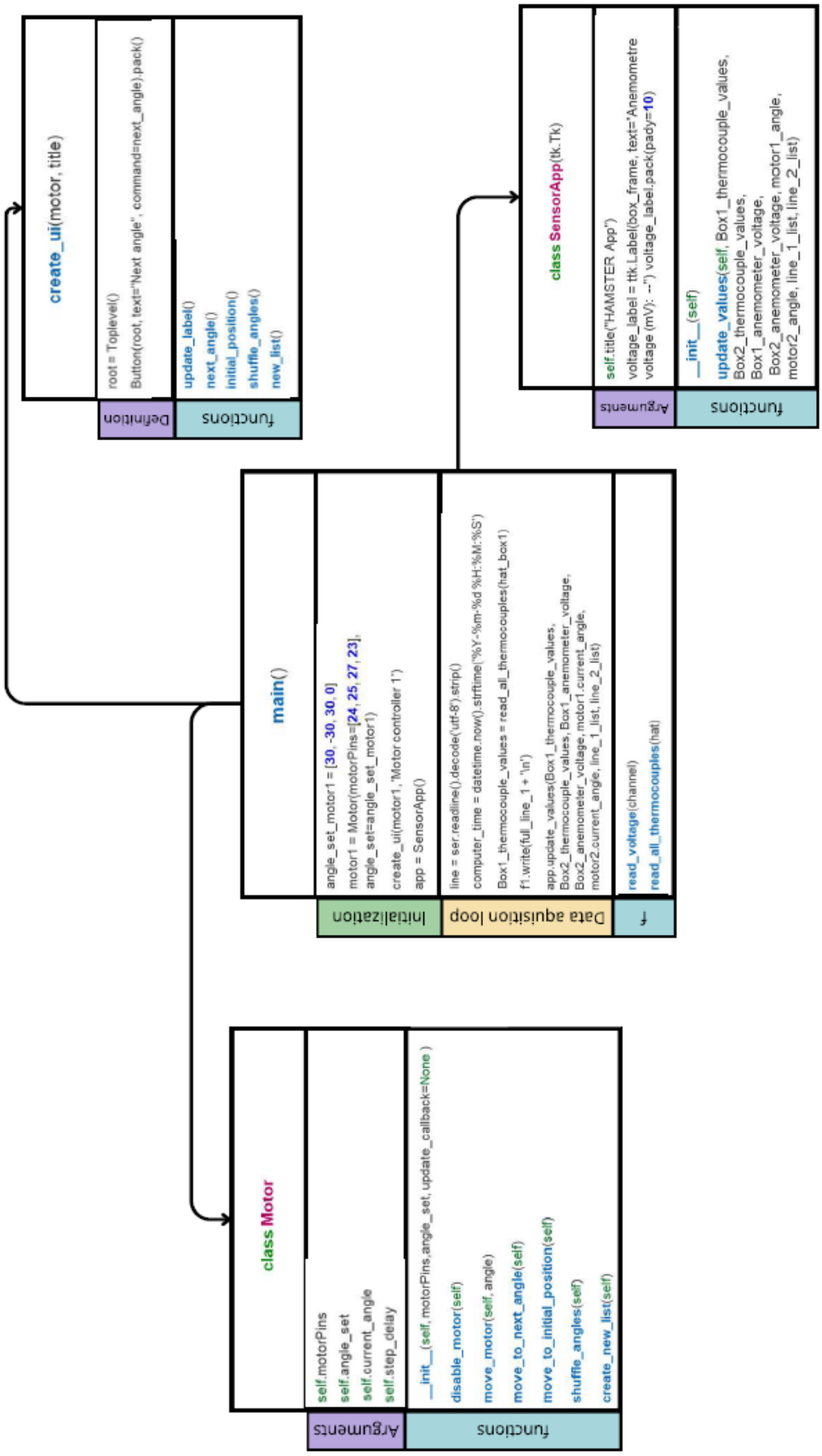

Figure 4-22 *Code structure diagram for the experiment*

4.2 Design of experimental campaign

4.2.1 Parabolic flight

A parabolic flight is a specific type of aerial manoeuvre designed to create short periods of microgravity or altered gravity conditions. During a parabolic flight, the aircraft follows a parabolic trajectory that alternates between steep climbs and free-fall descents (Petersen et al., 2021). It enables researchers to conduct microgravity experiments while maintaining direct interface with their equipment during flight.

Microgravity is achieved by flying the aircraft in a parabolic trajectory (Figure 4-23). To achieve microgravity conditions, the aircraft first climbs steeply. During this phase, the aircraft experiences an increased gravitational force, up to 1.8 times the normal gravitational pull, in what is called the hypergravity phase. After reaching the top of its climb, the aircraft enters a free-fall arc for approximately 22 seconds; this phase is called the microgravity phase. During this period, both people and items onboard experience weightlessness. The airplane then descends, encountering a second hypergravity phase. After that, the airplane levels out.

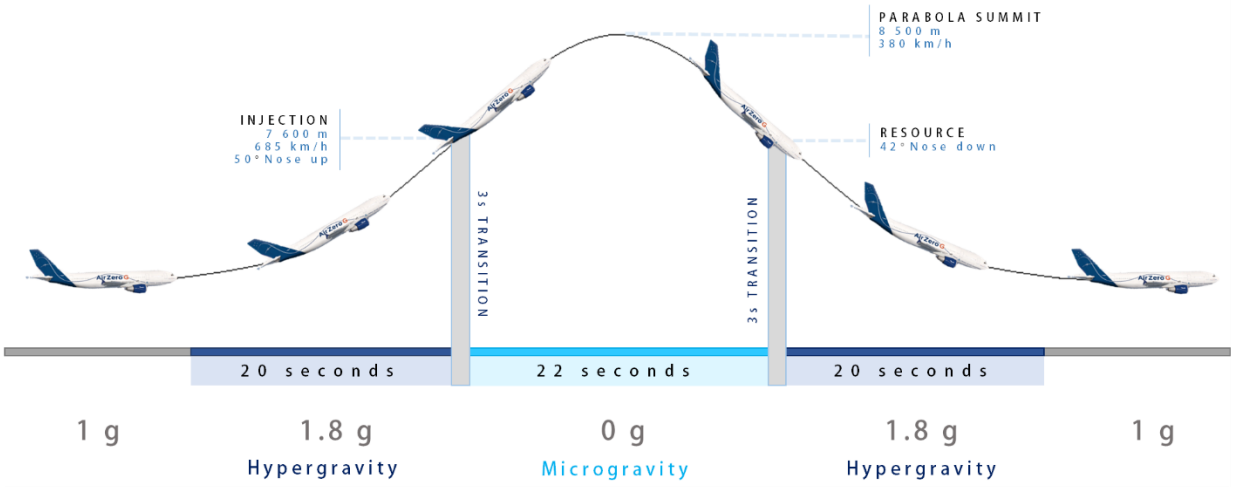

Figure 4-23 *The parabolic flight manoeuvre of the Airbus A310 (Credit: www.airzerog.com).*

These manoeuvres are repeated 31 times during a single flight, allowing for the execution of several combinations or repetitions (Figure 4-24).

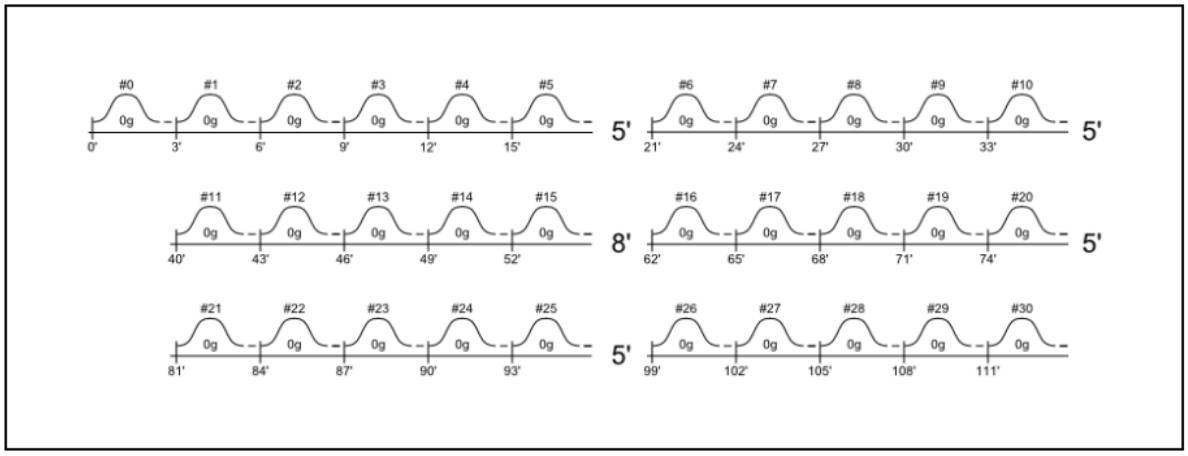

Figure 4-24 *Typical flight profile (Credit: Novespace).*

Between two parabolas, there is a recovery period of around 1 minute and 40 seconds, during which the aircraft returns to normal gravity conditions, allowing experimenters to reset or adjust their equipment. Usually, the flight lasts between three to five hours, depending on the specific conditions of the campaign. A typical day of manoeuvres during a flight campaign can be divided as described below:

1. Parabola 0 - Initial Test Parabola

Parabola 0: Initial test, the flight's first parabola, it allows pilots and experimenters to test the performance of all systems and ensure preparation for the next move. As a result, the first set contains six parabolas in total.

2. Parabolas 1-5 - First Set

After completing Parabola 0, the flight moves on to the parabolas 1–5. This set follows the same parabolic trajectory as previously described, with each parabola causing alternate hypergravity and microgravity phases.

3. Longer Breaks After Sets of 5 Parabolas

An extended normal gravity phase is entered by the aircraft, after each set of five parabolas, there is a 5-minute break after parabolas 5, 10, and 20 and an 8-minute break after parabola 15.

4. Parabolas 6-30 - Remaining Sets

The remaining sets of parabolas follow the same structure, with 5 parabolas per set, followed by a longer break.

4.2.2 1st Parabolic Flight Campaign

The primary goal of this experiment was to understand how variations in air velocity and/or inclination angle affect heat and mass transfer on the leaf replica surface under microgravity and hypergravity conditions. Different angles and ai velocity were tested to compare forced convection effects to free convection in a microgravity environment.

4.2.2.1 Experimental design

Different angles were tested for several air velocities. The angles where the non-evaporative side of the leaf replica faces the airflow are referred to as negative angles, and the cases where the evaporative side of the leaf replica faces the airflow are referred to as positive angles (Figure 4-25). The case where the leaf replica is aligned with the streamline will be referred to as angle 0 or neutral inclination.

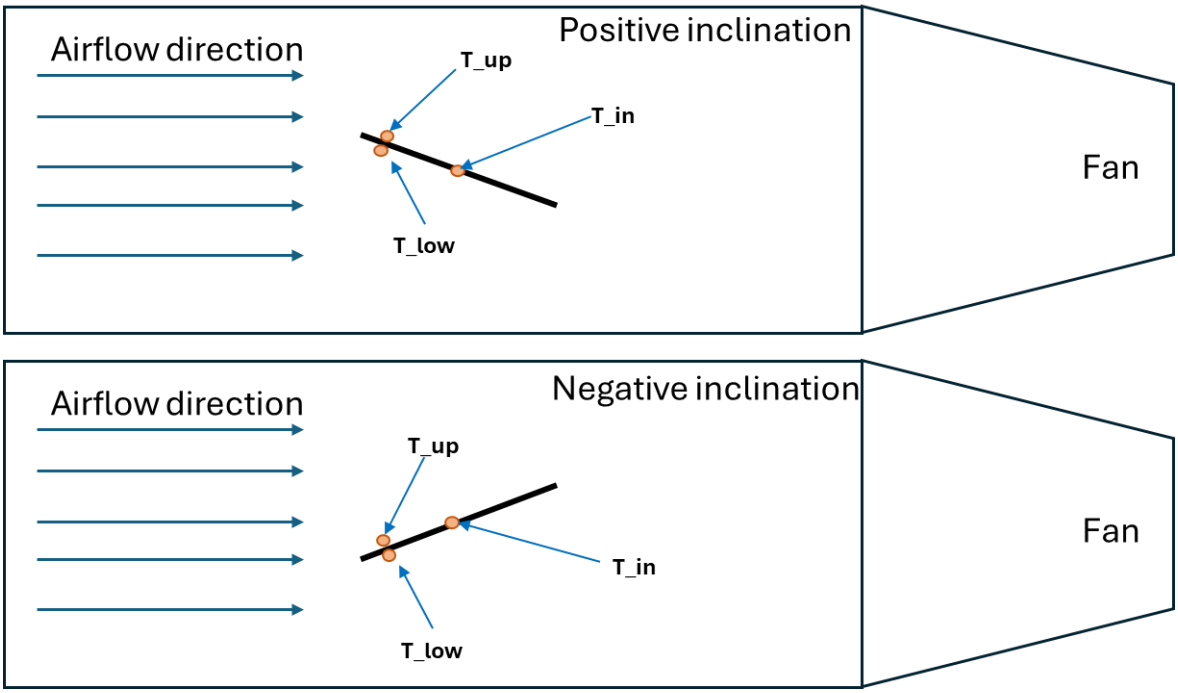

Figure 4-25 *Visualisation of tested position and angles naming*

4.2.2.2 Experimental set-up and tested parameters

During the 1st Parabolic flight campaign, the following combinations of angle and air velocities have been tested (Figure 4-26). As mentioned before, these values have been chosen based on the CC design.

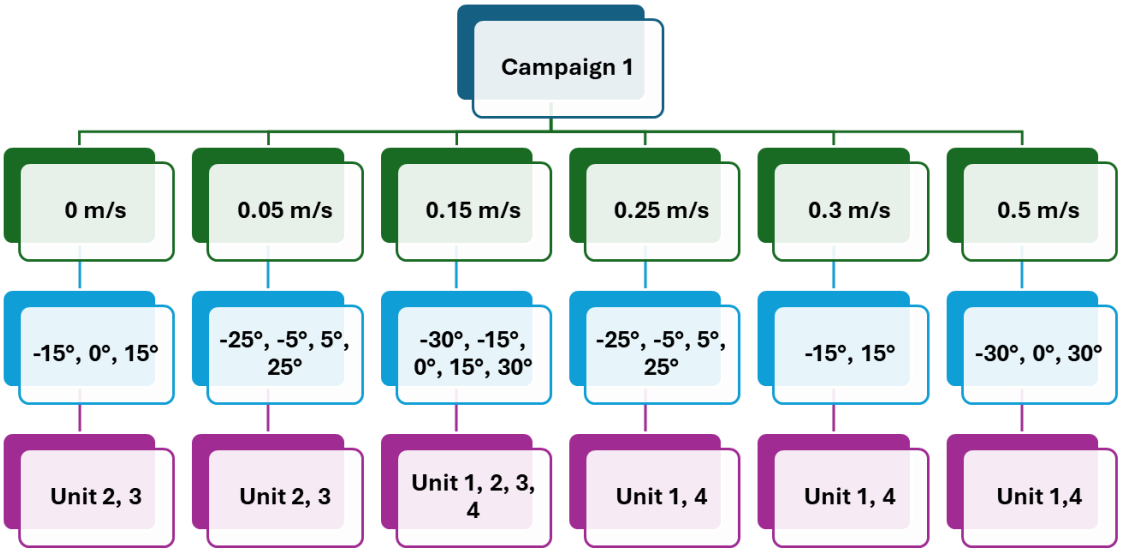

Figure 4-26 *Air velocity – angle combinations tested during the 1st campaign*

This design has allowed to repeat 15-18 times each combination of a tested angle and air velocity. The order of tested values has been randomized; however, the randomization was limited by the parabolic flight nature. Because changing the air velocity and angle between each parabola was not feasible, air velocity adjustments were made per set of parabolas, while angles were modified for each individual parabola (Figure 4-27 shows the timing of parameter changes).

Conceptual design, development, and experimental protocols of the leaf replica test system

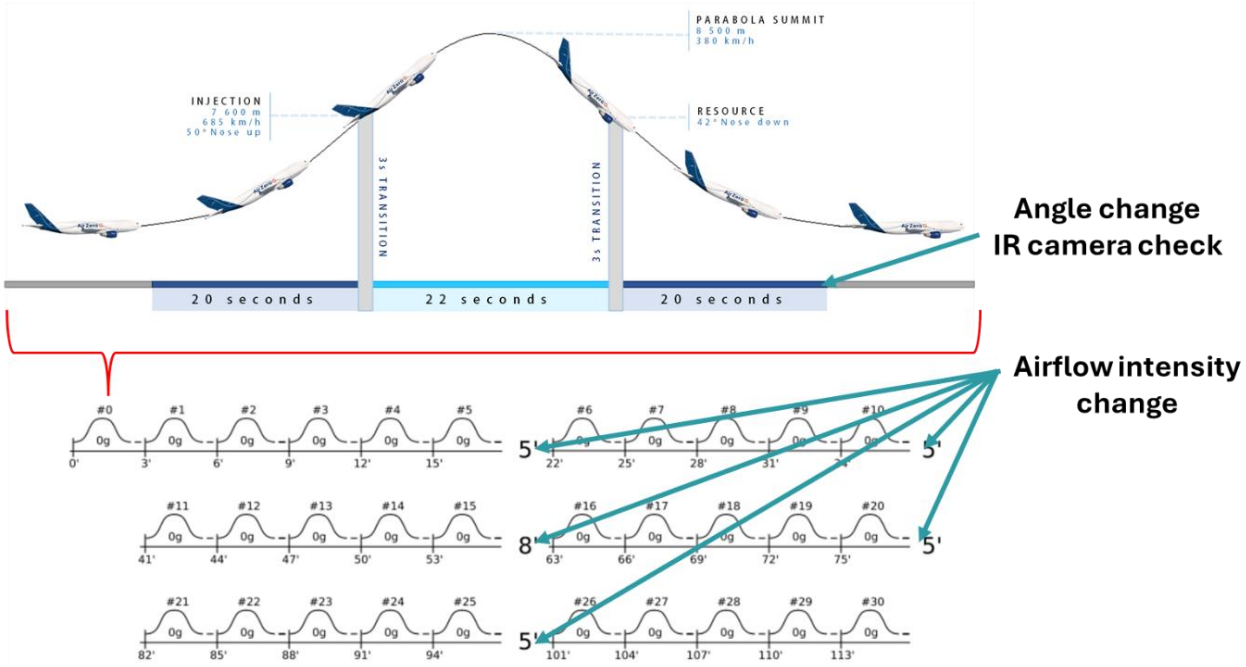

Figure 4-27 *Parameters change time during the campaign*

In the aircraft environment, the ambient temperature and relative humidity levels were monitored but not controlled. These parameters were recorded throughout the flight to account for any external fluctuations in the environmental conditions that could impact experimental outcomes. The targeted air velocity values were as follows: 0, 0.05, 0.15, 0.25, 0.3, and 0.5 m/s, as velocities above this threshold reduce the free convection effect almost completely for the investigated temperature range. The angles were limited to ±30 degrees to keep the leaf replicas clearly visible within the IR camera frame.

Each morning, the initial angle alignment (angle 0) was verified for each leaf replica to ensure consistency. During the flight, two persons were required to perform these experiments.

While the first person was monitoring the computer interface, changing the angles and performing flat field correction for IR cameras; the second one was responsible for visual inspection of the experimental units and air velocity change. This person was also responsible for the visual check of an angle change.

During the parabolic flight campaign, the experiment collected the data over 3 consecutive days:

- First day - 31 parabolas

- Second day - Two flights (3 parabolas in first flight and 31 parabolas in the second one)
- Third day - 31 parabolas

Given the design, multiple repetitions of each parameter combination were collected to analyse the distribution and average values across the dataset. During the parabolic flight, data collection was monitored, and any issues, such as interruptions in the IR camera data stream, could be addressed immediately. Data collection was initiated before Parabola 0 and continued until the end of the 30th parabola, providing a single continuous dataset across all flight phases. The exact combination and order of the values tested during the parabolic flight campaign can be found in Appendix E.

4.2.3 2nd Campaign of the Parabolic Flight

In the 2nd campaign, the aim was to further investigate the effects of air velocity and angle on heat and mass transfer over leaf replicas under microgravity and hypergravity conditions, with an emphasis on comparing evaporative versus non-evaporative leaf replicas. Following observations from the 1st campaign, adjustments were made to the angle ranges and air velocity values.

4.2.3.1 Experimental set-up and tested parameters

In this experiment, Units 1 and 2 contained non-evaporative leaf replicas, while Units 3 and 4 contained evaporative leaf replicas. Based on the results of the previous campaign, we observed no significant variation between angle 0 and ±5°, between 25° and 30° and -25° and -30°. Thus, these angles were not investigated. Furthermore, the maximum air velocity was limited to 0.3 m/s, as higher values showed no notable effect. For the 2nd Parabolic Flight Campaign, the combinations of angle and air velocity tested are presented in Figure 4-28. This design allowed for 6-7 repetitions of each angle and air velocity combination. The order of tested values was randomized within the same constraints as before. As with the 1st campaign, changes in air velocity were conducted by adjusting voltage settings across sets of parabolas, while angles were modified for each individual parabola.

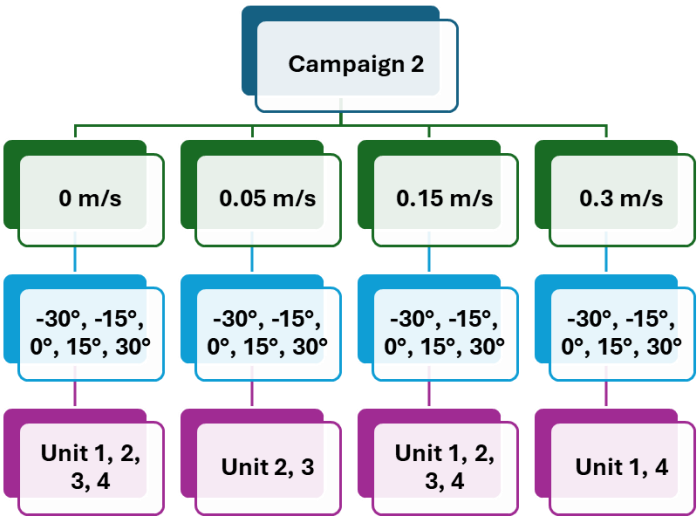

Figure 4-28 *Air velocity – angle combinations tested during the 2nd campaign*

Data were collected over the course of three flight days as follows:

- First day - 26 parabolas
- Second day - Two flights (31 parabolas in the first flight and 6 parabolas in the second)
- Third day - 31 parabolas

The detailed sequence and combination of values tested for each flight can be found in Appendix E.

4.2.4 Ground Reference Experiment

The Ground Reference Experiment aims to provide a baseline to analyse heat and mass transfer coefficients in a controlled environment, supporting comparative analysis with data from the parabolic flight campaign. Additionally, it was designed to reach a steady-state condition, which was not possible during the parabolic flight campaigns.

The objective of the Ground Reference Experiment was to collect data on heat and mass transfer for the leaf replicas and the environment under stable and controlled temperature and relative humidity conditions. These data have provided a basis to validate results from the parabolic flight experiment.

4.2.4.1 Experimental setup and tested parameters

The experiment took place in the Higher Plants Chamber (HPC) within the MELiSSA Pilot Plant at the Universitat Autonoma de Barcelona. The goal was to replicate the temperature and relative humidity conditions from the parabolic flight; however, the lowest achievable relative humidity setting was 50% due to chamber limitations. Temperature settings were chosen based on the chamber's capacity to maintain this relative humidity level rather than matching the exact conditions from the parabolic flight.

In the parabolic flight campaign, the temperature ranged from 13°C to 21°C with relative humidity not exceeding 35%. Due to the constraints of the HPC, the temperature levels for the ground experiment were set at 18°C, 19.5°C, and 21°C — the highest temperature approximates the upper limit of the parabolic flight and the lowest temperature being the minimum achievable with the chamber limitation for relative humidity level.

The experimental platform was placed inside the HPC perpendicular to the internal airflow direction within the chamber (Figure 4-29).

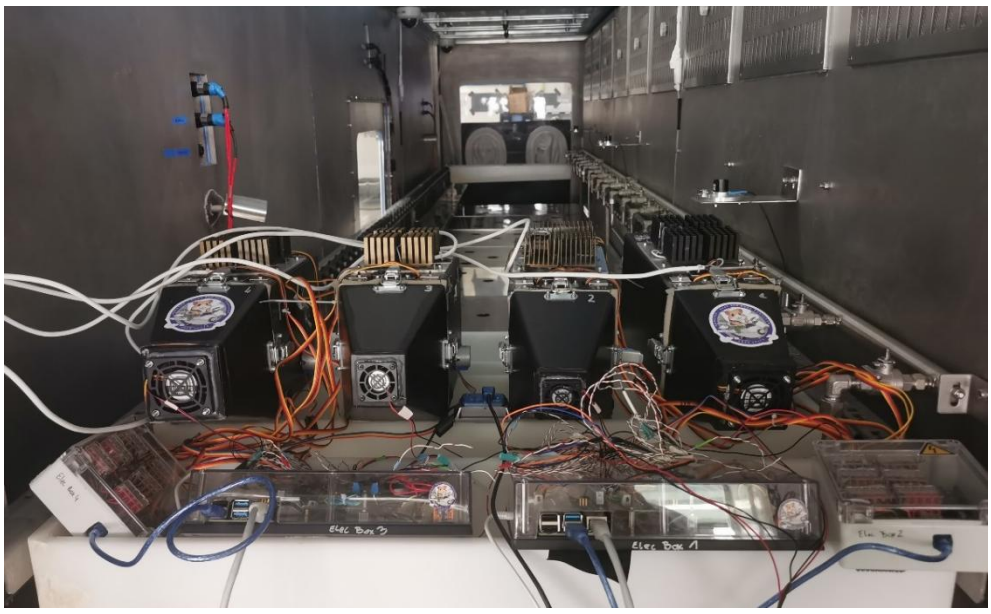

***Figure 4-29** Hardware placement inside HPC*

Thanks to this orientation, the internal airflow of the HPC, needed for maintaining stable relative humidity and temperature levels, did not affect the airflow within each unit.

The tested combination can be seen in Figure 4-30.

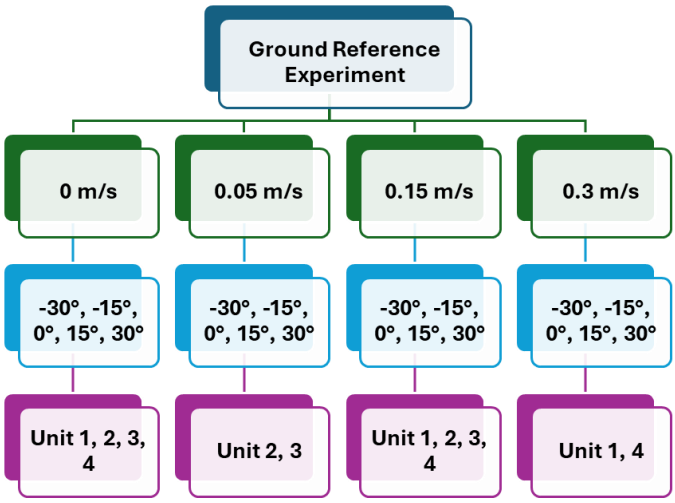

Figure 4-30 *Air velocity – angle combinations tested during the Ground Reference Experiment*

Two types of tests were conducted: in the first, all units contained wet replicas, and in the second, Units 1 and 2 contained dry replicas while Units 3 and 4 contained wet replicas. Each configuration was tested for three temperature settings, with at least five repetitions per configuration of angle, air velocity, and replica type. Test sequences were randomized.

4.3 Statistical analysis

To evaluate the effects of the experimental parameters on surface temperature increase, statistical analysis was conducted using Welch's Analysis of Variance (ANOVA) with a significance level of $p < 0.05$. The significance of the following factors was tested - gravity phase, air velocity, unit, day and inclination on the surface and internal temperature readings of leaf replica. The analysis was conducted in Python, with the statsmodels library.

Welch's ANOVA was used due to unequal variances and sample sizes across groups. Post hoc Tukey HSD tests were conducted to identify specific pairwise differences. Additionally, residual normality was checked using the Shapiro-Wilk test, and Levene's test was applied to check the homogeneity of variances. For visual evaluation, Q-Q plots were created.

4.4 Main outcomes of the chapter

- Design, description and assembly of an experimental setup that studies heat and mass transfer processes and their dependence on air velocity and inclination between a leaf replica and its environment in normal and different gravity conditions.
- Design and integration of mechanical, electrical, and software systems for monitoring, controlling, and data acquisition from all of the sensors and actuators, including T&RH sensors, fan, thermocouples, anemometers, motors, and MSR sensor.
- Planification and realization of ground reference experiment and parabolic flight experiment
- Definition of reproducible measurement protocols.

5 Experimental results and statistical analysis for ground reference and parabolic flight experiments

This chapter presents the data analysis conducted for both the Ground Reference Experiment and the Parabolic Flight Experiment, focusing on the thermal responses of non-evaporative and evaporative leaf replicas under varying environmental conditions. The primary objectives were to assess the effects of the air velocity, angle of orientation, and gravity on surface and internal temperatures in a controlled environment, followed by an evaluation of temperature dynamics in normal and altered gravity conditions.

5.1 Ground Reference Experiment

The goal of the Ground Reference Experiment was to collect data about the steady state in an environment with controlled relative humidity and temperature outside the unit.

All 4 units were placed in the HPC at MPP, and the surface temperatures of leaf replicas were measured for 20 to 45 minutes to record steady-state conditions.

The temperature data taken into consideration for statistical purposes were collected from four units (Unit 1 to Unit 4) at three thermocouple locations (T_{up}, T_{low}, and T_{in}) as can be seen in Figure 5-1, under various air velocities (0.0, 0.05, 0.15, and 0.3 m/s) and angle (-30°, -15°, 0°, 15°, 30°) conditions. The thermocouple is attached to the upper and lower surface with the same black aluminium tape like the one used for creating upper surface of leaf replica.

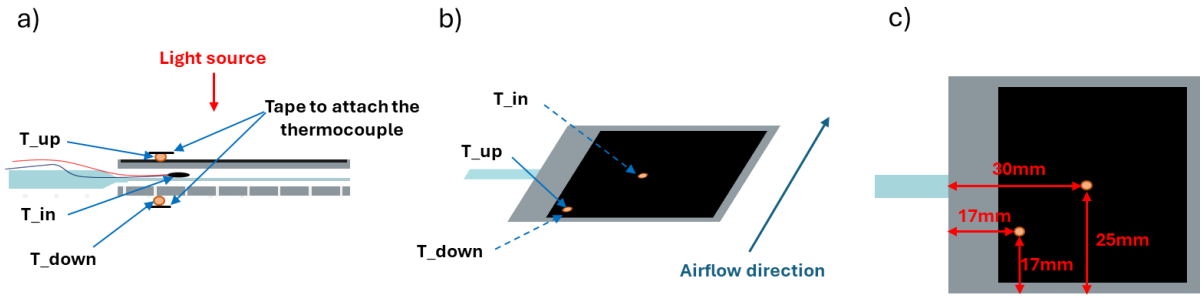

Figure 5-1 *Location of temperature measurements on the leaf replica. (a) side view, (b) perspective view, (c) top view.*

5.1.1 Conditions inside the chamber

To provide stable environmental conditions for the Ground Reference Experiments, the setup was placed inside the MPP where it is possible to maintain stable temperature and relative humidity conditions. A stability test of the chamber was conducted with temperature and RH setpoints respectively at 18°C and 50%. The readings from all of the units were recorded to check the stability of relative humidity and temperature.

For this experiment, an **evaporative leaf replica** was placed inside the unit (Figure 5-2).

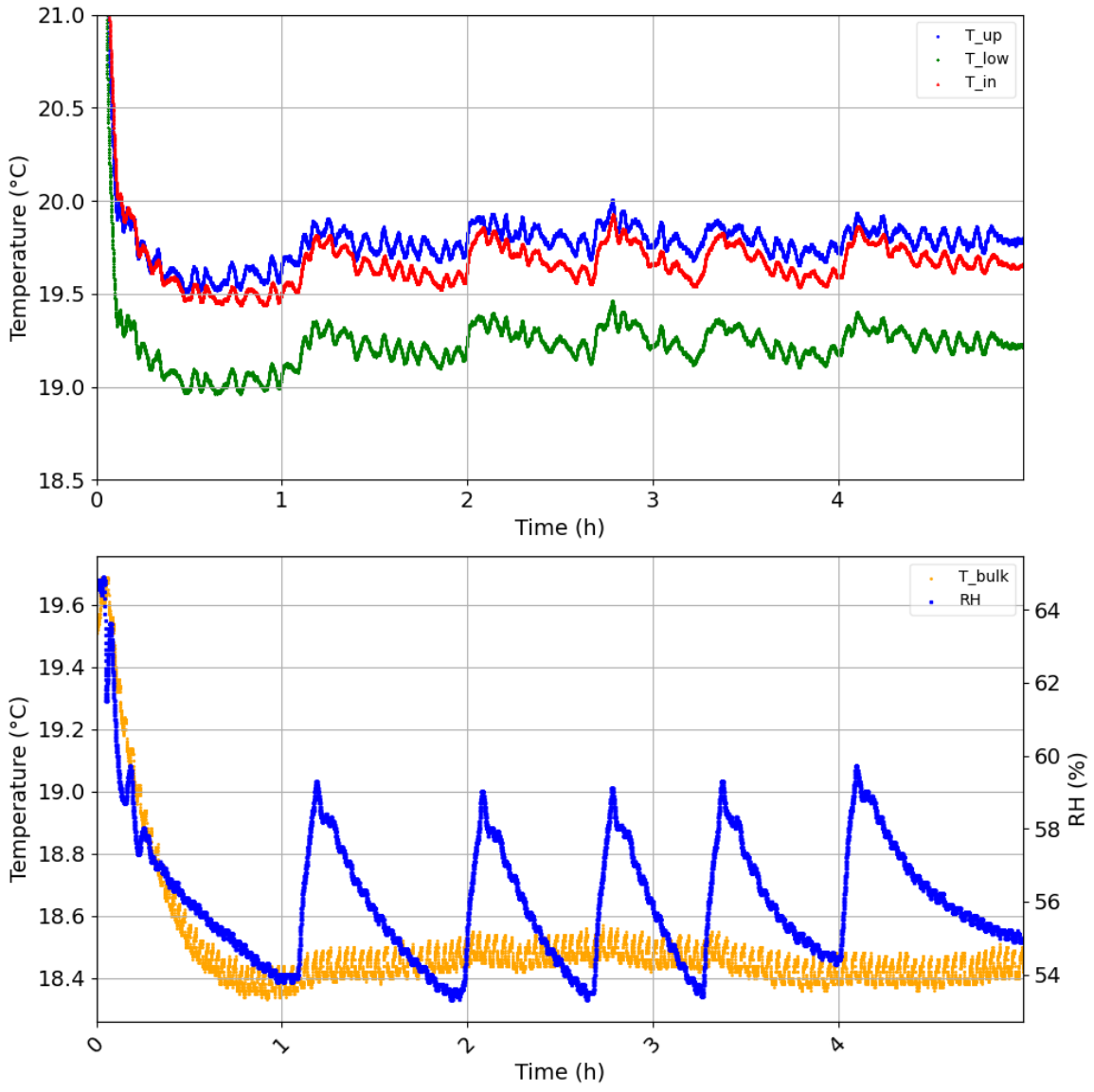

Figure 5-2 *Stability test results of Higher Plants Chamber and temperature readings form evaporative leaf replica the case 0° angle and no airflow. Top: temperature for the upper (T_up) and lower (T_low) surfaces, and for the temperature inside the leaf replica (T_in). Bottom: chamber's temperature (T_bulk) and relative humidity (RH) over time with setpoints at 18°C and 50% RH.*

Experimental results and statistical analysis for ground reference and parabolic flight experiments

Once steady state conditions are reached (approximately 1 hour 5 minutes after the start of the control system), the chamber demonstrates good stability in both temperature and relative humidity during the whole duration of the test. The bulk temperature fluctuates between 18.3°C and 18.6°C, while the relative humidity value oscillates between 54% and 59%. Periodic oscillations are caused by the chamber environmental control mechanism. For the leaf replica inside the units, the temperature readings remained almost steady with small temperature raises (ca. 0.2°C) when the highest relative humidity level (59%) inside the HPC was recorded.

5.1.2 General trends and observations

In the **non-evaporative** setup, all recorded temperatures (lower, upper, internal) show an initial increase as the system adjusts after being set to the experimental conditions. After approximately 5 minutes, the temperatures stabilize, indicating that the system has reached a steady state as shown in Figure 5-3, which is an example of the general trend observed for most of the measurements. The change of humidity is related to the oscillations shown in Figure 5-2.

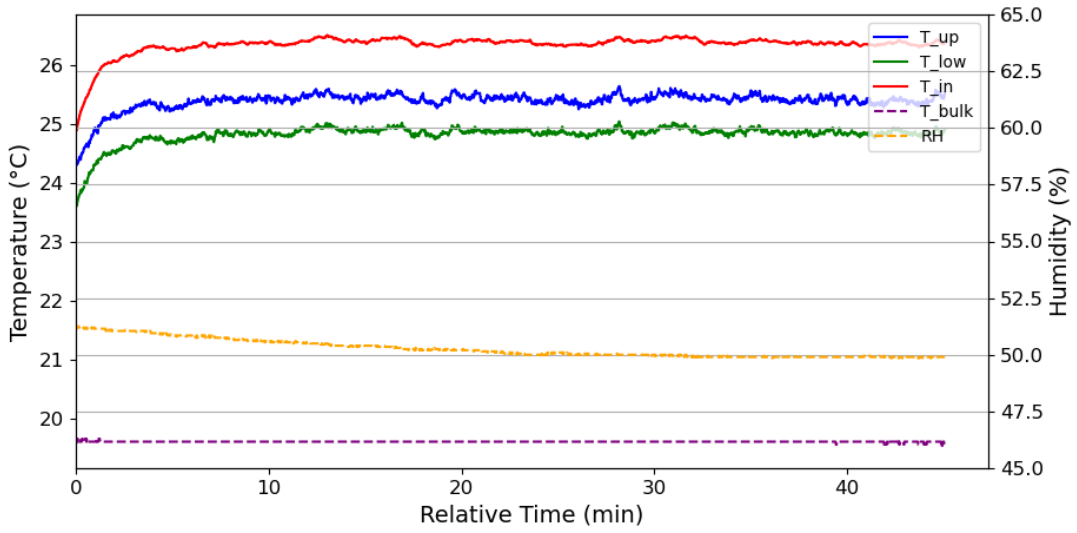

Figure 5-3 *Temperature and relative humidity trends for non-evaporative replica under steady-state conditions, angle 0, no airflow. The graph shows the temperature for the upper (T_up), lower (T_low) surfaces and for the temperature inside the leaf replica (T_in) as well as relative humidity (RH) and air temperature inside the unit (T_Bulk) with chamber setpoints at 18°C and 50% RH.*

The temperature distributions follow the following patterns:

- The internal temperature of the leaf replica stabilizes at the highest value (around 26.5°C in Figure 5-3), which is different for each HPC temperature, angle and air velocity

combination. The lowest recorded value for this location was 21.4°C for 0.3 m/s air velocity, angle 30°, and the highest was 31.2°C for 0 m/s air velocity and angle -15°.

- The upper surface temperature stabilizes at a lower value (around 25.5°C in Figure 5-3). The smallest registered difference between these two points was 0.03°C for 0.05 m/s air velocity, angle 0°, and the highest was 2°C for 0 m/s air velocity and angle -15°.
- The lower surface temperature stabilizes either at the lowest temperature value or slightly higher than the upper surface temperature. The highest registered difference between the upper and lower surfaces was 0.7°C for air velocity equal to 0.15 m/s and angle -30°, and 1.1°C for air velocity equal to 0.05 m/s and angle 15°.

Relative humidity and bulk air temperature were measured by the sensors placed inside the unit. The values were averaged from the sensor readings. The oscillation for the relative humidity is not higher than the accuracy of the sensor, which is 3%, so the sensors recorded it as a constant value.

In the setup with an evaporative replica inside, the general trends are similar, with the system reaching a steady state after about 5 minutes. However, the temperatures are lower by 3.1°C to 3.8°C due to the cooling effect of evaporation, as shown in Figure 5-4. The Humidity was not constant due to the chamber regulation cycles presented in the Figure 5-2.

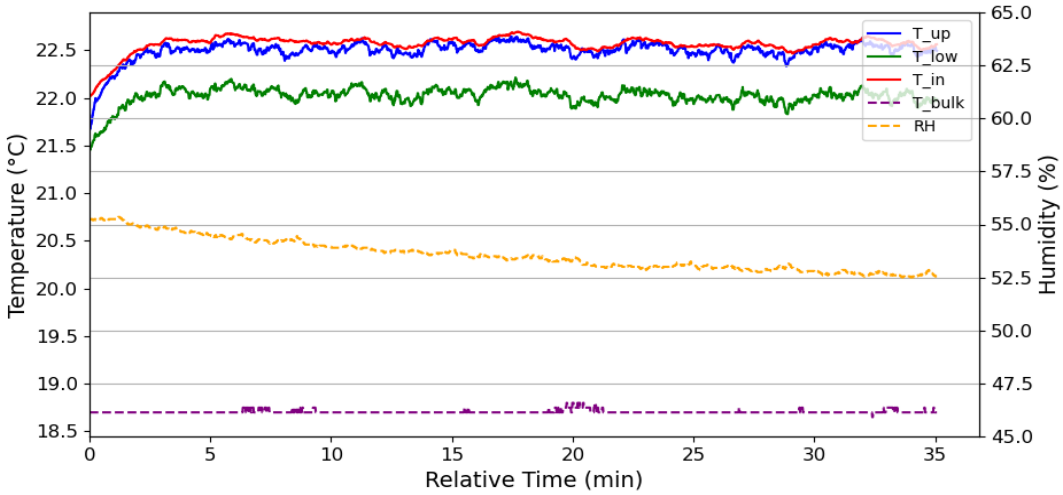

Figure 5-4 *Temperature and relative humidity trends for evaporative replica under steady-state conditions, angle 0, no airflow. The graph shows the temperature for the upper (T_up), lower (T_low) surfaces and for the temperature inside the leaf replica (T_in) as well as relative humidity (RH) and air temperature inside the unit (T_Bulk) with chamber setpoints at 18°C and 50% of RH.*

The temperature distribution for an evaporative leaf replica in steady state follows these trends:

- The upper and lower surface temperatures are similar (0.1°C higher maximum for the upper temperature).
- The internal temperature stabilizes as the lowest temperature in average by 0.3 lower than the upper surface temperature, which indicates that part of the cold generated by evaporation is stored by water inside the replica.

5.1.3 Statistical analysis

Due to the transient conditions at the beginning of the measurement, the first 5 minutes of the data has been removed in order to perform the analysis on the steady state part of the data.

As can be seen in the Q-Q plot in Figure 5-5, most of the data points (blue dots on the graph) closely follow the theoretical quantile line (red line), particularly in the middle region, indicating that the residuals are approximately normally distributed in this range. Minor deviations are visible at the tails, suggesting potential slight non-normality at extreme values.

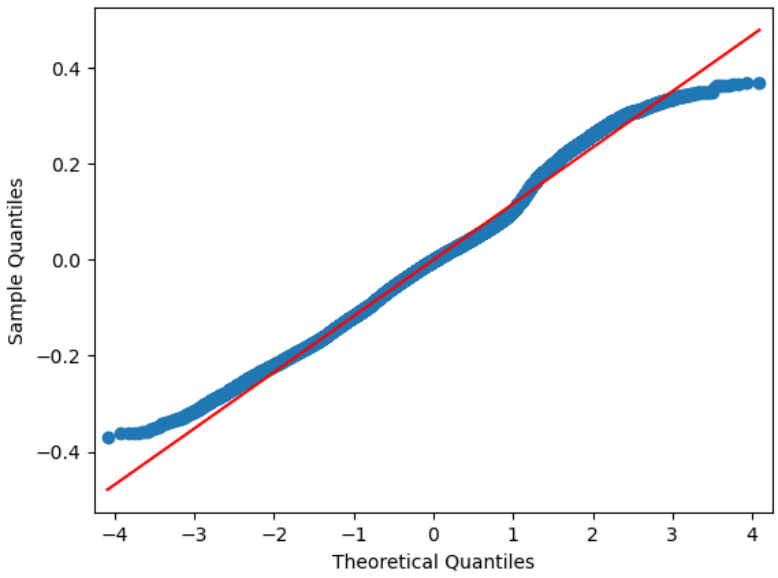

Figure 5-5 *Q-Q plot of temperature inside the leaf replica for no airflow and all tested angles. The red line represents the expected quantiles from a theoretical normal distribution, and blue dots show the measured values.*

A Welch ANOVA analysis was conducted to assess the impact of air velocity, angle, bulk temperature (T_{bulk}), and relative humidity (RH) on the temperature differences between the upper surface (T_{up}), the lower surface (T_{low}), and inside the leaf replica (T_{in}) for two types of leaf replicas – evaporative and non-evaporative. The analysis was performed at three different bulk air temperatures: 18°C, 19°C, and 21°C. The results of the analysis can be seen in Table 5-1 and Table 5-2.

		18 deg				19 deg				21 deg			
		sum_sq	df	F	PR(>F)	sum_sq	df	F	PR(>F)	sum_sq	df	F	PR(>F)
T_up	airflow	254775	3	122682	0	163165	3	80941	0	217402	3	234923	0
	angle	356744	4	128837	0	28648	4	10658	0	114860	4	93088	0
	T_bulk	3953	1	5711	0	2761	1	4110	0	328	1	1064	0
	RH	35	1	50	1.6E-12	3026	1	4503	0	42219	1	136864	0
	Residual	527936	762650			145103	215943			189545	614466		
T_low	airflow	194561	3	107760	0	54001	3	84560	0	69432	3	249601	0
	angle	351876	4	146168	0	33819	4	39718	0	95782	4	258245	0
	T_bulk	4000	1	6646	0	174	1	818	1.7E-179	586	1	6316	0
	RH	28	1	46	1.2E-11	1148	1	5395	0	11381	1	122740	0
	Residual	458990	762650			45968	215943			56976	614466		
T_in	airflow	113050	3	119976	0	35070	3	142235	0	57954	3	337151	0
	angle	265453	4	211288	0	43138	4	131219	0	110847	4	483639	0
	T_bulk	523	1	1664	0	30	1	365	2.2E-81	908	1	15851	0
	RH	65	1	208	3.8E-47	744	1	9050	0	7618	1	132948	0
	Residual	239541	762650			17748	215943			35208	614466		

Table 5-1 *Welch ANOVA results: effect of air velocity, angle, bulk temperature, and relative humidity on non-evaporative leaf replica upper, lower, and internal temperature, where 18 deg, 19 deg and 21 deg refers to the temperature inside HPC, sum_sq – Sum of squares, df – Degrees of freedom, F – F-statistic and PR(>F) – p-value.*

		18 deg				19 deg				21 deg			
		sum_sq	df	F	PR(>F)	sum_sq	df	F	PR(>F)	sum_sq	df	F	PR(>F)
T_up	airflow	19192	3	152122	0	6307	3	156768	0	57363	3	118898	0
	angle	25322	4	150536	0	6478	4	120760	0	40090	4	62322	0
	T_bulk	1507	1	35840	0	1069	1	79696	0	2771	1	17234	0
	RH	19636	1	466932	0	453	1	33758	0	1963	1	12204	0
	Residual	32460	771878			2872	214135			98466	612281		
T_low	airflow	11408	3	139645	0	12545	3	181720	0	38235	3	90194	0
	angle	6638	4	60945	0	5693	4	61845	0	24009	4	42476	0
	T_bulk	1963	1	72082	0	2231	1	96946	0	2212	1	15654	0
	RH	742	1	27235	0	2834	1	123143	0	21740	1	153848	0
	Residual	21019	771878			4928	214135			86520	612281		
T_in	airflow	10112	3	186615	0	7297	3	106143	0	68183	3	92456	0
	angle	20587	4	284954	0	13577	4	148108	0	31712	4	32251	0
	T_bulk	1676	1	92815	0	1882	1	82138	0	2287	1	9302	0
	RH	534	1	29574	0	587	1	25609	0	12189	1	49587	0
	Residual	13941	771878			4907	214135			150511	612281		

Table 5-2 *Welch ANOVA results: effect of air velocity, angle, bulk temperature, and relative humidity on evaporative leaf replica upper, lower, and internal temperature, where 18 deg, 19 deg and 21 deg refers to the temperature inside HPC, sum_sq – Sum of squares, df – Degrees of freedom, F – F-statistic and PR(>F) – p-value.*

The results show that all factors have a statistically significant effect ($p<0.05$) on the surface and internal temperature of both evaporative and non-evaporative leaf replica, air velocity and angle being the strongest influence (highest F values) where RH has much stronger effect on evaporative leaf replica.

As expected, air temperature (T_{bulk}) directly affects the temperatures of the leaf replica surfaces and the temperature inside.

The impact of relative humidity (RH) differed significantly between the non-evaporative and evaporative leaf replicas for the test conducted in 18°C and 19.5°C.

- For the non-evaporative leaf replica, RH had a weaker but still statistically significant effect ($p<0.05$, F value 16-2500 times smaller than for F value for the air velocity). This suggests that in the absence of evaporation, relative humidity still plays a role, but its impact on temperature is limited.
- For the evaporative leaf replica, RH had a much stronger influence ($p<0.05$, F value being in a range of 0.3 to 10 times smaller than the F value for the air velocity). This confirms that relative humidity strongly affects the evaporative cooling process, altering the temperature of both the upper and lower surfaces as well as inside the leaf replica.

To check if there is a statistically significant difference between the angles for all the combinations of air velocity, angle, and HPC temperature, a Tukey HSD analysis was performed (Table 5-3).

18 °				19.5 °				21 °			
Unit	Thermocouple	Airflow	Angle Pair	Unit	Thermocouple	Airflow	Angle Pair	Unit	Thermocouple	Airflow	Angle Pair
3	T_low	0	0° vs. 15°	2	T_up	0.15	-15° vs. 0°	1	T_in	0	-30° vs. 15°
3	T_in	0.15	-15° vs. 0°	3	T_up	0.15	0° vs. 15°	1	T_low	0.15	-30° vs. 0°
4	T_in	0.15	-15° vs. 0°	3	T_in	0.05	-30° vs. 30°	3	T_low	0.05	-15° vs. 0°
4	T_in	0.3	-15° vs. 0°	4	T_up	0.15	0° vs. 30°	3	T_in	0.05	-15° vs. 0°
				4	T_low	0.15	-30° vs. -15°	4	T_up	0.15	-15° vs. 30°
								4	T_up	0.15	0° vs. 15°

Table 5-3 *Angle, air velocity in m/s combinations with no statistically significant difference for Ground Control Experiment for the HPC seetings of 18, 19.5 and 21°C*

For the **non-evaporative** leaf replica, the surface temperature of the leaf replica, measured in steady-state conditions, shows dependence on the air velocity and the orientation, as can be seen in Figure 5-6. With no inlet air velocity (v = 0.0 m/s), the surface temperature was consistently higher than for other air velocities cases across all angles. As the air velocity increased, a cooling effect was observed, due to enhanced forced convection.

For the upper surface, angle-dependent trends showed that the surface temperature increased from -30° to 0°, and then decreased from 0° to 30° for all air velocities in a non-symmetric way as can be seen in Figure 5-6a (no inlet airflow). The highest temperatures were observed for angle 0°, and the lowest occurred at the extreme angles (-30° and 30°). This behaviour comes from variations in the airflow interaction with the leaf replica external surfaces, where a tilted position of the leaf replica (-30° and 30°) induces modified boundary layers compared to a horizontal position (0°). The higher steady-state temperature at 0° is probably caused by the formation of the thermal boundary layer, with counter-current vortices created on top of the upper surface. When the leaf replica is fully aligned with the airflow, the boundary layer grows smoothly, increasing inertia in heat transfer and reducing convective cooling efficiency. For the angled surface, the airflow may induce small turbulence, which can disturb the boundary layer and improve convective heat transfer.

A statistically significant difference in cooling efficiency was observed between positive and negative angles. At negative angles, where upper surface faces the airflow, lower temperatures were recorded for all measured surfaces. In contrast, at positive angles, where the airflow cools the lower surface, higher surface temperatures were observed. This indicates that airflow directly across the illuminated surface (negative angles) is more effective at dissipating heat, whereas cooling the lower surface (positive angles) is less efficient.

For the lower surface, angle-dependent trends revealed that the surface temperature increased from -30° to 0° and then decreased from 0° to 30° for a given air velocity. However, a difference was noted: temperatures at negative angles (-30°, -15°) were higher in average by 0.5°C than those at the corresponding positive angles (15°, 30°), as can be seen in Figure 5-6b. The same behaviour is observed with the internal temperature as opposed to the upper one. It could be due to the radiation that warms the upper surface, and that effect is not transmitted by the water stored in the replica.

The measurements of internal temperature exhibit trends identical to those observed for the lower surface with surface temperatures following a parabolic pattern and negative angles showing slightly higher temperatures compared to their corresponding positive angles as can be seen in Figure 5-6c. This shows that the global heat transfer (both sides) is higher with positive angles.

When an inlet flow is imposed, all boundary layers are totally different, as a dynamic boundary layer is imposed by the inlet flow, at least for the largest velocities investigated. When the leaf replica is fully aligned with the airflow (θ = 0°), the dynamic boundary layer grows smoothly with the length. The Reynolds number of the flow over the replica (based on the length of the replica) is about Re≈1.6x10^3 for a velocity v = 0.5 m/s, which is far from the critical Reynolds number for a transitional flow (Re≈5x10^5), this aspect will be further described in Chapter 6.

When the angle is negative (upper surface facing the stream), the streamlines are curved above the leaf replica and induce a non-regular and thinner boundary layer at the end, as the curved streamlines face the stream. Below the replica, a detached flow develops (vortices opposite to the flow direction) and induce reinforced heat exchange along the lower surface. When the angle is positive (lower surface facing the stream), a detached flow develops on top of the upper surface as described for a negative angle. The dissymmetry observed in Figure 5-6 is due to the radiation issued by the lighting system that make the thermal boundary layers different on both sides, as only the upper surface is under radiation. This generation of flow may start at lower air velocities.

For the **evaporative** leaf replica, the surface temperatures of the evaporative leaf replica are dependent on both the air velocity and the angle of orientation, as can be seen in Figure 5-6. The surface temperature of the evaporative leaf replica was lower by ca. 3 °C compared to the non-evaporative leaf replica due to the evaporation from the lower surface. This results in lower temperatures at all measured points for the evaporative replica at all angles and air velocities.

For the upper surface as can be seen in Figure 5-6a, the angle-dependent trends followed the same pattern observed for the non-evaporative replica: the temperature increased from -30° to 0°, then decreased from 0° to 30°. Similar to the non-evaporative replica, the highest temperatures were recorded at 0°, while the lowest temperatures were observed at the

extreme angles (-30° and 30°). The trend, however, was much flatter and reveals a weaker effect of the inclination of the replica.

For the lower surface, a similar parabolic trend was observed as can be seen in Figure 5-6b. Temperatures increased from -30° to 0° and decreased from 0° to 30° for a given air velocity. The difference between negative angles (-30°, -15°) and positive angles (15°, 30°) was less visible compared to the non-evaporative leaf replica. It suggests that evaporative cooling contributed more uniformly across the lower surface.

For the internal temperature shown in Figure 5-6c, the trends mirrored those observed for the lower surface. A parabolic pattern, with the highest temperatures recorded at 0° and lower temperatures at extreme angles (-30°, 30°). The evaporative cooling mechanism led to significantly lower internal temperatures compared to the non-evaporative replica.

For the evaporative replica, the surface temperature at +30° was consistently lower than at -30°, except for the upper surface. This behaviour can be attributed to the combined effect of evaporation and convection occurring on the lower surface at +30°, which enhances cooling and also affects the internal temperature. In contrast, the upper surface at +30° did not benefit from either evaporative cooling or effective convective heat transfer, resulting in comparatively higher temperatures.

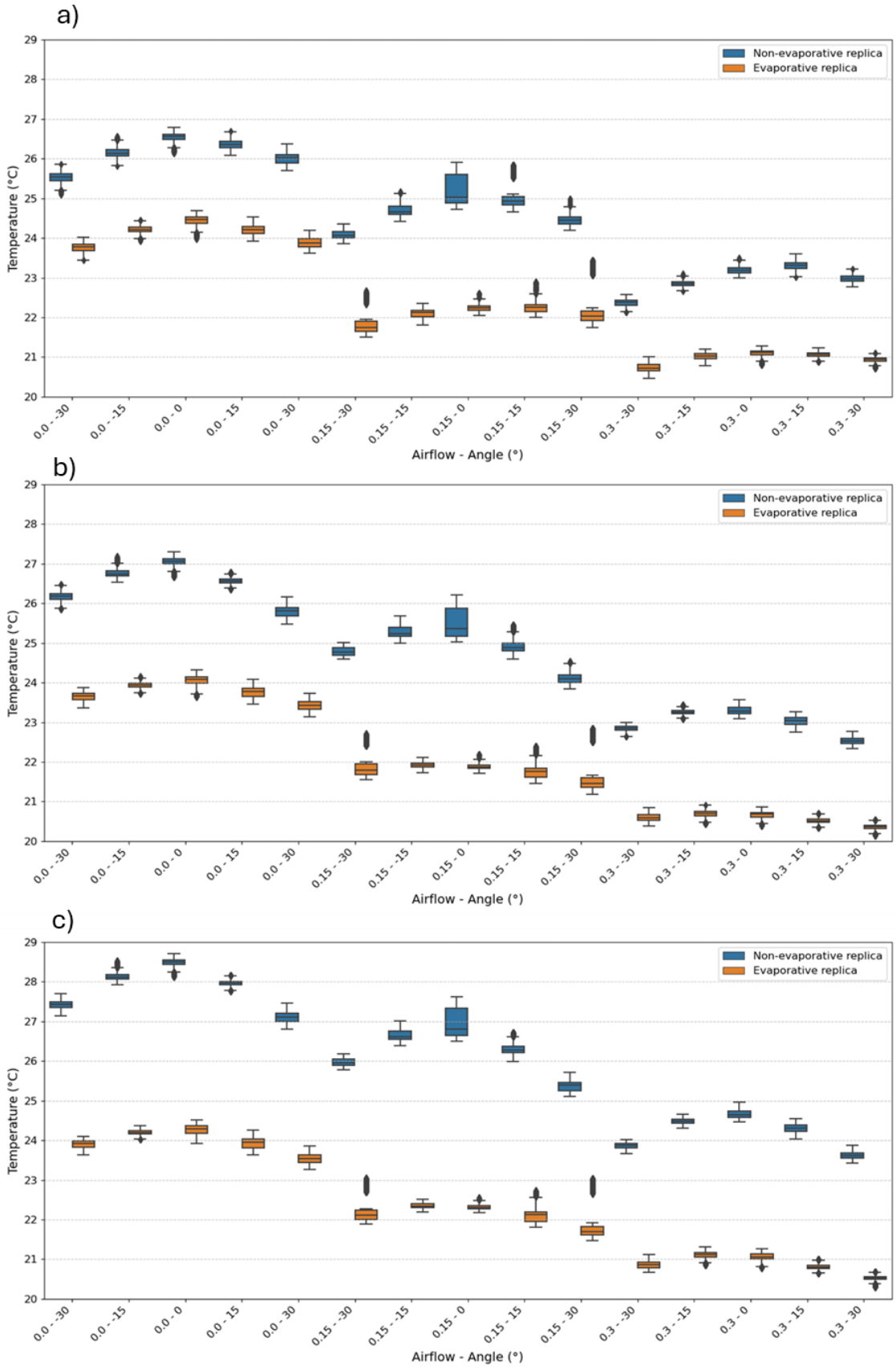

Figure 5-6 *Boxplot of steady state temperature recordings for upper (a), lower (b), and temperature inside leaf replica (c) for non-evaporative and evaporative leaf replicas for various air velocities (0.0, 0.15, 0.3 in m/s) and angels (-30, -15, 0, 15, 30).*

5.2 Parabolic flight experiment

5.2.1 Conditions during the flight

During the parabolic flight campaigns, RH is decreasing over time across all days and campaigns. Campaign 2 showed greater variability in RH, around 32% at the beginning of the flight and near 15% at the end. In contrast, Campaign 1 demonstrated much smaller variation in RH with the recorded values ranging from 22 to 13%. Despite these differences, the RH values for both campaigns converged to a similar range of approximately 15% to 20% by the end of the monitoring period. The graph illustrating the RH change over the campaign days can be seen in Figure 5-7.

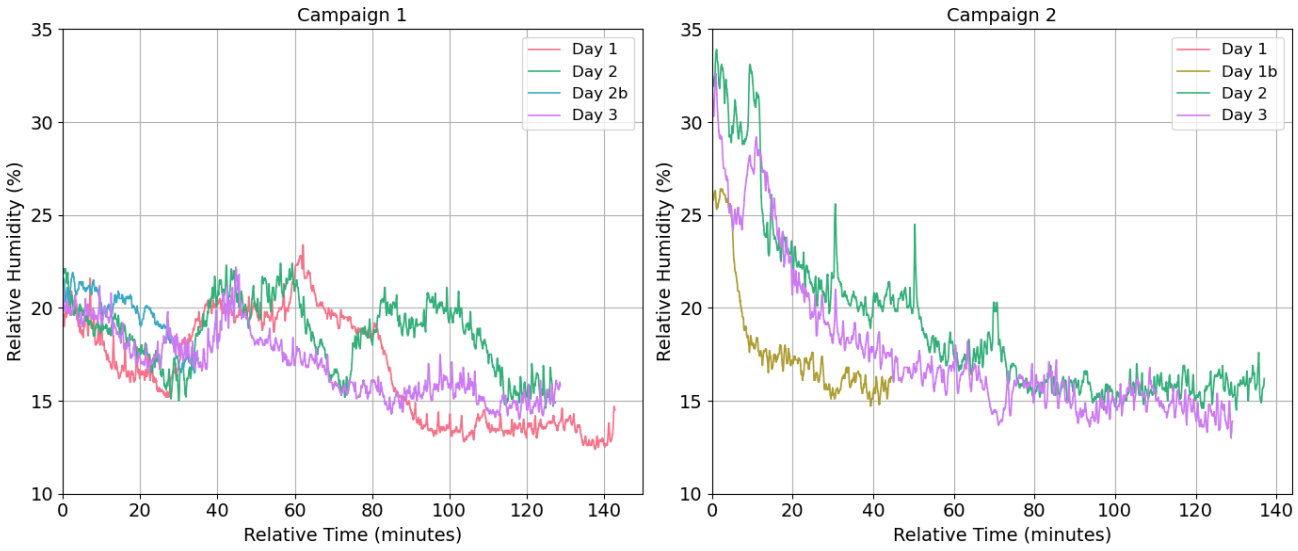

Figure 5-7 *Relative humidity profile during the parabolic flight campaigns, on the left side for the 1st and on the right for 2nd Parabolic Flight Campaign.*

The same type of recording has been done for the temperature inside the airplane. Temperature data for day 1, and campaign 2 were not recorded, leaving a gap in the dataset.

Campaign 1 demonstrated better stability in temperature across all monitored days, with gradual increases over time and temperature readings from 17 to 21°C, over all of the days. On day 1, the temperature rose steadily from 18°C to 21°C, and on day 3, it showed similar stability, converging near 21°C by the end of the measurement period. During campaign 2, larger temperature changes were observed. On day 2, the temperature increased from 13°C to 21°C, and on day 3, campaign 2 increased from 15°C to 21°C.

Experimental results and statistical analysis for ground reference and parabolic flight experiments

In general, Campaign 1 provided more stable thermal conditions, with slower and more consistent changes in temperature. This discrepancy in temperature and RH conditions between the two campaigns comes from the fact that Campaign 1 happened in the Fall (sunny weather without rain), while Campaign 2 happened in the Spring (cold, rainy weather). The graph illustrating the temperature change over the campaign days can be seen In Figure 5-8.

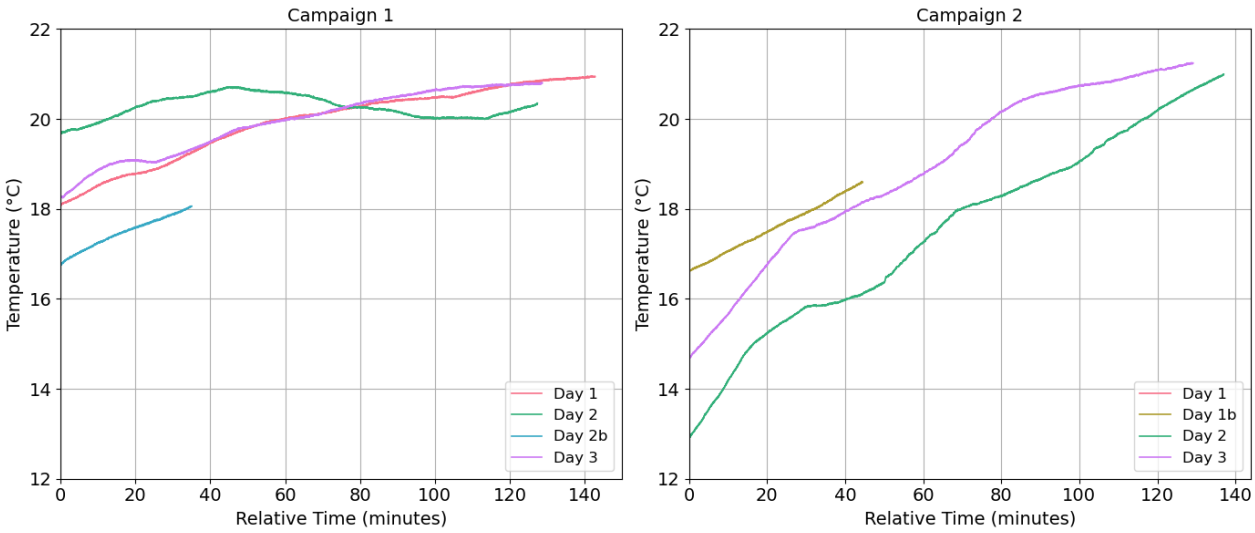

Figure 5-8 *Temperature profile during the parabolic flight campaigns, on the left side for the 1st and on the right for 2nd Parabolic Flight Campaign.*

5.2.2 General trends and observations

It was possible to see the effect of gravity on the surface temperature readings, as variations in temperature align closely with changes in the gravitational profile. Figure 5-9 shows an example of the observed trends across all days and campaigns. The alternating phases of hypergravity and microgravity in the bottom graph correspond to noticeable changes in the temperature data.

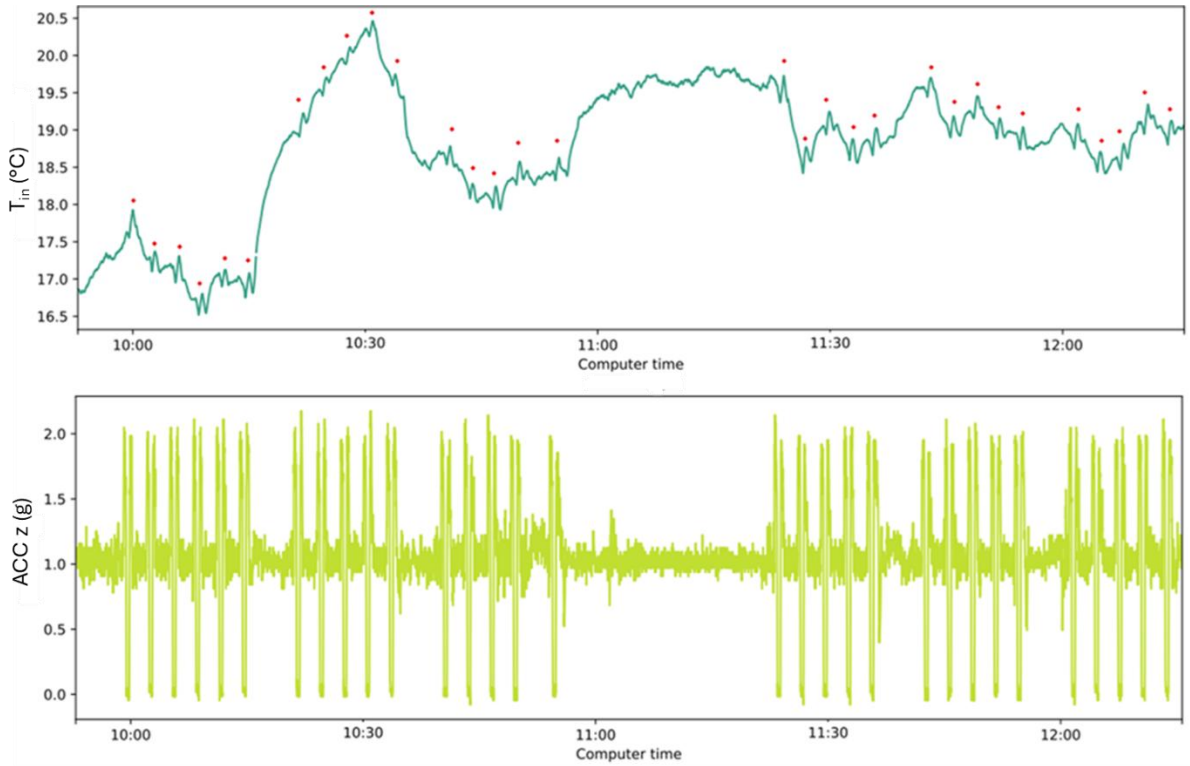

Figure 5-9 *Effect of gravitational phases on leaf replica internal temperature during parabolic flight (top graph) and gravity profile during the parabolic flight (bottom graph). Red dots show the peak temperature value at the end of the microgravity phase.*

Figure 5-10 shows the recording of the upper surface temperature during the first set of parabolas.

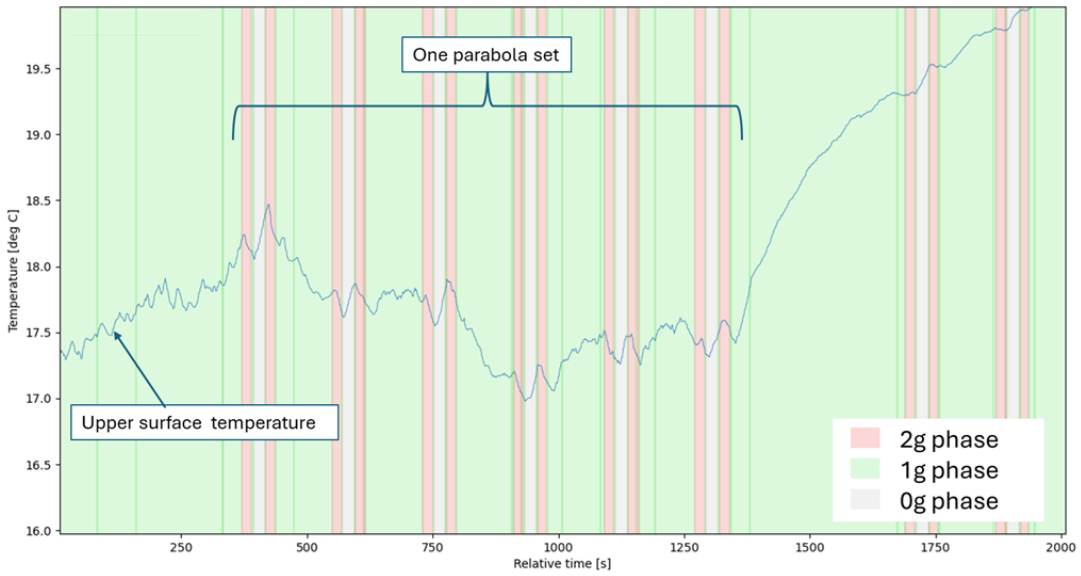

Figure 5-10 *Upper surface temperature response during one set of parabolas for different gravity phases for one set of parabolas in campaign 1, day 1, unit 1. The shaded regions correspond to the gravity phases: green indicates the 1g phase, pink represents the 2g phase, and white denotes the 0g (microgravity) phase.*

Each parabola corresponds to a different angle, and the first 5 visible parabolas represent measurements taken under a single air velocity condition. As can be seen, the steady-state conditions were never achieved. A temperature drop is observed during the hypergravity phase (0.1 to 0.4°C), while temperature increases systematically during the microgravity phase (between 0.3 and 0.7°C). The large temperature increase visible at the end of the fifth parabola in 1g is caused by the change in the air velocity, ahead of a new group of parabolas.

5.2.2.1 Comparison of evaporative and non-evaporative leaf replicas

The difference in temperature recordings between the evaporative and non-evaporative leaf replicas is illustrated in Figure 5-11. The figure presents temperature data collected over one day of a parabolic flight campaign, comparing both types of leaf replicas under different air velocities.

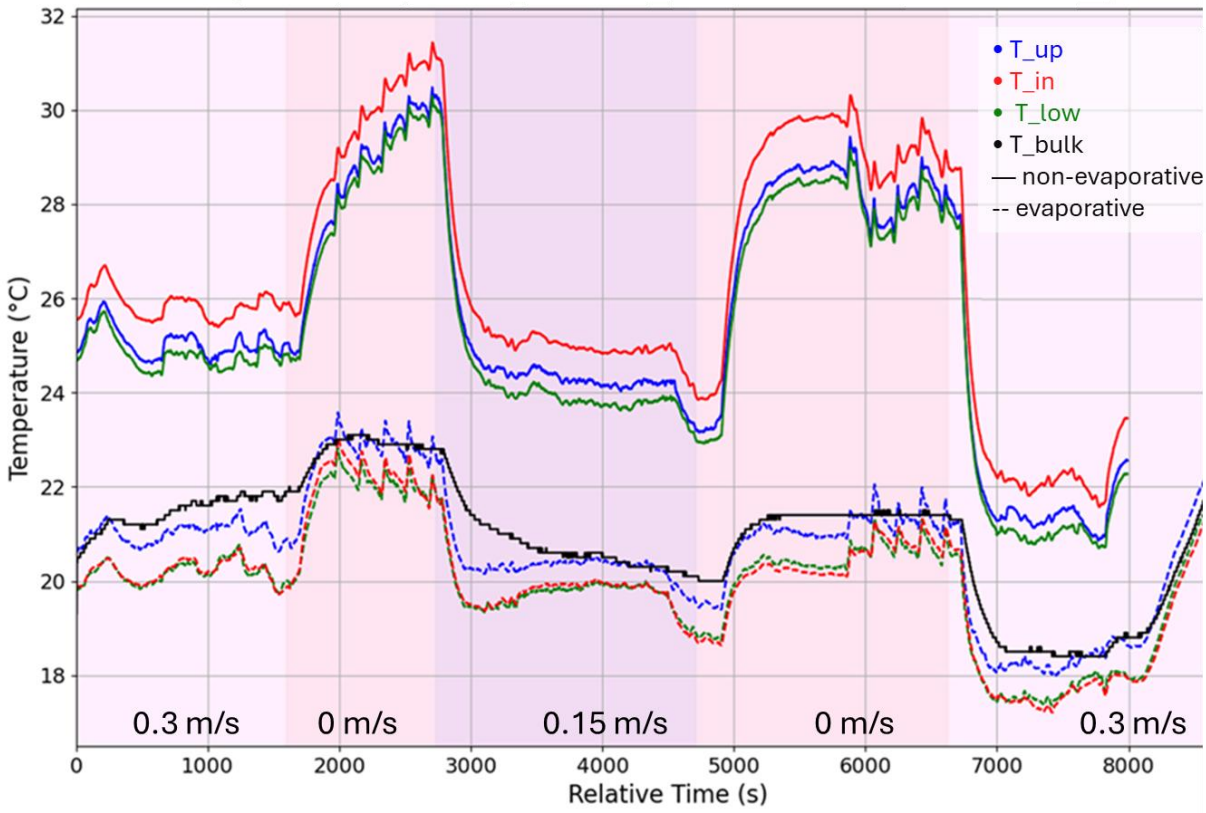

Figure 5-11 *Temperature response of evaporative and non-evaporative leaf replicas under varying air velocities during 1st day of the 66th CNES parabolic flight campaign.*

Measurements were taken at 3 locations: the upper surface, inside the leaf replica, and the lower surface. The non-evaporative replica showed higher temperature values for all locations, reaching up to 31°C for the no-airflow case. The evaporative leaf replica indicates temperatures lower by 5°C to 10°C, maintaining values between 19°C to 23°C, which are just below the bulk temperature except for a few peaks in microgravity. The temperature raise is much higher without evaporation and keeps increasing during the set of parabolas, while it decreases by almost 1°C with evaporation at each parabola. As a result, evaporation plays a crucial role in regulating temperature trends more closely to the bulk temperature variations, and also a faster kinetics of the global heat transfer phenomena when evaporation takes place. This shows a markedly influence of evaporation on surface temperature.

For the non-evaporative leaf replica, the internal temperature of the leaf replica was constantly the highest, by 0.5 to 1.2°C, compared to the upper and lower surface temperatures. In contrast for the evaporative leaf replica, the internal temperature closely follows the lower surface temperature, with the upper surface having the highest temperature by up to 1°C.

The difference between the evaporative and non-evaporative leaf replicas can also be seen when only looking at the microgravity phase. Figure 5-12 compares the temperature difference (T_{up}–T_{bulk}) for non-evaporative and evaporative leaf replicas during the microgravity phases in parabolas where the same air velocities and angle were tested.

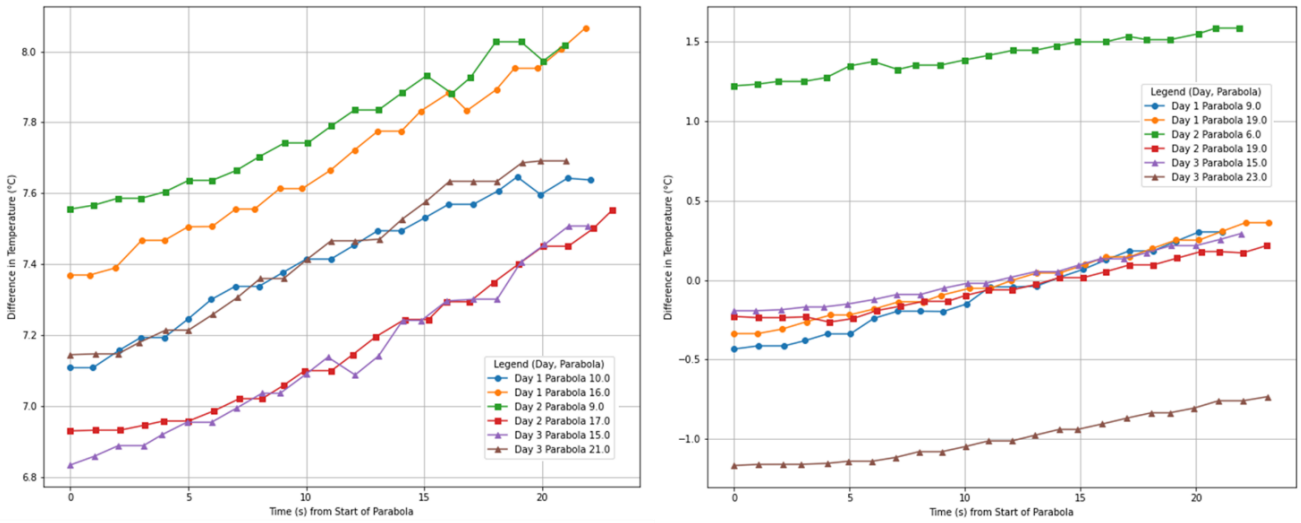

Figure 5-12 *Temperature differences (between the upper surface temperature and bulk air) for non-evaporative (left side) and evaporative (right side) leaf replicas during the microgravity phase, for no airflow case, angle 0°*

The graphs show data for the no-airflow case with the leaf replica aligned with the airflow (0°). For the non-evaporative leaf replica, the temperature is consistently higher than the surrounding environment across all cases, as seen on the left side of the graph. Additionally, the slope of the non-evaporative replica is consistently steeper (>0.5°C in 20 s) than for the evaporative case (<0.5°C in 20 s). This indicates not only a difference in steady-state temperature relative to the bulk air, but also in the thermal response dynamics, with evaporation moderating the rate of temperature change.

The discrepancy between all graphs is related to the initial conditions that are not similar. As mentioned here above evaporation induce average temperatures with a more stable and similar behaviour as the bulk air temperature.

The evaporative leaf replica, shown on the right side, has 3 different cases:

1. The replica's temperature is lower than the bulk air temperature throughout the microgravity phase.
2. The temperature of the replica initially starts lower than the bulk temperature but becomes higher during the microgravity phase.
3. The replica's temperature is consistently higher than the bulk temperature.

Due to this variation, different analytical approaches are applied to interpret these cases, focusing on the slope of temperature change and the transitions between the microgravity and environmental phases to capture thermal responses.

The thermal response for the upper and lower surfaces as well as the internal temperature of the leaf replica can be seen in Figure 5-13. As shown, the trends are linear based on the R^2 values, which are very close to 1.

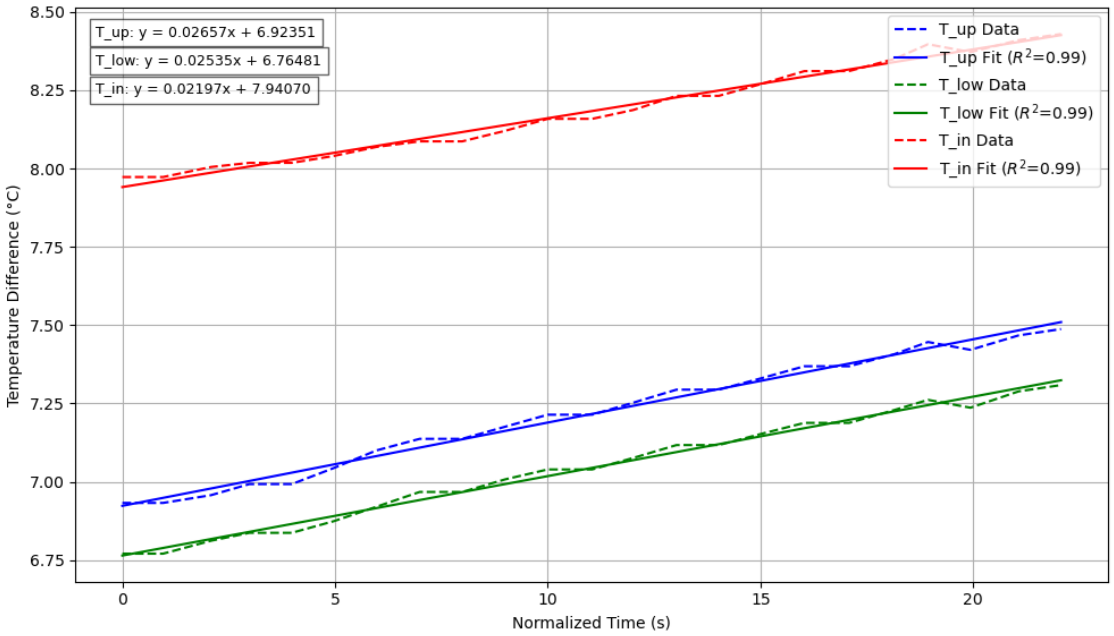

Figure 5-13 *Linear temperature increase during the microgravity phase for the non-evaporative leaf replica for angle 0° and no-airflow case.*

The temperature increase rates differ across the thermocouples, with T_{up} showing the highest slope, followed by T_{low}, and T_{in}. While this graph represents one parabola, similar patterns were observed across other parabolas.

5.2.3 Statistical analysis

Due to the unequal duration of all of the gravity phases for the statistical analysis, the 20s of each phase has been chosen. Additionally, the difference between the readings from the thermocouples and bulk air was used to perform the analysis. As can be seen in the Q-Q plot in Figure 5-14, similar to the data from the Ground Reference Experiment, most of the data points the data points (blue dots on the graph) closely follow the theoretical quantile line (red line), for the non-evaporative, and evaporative leaf replica. Deviations are visible at the tails, suggesting potential slight non-normality at extreme values.

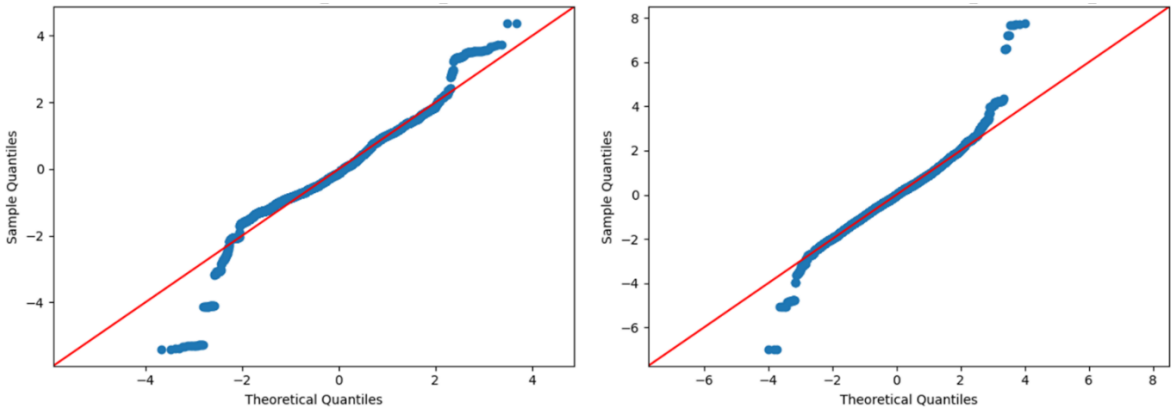

Figure 5-14 *Q-Q plots of the surface temperatures flight campaign data for the non-evaporative (left graph) and evaporative (right side) leaf replicas. Red line represents the expected quantiles from a theoretical normal distribution and blue dots show the measured values.*

To further assess normality, the Shapiro-Wilk test was performed. The results confirmed that both datasets deviate significantly from normality. Additionally, Levene's test for equality of variances was conducted to compare variability within these 2 datasets. The results indicated a statistically significant difference in variance, suggesting heteroscedasticity for both datasets. The results of the tests can be seen in Table 5-4.

	non- evaporative				evaporative			
	Shapiro-Wilk		Levene's		Shapiro-Wilk		Levene's	
	Statistic	p-value	Statistic	p-value	Statistic	p-value	Statistic	p-value
T_up	0.96	6.6E-42	230	3.4E-143	0.98	0	870	0
T_low	0.96	1.1E-42	230	5.0E-143	0.93	0	389	4.6E-244
T_in	0.95	8.4E-45	130	5.6E-82	0.99	5.6E-45	568	0

Table 5-4 *Statistical test results for normality and variance for non-evaporative and evaporative leaf replica data, where statistic is the calculated value from the test formula, and p-value is p-value.*

For the **non-evaporative** leaf replica Welch's ANOVA revealed that factors, air velocity, day, angle and gravity phase for T_{up} and T_{low} are significantly influenced the temperature differences ($p < 0.05$) , as can be seen in Table 5-5.

	T_up				T_low				T_in			
	sum_sq	df	F	PR(>F)	sum_sq	df	F	PR(>F)	sum_sq	df	F	PR(>F)
Gravity Phase	8	2	6	3.1E-03	7	2	5	7.1E-03	2	2	2	1.3E-01
Airspeed	15795	3	7971	0.0E+00	15614	3	7804	0.0E+00	13061	3	7380	0.0E+00
Day	19	2	14	6.6E-07	18	2	14	1.1E-06	19	2	16	8.6E-08
Angle	584	4	221	1.7E-180	467	4	175	4.4E-144	734	4	311	2.0E-249
Residual	5382	8148			5434	8148			4807	8148		

Table 5-5 *Welch ANOVA results: effect of gravity phase, air velocity, angle, and day on non-evaporative leaf replica upper, lower, and internal temperature, where sum_sq – Sum of squares, df – Degrees of freedom, F – F-statistic and PR(>F) – p-value.*

The results indicate that air velocity is the most statistically significant factor influencing the temperature increases across all measured locations, with the F value 17-33 times higher than the value for the second-highest factor (angle). This suggests that variations in air velocity have a dominant effect on temperature changes, likely due to the direct impact of convective heat transfer. Angle has the 2nd highest F-value for all temperature measurement locations, which reflects that heat transfer is strongly related to the streamlines close to the replica. Day shows a statistically significant effect, which may be linked to fluctuations in environmental conditions such as relative humidity, potentially influencing heat dissipation and/or ambient temperature. The gravity phase has a weaker but still notable effect, except for the internal temperature (p=0.13).

Similarly, for the **evaporative** leaf replica, Welch's ANOVA revealed that all factors, including gravity phase, air velocity, unit, day, campaign, and angle, significantly influenced the temperature differences ($p < 0.05$) as can be seen in Table 5-6.

	T_up				T_low				T_in			
	sum_sq	df	F	PR(>F)	sum_sq	df	F	PR(>F)	sum_sq	df	F	PR(>F)
Gravity Phase	28	2	72	5.7E-32	12	2	12	5.72E-06	49	2	104	8E-46
Airspeed	948	5	987	0.0E+00	2420	3	1595	0	1818	5	1556	0E+00
Angle	980	10	510	0	515	4	254	2.00E-212	1850	10	792	0.00
Day	1800	4	2341	0.0E+00	1246	2	1232	0	2463	4	2636	0E+00
Unit	2382	3	4131	0.0E+00	-	-	-	-	2218	3	3165	0E+00
Campaign	824	1	4288	0.0E+00	-	-	-	-	1106	1	4735	0E+00
Residual	5996	31197			8255	16328			7287	31197		

Table 5-6 *Welch ANOVA results: effect of gravity phase, air velocity, angle, and day on evaporative leaf replica upper, lower, and internal temperature, where sum_sq – Sum of squares, df – Degrees of freedom, F – F-statistic and PR(>F) – p-value.*

The most influential factors for the upper surface and internal temperature are the unit and day. This is most likely due to variations in relative humidity and ambient temperature between days, which have a direct impact on heat and mass transfer. The variation due to the unit number is probably related to the difference in the illumination for each of the units as shown in Table 4-4 and due to the slightly different fan characteristics as shown in Figure 4-18.

The main difference between the evaporative and non-evaporative leaf replicas lies in the dominant heat transfer mechanisms and how angle influences airflow exposure of both surfaces. For the non-evaporative leaf replica, cooling is mainly driven by convective heat

transfer. Because of this, air velocity becomes the dominant factor, as increased air velocity directly enhances heat dissipation, with transitional flows developing behind the leaf replica. Additionally, angle contributes to enhanced convective heat loss by generating surface turbulence, especially at higher inclinations. this scenario, angle plays a lesser role because there is no additional cooling from evaporation and heat removal depends only on how airflow interacts with the surface.

For the evaporative leaf replica, the cooling process is more complex due to the presence of two different surfaces: an upper illuminated, and a lower evaporative. The angle of the replica determines whether the airflow interacts with the evaporative or illuminated surface. When airflow is directed towards the evaporative surface (positive angles), evaporation is enhanced by turbulent convection.

5.2.3.1 Non-evaporative leaf replica

The upper surface temperature increase of the leaf replica during the microgravity phase, exhibited a clear dependence on both air velocity and the angle of orientation, as shown in Figure 5-15. For 0.3 m/s forced convection is almost strong enough to generate similar thermal variations (about 0.2-0.5°C) for all angles. At lower air velocities, the responses transitions to a parabolic trend. These trends are similar to those observed in ground-based experiments. The trend remains similar also for the lower surface temperature and the temperature inside leaf replica, as can be seen in Figure 5-15.

5.2.3.2 Evaporative Leaf Replica

The surface and internal temperature increase of the evaporative leaf replica, during the microgravity phase, exhibited much smaller dependence on both air velocity and the angle of orientation. The cooling effect was significantly enhanced compared to the non-evaporative leaf replica due to the additional evaporative cooling mechanism, resulting in lower overall temperatures for the evaporative replica at all angles and air velocities. With less visible effect of the air velocity and angle on temperature increase, as already seen in steady state (in 5.1.3.1.2).

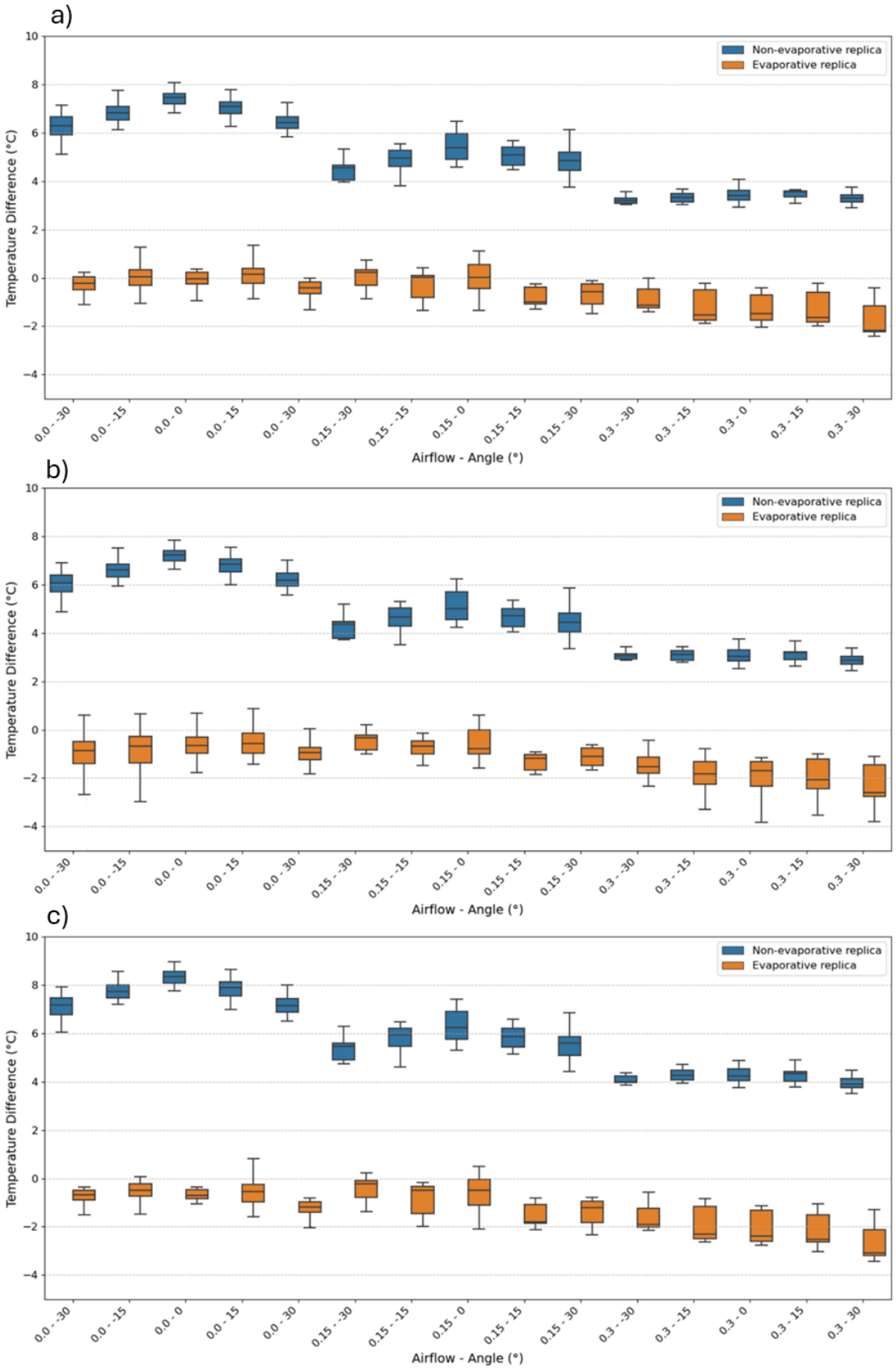

Figure 5-15 *Boxplot of temperature increase recordings for upper (a), lower (b), and temperature inside leaf replica (c) for non-evaporative and evaporative leaf replica for various air velocities (0.0, 0.15, 0.3 in m/s) and angels (-30, -15, 0, 15, 30).*

5.3 Main outcomes of the chapter

- The airflow velocity and surface orientation are the dominant factors influencing surface temperature on both evaporative and non-evaporative leaf replicas.
- Gravitational acceleration has a measurable, statistically valid, but weaker, effect on thermal behaviour, compared to other factors.
- RH strongly affects evaporative cooling efficiency in the evaporative replicas.
- The thermal responses are angle-dependent and non-linear, with maximum temperatures for horizontal positions and decreasing with inclinations.

6 Interpretation and modelling of experimental results

This chapter is the result of numerous discussions and close collaboration with Prof C.G. Dussap, particularly for the development of physical models. The basic concepts are rooted in those of chemical engineering, drawing on classical textbooks like (Beek et al., 2000a; Bird et al., 2007). The writing of this part was conceived so that this work can be continued, amended or corrected by others. The goal is to enrich the physical understanding of the observed phenomena. The basic concepts, such as those of boundary layer and transfer phenomena, are detailed. They are adapted to the specific case of the experiments presented in the previous chapters.

All of the data collected in described experiments can be found on the following page: https://recherche.data.gouv.fr/fr, in the HAMSTER catalogue of Université Clermont-Auvergne - https://entrepot.recherche.data.gouv.fr/dataverse/uca_ip_hamster

All of the variables used in this chapter and their units are listed in the Table 6-1 below.

Name	Symbol	Unit	Name	Symbol	Unit
Surface area	A	m^2	Curvature of the interface	$\mathcal{R}$	m
Friction factor	C_f	-	Hydraulic Radius	R_h	m
Specific heat capacity	C_p	$J\ kg^{-1}K^{-1}$	Thermal resistance	$\mathcal{R}^T$	$K\ m^2\ W^{-1}$
Diffusion coefficient	D	$m^2\ s^{-1}$	Reynolds number	Re	-
Pore diameter	d	m	Surface area	S	m^2
Total energy	E	W	Schmidt number	Sc	-
Thickness of the layer	e	m	Sherwood number	Sh	-
Absorption coefficient	E_a	m^{-1}	Time	t	s
Fourier number	Fo	-	Bulk temperature	T_{bulk}	°C
Gravitational acceleration	g	$m\ s^{-2}$	Internal temperature of leaf replica	T_{int}	°C
Grashof number	Gr	-	Lower surface temperature	T_{low}	°C
Heat transfer coefficient	h	$W\ m^{-2}\ K^{-1}$	Upper surface temperature	T_{up}	°C
Heat transfer coefficients at the lower surface	h_{low}	$W\ m^{-2}\ K^{-1}$	Air velocity in bulk air	u_∞	$m\ s^{-1}$
Heat transfer coefficients at the upper surface	h_{up}	$W\ m^{-2}\ K^{-1}$	Velocity of the plate	v_0	$m\ s^{-1}$
Kozeny constant	K	-	Water flux	w	$kg\ m^{-2}s^{-1}$
Convective mass transfer coefficient	k	$m\ s^{-1}$	Distance from the surface	z	m
Distance between the pores	L	m	Thermal diffusivity	a	$m^2\ s^{-1}$
Depth of the porus	l_0	m	Hydrodynamic boundary layer thickness	δ_H	m
Vaporisation enthalphy	L^V	$J\ kg^{-1}$	Mass boundary layers thickness	δ_M	m
Total mass	m_{total}	kg	Thermal boundary layer thickness	δ_T	m
Molar mass of the air	M	kg	Porosity	ϵ	-
Molar mass of water	M_w	kg	Angle of the leaf replica	θ	°
Pore Density	n	m^{-2}	Thermal conductivity of the medium	λ	$W\ m^{-1}\ K^{-1}$
Nusselt number	Nu	-	Dynamic viscosity of the fluid	μ	$kg\ m^{-1}\ s^{-1}$
Volume	V	m^{-3}	Kinematic viscosity of the fluid	ν	$m^2\ s^{-1}$
Pressure	Pr	Pa	Density of the fluid	ρ	$kg\ m^{-3}$
Generated power	P_{gen}^T	W	Surface tension of the liquid	Φ_{up}^{rad}	$J\ m^{-2}$
Power generated per volume	p_{gen}^T	$W\ m^{-3}$	Shear force at the wall	τ_w	N
Prandtl Numnber	Pr	-	Heat flux	ϕ^T	$W\ m^{-2}$
Water partial pressure in bulk air	p_{w_bulk}	Pa	Incoming thermal flux	ϕ_{in}^T	$W\ m^{-2}$
Water partial pressure at the lower surface	p_{w_low}	Pa	Radiative light power intensity on the lower surface	ϕ_{low}^T	$W\ m^{-2}$
Relative humidity	RH	%	Outgoing thermal fluxes	ϕ_{out}^T	$W\ m^{-2}$
Ideal gas constant	R	$J\ mol^{-1}K^{-1}$	Radiative light power intensity on the upper surface	ϕ_{low}^T	$W\ m^{-2}$
Resistance	$\mathcal{R}$	$s\ m^{-1}$	Subscript i refers to, bulk, internal, lower and upper surface	i_{bulk}, i_{int}, i_{low}, i_{up}	-

Table 6-1 *Summary of the symbols and notations used in this chapter*

6.1 Data analysis and physical models of heat, radiative and mass transfer: global positioning of the problem

6.1.1 Introduction: global overview of modelling objectives

Based on the results presented in Chapter 5, the aim of the model development is to establish a comprehensive framework that captures the coupling between mass, heat, and radiative transfers at the level of the leaf replica. To reach this objective, the following data were used: the replica surface temperatures at the lower and upper surface (T_{up}, T_{low}), as well as the internal temperature (T_{int}), in different conditions, as described in Table 6-2. For all these cases, the results are obtained for different inclinations and different air velocities.

	Ground experiment	**Parabolic Flight**
Evaporative leaf replica	Steady state Duration: 20-45 min Gravity: 1g	Transient state Duration: 20-22 s Gravity: 0 to 2g
Non-evaporative leaf replica	Steady state Duration: 20-45 min Gravity: 1g	Transient state Duration: 20-22 s Gravity: 0 to 2g

Table 6-2: *Overall view of available data obtained from previous experiments*

In addition to the surface temperature data, the bulk air temperature T_{bulk}, RH and the radiative light power intensity on the upper surface ϕ_{up}^{rad} (W m^{-2}) were used.

The objective of the development of physical models is to derive the heat transfer coefficients for the upper and lower surfaces for the non-evaporative leaf replica and the mass transfer coefficient at the lower surface for the evaporative leaf replica. Experimental observations indicate that changes in gravitational conditions induce rapid variations in surface temperatures at all measurement points. Specifically, temperature increases are observed during the microgravity phase and decreases during the hypergravity phase, as illustrated in Figure 5-10. This shows that the transfer coefficients are modified when gravity changes.

Therefore, the modelling strategy can be divided into three steps:

- Modelling of heat transfer in terrestrial gravity for a non-evaporating system at steady state.

- Considering the heat transfer coefficients remain predicted by the same model when the system is evaporating, modelling the mass transfer when the system is evaporating at steady state.
- Modelling of heat and mass evolution when the gravity conditions are changed from a transient evolution of the temperatures.

6.1.2 A first simple approach: the global thermal balance

An initial modelling approach assumed that the heat transfer coefficients at the upper (h_{up}) and lower (h_{low}) surfaces of the leaf replica were identical and equal to h. When the leaf replica is not evaporating, the global thermal balance is written as follows at steady state:

$$\phi^T = h_{up}(T_{up} - T_{bulk}) + h_{low}(T_{low} - T_{bulk}) = h\left(T_{up} + T_{low} - 2\,T_{bulk}\right) \qquad \textit{Eq. 1}$$

Given the measured temperatures T_{up}, T_{low}, T_{bulk} and knowing the heat flux ϕ^T (Table 4-6), considered as the radiative dissipated power, leads to determining the heat transfer coefficient.

This estimation permits reaching a satisfactory order of magnitude of the heat transfer coefficient h. But the hypothesis of identical heat transfer coefficients on both surfaces appears insufficient. As the surfaces are both at higher temperatures than the bulk, the convection-driven heat fluxes might be in opposite directions: it might have a positive effect at the upper surface and a negative effect at the lower surface, due to reversed gas density gradients under standard gravity. Because of that, heat transfer coefficients at the upper and lower surfaces were evaluated separately.

6.1.3 Selection of a suitable dataset for validating the structure of the model

As previously described, three degrees of freedom have been investigated at terrestrial gravity for non-evaporating leaf replica: air velocity, bulk temperature and leaf replica inclination angle. For each of these cases, several measurements have been done. In order to validate a physical model, a basal position was selected: no airflow (0 m s^{-1}) and horizontal position of the leaf replica (angle 0°). Representative reference values for surface and bulk temperatures for testing the heat transfer models under these conditions are provided in Table 6-3. The

corresponding reference value for the radiative flux on the upper surface is $\phi_{up}^{rad} = 156\ W\ m^{-2}$.

Air velocity (m s^{-1})	Angle (°)	T_{bulk} (°C)	T_{up} (°C)	T_{low} (°C)	T_{int} (°C)
0	0	19.56	25.6	25.11	26.43

***Table 6-3**: Typical reference values of temperatures for non-evaporating leaf replica*

In order to determine the physical properties of the leaf replica, the thickness, conductivity, and heat capacity of each of its layers have been determined. The detailed structure of the leaf replica is given in Figure 6-1. The physical properties of each layer are given in Table 6-4.

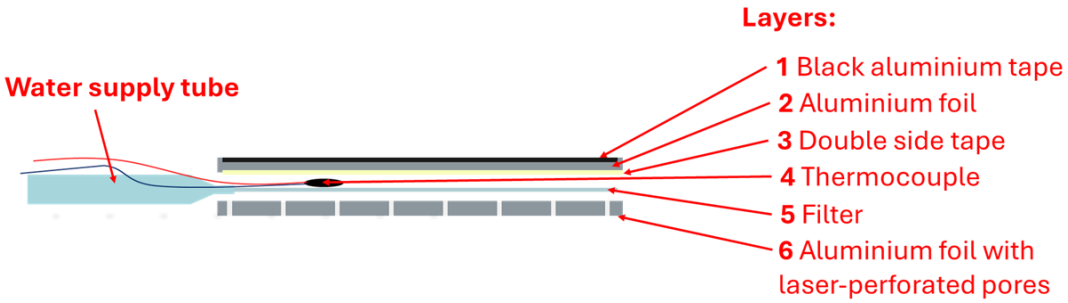

***Figure 6-1**: Structure of the leaf replica*

	Thickness (e: µm)	Mass (m: g)	Heat conductivity (λ: W m^{-1} K^{-1})	Heat capacity (C_p : J g^{-1} K^{-1})	Light absorption coefficient) (Ea: m^{-1})
Black Al tape	30	0.198	5	0.9	10000
Al foil	30	0.281	5	0.9	10000
Double side tape	70	0.195	0.28	1.76	15000
Glue	170	0.314	0.13	1.47	1000
Internal space thermocouple	700	0 (air) 0.880 (water)	0.025 (air) 0.6 (water)	1.03 (air) 4.18 (water)	4000
Filter	110	0.217	0.024	1.4	5000
Al foil	30	0.198	3	0.9	10000
Total	1140	1.403 (empty replica) 2.283 (wet replica)			

***Table 6-4**: Main dimensions and physical properties of the leaf replica*

The values of the thicknesses shown in Table 6-4. were calculated based on the mass, densities of the constituent materials, and the surface area of each layer, as described in Chapter 4. The total heat capacity of the leaf replica is given by:

$$m_{total}\, C_p = \sum_i m_i C_{pi} \qquad \textit{Eq. 2}$$

The total heat capacity is different when the interstitial space is filled with water (evaporating leaf replica) or with air (non-evaporating leaf replica).

- Non-evaporating: $m_{total}\, C_p == 1.72\ \mathrm{J\ K^{-1}}$
- Evaporating: $m_{total}\, C_p == 5.40\ \mathrm{J\ K^{-1}}$

The average conductivity calculated using the inverse sum of thermal resistances, as given by Eq. 9 (see below) are:

- Non-evaporating: $\lambda = 0.033\ \mathrm{W\ m^{-1}\ K^{-1}}$
- Evaporating: $\lambda = 0.155\ \mathrm{W\ m^{-1}\ K^{-1}}$

The values of the absorption coefficients given in Table 6-4 correspond to Lambert-Beer's law of radiative flux absorption by dense media (see Eq. 24). These coefficients were estimated from the known absorption behaviour of pigments (Tesfamichael et al., 2001) and represent approximations rather than experimentally validated physical constants. With these data, the transmittance of the superficial layer is lower than 20 % of total incident energy, meaning that the incident radiation is absorbed or eventually converted to IR radiation and transmitted to the other layers. For the superficial painted layers (aluminium foil), the estimation leads to values in the range 10 000 – 20 000 m^{-1}. The absorption within the internal layers is primarily associated with the conversion of light energy into heat. The order of magnitude of the absorption coefficients reported in Table 6-4 corresponds to typical values of the absorption coefficients by pigments (100 to 300 $m^2\ kg^{-1}$) in dense media (Foin et al., 2024). Considering that absorbed particles and molecules are in concentrations 10 – 50 kg m^{-3} in the different layers, this leads to absorption coefficients ranging between 1000 – 5000 m^{-1} in the internal layers, which is 10 times less than for the superficial painted layers. As a result, the overall transmittance through the leaf replica is low and can be considered negligible.

6.1.4 Development of a model for the interpretation of the data at steady state and non-evaporating leaf replica

6.1.4.1 Master equations for heat transfer

In a general form, the equation for heat transport in a non-moving medium by heat conduction in an element of volume V is given by:

$$\frac{dE}{dt} = \phi_{in}^{T} A - \phi_{out}^{T} A + \mathcal{P}_{gen}^{T}$$

Where E is the total energy (enthalpy) in the volume: $E = m\, C_p \left(T - T_{ref}\right)$ where m is the mass (kg) and C_p the heat capacity (J kg^{-1} K^{-1}). T_{ref} is an arbitrary-fixed reference temperature, indicating the enthalpy is fixed to within an additive constant. Assuming the mass remains constant in time and space, and normalizing by the area A, the equation becomes:

$$\frac{m}{A} C_p \frac{dT}{dt} = \phi_{in}^{T} - \phi_{out}^{T} + \frac{\mathcal{P}_{gen}^{T}}{A} \qquad \textit{Eq. 3}$$

Where $\phi_{in,out}^{T}$ represent the incoming and outgoing thermal fluxes (W m^{-2}). $\mathcal{P}_{gen}^{T}$ (W) is the power generated inside the volume *V*. A is the area through which the heat is conducted (m^2).

The principal assumption throughout this modelling framework is that heat and mass transfer are one-dimensional, occurring along the z-axis. Considering one-dimensional heat conduction along the z-axis over a slide of thickness Δz, this leads to:

$$\rho\, \Delta z\, C_p \frac{dT}{dt} = \phi_{z}^{T} - \phi_{z+\Delta z+}^{T} + \frac{\mathcal{P}_{gen}^{T}}{V} \Delta z$$

When considering an infinitely thin slide of thickness Δz, this expression leads to the differential form:

$$\rho\, C_p \frac{\partial T}{\partial t} = -\frac{\partial \phi^{T}}{\partial z} + \frac{\mathcal{P}_{gen}^{T}}{V} \qquad \textit{Eq. 4}$$

In a non-moving media, in the presence of a temperature gradient, heat is transported by molecular movement according to the Fourier's law:

$$\phi^{T} = -\lambda \frac{dT}{dz} \qquad \textit{Eq. 5}$$

Where λ is the thermal conductivity (W m^{-1} K^{-1}) of the media. The integration of Eq. 4 and Eq. 5 leads to the transient temperature profile description:

$$\rho\, C_p \frac{\partial T}{\partial t} = \lambda \frac{\partial^2 T}{\partial z^2} + \frac{\mathcal{P}_{gen}^T}{V} \qquad \textit{Eq. 6}$$

At steady state, Eq. 4 is rewritten as follows:

$$\frac{d\phi^T}{dz} = \frac{\mathcal{P}_{gen}^T}{V} \qquad \textit{Eq. 7}$$

When the power generated inside the volume is zero ($\mathcal{P}_{gen}^T = 0$), integration of Eq. 7 along the z-axis, leads to the fact that: $\phi^T = C^{ste}(z)$. Integration of Eq. 5 leads to:

$$T_{up} - T = \frac{z}{\lambda}\, \phi^T = \mathcal{R}^T(z)\, \phi^T$$

The temperature profile is therefore linear. $\mathcal{R}^T$ is the thermal resistance (*K* m^2 W^{-1}). Considering that conduction of heat occurs through an immobile layer of thickness *e* the previous equation becomes:

$$\phi^T = \frac{\lambda}{e}\,(T_{up} - T_{low})$$

The thermal resistance of the entire layer of thickness *e* is given by:

$$\mathcal{R}^T = \frac{e}{\lambda} \qquad \textit{Eq. 8}$$

For multi-layered systems composed of different materials, the total thermal resistance is calculated as the sum of individual resistances in series, following Kirchhoff's law:

$$\mathcal{R}^T = \sum_i \frac{e_i}{\lambda_i} \qquad \textit{Eq. 9}$$

The average conductivity is then given by:

$$\lambda = \frac{e}{\mathcal{R}^T} \qquad \textit{Eq. 10}$$

This equation has been applied for the calculation of the average conductivities of the leaf replica in the presence of water and air.

When heat is transported by convection into a fluid media (air) between a bulk region at T_{bulk} and a wall at T, the heat transfer flux is proportional to the difference $(T - T_{bulk})$. The

proportionality constant is a purely phenomenological quantity corresponding to the heat transfer coefficient h (W m^{-2} K^{-1}):

$$\phi^T = h\,(T - T_{bulk}) \qquad \textit{Eq. 11}$$

This convective exchange can be represented by an equivalent stationary boundary layer of thickness δ^T through which heat is conducted in a medium of conductivity λ_{air}(in this case it is the conductivity of air surrounding the leaf replica). The relationship between δ^T and h is as follows:

$$h = \frac{\lambda_{air}}{\delta_T} \qquad \textit{Eq. 12}$$

Thus, the knowledge of the equivalent boundary layer thickness δ_T allows the transfer coefficient h to be calculated and vice versa.

By integration of Eq. 6 at steady state when the power generated inside the volume is zero $\mathcal{P}_{gen}^T = 0\ W\ m^{-2}$ the conductive transport of heat through a solid layer without considering what happens at the upper and lower surfaces is represented in Figure 6-2. The parameters have been chosen to approximate values representative of the leaf replica that have been studied. The two boundary conditions are chosen in temperature at upper and lower surfaces ($T_{up} = 25.6\ °C\ and\ T_{low} = 25.11\ °C$). The obtained temperature profile is linear and the thermal flux is constant and positive (in the direction of the z-axis) and identical at the upper and lower surfaces.

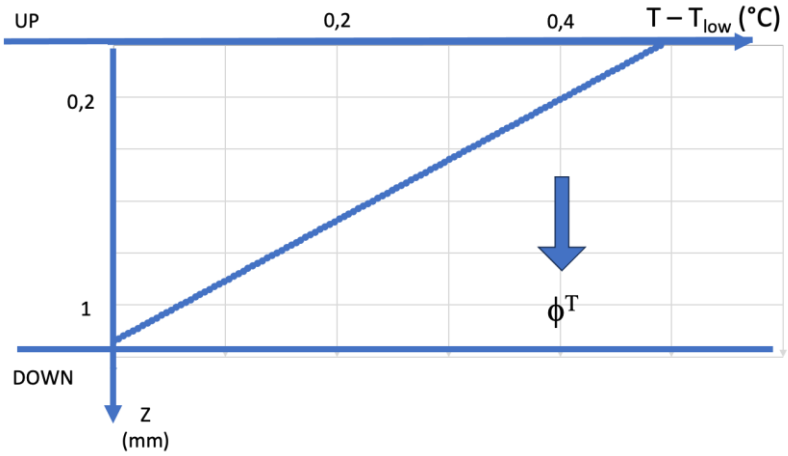

***Figure 6-2** : Temperature profile in a solid: steady state l = 0.027 W m^{-1} K^{-1}, e = 1.14 mm, $\mathcal{P}_{gen}^T = 0$. Boundary conditions $T_{up} = 25.6\ °C$; $T_{low} = 25.11\ °C$. (Eq. 6)*

The calculated heat flux is $\phi^T = 11.6\ \mathrm{W\ m^{-2}}$. Such a behaviour is not relevant as a descriptive model for our experiments because it does not match the direction of the heat fluxes at the two surfaces (Eq. 11): as the differences between surface temperatures and bulk temperature are always positive (higher temperatures on the surfaces than in the bulk) , this means that the convective fluxes at the surface are in opposite directions (downside at the *lower*, i.e. positive with current choice of the z-axis direction; upside at the upper surface, i.e. negative).

6.1.4.2 Homogeneous dissipation of radiative power dissipated

A first approach to remediate this problem is to consider that the radiative power brought to the leaf replica is homogenously dissipated. Eq. 6 is then rewritten as follows:

$$\rho\, C_p \frac{\partial T}{\partial t} = \lambda \frac{\partial^2 T}{\partial z^2} + \frac{\phi_{up}^{rad}}{e} \qquad \textit{Eq. 13}$$

The last right-hand term in Eq. 13 is the volumetric power dissipated:

$$\frac{\mathcal{P}_{gen}^T}{V} = \frac{\phi_{up}^{rad}}{e} = \wp_{gen}^T \qquad \textit{Eq. 14}$$

At steady state, it becomes:

$$\lambda \frac{\partial^2 T}{\partial z^2} = -\wp_{gen}^T \qquad \textit{Eq. 15}$$

As previously, Eq. 15 is integrated imposing boundary conditions in temperatures at the upper and lower surfaces T_{up} and T_{low}. This leads to the following parabolic profile:

$$T - T_{low} = \frac{1}{2}\frac{\wp_{gen}^T}{\lambda} z(e - z) + \left(T_{up} - T_{low}\right)\left(1 - \frac{z}{e}\right) \qquad \textit{Eq. 16}$$

Introducing the thermal resistance (Eq. 8) and the light flux (Eq. 14), the maximum of temperature has the following coordinates:

$$z_{max} = \frac{e}{2} - \frac{\lambda}{\phi_{up}^{rad}}\left(T_{up} - T_{low}\right)$$

$$\left(T_{max} - T_{low}\right) = \frac{1}{8}\,\mathcal{R}^T \phi_{up}^{rad} + \frac{1}{2}\left(T_{up} - T_{low}\right)\left(1 + \frac{T_{up} - T_{low}}{\mathcal{R}^T \phi_{up}^{rad}}\right) \qquad \textit{Eq. 17}$$

The thermal fluxes at the 2 surfaces are also calculated by (Eq. 5):

$$\phi^T(z) = \wp_{gen}^T\left(z - \frac{e}{2}\right) + \frac{\lambda}{e}\left(T_{up} - T_{low}\right) \quad \textit{Eq. 18}$$

$$\phi_{up}^T = -\frac{1}{2}\phi_{up}^{rad} + \frac{\lambda}{e}\left(T_{up} - T_{low}\right) \quad \textit{Eq. 19}$$

$$\phi_{low}^T = \frac{1}{2}\phi_{up}^{rad} + \frac{\lambda}{e}\left(T_{up} - T_{low}\right) \quad \textit{Eq. 20}$$

From the previous equations, the heat transfer coefficients at both phases are determined (Eq. 11):

$$h_{up} = \frac{\phi_{up}^T}{\left(T_{bulk} - T_{up}\right)} \quad \textit{Eq. 21}$$

$$h_{low} = \frac{\phi_{low}^T}{\left(T_{low} - T_{bulk}\right)} \quad \textit{Eq. 22}$$

It is outlined that Eq. 18 to Eq. 22 are valid in an algebraic sense, when the flux is negative at the upper surface and positive at the lower surface. The algebraic sum $\phi_{low}^T - \phi_{up}^T$ is equal to ϕ_{up}^{rad} indicating that the global thermal balance over the complete leaf replica is correctly tackled. The two heat transfer coefficients are positive considering the surface temperatures are always greater than the bulk temperature. The results of integration given by Eq. 16 with the same thickness and conductivity as previously and with a power dissipated calculated by Eq. 14 with the reference value of the radiative flux $\phi_{up}^{rad} = 156$ W m^{-2} is represented in Figure 6-3.

Under these conditions, the heat fluxes are – 66.4 W m^{-2} at the upper surface and 89.6 W m^{-2} at the lower surface. For T_{bulk}= 19.56 °C, the calculated heat transfer coefficients are respectively h_{up} = 11.0 W m^{-2} K^{-1} and h_{low}= 16.1 W m^{-2} K^{-1}. The calculated maximum temperature inside the layer is $T_{max} = 26.2\ °C$ for an abscissa $z_{max} =$ 485 µm.

Compared to the previous results (Figure 6-2), the directions of the heat fluxes at the upper and lower surfaces are now physically consistent with the thermal gradients. However, the values of the two heat transfer coefficients and of the two heat fluxes at the upper and lower

surfaces do not appear to be in a correct ratio. With this model h_{low} is almost 50 % larger than h_{up}.

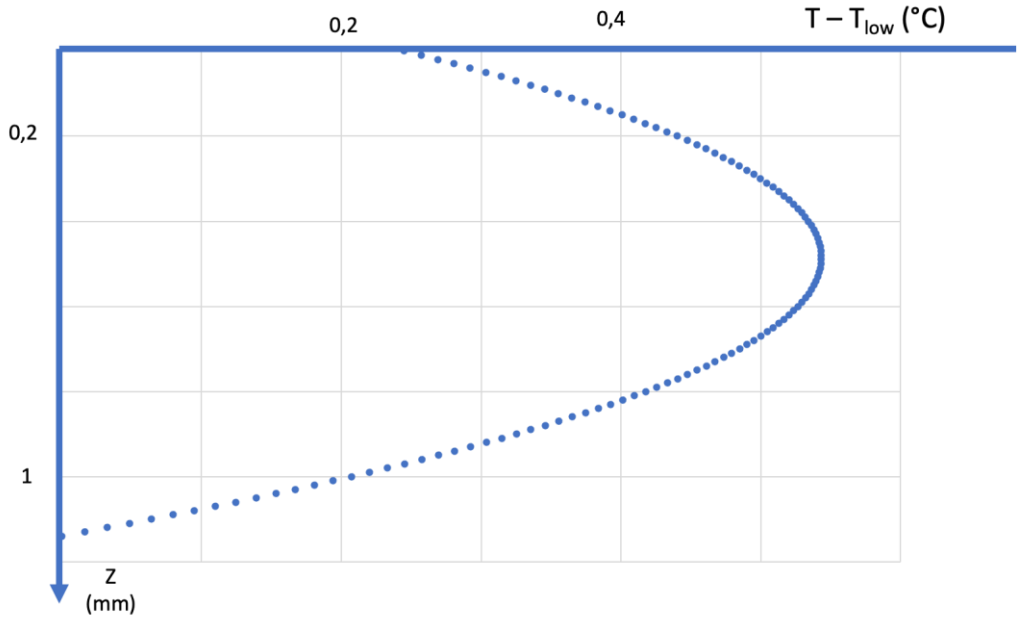

***Figure 6-3**: Temperature profile in a solid layer (parabolic profile) at steady state: l = 0.027 W m^{-1}K^{-1}, e = 1.14 mm, $\phi_{up}^{rad} = 156$ W m^{-2}. Boundary conditions $T_{up} = 25.6°C$; $T_{low} = 25.11\ °C$. (Eq. 16)*

In fact, contrary to the prediction of this parabolic model, the heat transfer would have to be higher at the upper surface where the incident radiative flux illuminates than at the lower surface. This can only be assessed if the dissipation of heat inside the layer is not considered as homogeneous. A more accurate representation requires consideration of the spatial distribution of radiative power dissipation within the layer, which is the object of the next paragraph.

6.1.4.3 Master equations for coupled radiative and heat transfers

The assumption that the dissipation of heat is not homogeneous leads to considering separately radiative and heat transfers. The master equation for heat transfer is not changed. The radiative transfer between abscissa z and $z + \Delta z$ is described by (steady state):

$$\phi_{|z}^{rad} - \phi_{|z+\Delta z}^{rad} - E_a \Delta z\, \phi^{rad} = 0 \qquad \textit{Eq. 23}$$

Where E_a is the absorption coefficient (m^{-1}). The enthalpy balance inside the layer indicates that the radiative energy dissipated is recovered into heat. The coupling with the thermal balance is defined by:

$$\phi^T_{|z} - \phi^T_{|z+\Delta z} + E_a \Delta z \, \phi^{rad} = 0 \qquad \textit{Eq. 24}$$

The differential form of Eq. 23 is written:

$$\frac{d\phi^T}{dz} = E_a \, \phi^{rad} = E_a \phi^{rad}_{up} \, e^{-E_a z}$$

This leads to the Lambert-Beer equation:

$$\phi^{rad} = \phi^{rad}_{up} \, e^{-E_a z} \qquad \textit{Eq. 25}$$

An average value of the absorption coefficient $E_a = 3000 \ \mathrm{m}^{-1}$ and a thickness of 1.14 mm (Table 6-4) leads to estimate that 97 % of the incident radiation is converted to heat inside the layer: $\phi^{rad}_{low} = 0.03 \ \phi^{rad}_{up}$

The differential form of Eq. 24 is written:

$$\frac{d\phi^T}{dz} = E_a \, \phi^{rad} = E_a \phi^{rad}_{up} \, e^{-E_a z}$$

Considering the heat transfer by conduction (Eq. 5), the previous equation is integrated for obtaining the temperature profile. The physical properties (E_a, λ) are assumed constant throughout the leaf replica. The solution which can be developed analytically is the following:

$$T - T_{low} = \left(T_{up} - T_{low}\right)\left(1 - \frac{z}{e}\right) + \frac{\phi^{rad}_{up}}{E_a \lambda}\left[1 - e^{-E_a z} - \frac{z}{e}\left(1 - e^{-E_a e}\right)\right] \qquad \textit{Eq. 26}$$

As in the previous analysis, the temperature profile exhibits a maximum. The location of this maximum is given by:

$$z_{max} = -\frac{1}{E_a} ln\left[\frac{1}{E_a e}\left(1 - e^{-E_a e}\right) + \frac{\lambda}{\phi^{rad}_{up} e}\left(T_{up} - T_{low}\right)\right] \qquad \textit{Eq. 27}$$

The thermal fluxes at the two surfaces are also calculated:

$$\phi^T_{up} = \phi^{rad}_{up}\left(-1 + e^{-E_a z_{max}}\right) \qquad \textit{Eq. 28}$$

$$\phi^T_{low} = \phi^{rad}_{up}\left(e^{-E_a z_{max}} - \ e^{-E_a e}\right) \qquad \textit{Eq. 29}$$

As previously observed ϕ^T_{up} is negative. The quantity $-\phi^T_{up} + \phi^T_{low}$ represents the total heat flux removed by convection on the two surfaces of the leaf replica. $\phi^{rad}_{up} - \left(-\phi^T_{up} + \phi^T_{low}\right) = \phi^{rad}_{up} e^{-E_a e}$ corresponds to the portion of radiative energy transmitted through the layer and released at the lower surface. This validates the global heat balance. Consequently, radiative

heat transfer at the lower surface must be subtracted from the energy dissipated within the layer.

The results of integration are given by Eq. 26 with the same thickness and conductivity as previously, with $\phi_{up}^{rad} = 156$ W m^{-2} and an average absorption coefficient E_a = 3000 m^{-1} is represented in Figure 6-4 .

Under these conditions, the heat fluxes are – 100.3 W m^{-2} at the upper surface and 50.6 W m^{-2} at the lower surface. For T_{bulk}= 19.56 °C, the heat transfer coefficients are h_{up}= 16.7 W m^{-2}K^{-1} and h_{low}= 9.1 W m^{-2} K^{-1}. The calculated maximum temperature inside the layer is T_{max}= 26.1 °C for an abscissa z_{max} = 343 µm.

The temperature profile has the same general shape as when considering homogeneous dissipation of heat inside the layer, but the maximum temperature and the dissipation of radiative energy occur closer to the upper surface, leading to an estimated larger heat exchange at the upper surface than at the lower one. With this model, the h_{up} is almost twice larger than h_{low}.

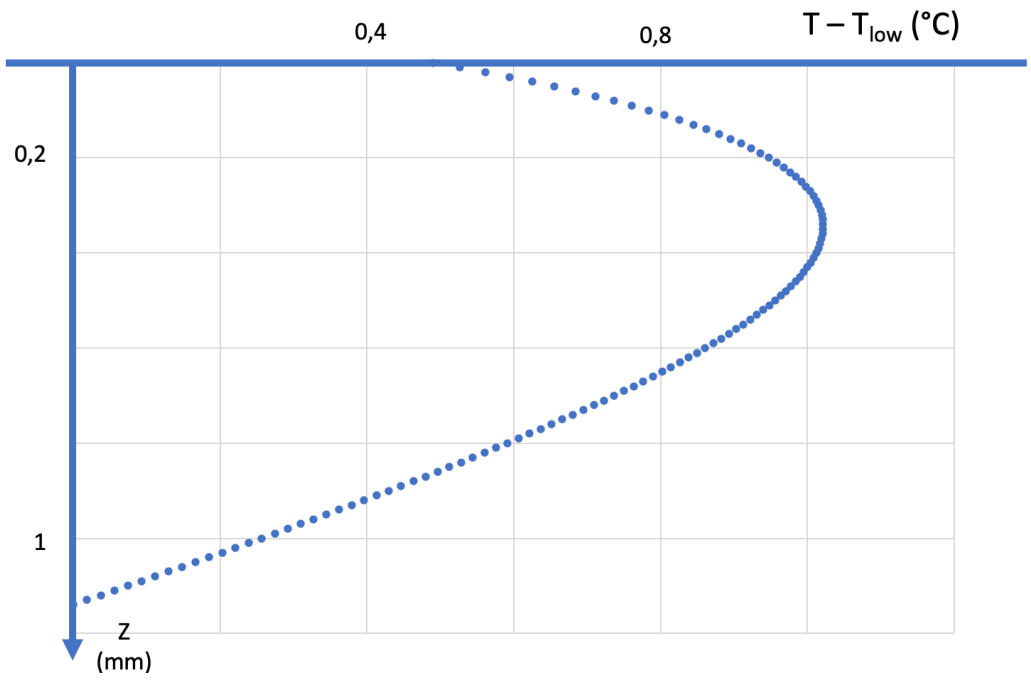

Figure 6-4 *Temperature profile in a solid layer at steady state: λ = 0.027 W m^{-1} K^{-1}, e = 1.14 mm, $\phi_{up}^{rad} = 156$ W m^{-2}, E_a= 3000 m^{-1} Boundary conditions $T_{up} = 25.6$ °C; $T_{low} = 25.11$ °C (Eq. 26).*

6.1.4.4 Sensitivity analysis

In order to test the sensitivity of the model, the influence of the conductivity, of the thickness and the extinction coefficients of the different constitutive layers has been studied. With

variable values of the parameters issued from the value of Table 6-4, the analytical mathematical solution (Eq. 26 and Eq. 27) of coupled heat and radiative transfer equation is not applicable. The resolution of coupled Eq. 23 and Eq. 25 has been done numerically. As the boundary conditions are not located at the same abscissa (the temperatures on the two surfaces), the resolution has been done by a matrix resolution with a griding of the thickness. The calculated heat fluxes resulting from this simulation are - 102.2 W m^{-2} at upper surface and 50.9 W m^{-2} at the lower surface. For T_{bulk}= 19.56 °C, the calculated heat transfer coefficients are h_{up}= 16.9 W $m^{-2}K^{-1}$ and h_{low}= 9.2 W m^{-2} K^{-1}. The calculated maximum temperature inside the layer is T_{max}= 26.1 °C for an abscissa z_{max} = 515 mm. The calculated profile is represented in Figure 6-5.

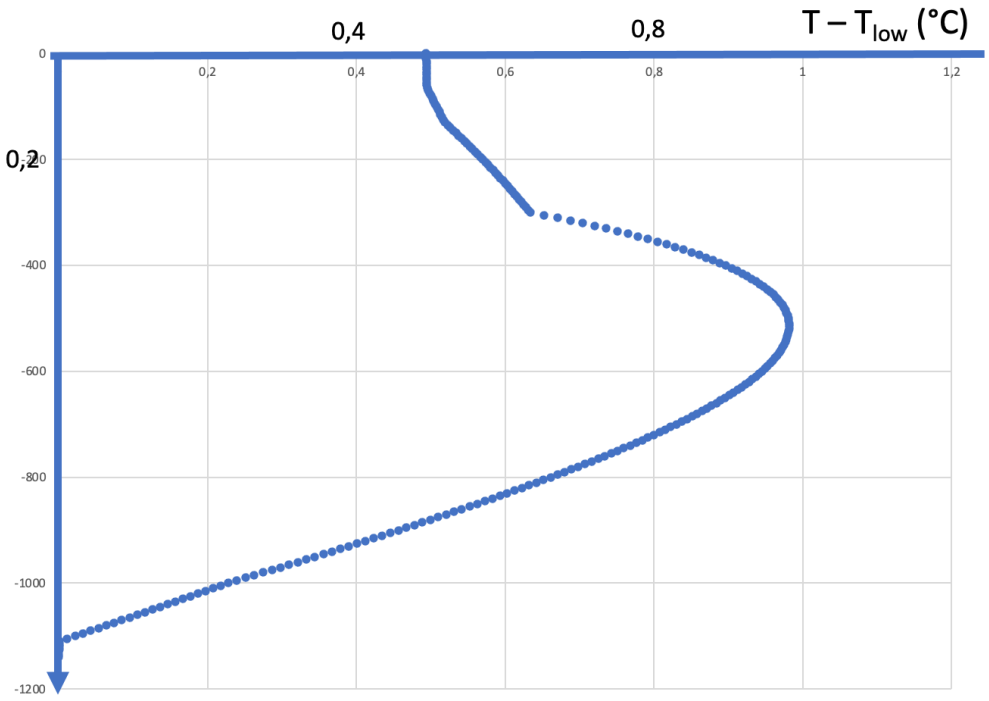

***Figure 6-5**: Simulated temperature profile with variable absorption coefficient and conductivities of the different constitutive layers. e = 1.14 mm, $\phi_{up}^{rad} = 156$ W m^{-2}, Values of the conductivities and absorption coefficient given in Table 6-4. Boundary conditions $T_{up} = 25.6\ °C$; $T_{low} = 25.11\ °C$*

Although the calculated profiles appear to be much less regular with heterogeneous extinction and conductivity in the constitutive layers than in the previous simulation (homogeneous extinction of the radiation and average conductivity Figure 6-4), the main results (heat fluxes, transfer coefficients and maximum temperature) remain largely consistent. The most notable difference lies in the position of the temperature maximum: in the heterogeneous model, it is at 515 µm instead of 343 µm in the homogeneous extinction model (therefore much closer to the axis of the deaf replica for the complete model) but as no accurate information is accessible

for a precise determination of the location of this maximum, it is not possible to take this argument into consideration.

Therefore, the analytical model (Eq. 25 to Eq. 29) is considered valid for characterizing coupled heat and radiative transfer through the leaf replica, using averaged values for the absorption coefficient and thermal conductivity derived from Table 6-4: E_a= 7000 m^{-1} λ = 0.0*33* W m^{-1} K^{-1} for the non-evaporating leaf replica.

In comparison, the calculated maximum temperature remains slightly below the experimentally measured value by approximately 0.4 °C. This discrepancy is likely due to the spatial offset between the internal thermocouple and the two surface-mounted thermocouples, which introduces variations in the local thermal gradient. Additionally, the transversal fluxes are also not considered so that the development of more accurate models would certainly provide a more detailed prediction of the temperature profile.

As a simplified alternative for estimating the two heat transfer coefficients, Eq. 1 can be revisited by introducing the ratio of the coefficients, leading to the following formulation:

$$\phi^T = h_{up}\left[T_{up} + \frac{1}{\alpha}T_{low} - \frac{1+\alpha}{\alpha}T_{bulk}\right] \qquad \textit{Eq. 30}$$

If α is correlated, this permits a simple calculation of h_{up} and the estimation of h_{low}. The value of α will be calculated after treatment of the available experimental data for non-evaporating leaf replica in the different experimental conditions.

The influence of the values of the absorption coefficient and conductivity on the prediction of the transfer coefficients has been evaluated numerically. The results are summarized in Table 6-5. This shows that the proportionality coefficients between the incertitude on the physical properties of the leaf replica (λ and E_a) and the incertitude on the heat transfer coefficients are always smaller than unity. The values reported in Table 6-5 also indicate that h_{up} is less sensitive to imprecise estimation of physical variables than h_{low}.

	k_1: coefficient for $\frac{\Delta\lambda}{\lambda}$	k_2: coefficient for $\frac{\Delta E_a}{E_a}$
$\frac{\Delta h_{up}}{h_{up}}$	0.11	0.39
$\frac{\Delta h_{low}}{h_{low}}$	0.34	0.81
$\frac{\Delta\alpha}{\alpha}$	0.23	0.42

Table 6-5: Sensitivity analysis for the determination of heat transfer coefficients: values of the proportionality constants: $\frac{\Delta h}{h} = k_1 \frac{\Delta \lambda}{\lambda} + k_2 \frac{\Delta E_a}{E_a}$. Pivot values E_a= 3000 m^{-1}; λ = 0.027 W m^{-1} K^{-1}. $\alpha = \frac{h_{up}}{h_{low}}$

Accounting for the different uncertainties on the estimation of the physical variables and on the measurements, it is considered that the values of the heat transfer coefficients at upper and lower surfaces are estimated with a precision of 20 % and 30 %, respectively when the conductivity and the absorption coefficient and the conductivity are known with 20 and 50% accuracy, respectively. Importantly, it is confirmed that the two heat transfer coefficients are significantly different and that the treatment of the surface temperatures would permit a separate evaluation of the two transfer coefficients.

6.1.5 Identification of heat transfer coefficients from the experimental data

Up to now, the test reference values for surface temperatures given in Table 6-3 have been considered for establishing the structure of the model of heat conduction through the leaf replica. The next step involves evaluating the heat transfer coefficients of the non-evaporating leaf replica using the actual surface temperature measurements obtained under various experimental conditions. This has been done as a function of three degrees of freedom: bulk temperature, the inclination of the leaf replica, and air velocity. The results are given in Table 6-6 and include the steady state data for 3 different temperature settings of HPC. Each temperature value is an average value from the steady state of at least 5 measurement cycles as described in section 4.2.4

It is observed that:

- The heat transfer coefficients are significantly different at the upper and lower surfaces of the leaf replica.
- The air velocity increases the heat transfer coefficient, both at the upper and lower surfaces.
- The bulk temperature does not have a statistically significant influence on the calculated heat transfer coefficients.
- The inclination of the leaf replica with a positive angle increases the heat transfer coefficient at the upper whereas this influence is not really observed with the lower heat transfer coefficient.

HPC set °C	θ °	u_∞ m s^{-1}	T_{bulk} °C	T_{up} °C	T_{low} °C	h_{up} W m^{-2} K^{-1}	h_{low} W m^{-2} K^{-1}
18	-30	0.00	19.45	27.38	26.8	21.0	3.2
18	-30	0.05	19.44	26.77	26.1	22.4	3.9
18	-30	0.15	18.89	25.42	24.9	25.7	3.7
19.5	-30	0.00	21.63	27.94	27.3	26.2	4.3
19.5	-30	0.05	21.56	27.53	26.8	27.3	5.1
19.5	-30	0.15	20.86	26.07	25.6	32.2	4.7
21	-30	0.00	23.86	30.27	29.5	25.4	4.9
21	-30	0.05	23.31	29.12	28.3	27.4	6.3
21	-30	0.15	22.92	28.21	27.6	31.3	5.3
18	-15	0.00	19.53	27.99	27.4	19.6	3.1
18	-15	0.05	19.45	27.43	26.7	20.4	3.8
18	-15	0.15	18.90	25.96	25.4	23.7	3.6
19.5	-15	0.00	21.60	28.63	28.0	23.4	4.0
19.5	-15	0.05	21.53	28.10	27.4	24.6	4.9
19.5	-15	0.15	21.04	26.85	26.3	28.5	4.7
21	-15	0.00	23.83	30.95	30.1	22.5	4.7
21	-15	0.05	23.36	29.77	28.8	24.4	6.2
21	-15	0.15	22.94	28.74	28.1	28.3	5.1
18	0	0.00	19.52	27.80	27.2	20.1	3.1
18	0	0.05	19.49	27.28	26.6	20.9	3.9
18	0	0.15	18.94	25.88	25.4	24.2	3.5
19.5	0	0.00	21.60	28.86	28.2	22.5	4.1
19.5	0	0.05	21.56	28.20	27.4	24.2	5.2
19.5	0	0.15	20.93	26.90	26.3	27.5	4.9
21	0	0.00	23.79	31.16	30.2	21.4	5.1
21	0	0.05	23.43	29.89	28.9	24.0	6.5
21	0	0.15	22.95	28.85	28.1	27.5	5.4
18	15	0.00	19.54	27.01	26.5	22.3	3.4
18	15	0.05	19.54	26.53	25.9	23.4	4.3
18	15	0.15	18.98	25.28	24.7	26.4	4.2
19.5	15	0.00	21.69	28.53	27.8	23.8	4.5
19.5	15	0.05	21.61	27.74	27.0	26.2	5.5
19.5	15	0.15	21.13	26.73	26.1	29.3	5.3
21	15	0.00	23.89	30.76	29.9	23.1	5.3
21	15	0.05	23.46	29.39	28.3	25.9	7.5
21	15	0.15	23.02	28.45	27.7	29.7	6.2
18	30	0.00	19.57	25.86	25.4	26.9	3.7
18	30	0.05	19.49	25.22	24.7	29.3	4.3
18	30	0.15	19.20	24.56	24.1	31.3	4.6
19.5	30	0.00	21.74	27.67	27.0	27.7	4.9
19.5	30	0.05	21.66	26.84	26.1	31.3	6.3
19.5	30	0.15	21.01	25.82	25.2	34.1	6.2
21	30	0.00	23.92	29.84	29.0	26.9	6.0
21	30	0.05	23.50	28.46	27.4	31.2	9.1
21	30	0.15	23.04	27.62	26.9	35.4	7.2

Table 6-6 *Calculation of heat transfer coefficients. Unit 2;* $\phi_{up}^{rad} = 183.3\ W\ m^{-2}$

6.2 Development of a predictive model of the heat transfer coefficients for non-evaporating leaf replica

The experimental data have enabled the identification of the heat transfer coefficients at both the upper and lower surfaces of the leaf replica, based on surface temperature measurements. The developed model uses combined radiative and heat transfer by conduction in the leaf replica. The next objective is to construct a model capable of explaining the observed trends and the experimentally derived heat transfer coefficients, and to compare these findings with established heat transfer models. This modelling framework will subsequently be extended to address mass transfer phenomena in the case of the evaporating leaf replica.

6.2.1 Definition of the hydrodynamic boundary layer

The concept of the boundary layer is foundational in chemical engineering and widely used to characterize transport resistances for both heat and mass transfer. It provides a basis for correlating transfer coefficients with the hydrodynamic behaviour in the region between a solid surface and a flowing fluid (Beek et al., 2000a). This concept has been successfully used by (Poulet, 2018) to address the influence of reduced gravity conditions on the transfer characteristics near real leaves of higher plants. The boundary layer concept is useful for understanding the influence of shear dissipation near a wall. This leads to correlations for predicting the transfer coefficients in industrial equipment. However, the influence of natural convection, driven by gravity, is less obvious. Natural convection effects are generally hidden and lumped in semi-empirical correlations that are explicitly developed for terrestrial conditions. In the framework of this study, this calls for a complete setting of the boundary layer concept for deciphering the complementary influences of the operational variables, i.e., air velocity, gravity and inclination of the leaf replica. This is the objective of this paragraph.

In the following sections, all the developments are done for a laminar flow regime. Considering the involved Reynolds numbers, this assumption will remain valid.

In chemical engineering literature, the boundary layer concept is used for defining an idealised image representing the transient transfer of momentum between a bulk fluid and a wall. The thought experiment is as follows: a large flat horizontal plate immersed in a quiescent fluid is moved at a constant velocity v_0 from $t = 0$ in the direction x. The transient momentum

transport in the *y* direction takes place resulting in a velocity distribution which is a function of time and *y* coordinate, $v_x(t,y)$. Applying the momentum balance equation, the velocity distribution is represented by the error function.

$$\frac{\partial v_x}{\partial t} = \nu \frac{\partial^2 v_x}{\partial y^2} \qquad t < 0 \ \forall y: \ v_x = 0 \ \text{and} \ \ t > 0 \ \ y = 0: \ v_x = v_0 \qquad \textit{Eq. 31}$$

$$v_x = \ v_0 \left(1 - \text{erf}\left(\frac{y}{\sqrt{4\,\nu\,t}}\right)\right) \qquad \textit{Eq. 32}$$

In the above, ν ($m^2\ s^{-1}$) is the kinematic viscosity of the fluid:

$$\nu = \frac{\mu}{\rho} \qquad \textit{Eq. 33}$$

v_0 being the velocity of the plate at $t > 0$, the slope of $v_x(t,y)$ at the surface of the plate is equal to:

$$\frac{dv_x}{dy}_{|y=0} = \ - \frac{v_0}{\sqrt{\pi\,\nu\,t}} \qquad \textit{Eq. 34}$$

By definition, μ being the dynamic viscosity (Pa·s), the shear force at the wall τ_w representing the friction loss is given at time *t* by:

$$\tau_w = - \mu \ \frac{dv_x}{dy}_{|y=0} = \mu \frac{v_0}{\sqrt{\pi\,\nu\,t}} \qquad \textit{Eq. 35}$$

The hydrodynamic boundary layer (BL) concept is then defined as a virtual layer of fluid submitted to a constant shear force that is equal to the shear force at the wall at time *t*. Of course, this is not the exact situation, knowing the constraint is varying within the layer ($\frac{dv_x}{dy}$ is not constant with *y*). Therefore, the BL must be considered as a concept which represents the penetration of momentum into the fluid layer at a constant rate, more than the reality. The consequence is that the virtual velocity profile associated to the boundary layer is linear (constant shear force) throughout the depth in the layer. The thickness of the BL δ_H is defined as the region where the velocity profile is linearly changing from 0 to v_0.

$$\tau_w = \tau = - \mu \ \frac{dv_x}{dy} = - \mu \ \frac{v_0}{\delta_H} \qquad \textit{Eq. 36}$$

For the above system (moving plate into a quiescent fluid at transient state), this leads to:

$$\delta_H = \sqrt{\pi\,\nu\,t} \qquad \textit{Eq. 37}$$

Considering the distance x crossed in time *t* at velocity v_0 the previous equation leads to:

$$\frac{\delta_H}{x} = \sqrt{\pi}\left(\frac{\nu}{x\, v_0}\right)^{1/2} = 1.772\, Re_x^{-1/2} \qquad \textit{Eq. 38}$$

Re_x is the Reynolds number at abscissa x. The friction factor C_f is defined as:

$$|\tau_w| = \frac{1}{2}\,\rho\, C_f\, v_0^2 \qquad \textit{Eq. 39}$$

This leads to:

$$C_f = 1.128\, Re_x^{-1/2} \qquad \textit{Eq. 40}$$

Combining the different previous equations Eq. 36 and Eq. 39 leads to a useful relation between the thickness of the BL and the friction factor C_f:

$$\frac{x}{\delta_H} = \frac{1}{2}\, C_f\, Re_x \qquad \textit{Eq. 41}$$

Equation Eq. 41 is not linked to a special model of momentum transfer. This is the reason why it will be extensively used later.

In summary, the hydrodynamic boundary layer concept represents the system as if it were separated in two regions: the bulk region is perfectly homogenous; the boundary layer region has a linear velocity profile between the bulk and the wall corresponding to the penetration of momentum at a constant rate.

6.2.2 Equivalence between hydrodynamic, heat and mass transfer boundary layers

Knowing the symmetry between heat and mass transfer governing equations, both cases are treated in parallel in this section. The important asset of the above definition is that it is transposable without any difficulty to heat and mass transfer phenomena. The reason is that transient thermal and mass balances have the same form as Eq. 31 with similar boundary conditions. T and C being the temperature and the concentration, the description has the following form:

$$\frac{\partial T}{\partial t} = a\frac{\partial^2 T}{\partial y^2} \qquad t < 0\ \ \forall y: T = T_0 \ \text{ and } \quad t > 0\ \ y = 0:\ \ T = T_w \qquad \textit{Eq. 42}$$

$$\frac{\partial C}{\partial t} = \mathcal{D}\,\frac{\partial^2 C}{\partial y^2} \qquad t < 0 \;\; \forall y: C = C_0 \;\; \text{and} \;\; t > 0 \;\; y = 0: \;\; C = C_w \qquad \textit{Eq. 43}$$

$\mathcal{D}$ ($m^2\ s^{-1}$) is the diffusion coefficient of the compound. a ($m^2\ s^{-1}$) is the thermal diffusivity:

$$a = \frac{\lambda}{\rho\ C_p} \qquad \textit{Eq. 44}$$

This leads to define Prandtl and Schmidt dimensionless numbers:

$$Pr = \frac{\nu}{a} = \frac{C_p\,\mu}{\lambda} \;\text{ and }\; Sc = \frac{\nu}{\mathcal{D}} = \frac{\mu}{\rho\,\mathcal{D}} \qquad \textit{Eq. 45}$$

The complete correspondence and the analogy between heat, hydrodynamic and mass transfers is achieved when comparing the "length units" in terms of random walk at the molecular level and/or at eddies mobilities. $\delta_H,\ \delta_T,\ \delta_M$ being hydrodynamic, thermal, and mass boundary layers respectively, the fluctuation dissipation theory shows that the volumes of the eddies for each type of transfer is proportional to the diffusivities (Mauri, 2013) so that:

$$C\ \delta_H^3 = \nu \qquad C\ \delta_T^3 = a \qquad C\ \delta_M^3 = \mathcal{D}$$

C is the proportionality constant. It is calculated from the previous description of hydrodynamics BL. This leads to the simple relations between the hydrodynamic, heat transfer and mass BL:

$$\frac{\delta_H}{\delta_T} = Pr^{1/3} \qquad \frac{\delta_H}{\delta_M} = Sc^{1/3} \qquad \textit{Eq. 46}$$

As a consequence, the hydrodynamic BL is suitably modelled or correlated, the thicknesses of thermal and mass BL are easily determined.

The analogy between momentum, heat and mass transfer are prolonged in terms of definition of the heat and mass transfer BL. The heat and mass transfer coefficients h and k are given by:

$$h = \frac{\lambda}{\delta_T} = \frac{\lambda}{\delta_H}\,Pr^{1/3} \qquad k = \frac{\mathcal{D}}{\delta_M} = \frac{\mathcal{D}}{\delta_H}Sc^{1/3} \qquad \textit{Eq. 47}$$

The dimensionless numbers Nusselt and Sherwood are defined:

$$Nu_x = \frac{h\,x}{\lambda} = \frac{x}{\delta_T} \qquad Sh_x = \frac{k\,x}{\mathcal{D}} = \frac{x}{\delta_M} \qquad \textit{Eq. 48}$$

The heat and mass transfer resistances are also obtained from Eq. 8 and Eq. 9 leading to combine the resistances in series or in parallel.

6.2.3 Parallel flow tangentially along a flat plate

The situation is the case of a bulk fluid flowing at a velocity v_∞ above the surface of a flat plate. This classical case has been integrated numerically (Blasius relation). The friction factor at the wall is correlated as follows:

$$C_f = 0.664\ Re_x^{-1/2} \qquad \textit{Eq. 49}$$

This leads to (Eq. 41):

$$\frac{\delta_H}{x} = 3.012\ Re_x^{-1/2} \qquad \textit{Eq. 50}$$

$$|\tau_w| = \frac{1}{2}\ \rho\ C_f\ v_\infty^2 \qquad \textit{Eq. 51}$$

Compared to the previous situation when the plate is moving in a quiescent fluid, the BL thickness appears to be almost twice in the case of a moving fluid. This is finally a normal situation, considering that the streamlines are slow down near the surface of the plate, leading to an up-flow of the fluid out the BL. This leads to an increased thickness of the BL. Comparison Eq. 38 and Eq. 48 leads to consider that this up-flow of fluid creates an increased BL thickness equal to:

$$\frac{\Delta\delta_H}{x} = (3.012 - 1.128)\ Re_x^{-\frac{1}{2}} = 1.884\ Re_x^{-\frac{1}{2}} \qquad \textit{Eq. 52}$$

This corresponds to a flow velocity perpendicular to the surface of $v_\infty/2$.

Error! Reference source not found. also leads to a well-known correlation of Nusselt number (Eq. 48) in laminar flow:

$$Nu_x = 0.332\ Re_x^{1/2}\ Pr^{1/3} \qquad \textit{Eq. 53}$$

This relation is widely used for correlating the heat transfer coefficients in heat exchangers. It has been also for used by (Poulet, 2018; Poulet et al., 2020, 2018) for representing the effect of tangential velocity of heat transfer along a plant leaf.

6.2.4 Change of orientation of the flow in the vicinity of a flat plate

As it has been shown, the determination of the friction factor is the entrance point, but the rigorous analysis is no longer in use for this case. For turbulent flow, the friction factor is generally correlated as follows (Beek et al., 2000a):

$$C_f = 0.131 \ \frac{\theta}{90} \qquad \textit{Eq. 54}$$

Where θ is the angle (degree) between the direction of the flow and the direction of the plate.

$$\frac{x}{\delta_H} = 0.065 \ \frac{\theta}{90} \ Re_x \qquad \textit{Eq. 55}$$

A more accurate correlation should be obtained at low Reynolds numbers and near the edge of the plate by numerical simulations.

6.2.5 Boundary layer created by natural convection driven by gravity on a horizontal surface: upper surface

The influence of gravity on horizontal surfaces must be examined. This is the case where the acceleration is perpendicular to the surface.

As indicated by the experimental results, the leaf replica surface is warmer than the bulk. This generates, at least at the upper surface of the leaf replica, a convection stream between the bulk and the region near the surface as the fluid is less dense at the wall. We develop a simple approach based on BL theory.

Let $\Delta\rho = \rho_{bulk} - \rho_{up}$ the density difference upon the BL thickness δ_H. The mechanical energy balance, that is the Bernoulli energy balance, at the upper surface of the BL leads to consider that the energy input into the BL introduced by the density difference is converted into kinetic energy, so that (in terms of energy per unit of mass):

$$\frac{1}{2} v^2 = \frac{\Delta\rho}{\rho} g \ \delta_H \qquad \textit{Eq. 56}$$

The definition of the BL is still operating, so that the energy loss per unit of mass is represented by (Eq. 36):

$$\frac{1}{2}v^2 = \nu\frac{v}{\delta_H} \qquad \textit{Eq. 57}$$

Eliminating v between Eq. 56 and Eq. 57, this leads to:

$$\delta_H^3 = 2\frac{\rho}{\Delta\rho}\frac{\nu^2}{g} \qquad \textit{Eq. 58}$$

Introducing the Grashof dimensionless number, this leads to:

$$Gr_x = \frac{\Delta\rho\ g\ x^3}{\rho\ \nu^2} \qquad \frac{x}{\delta_H} = 0.794\ Gr_x^{1/3} \qquad \textit{Eq. 59}$$

It is noteworthy that the calculated equivalent BL thickness accounting for natural convection is constant along the abscissa (Eq. 58).

It is possible to improve the previous model accounting for friction losses inside the BL. This means that the Bernoulli balance must incorporate the friction factor. Here it must be considered that the flow is a creeping flow leaching the surface, leading to prefer penetration model instead of Blasius correlation, so that Eq. 40 is used for C_f. Eq. 56 and Eq. 57 are rewritten, so that:

$$\frac{1}{2}\left(1 + C_f\right)v^2 = \frac{\Delta\rho}{\rho}g\ \delta_H \qquad \textit{Eq. 60}$$

$$\frac{1}{2}\left(1 + C_f\right)v^2 = \nu\frac{v}{\delta_H} \qquad \textit{Eq. 61}$$

This leads to:

$$\delta_H^2 = 2\frac{\rho}{\Delta\rho}\frac{\nu^2}{g}\frac{1}{\delta_H + 1.128\,\nu\sqrt{\frac{\rho}{\Delta\rho\ g\ x}}} \qquad \textit{Eq. 62}$$

The analytical expression cannot be explicitly established. But the numerical resolution for calculating the BL thickness is easily done numerically from Eq. 62.

6.2.6 Boundary layer created by natural convection driven by gravity on a horizontal surface: lower surface

Like for the upper surface, the lower surface is warmer than the bulk. The density gradient is therefore stable hydrodynamically. Air density is lower on the surface than in the bulk. The

previous explanation of a flow of fluid through the external upper surface of the BL does not hold in this case. This leads to the conclusion that the transfer coefficients are different on the upper and lower surfaces. However, before the edge of the leaf replica the density of the fluid is equal to the bulk density. It is therefore higher than the density onto the surface. The consequence is that a fluid flow is entering the BL at the external edge of the plate. This is exactly the same situation as for the upper surface except that the kinetic energy term in the Bernoulli balance is not considered, the only remaining term being the friction loss. Eq. 56 and Eq. 57 are also rewritten, so that:

$$\frac{1}{2}\, C_f v^2 = \frac{\Delta\rho}{\rho} g\, \delta_H \qquad \textit{Eq. 63}$$

$$\frac{1}{2} C_f v^2 = \nu \frac{v}{\delta_H} \qquad \textit{Eq. 64}$$

After some manipulations, this leads to:

$$Gr_x = \frac{\Delta\rho\, g\, x^3}{\rho\, \nu^2} \qquad \frac{x}{\delta_H} = 0.751\, Gr_x^{1/4} \qquad \textit{Eq. 65}$$

This last formula gives an interpretation for a non-infinite BL at the lower surface, explaining significant heat transfer coefficients though they are lower than at the upper surface.

6.2.7 Boundary layer created by natural convection driven by gravity on a vertical surface

For understanding the effect of inclination, the influence of gravity on vertical surfaces must be examined. In this case, the acceleration is parallel to the surface. The situation is different from the case of horizontal plate. When there is a density gradient near the surface, this creates a shear between the bulk and the surface. This shear stress is given by:

$$\tau_w = \Delta\rho\, g\, \delta_H \qquad \textit{Eq. 66}$$

Using the definition of the boundary layer Eq. 35 and Eq. 36, this leads to:

$$\tau_w = \Delta\rho\, g\, \delta_H = \mu \frac{\Delta v}{\delta_H} \qquad \textit{Eq. 67}$$

Δv is the velocity gradient between the bulk and the surface. Considering again the penetration theory is the correct vehicle for representation of this velocity gradient, δ_H is given by Eq. 37. This leads to:

$$Gr_x = \frac{\Delta\rho\ g\ x^3}{\rho\ \nu^2} \qquad \frac{x}{\delta_H} = \frac{1}{\pi^{1/4}}\left(\frac{\Delta\rho\ g\ x^3}{\rho\ \nu^2}\right)^{1/4} = 0.751\ Gr_x^{1/4} \qquad \textit{Eq. 68}$$

This relation is used for example to characterise heat transfer on vertical walls in heat exchangers when the temperature gradient between the vertical surface and the bulk is sufficient for creating a significant density gradient. This relation has been also proposed by (Poulet, 2018; Poulet et al., 2020) for assessing the role of gravity in a plant canopy. For our study it will be used when the leaf replica is inclined.

6.2.8 Sum of the different contributions constituting the total boundary layer

Different contributions that have been described above are acting jointly for constituting the global BL. Contrarily of what happens inside the leaf replica, the different contributions in the gas phase behave as resistances functioning in parallel, which means that the resulting conductance is given by the sum of the inverse of elementary resistances (Kirchhoff law):

$$\frac{1}{\mathcal{R}^T} = \sum_i \frac{1}{\mathcal{R}_i} \qquad \textit{Eq. 69}$$

Elementary resistances are given by:

$$\mathcal{R}_i = \frac{1}{h_i} \qquad \textit{Eq. 70}$$

So that:

$$\frac{1}{\mathcal{R}^T} = \sum_i h_i = \ \lambda\ Pr^{1/3}\ \sum_i \frac{1}{\delta_{Hi}} \qquad \textit{Eq. 71}$$

This hypothesis of addition of parallel resistances finally means that the sum of the inverse of BL thicknesses contributions must be considered to derive a predictive model of the global heat transfer coefficients.

6.3 Comparison of the results of the predictive model of the heat transfer coefficients with the experimental data

6.3.1 Values of the physical properties of the gas phase (air)

The values of the physical properties to be considered are summarized in Table 6-7.

Molar mass M	**Density** ρ	**Heat capacity** C_p	**Dynamic viscosity** μ	**Kinematic viscosity** $\nu = \frac{\mu}{\rho}$	**Diffusion coefficient** $\mathcal{D}_{H2O}$	**Heat conductivity** λ	**Thermal diffusivity** $\frac{\lambda}{\rho\, C_p}$
g mol^{-1}	kg m^{-3}	J kg^{-1} K^{-1}	Pa s	$\mathrm{m^2\ s^{-1}}$	$\mathrm{m^2\ s^{-1}}$	W m^{-1} K^{-1}	$\mathrm{m^2\ s^{-1}}$
28.98	1.3345	1006	1.834 10^{-5}	1.37 10^{-5}	2.56 10^{-5}	2.59 10^{-2}	1.93 10^{-5}

Table 6-7: *Values of the physical properties of dry air at 1 bar and average temperature of 22°C (295 K)*

The molar mass of dry air composed of 78.11 % N_2, 20.93 % O_2 and 0.97 % Ar is equal to:

$$M = 0.7811 * 28.03 + 0.2093 * 32.00 + \ 0.009678 * 39.95 = 28.98\ \mathrm{g\ mole^{-1}}$$

This leads to Prandtl and Schmidt numbers of 0.71 and 0.54 respectively.

For a non-evaporating leaf replica, the value of the ratio $\frac{\rho_{bulk}-\rho_{wall}}{\rho}$ is approximated by $\frac{T_{wall}-T_{bulk}}{T}$, T being the average temperature between both temperatures. In case of evaporating leaf replica, the total pressure at the wall and the variation of molar mass accounting for the water vapor partial pressure must be considered, the water partial pressure at saturation being given by the Antoine law.

6.3.2 Detailed scheme of the leaf replica

Figure 6-6 shows the design of the leaf replica used for the computations and model development. Defining the x-axis parallel to the airflow, the value of the abscissa to be considered in the previous models for Re_x, Nu_x, Gr_x, Sh_x is $x = 17\ \mathrm{mm}$. This is the abscissa of the location of the thermocouples behind the surface of the leaf replica.

With these parameters, it is confirmed that Reynolds number values are always lower than 500 for all the conditions we have tested, so that the laminar flow regime hypothesis remains valid.

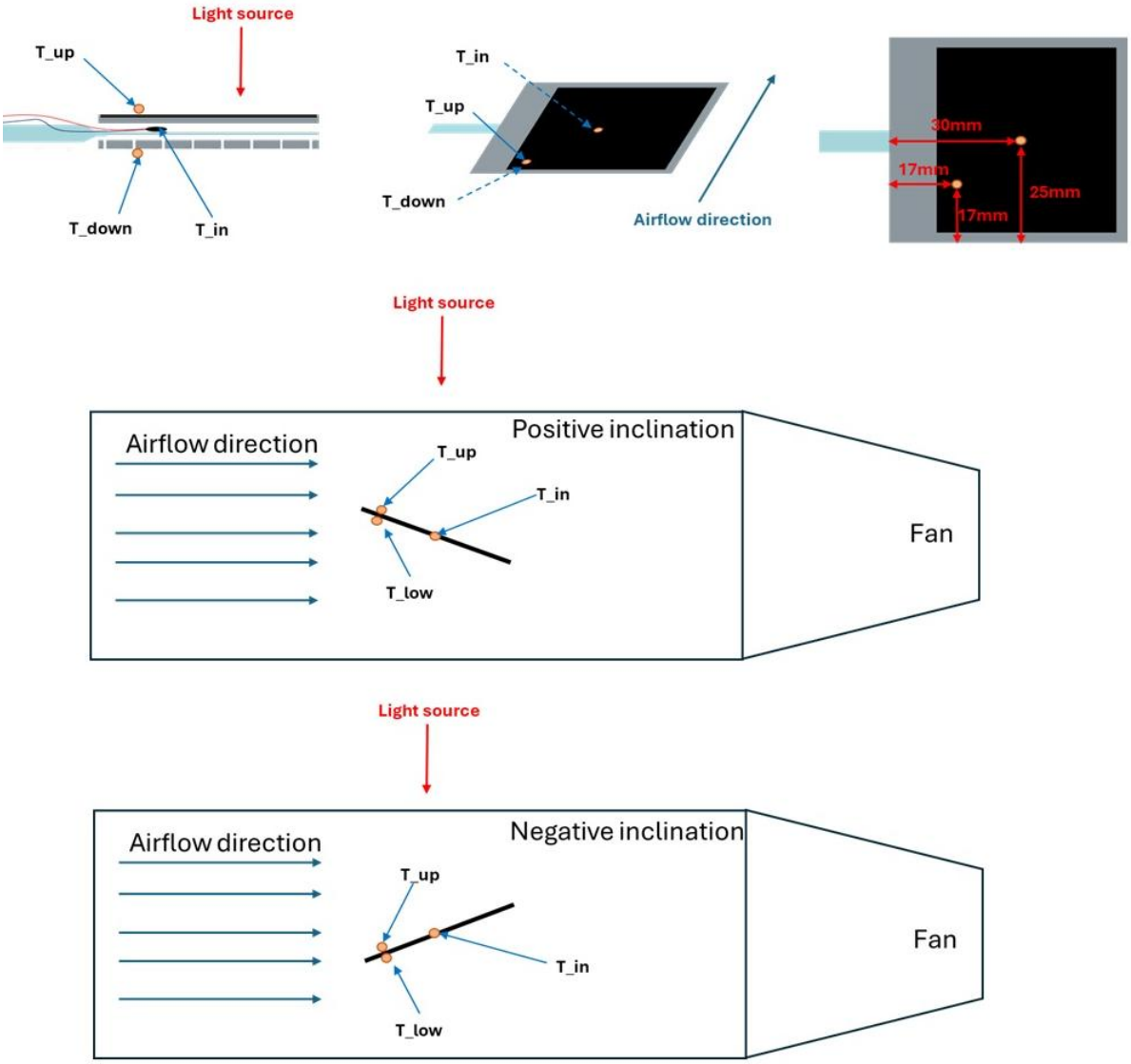

Figure 6-6 *Scheme of the design used for leaf replica experiments*

6.3.3 Comparison of the model prediction to the experimental results

The first thing is to assess the predictability of the model in case of no forced airflow and a horizontal position, i.e., with only with natural convection, the proposed model (Eq. 62) being specific for this work. The results in Table 6-5 indicate that the experimental average value of the heat transfer coefficient at the upper surface is 22 W m^{-2} K^{-1}. Applying Eq. 62, with the measured temperatures, an identical value is obtained. This result indicates that the heat transfer coefficients can be at least estimated with a good accuracy with this model. The heat transfer coefficient at the lower surface is evaluated with Eq. 65 The model leads to an average

value of 7 W m^{-2} K^{-1}. The average experimental values (Table 6-6) are at average 4.5 W m^{-2} K^{-1}. The fit between the model predictions and the results obtained after processing the experimental values of surface temperatures is less satisfactory for the lower surface than for the upper surface. This is consistent with the predictions of the sensitivity analysis reported in Table 6-5. The accuracy remains nevertheless correct.

Considering all constitutive parts of the model with the different contributions to transfer resistance (Eq. 71), the comparison between the predictions of the BL model and the experimental values obtained from surface temperature measurements are shown in Figure 6-7. The comparison of the BL model predictions with the experimental values for the lower surface is given in Figure 6-8.

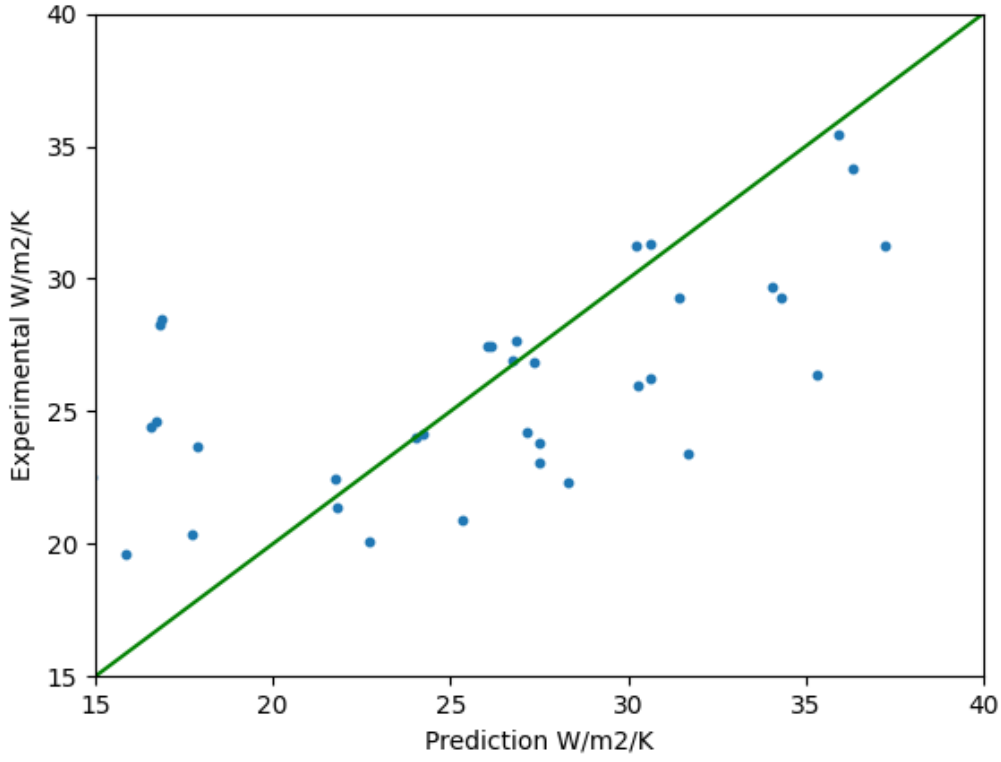

Figure 6-7 *Comparison of the predictive model of the heat transfer coefficient at the upper surface with the experimental values*

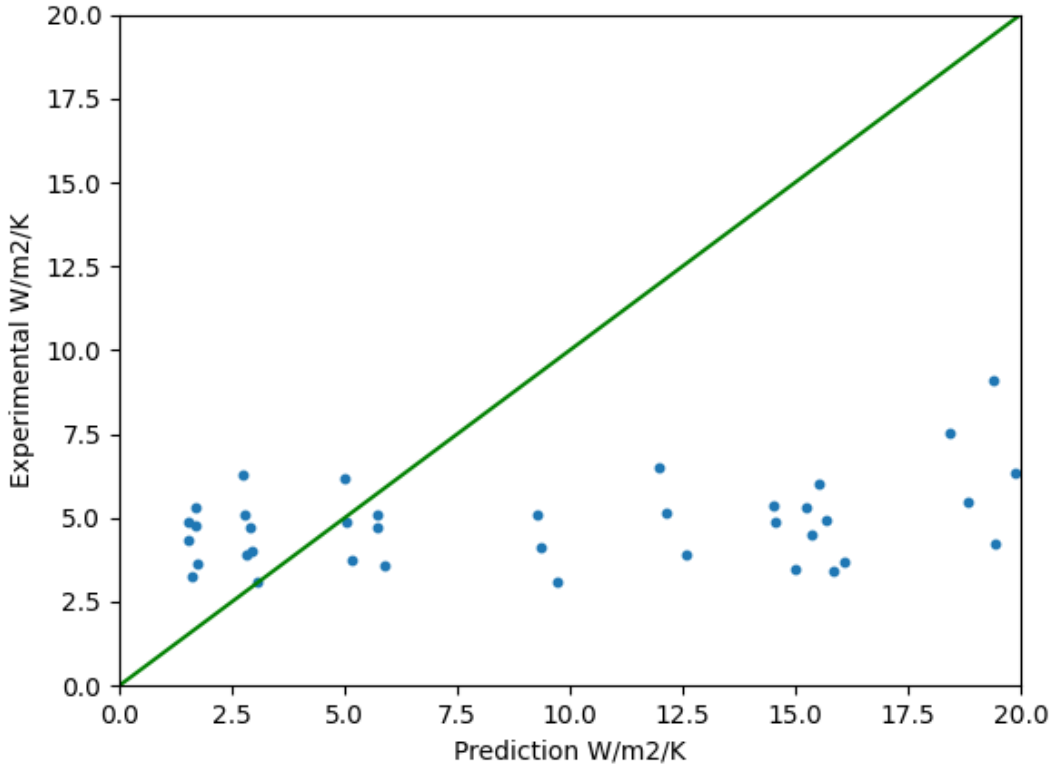

Figure 6-8 *Comparison of the predictive model of the heat transfer coefficient at the lower surface with the experimental values*

The standard deviations between predictions and experiments are 7.8 W m^{-2} K^{-1} for both surfaces. Since the heat transfer coefficients on the lower surface are lower, this means that the relative uncertainty in their determination is higher. Although imperfect, the developed heat transfer model therefore constitutes a good starting point for developing a comprehensive predictive heat transfer model. The orders of magnitude of the transfer coefficients are obtained, and the ratio between the upward and downward coefficients is accurately assessed.

This determination of heat transfer coefficients from experimental values relies on estimating the temperature differences between the surface temperatures and the bulk temperature, which affects the accuracy of the final results based on experimental determinations. Furthermore, these experimental values are extracted from a complex model of coupling between heat diffusion and radiative transfer, which justifies some caution in considering the results.

In terms of model development, it should be kept in mind that the assumption involving the addition of thermal resistances in parallel remains questionable. A more comprehensive analysis of how to combine the different resistances might need to be developed in the future.

It is observed that the experimental values of the heat transfer coefficients on the lower surface remain relatively constant. This would indicate that they are not influenced by external conditions, which is inconsistent with the results, given that the model predicts a slight increase with increasing air velocity and a dependence on the orientation angle. It also appears that the largest differences are related to the negative orientation angle of the leaf replica, for both the upper and lower surface coefficients.

In summary, the main advantage of this approach lies in its ability to link hydrodynamics with heat and mass transfer, given the equivalence between heat, mass, and hydrodynamics. With this approach, it appears possible to predict the heat transfer coefficients on both the upper and lower surfaces. The preliminary analysis of the results indicates that over 80% of the contribution to the heat transfer coefficients, under the experimental conditions studied, is related to natural convection, with an explicit contribution from the Grashof number. This is an important finding for our study, the Grashof number being directly proportional to gravity, therefore supporting the influence of gravity conditions.

This will be improved in the next paragraph developing a semi empirical correlation based on the previous theoretical approach, grouping all the available results on non-evaporating leaf replica.

6.3.4 Improvement of the correlation of heat transfer coefficients

Up to now, the representation of heat transfer coefficients has been based on a purely theoretical analysis of the different contributions acting on momentum and heat exchanges. These contributions with associated theoretical relations are the followings:

- Contribution of friction by parallel velocity influence (Eq. 50): $\frac{x}{\delta_H} = 0.332\ Re_x^{1/2}$
- Change in orientation of the leaf replica (Eq. 55): $\frac{x}{\delta_H} = 0.065\ \frac{\theta}{90}\ Re_x$
- Convective exchange normal to the surface driven by gravity $\Delta\rho\ g > 0$ (Eq. 59 to Eq. 62) (upper surface): $\frac{x}{\delta_H} = 0.794\ Gr_x^{1/3}$
- Convective exchange normal to the surface driven by gravity $\Delta\rho\ g < 0$ (Eq. 65) (lower surface): $\frac{x}{\delta_H} = 0.751\ Gr_x^{1/4}$

- Convective exchange parallel to the surface driven by gravity (Eq. 68) (both upper and lower surfaces): $\frac{x}{\delta_H} = 0.751\ Gr_x^{1/4}$

A deeper analysis of these different contributions on the basis of the experimental results leads to several observations:

- The contribution due to the orientation of the plate could be improved accounting for the positive and negative angles. It must be considered that when the flow is directed towards the surface, the thickness of the BL is reduced (negative angle for upper surface and positive angle for lower surface) and when the flow is directed out of the surface, the contribution acts in opposite directions.
- When the angle is negative, the abscissa for evaluating the convective exchange parallel to the surface must account for the total width of the plate (Figure 6-6) considering the parallel flow comes from the other side of the plate.
- The contribution related to friction would have to account for the parallel component of the velocity and not the overall velocity.

In order to take these observations into account, the normal and perpendicular velocities and acceleration components have been considered separately:

$$v_{\parallel} = v_{\infty}\ cos\theta \qquad g_{\parallel} = g\ sin|\theta|$$

$$v_{\perp} = v_{\infty}\ sin|\theta| \qquad g_{\perp} = g\ cos\theta$$

The Reynolds numbers ($Re_{\parallel}, Re_{\perp}$) and the Grashof numbers ($Gr_{\parallel\_up}, Gr_{\parallel\_low}, Gr_{\perp\_up}, Gr_{\perp\_low}$) are then determined consequently.

A multilinear regression has then been done. The heat transfer coefficients obtained for the two non-evaporating units 1 and 2 and for both surfaces have been considered together, gathering the 2·45·2 = 180 values for both upper and lower surfaces. Considering that the different contributions to the heat transfer coefficients act in parallel, the structure of the correlation is the following:

$$\text{Upper surface: } \Delta\rho\ g > 0: \quad h = \lambda\ Pr^{1/3}\left(\frac{C_1}{x}Re_{\parallel x}^{1/2} \pm \frac{C_2}{x}Re_{\perp x}^{1/2} + \frac{C_3}{x}Gr_{\perp x}^{1/3} + \frac{C_4}{x'}Gr_{\parallel x'}^{1/4}\right)$$

$$\text{Lower surface: } \Delta\rho\ g < 0: \quad h = \lambda\ Pr^{1/3}\left(\frac{C_1}{x}Re_{\parallel x}^{1/2} \pm \frac{C_2}{x}Re_{\perp x}^{1/2} + \frac{C_5}{x}Gr_{\perp x}^{1/4} + \frac{C_4}{x'}Gr_{\parallel x'}^{1/4}\right)$$

The contribution related to the friction due to the normal component of the velocity (coefficient C_2 in the above relation) has been considered with opposite signs at upper and lower surfaces (positive on the upper surface and negative on the lower surface for negative angles). The abscissa 'x' is equal to 17 mm for positive angles and 50 - 17 = 33 mm for negative angles. Considering that the approach represented by Eq. 54 and Eq. 55 did not lead to satisfactory results, the contribution due to the normal velocity component has been considered to be proportional to $Re_{\perp x}^{1/2}$ consistently with the evaluation that is proposed by Eq. 52.

The results of the multilinear regression are reported in Table 6-8 and represented on Figure 6-9. The results for the two non-evaporating units are grouped. The standard deviation for all data is 6.1 W m^{-2} K^{-1} which is a significant improvement from the previous approach.

Coefficient	C1	C2	C3	C4	C5
	0.412	0.377	0.845	0.188	0.532
95% Confidence interval	0.333 – 0.502	0.272 - 0.481	0.735 – 0.958	- 0.032 - 0.407	0.249 – 0.815
Theoretical values	0.332	-	0.794	0.751	0.751

***Table 6-8**: Results of multilinear regression of heat transfer coefficients*

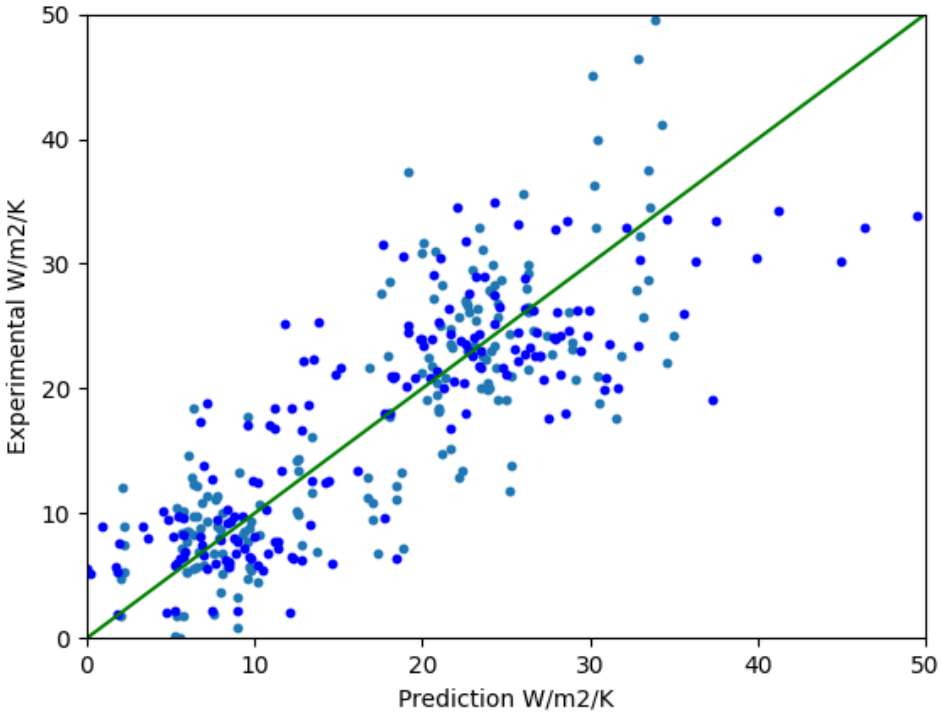

***Figure 6-9**: Results of the multilinear regression of the heat transfer coefficients for upper and lower surfaces. Non-evaporating units 1 (blue) and 2 (light blue)*

It is noticed that the coefficients identified for the first contribution (friction loss by parallel flow - coefficient C_1), the third contribution (convective friction due to positive density gradient at upper surface – coefficient C_3) and the forth contribution (friction due to parallel flow generated by density gradients – coefficient C_4) are consistent with the previous theoretical approach. It is noticed that the theoretical values previously obtained with the model structure development are in the range of the confidence intervals obtained after identification for these three coefficients. The contribution related to convective friction due to negative density gradient at lower surface (coefficient C_5) is significantly different from the value obtained by theoretical development. The estimate of this coefficient remains imprecise (large confidence interval). However, the obtained value for this coefficient remains statistically significative.

6.3.5 Discussion of the results

Even if the experimental values extracted from the complex model of heat diffusion coupled with radiative transfer might be considered with caution, it is concluded that the developed model correctly accounts for dissymmetry between up and lower surfaces and at least provides satisfactory estimations of the evolution of the variables in the range of the parameters that have been investigated (bulk temperature, air velocity, inclination of the leaf replica).

It is confirmed that the complete predictions of the heat transfer coefficients, both at upper and lower surfaces seem possible. The correlation that has been derived provides relevant values of the heat transfer coefficients in reasonable agreement with the experimental values that have been obtained from surface temperature measurements.

One important result concerns the ratio of the heat transfer coefficients $\alpha = \frac{h_{up}}{h_{low}}$ (Eq. 30). The results are summarized in Figure 6-10. For the horizontal plate, this ratio varies from 9.1 to 2.1, for air velocities ranging from 0 to 0.3 m s^{-1}. With no airflow, the ratio also varies from 9.1 to 3.3 when the inclination of the plate is changed from 0 to 30°. With an airflow velocity 0.3 m s^{-1}, the ratio varies from 4.2 for θ = - 30° to 0.9 for θ = 30°. These results indicate that the ratio $\frac{h_{up}}{h_{low}}$ is strongly depending on the air velocity and on the inclination of the plate. In any case, it seems difficult to consider that this ratio is equal to 1 assuming the transfer coefficients on

the two surfaces are equal. An important asset of the developed heat transfer model is to permit an estimation of this ratio.

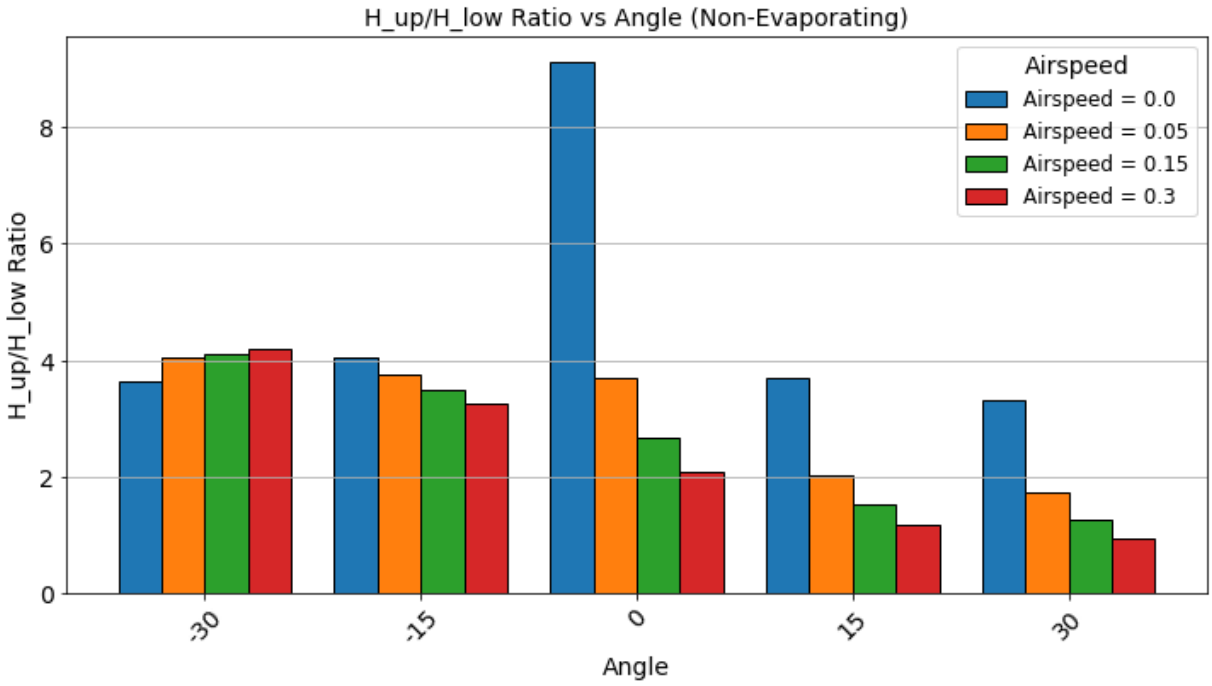

Figure 6-10: *Ratio of heat transfer coefficients on upper and lower surfaces predicted by the model.*

The second result concerns the proportion of gravity driven transfer (that is Grashof dependent) versus friction driven transfer (mainly related to Reynolds number). With no airflow, the totality of the transfer is generated through gravity effect. This is a normal situation. This proportion decreases down to 50 % for the highest air velocities on the upper surface for the angle with negative inclination whereas it may decrease more pronouncedly on the lower surface (33 %) for the highest velocities and positive angles. The results are reported on Figure 6-11.

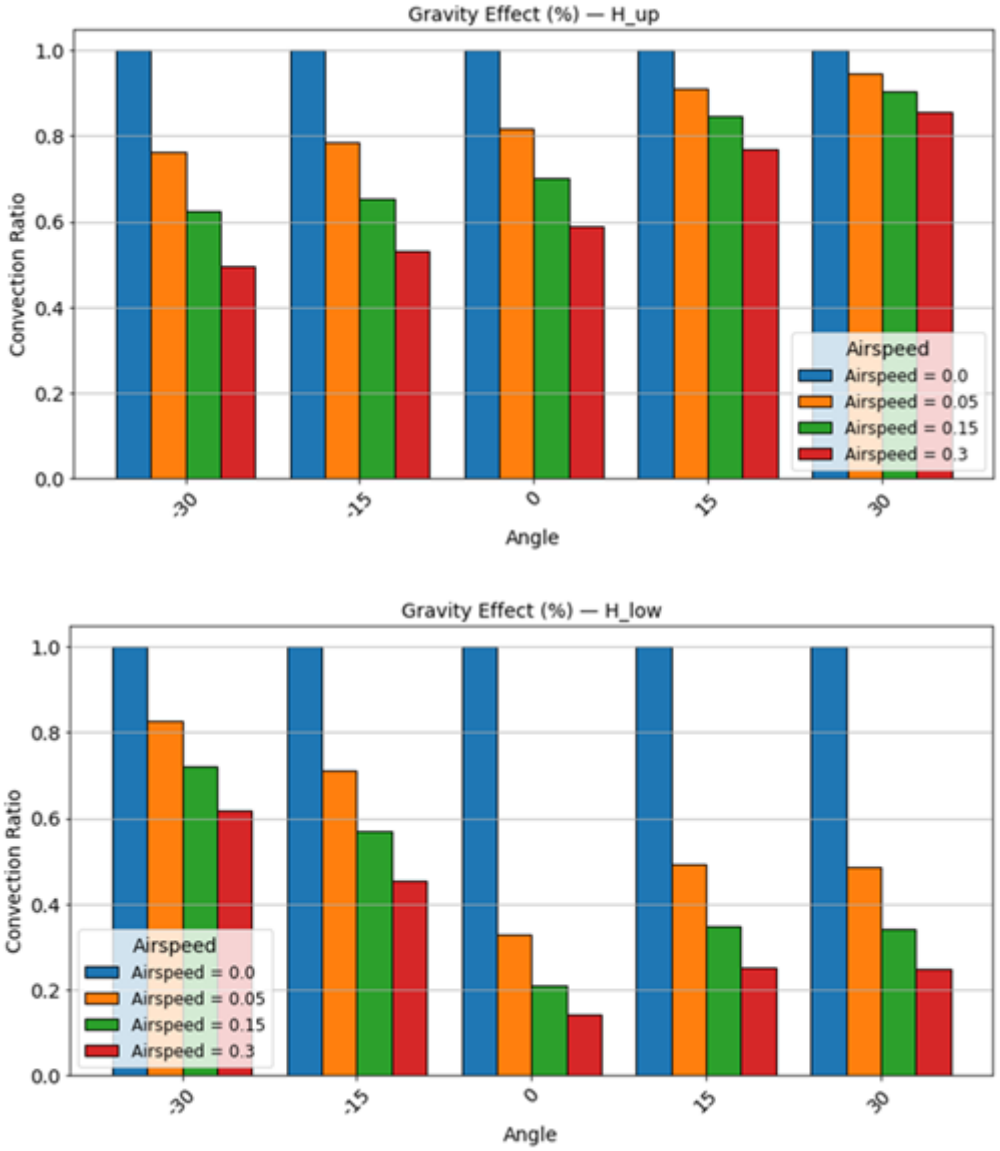

***Figure 6-11**: Predicted proportions of gravity-driven and friction contributions for heat transfer coefficients on both surfaces: for h_{up} (top graph) and for h_{low} (bottom graph)*

The last observation concerns the evaluation of the transfer at the lower surface. It must be noticed that the fourth term in the correlation is more imprecise than the other ones with a large confidence interval for the coefficient (Table 6-8). This means that the gravity-driven contribution at the lower surface remains uncertain, which may impair the estimation of heat transfer for the lowest air velocities.

At the end, it must be kept in mind that the addition of thermal resistances in parallel remains a hypothesis. This rule is considered to be valid by most authors. However, it cannot be excluded that more complex interactions between the different mechanisms of transfer are playing a non-negligible role. A more complete analysis of the way of combining these different resistances might be developed.

This will have to be done by Computer Fluid Dynamics (CFD) simulations leading to local values of transfer coefficients. The estimation of the order of magnitude of the boundary layer thickness that are predicted by the developed model is in the range of 1 mm or even smaller. This requires a griding of the space near the surface which is at least one tenth of this value, i.e., 0.1 mm, which is already challenging if this has to be integrated in large containers.

6.4 Identification of mass transfer coefficient from the experimental data for the steady state

6.4.1 Implementation of descriptive balances

Compared to the previous situation, there are now 4 degrees of freedom instead of 3 for the operation of the system: air velocity, inclination angle, bulk temperature and relative humidity.

The heat transfer coefficients are taken from the previously presented calculations of heat transfer coefficient for the non-evaporative leaf replica. The main assumption is that the heat transfer coefficients for evaporative and non-evaporative leaf replicas are given by the same expressions as function of velocities and density gradients at both surfaces. This permits to calculate the heat flux that is released from the leaf replica by heat transfer. The difference of this quantity with the total radiative heat flux leads to the heat removed by the evaporation of water. Formally, this leads to the following description obtained from a global enthalpy balance at steady state:

$$\phi_{up}^{rad} = -\phi_{up}^{T} + \phi_{low}^{T} + \phi_{low}^{M} \qquad \textit{Eq. 72}$$

In the previous equation ϕ_{up}^{T} has negative values considering the orientation of the z-axis. ϕ_{up}^{rad}, ϕ_{low}^{T} and ϕ_{low}^{M} have positive values. The next steps require to link the mass flux of evaporated water to enthalpy flux ϕ_{low}^{M}.

The vaporization enthalpy of water (latent heat) at 20°C is $L^V = 2454\ kJ\ kg^{-1}$ (Cox et al., 1989). The convective flux of water vapor at the lower surface (mass flux) is noted w $(kg\ m^{-2}s^{-1})$ such as:

$$\phi_{low}^{M} = 2.454\ 10^{6}\ w \qquad \textit{Eq. 73}$$

The mass flux is now determined by the convective transport model previously established for heat transfer, considering the Schmidt number instead of the Prandtl number (Eq. 47). As

previously mentioned, the determination of the density gradients at the surfaces is required for assessing gravity influence. This is done with the following sequence of calculation. The saturation vapor pressure is given by Antoine empirical law (Reid et al., 1977).

$$\ln P^0(T) = 23.1961 - \frac{3816.44}{T - 46.13} \qquad T\ (\mathrm{K});\ P^0\ (\mathrm{Pa}) \qquad \textit{Eq. 74}$$

The water partial pressure in the bulk is given by:

$$p_{w\_bulk} = \mathcal{H}_{bulk}\, P^0(T_{bulk})$$

The water partial pressure at the lower surface of the leaf replica is given by:

$$p_{w\_low} = P^0(T_{low}) \qquad \textit{Eq. 75}$$

The mass concentrations (kg m^{-3}) difference between the bulk liquid and the evaporating surface is given by:

$$C_{w\_low} - C_{w_{bulk}} = \left(\frac{P^0(T_{low})}{T_{low}} - \frac{\mathcal{H}_{bulk}\, P^0(T_{bulk})}{T_{bulk}}\right)\frac{M_w}{R} \qquad \textit{Eq. 76}$$

Combining Eq. 72 and Eq. 76 leads to:

$$k\, L^V \left(\frac{P^0(T_{low})}{T_{low}} - \frac{\mathcal{H}_{bulk}\, P^0(T_{bulk})}{T_{bulk}}\right)\frac{M_w}{R} = \phi_{up}^{rad} - \phi_{low}^{T} + \phi_{up}^{T} \qquad \textit{Eq. 77}$$

k is the mass transfer coefficient (m s^{-1}). This coefficient is the total leaf conductance g_{tw} for water vapor (Lehmann and Or, 2015; Schymanski et al., 2017). This notation will be used later with a complete and accurate definition.

The objective is to calculate the coefficient k from the experimental results obtained for the evaporating leaf replica by applying the global enthalpy balance (Eq. 72), provided that the two heat fluxes ϕ_{low}^{T} and ϕ_{up}^{T} are calculated by the model developed in the previous section. As this calculation is based on the ratio of two differences (difference of heat fluxes and difference of water vapor concentration - Eq. 76).

It has been previously observed that the density gradient across the BL is an important variable for assessing the heat transfer coefficients and the heat transfer fluxes at upper and lower surfaces. As the composition of vapor phase is no longer homogeneous at the lower surface. The density of vapor phase varies with its composition i.e., with the water partial pressure. This must be taken into account. Let Δp_w the water partial pressure difference between lower phase and the bulk:

$$\Delta p_w = P^0(T_{low}) - \mathcal{H}_{bulk}\, P^0(T_{bulk}) = p_{w\_low} - p_{w\_bulk}$$

The molar mass M is affected by vapor phase composition, such as:

$$y_w = \frac{p_w}{p_T} \qquad M = 28.98\left(1 - y_w\right) + 18\, y_w$$

y_w is the water vapor mole fraction. The total pressure is identical throughout the gas phase between the evaporating surface (at the level of the ore) and the bulk.

$$p_{T\_low} = p_{T\_bulk}$$

This set of three relations leads to compute the density difference at lower surface of the leaf replica:

$$\Delta\rho_{low} = \rho_{low} - \rho_{bulk} = \frac{1}{R}\left(\frac{p_{T\_low} M_{low}}{T_{low}} - \frac{p_{T\_bulk} M_{bulk}}{T_{bulk}}\right) \qquad \textit{Eq. 78}$$

This difference is calculated without any difficulty with the previous set of relations. It must be noticed that the density difference is simultaneously affected by the temperatures at lower surface and in the bulk and by the molar mass of the gas, which is also depending on temperature and humidity. At the upper surface, there is no change compared to the previous analysis for non-evaporating leaf replica.

$$\Delta\rho_{up} = \rho_{bulk} - \rho_{up} = \frac{p_{T\_bulk} M_{bulk}}{R}\left(\frac{1}{T_{bulk}} - \frac{1}{T_{up}}\right) \qquad \textit{Eq. 79}$$

6.4.2 Exploitation of the results for units 3 and 4

Using the results obtained for the two evaporating units (units 3 and 4), the first observation is that the density differences are still of the same order of magnitude as for non-evaporating leaf replica. Importantly, it is observed that these density differences remain negative at the lower surface, whatever the conditions, accounting for measured temperature and water partial pressure differences (Eq. 78). The absolute values of these density differences are in the range of 2 % of the density of the bulk as previously for units 1 and 2. The consequence is that the convective heat and mass transfer fluxes are in the same range. Their ratios are similar to those represented in Figure 6-10 and Figure 6-11. However, their exact values are different due to the fact that the temperature differences between the surfaces and the bulk are significantly lower for evaporating leaf replica than for non-evaporating ones.

Applying the established correlation for calculating the heat transfer coefficients on the two surfaces and using the measured temperatures differences, the heat fluxes ϕ_{up}^{T} and ϕ_{low}^{T} are determined. Using the global heat transfer balance (Eq. 72) the heat flux transported by evaporation of water ϕ_{low}^{M} is determined. The results are reported in

Figure 6-12. It is observed that the heat transfer by water evaporation represents from 35 up to 65 % of total energy flux, respectively. The ratio between the heat transfer transported at the lower and at the upper surfaces varies as previously observed. The main observation is that, even if it significantly varies with the external conditions (air velocity and angle) ϕ_{low}^{M} represents the major contribution to heat transfer of the leaf replica.

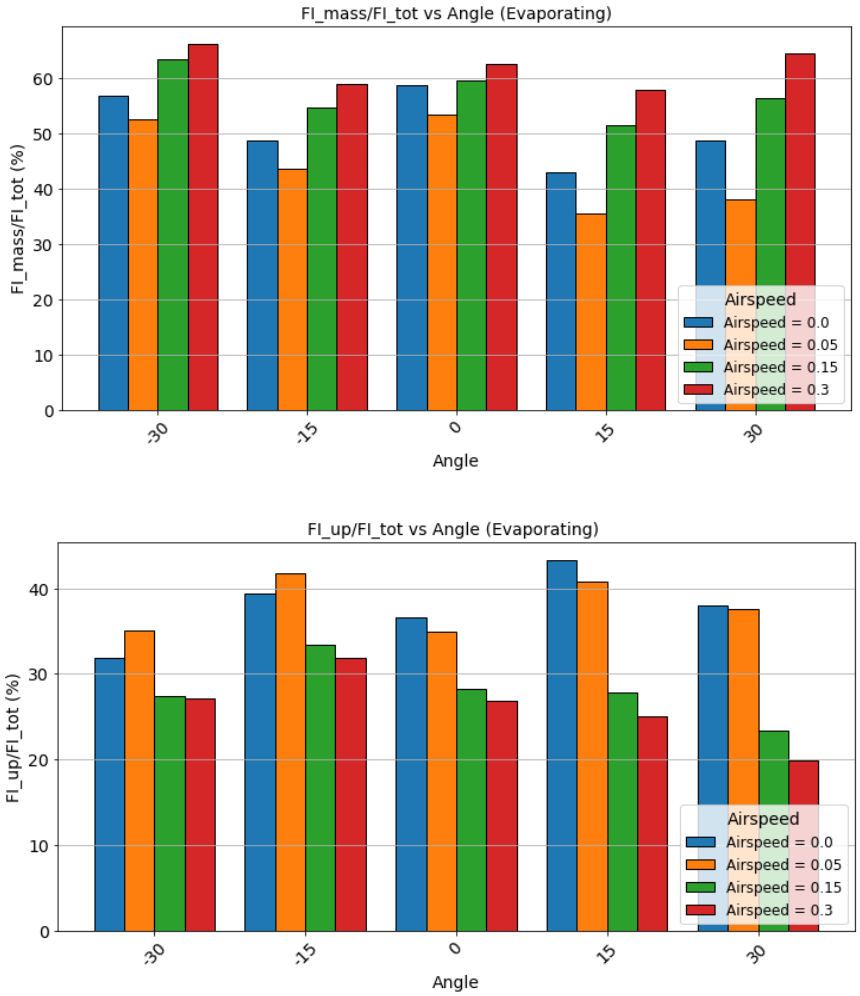

Figure 6-12: *Ratios of heat transfer fluxes (% of total heat flux transported) transported by evaporation of water (up) and on the upper surface by heat transfer (below). The complement is the flux transported at the lower surface.*

Using the calculated heat flux transported by water evaporation, the mass flux (w) is determined (Eq. 73) as a function of the operating conditions. The results are shown in Figure 6-13. Average values for all temperatures for units 3 and 4 (with the evaporating leaf replica inside) are reported. Consistently with the previous results, the water flux varies nearly by a factor of 2, ranging between 25 and 45 mg m^{-2} s^{-1} when modifying the experimental conditions. It is also noted that the values of mass flux slightly vary with the bulk temperature. This indicates that the mass transfer is significantly affected by all external conditions: air velocity, inclination angle, bulk humidity and bulk temperature.

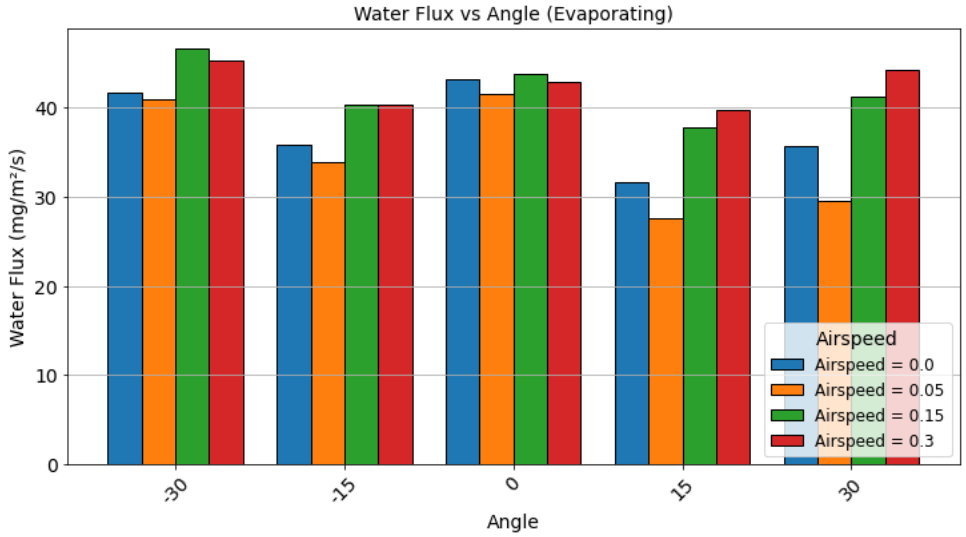

***Figure 6-13**: Determination of water mass flux (mg m^{-2} s^{-1}) evaporated at the lower surface of the leaf replica*

From Eq. 77, the mass transfer coefficient k is calculated. The values are compared with the mass transfer coefficient related to the gas boundary layer k_{BL} obtained from the correlation at lower surface.

$$k_{BL} = \mathcal{D}\, Sc^{1/3} \left(\frac{C_1}{x} Re_{\parallel x}^{1/2} \pm \frac{C_2}{x} Re_{\perp x}^{1/2} + \frac{C_5}{x} Gr_{\perp x}^{1/4} + \frac{C_4}{x'} Gr_{\parallel x'}^{1/4} \right)$$

The values of the constants are given in Table 6-8. The sign of the second term is defined for the lower surface: $C_2 > 0$ when $\theta > 0$.

The values of the two transfer coefficients k_{BL} and k are reported and compared in Figure 6-14. The values of k_{BL} are in the range $5\ 10^{-3} - 2\ 10^{-2}$ m s^{-1}. They are quite different from the values of k ($2\ 10^{-3}$ m s^{-1} at maximum). The values of the two transfer coefficients also seem to be mostly uncorrelated. The ratio of k_{BL} over k varies between 2 and 15 without

showing any apparent trend. This is explained by the fact that the resistance to mass transfer is a combination of a mass transfer resistance in the BL, characterised by the conductance of the BL k_{BL}, and a mass transfer resistance in the leaf replica itself. The overall conductance is characterised by k. In other words, these results show that the transfer resistance is mostly located inside the leaf replica. This is a result obtained by all authors (Poulet et al., 2020; Schymanski et al., 2017) working both on real plants and on leaf replicas. The proportion that is estimated from these results is also in a classical range, with 80 % of the average total resistance to mass transfer being located in the leaf replica by itself.

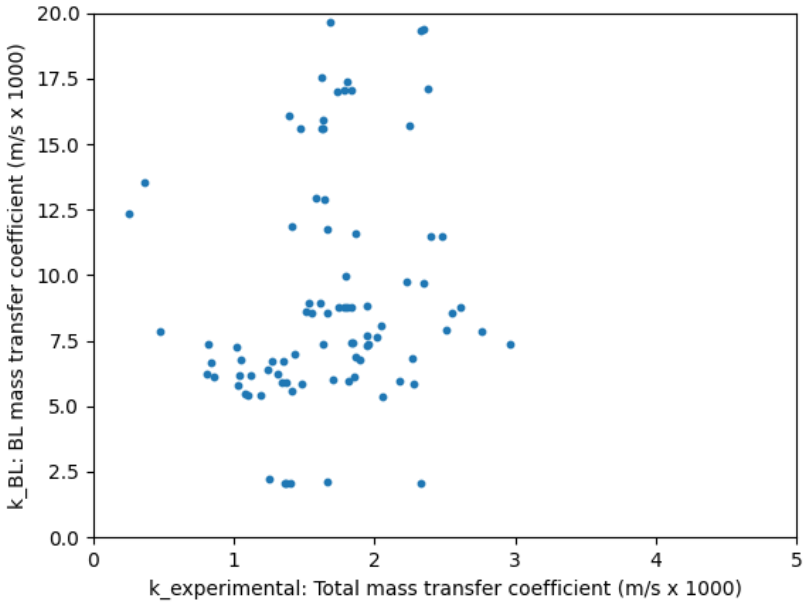

Figure 6-14 *Calculated BL mass transfer coefficient versus total mass transfer coefficient obtained from experimental values calculated with global heat balance with* ***Eq. 77***

6.4.3 Modelling of internal transfer resistance in the leaf replica

Of course, if it is required to predictively determine the surface temperatures when changing the external conditions, including gravity, it is necessary to include the prediction of the leaf replica resistance. Without this information, the resolution cannot proceed except if we adopt an empirical correlation of the leaf replica resistance.

Therefore, it is necessary to go in a deeper comprehensive model for the mass transfer resistance inside the pores of the leaf replica. Several studies have quantified the stomatal clustering effects on leaf gaseous diffusive conductance considering stomatal spacing and

stomatal depth (Lehmann and Or, 2015). This has also been applied to leaf replicas (Schymanski et al., 2017).

The basic approach is to consider that the mass transfer resistances of the leaf replica operate in series. The mass transfer resistance of the leaf replica has two components: one is related to the diffusion in the pore by itself $\mathcal{R}_{pore}$ and the other one represents the additional resistance due to spreading of the water vapor jet in the fluid boundary layer $\mathcal{R}_{end}$. Both resistances are multiplied by the ratio of the section of the pore to the total surface.

$L, d, l_0, n, \varepsilon$ are respectively the dimension of spacing between perforated pores, the diameter of the pore, the depth of the pore, the number of pores per unit surface and the fraction of surface of pores per unit of surface of the leaf replica. These parameters define the characteristics of the perforated aluminium foil and the pores. These values have been used for calculating the leaf replica conductance given in Table 4-3 (Used equations are described in Appendix C). These parameters are linked by the following relations; for the leaf replicas that have been used in this study, (Schymanski et al., 2017)

$$L = 380\ \mu\text{m} \qquad d = 50\ \mu\text{m}, \qquad l_0 = 30\ \mu\text{m}$$

$$n = \frac{1}{L^2} = 6.93\ 10^6\ \text{pores m}^{-2} \qquad \epsilon = \frac{\pi\ d^2}{4\ L^2} = 0.0136$$

At the scale of one pore, the resistance to diffusion is given by:

$$\mathcal{R}_{single\ pore} = \frac{l_0}{\mathcal{D}}$$

The model of resistance at the output of the pore (and entrance into the BL) was reviewed by (Lehmann and Or, 2015). Considering that the pores are sufficiently spaced, the diffusive resistance of interacting vapor shells can be neglected, so that:

$$\mathcal{R}_{single\ end} = \frac{\pi\ d}{8\ \mathcal{D}}$$

The pores are acting in parallel so that the lumped resistance for the leaf replica is then:

$$\mathcal{R}_{LR} = \frac{\mathcal{R}_{single\ pore} + \mathcal{R}_{single\ end}}{\varepsilon} = \frac{1}{\varepsilon\ \mathcal{D}}\left(l_0 + \frac{\pi\ d}{8}\right) \qquad \textit{Eq. 80}$$

The latter relation is obtained considering the flux through a unit surface S is related to the flux issued from the pores through their surface s by a global mass balance, such as:

$$\phi\, S = \phi_{single}\, s_{single}$$

The definition of the void fraction is:

$$\varepsilon = \frac{s_{single}}{S} = \frac{\phi}{\phi_{single}}$$

On the other hand, the fluxes are driven by the same potential difference, such as:

$$\mathcal{R}\, \phi = \mathcal{R}_{single} \phi_{single}$$

This demonstrates the following generic relation between the total resistance and the resistance in a single pore:

$$\mathcal{R} = \frac{\mathcal{R}_{single}}{\varepsilon}$$

The total resistance includes the resistance due to the boundary layer. The total resistance is the inverse of the mass transfer coefficient calculated for the BL. The total transfer coefficient is the inverse of the total resistance:

$$\mathcal{R}_{BL} = \frac{1}{k_{BL}}$$

$$\mathcal{R}_{Total} = \mathcal{R}_{BL} + \frac{\mathcal{R}_{single\ pore} + \mathcal{R}_{single\ end}}{\varepsilon} \qquad k_{Total} = \frac{1}{\mathcal{R}_{Total}} \qquad \textit{Eq. 81}$$

The values for k_{Total} obtained by this model are compared with the calculation of k obtained from the experimental values by Eq. 77. The results are reported in Figure 6-15.

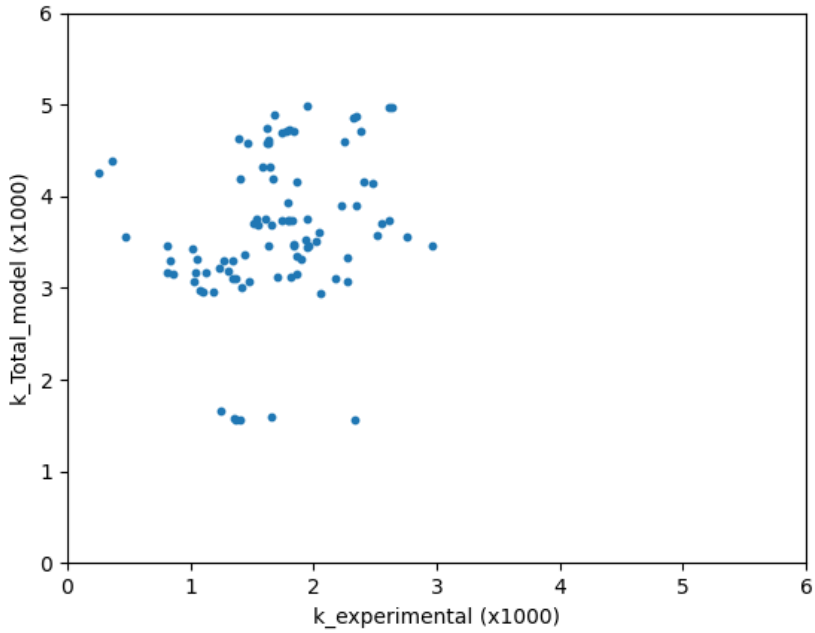

***Figure 6-15**: Calculated total mass transfer coefficient obtained for the model (Eq. 80 and Eq. 81) versus total mass transfer coefficient calculated with enthalpy balance with (Eq. 77).*

Compared to the previous results (Figure 6-14), the results obtained by the model defined by Eq. 81, which incorporates both leaf replica and BL resistances gives a better order of magnitude with the experimental values. This indicates that the leaf replica resistance has been reasonably well approached and that it plays an important role in the control of the evaporation process. The values of the conductance obtained by the physical model are, on average 1.7 – 2.5 times higher than the experimental ones, requiring further developments for a more accurate assessment of leaf replica resistance.

It is possible to adapt the resistance at the end of the pore $\mathcal{R}_{\mathrm{end}}$. Some authors (De Boer et al., 2011; Dow et al., 2014) have proposed to modify the coefficient $\frac{\pi\, d}{8}$ by $\frac{d}{2}$ in Eq. 80. Such a modification slightly improves the consistency between experimental and model values, with model conductance values that are still 40 – 60 % higher than the experimental ones. It remains possible to identify this coefficient for obtaining an improved adequacy, but it is observed that the dispersion of the results is not reduced. It is always possible to identify the best coefficient for matching the calculation of the average total conductance with the values obtained from the global enthalpy balance. But the standard deviation remains high.

6.4.4 Improvement of the mass transfer model: importance of capillarity effects

In order to complete the investigation of the possible controlling physical phenomena, the influence of capillarity needs to be investigated for correlating stomata conductance.

Apparently, this is not currently done for explaining the regulation of water evaporation by higher plants. But for a leaf replica with a well-defined pore geometry, an analysis of the influence of surface tension forces becomes more accurate for obtaining quantitative results than with a real plant leaf with a variable stomata distribution.

The first thing to consider is the equilibrium of the gas and liquid pressures inside the pores. The total hydrostatic pressures are schemed in Figure 6-16.

The main point to consider is that the forces on both sides of the gas-liquid interface must be equal, so that $F_L = F_G$. By definition, the system is evaporating with a flux of water molecules through the interface from the liquid to the gas phase. The situation is identical to what happens when a liquid droplet evaporates in a surrounding gas. In that case, it is known that the droplet is spherical with the concavity towards the liquid phase. The equality of the forces at dynamic equilibrium must be satisfied. σ being the surface tension of the liquid, r the curvature of the interface, $p_{droplet}$ and p_G the pressures in the liquid droplet and in the gas phase respectively, the equilibrium of forces expressed in terms of pressures are given by:

$$p_{droplet} - p_G = \frac{2\,\sigma}{r}$$

In the case of a pore, the water flow through the interface imposes the interface is bloated in the direction of the gas phase, so that the previous relation becomes:

$$p_L - p_G = \frac{\sigma}{d}$$

p_L is the pressure in the liquid into the pore of diameter d. This means that there is a discontinuity in static pressure along the streamline between p_L and p_G through the interface. When there is a flow of water through the interface due to evaporation, the interface is concave at the liquid side. This is due to superficial tension that acts as a cohesive force between the liquid molecules. This force is balanced by the evaporation flux.

The second point to consider is that the pressure in the liquid must be equal to the pressure in water reservoir p_0 , in order for the liquid inside the pore to stay in hydrostatic equilibrium with the reservoir:

$$p_L = p_0$$

This situation is similar to that used for the demonstration of Jurin's law. There is one common point: the total pressure into the liquid must be identical between the reservoir and the pore at the same height. But there are two important differences: *i)* there is no gravity effect, neither in the liquid nor in the gas phase, the terms $\rho g h$ being negligible compared to the other forces; *ii)* the interface curvature is reversed due to the water flow between liquid and gas phases (concavity towards liquid, convexity towards gas), so that the differences of pressures between liquid and gas are inversed.

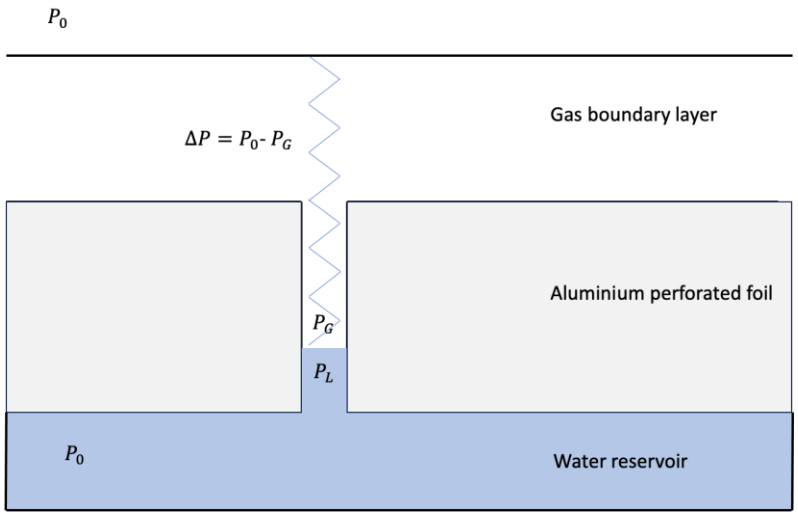

***Figure 6-16**: Scheme of pressure distribution inside the pore and equilibrium with external pressure*

The consequence is that the pressure in the gas phase, behind the interface is equal to:

$$p_G = p_0 - \frac{\sigma}{d}$$

As the pressure in the bulk is identical to the pressure in the water reservoir p_0 there is a pressure drop in the gas phase between the pressure at the interface and the pressure in the bulk. There is no exchange of dry air between the bulk phase and the water reservoir. Therefore, the partial pressure of dry air remains constant throughout the system. Then, the only solution is that the partial pressure of water at the interface during water evaporation is decreased and equal to:

$$p_w = P^0(T_{low}) - \frac{\sigma}{d}$$

The consequence is that the difference of mass exchange potential between liquid and gas phase is modified. This leads to a new definition of total leaf conductance calculated from the experimental results. It must be rewritten as follows:

$$g_{tw}\, L^V \left(\frac{P^0(T_{low}) - \frac{\sigma}{d}}{T_{low}} - \frac{\mathcal{H}_{bulk}\, P^0(T_{bulk})}{T_{bulk}} \right) \frac{M_w}{R} = \phi_{up}^{rad} - \phi_{low}^{T} + \phi_{up}^{T} \qquad \textit{Eq. 82}$$

Here the usual notation g_{tw} for the total leaf replica conductance was used, including the resistances in series of BL and leaf replica, instead of the previous notation k for the total mass transfer coefficient. Eq. 82 makes a significant modification compared to Eq. 77: the capillary contribution for $\sigma = 72\ 10^{-3}\ Pa\ m;\ d = 50\ \mu m$ is in the order of 1400 Pa whereas the difference between water partial pressure at the interface and the partial pressure in the bulk is in the order of 1700 Pa for a relative humidity of 50 % for 3°difference.

From the experimental values that have been obtained, the calculated values of g_{tw} (Eq. 82) are reported versus the water flux in Figure 6-17.

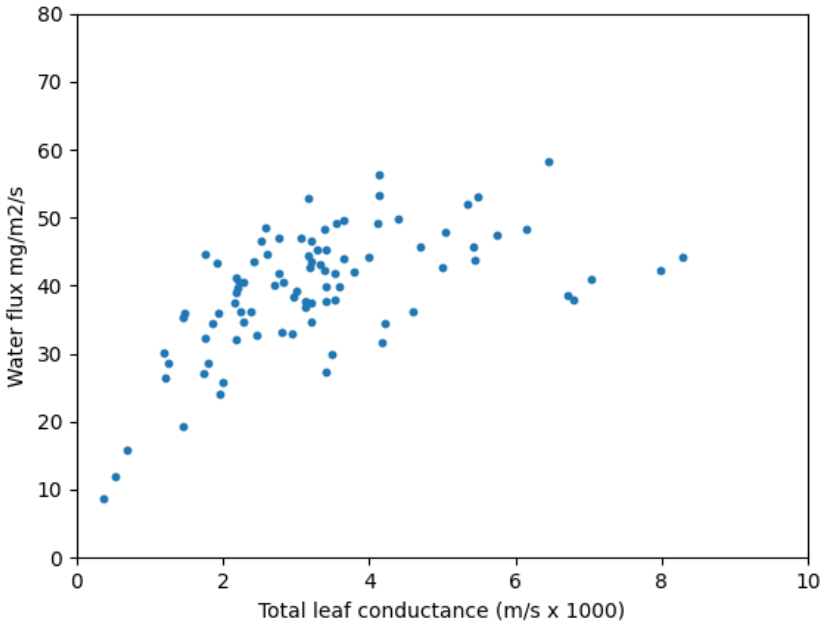

Figure 6-17: *Experimental leaf conductance g_{tw} versus water flux for the evaporating leaf replica*

The first observation is that the calculated total leaf replica conductance is almost twice the previous heat transfer coefficient (Figure 6-15). This is consistent with the fact the calculated

potential of exchange that represents the true driving force for the diffusion process is now almost two times less than before.

The other observation is that the water flux has a tendency to reach a plateau phase (about 40 – 60 mg m^{-2} s^{-1}) whatever the leaf conductance. This clearly indicates that the rate limiting process is not uniquely linked to transfer coefficients.

In order to get an insight into this, we consider that the difference of pressure between the water interface inside the pore and the pressure in the bulk (Figure 6-16). This means that the pressure depression inside the pore, is linked to an aspiration process through the pore and the boundary layer.

This aspiration is most likely due to the water flux or more exactly to the airflow far from the surface of the leaf replica toward the bulk. To quantify this pressure depression, the perforated foil is considered as a porous media. The pressure drop across a porous bed of particles is classically correlated with Blake - Kozeny equation for laminar regime (Beek et al., 2000a; Ozgumus et al., 2014):

$$\frac{\Delta p}{l} = K\ \rho\ \nu\ S^2\ \frac{(1-\varepsilon)^2}{\epsilon^3}\ v_\infty$$

Δp is the pressure drop, l is the length of the bed, v_∞ is the superficial velocity (external to the bed of particles), ε is the void fraction, S is the specific surface of the particles in the bed, ρ and ν are the density and the kinematic viscosity of the fluid and K is the Kozeny constant.

To represent the pressure drop, we adopt a procedure for correlating pressure drop throughout a packed bed (Bird et al., 2007). According to Hagen-Poiseuille law, in laminar flow, the pressure drop through a fixed bed of thickness l_0 is given by:

$$v = \frac{\Delta p}{2\ \rho\ \upsilon\ l_0}\ R_h^2$$

The hydraulic radius R_h is expressed in terms of void fraction (Bird et al., 2007). For cylindrical pores of diameter d, the hydraulic radius is:

$$R_h = \frac{Volume\ available\ for\ flow}{Total\ wetted\ surface}$$

For one pore, the volume available for flow is:

$$\pi \frac{d^2}{4}\, l_0$$

The total wetted surface is the external surface of the plate in contact with the gas in the bulk. Considering L is the length characterising the spacing between the pores, this wetted surface for one pore is:

$$(1-\varepsilon)\, L^2$$

Using the definition of void fraction, the hydraulic radius is then:

$$R_h = \frac{\varepsilon}{1-\varepsilon}\, l_0$$

The superficial velocity (velocity far from the plate) this leads to:

$$v_\infty = \varepsilon\, v = \frac{\Delta p}{2\,\rho\, \upsilon}\, \frac{\epsilon^3}{(1-\varepsilon)^2}\, l_0$$

This expression has the same form as the Blake – Kozeny equation. Here, the constant and the expression of the specific surface are determined by the previous theoretical developments. Assuming that the pressure drop is equal to the depression value inside the pore (Figure 6-16), this velocity is equal to:

$$v_\infty = \frac{\sigma}{2}\, \frac{l_0}{d}\, \frac{1}{\rho_{bulk}\, \upsilon}\, \frac{\epsilon^3}{(1-\varepsilon)^2} \qquad \textit{Eq. 83}$$

Eq. 83 shows that the superficial velocity far from the plate can be considered as a function of the geometry of the porous media and of the properties the fluid only. When considering the characteristics of the pores and the griding of the leaf replica ($d = 50\ \mu m$, $l_0 = 30\ \mu m$, $\varepsilon = 0.0136$), Eq. 83 leads to $v_\infty = 3.4\ 10^{-3}\ m\ s^{-1}$. The water flux is given by:

$$w = v_\infty\, \rho_{bulk}\, y_w\, \frac{18}{M} = \frac{\sigma}{2}\, \frac{l_0}{d}\, \frac{y_w}{\upsilon}\, \frac{18}{M}\, \frac{\epsilon^3}{(1-\varepsilon)^2}$$

Taking the average of experimental values of molar fractions, this leads to the order of magnitude of the mass flux of water out of the pores into the vapor phase:

$$w = 59\ mg\ m^{-2}\ s^{-1}$$

This theoretical value is in excellent agreement with the maximum values obtained from the enthalpy balance, which considers the heat removed by evaporation of water (Figure 6-17). Therefore, this way of reasoning with a hydrodynamic approach seems to correctly predict

the water vapor mass flow. It is consistent with the enthalpy balance. It must be outlined that this model only uses the geometrical characteristics of the pores and their distribution, that is the void fraction. It must be mentioned that the diameter of the pore has a huge influence on the result. Since the void fraction is proportional to d^2, the velocity is proportional to d^5. Two additional remarks must be done:

- When the mass flux calculated from the enthalpy balance is lower than the value obtained from the hydrodynamic model, this means that the pore is not completely filled with the gas mixture of gas (air and water vapor). Some liquid water remains at the bottom of the pore, the length of diffusion being shorter than l_0. Therefore, it must be kept in mind that Eq. 83 gives a maximum mass flux of water. In other words, the total mass flux of water obtained from the enthalpic balance finally leads to determine the length of diffusion l.
- Of course, the mass transfer flux predicted from the leaf conductance (Eq. 82) remains a valid description. This is even the driving phenomena. The question is now to develop a physical model of total leaf conductance in accordance with the previous findings.

After the estimation of the heat released through evaporation of water by the enthalpy balance, the degree of filling of the pore, i.e., the length l of diffusion of water vapor into the pore was calculated with Eq. 83. Considering that the pore is in reality conical, the average values of ϵ and ϵ^3 have been considered. The maximum diameter of the pore at the surface of leaf replica is $d_{max} = 55\ \mu m$. The minimum diameter at the bottom of the pore is $d_{min} = 43\ \mu m$ (Table 4-2). The results are represented in Figure 6-18. It is noticed that the degree of filling is highly variable depending on the external conditions. Noticeably, none of the predicted calculated values seem aberrant, the maximum values never exceed $27\ \mu m$ which is consistent with a maximum length of the pore $l_0 = 30\ \mu m$.

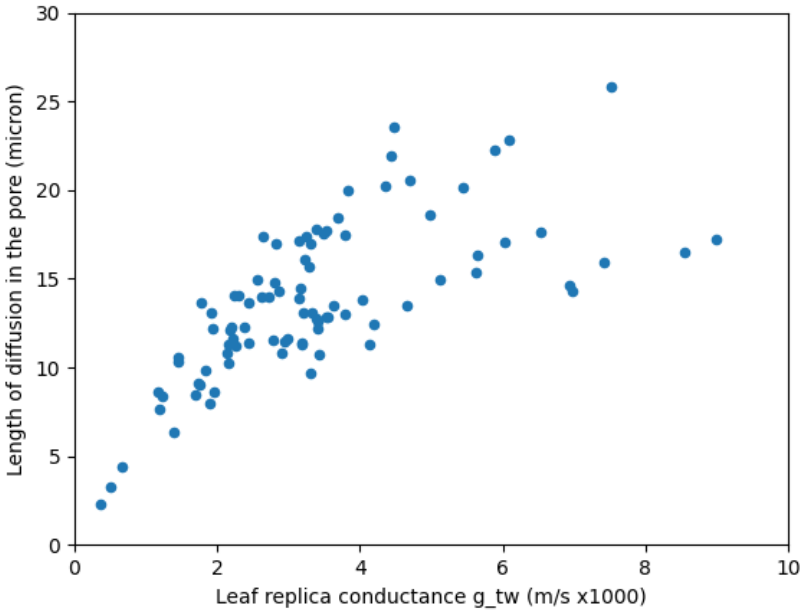

***Figure 6-18**: Length of the gas diffusion path inside of the pore calculated by Eq. 84.*

Therefore, the velocity in the bulk is now given by:

$$v_{bulk} = \frac{\sigma}{2}\frac{l}{d}\frac{1}{\rho_{bulk}\,v}\frac{\epsilon^3}{(1-\varepsilon)^2} \qquad \textit{Eq. 84}$$

In order to get a complete description of water evaporation, the last thing remains to address the modelling of lumped resistances of the leaf replica by itself. As previously mentioned, the total transfer resistance is composed of 3 terms. The pore resistance must now be considered acting on length l instead of l_0. Furthermore, applying Fick's law of diffusion, the apparent transfer resistance must be corrected by the convective term due to the migration of water molecules inside the pore by convective transfer:

$$\frac{1}{\mathcal{R}_{single\ pore}} = \frac{\mathcal{D}}{l} + \frac{v_{bulk}}{\varepsilon} \qquad \textit{Eq. 85}$$

The addition of the resistances of pores in parallel leads to the lumped resistance of the pores:

$$\frac{1}{\mathcal{R}_{pores}} = \frac{\varepsilon\,\mathcal{D}}{l} + v_{bulk} \qquad \textit{Eq. 86}$$

The calculation shows that the second term of right-hand side represents less than 10% of the final resistance. In any case, the replacement of the total depth of the pore l_0 by the actual length of diffusion l strongly decreases the total resistance of the pore.

The BL resistance is also slightly modified accounting for v_{bulk}.

$$\frac{1}{\mathcal{R}_{BL}} = k_{BL} + v_{bulk} \qquad \textit{Eq. 87}$$

The resistance at the output of the pore and before the entrance in the boundary layer $\mathcal{R}_{end}$ characterises the transition zone where the flows issued from the pores are mixed together and diluted inside the boundary layer. This transition zone is a progressive transformation of the addition of transfer resistances in parallel to the zone where resistances are added in series, i.e., the beginning of the boundary layer. An intuitive way of reasoning is to consider that after the output of the pore the vapor flow follows a cone up to the distance where the cones issued from the different pore are joining. As free diffusion phenomena dominate, the angle of the cone is 45°. This means that the cones overlap when the distance from the surface is $L/2$, L being the spacing between the pores. Because the output diameter of the pore is d_{max} this overlapping represents the minimal distance required to get a homogenous water partial pressure in the gas phase. The mass transfer resistance corresponding to the free diffusion cone into the gas phase is then given similarly to Eq. 85:

$$\frac{1}{\mathcal{R}_{single\ cone}} = \frac{2\,\mathcal{D}}{L} + \frac{v_{bulk}}{\varepsilon} \qquad \textit{Eq. 88}$$

As previously, the sum for all cones in parallel leads to:

$$\frac{1}{\mathcal{R}_{cones}} = \frac{2\,\epsilon\,\mathcal{D}}{L} + v_{bulk} \qquad \textit{Eq. 89}$$

An efficient way to proceed with the integration of diffusion law in conical geometry is to consider that the diffusion in the transition zone is the result of two processes in series. The first one is the diffusion in a virtual tube of a diameter equal to the diameter of the pore d_{max} from the surface of the leaf replica up to the end of the diffusion cone (length $L/2$). The second one is the dilution of the flow at the output of the diffusion cone from the diameter of the virtual tube d_{max} up to the diameter of the diffusion cone (diameter L). This leads to the expression of the transfer resistance relative to the transition zone:

$$\mathcal{R}_{end} = \frac{-L}{2\,\varepsilon\,\mathcal{D}} + \frac{\sqrt{2}}{v_{bulk}} \qquad \textit{Eq. 90}$$

The factor $\sqrt{2}$ comes from the calculation of the average upwards velocity in the diffusion cone of the transition zone. The comparison between experimental values and the prediction of $\mathcal{R}_{end}$ calculated with Eq. 90 is represented in Figure 6-19. The experimental values are

obtained by subtracting the resistance of the boundary layer and of the pores to the total resistance calculated from the enthalpy balance.

The fit between the two approaches is very satisfactory considering, on the one hand, that the model is totally predictive and, on the other hand, that the experimental points that lead to the estimation of $\mathcal{R}_{end}$ are the result of ratios of two differences of measured variables (Eq. 82).

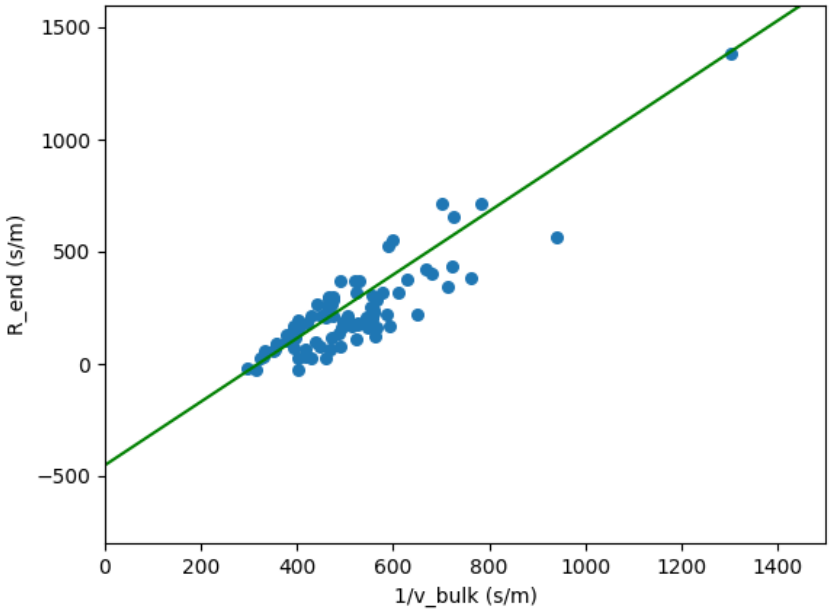

***Figure 6-19**: Comparison between experimental values of the mass transfer resistance in the transition zone and the prediction by Eq. 90*

The leaf replica conductance is calculated by Eq. 86 and Eq. 90, with the actual diffusion length inside the pore calculated by Eq. 84. This is an important information from the model, leading to a better representation of the physical processes involved. This physical model predicts a strong dependence on the geometric characteristics of the leaf replica, including the diameter of the pore and the spacing between the pores. Also, it must be noted that the conductance of the leaf replica by itself depends on its geometrical characteristics d, l_0, L and on the transfer intensity through the value of the water molecules velocity v_{bulk}, such as the higher the velocity, the lower the resistance and the higher the leaf replica's conductance.

The total conductance of the mass boundary layer is then calculated with the same approach as for heat transfer resistance introducing a small correction for the vapor water flow (Eq. 87). The inverse of the total leaf replica conductance is given by addition of the three transfer resistances (boundary layer, pores, end of the pores):

$$\frac{1}{g_{tw}} = \frac{1}{k_{BL} + v_{bulk}} + \mathcal{R}_{pores} + \mathcal{R}_{end} \qquad \textit{Eq. 91}$$

The comparison between the values of g_{tw} obtained by the enthalpy balance (Eq. 82) and with the previous theoretical model (Eq. 91) is given in Figure 6-20. All the experimental results for units 3 and 4 are joined, with variable air velocities, variable bulk temperature, variable humidity and variable orientation of the leaf replica.

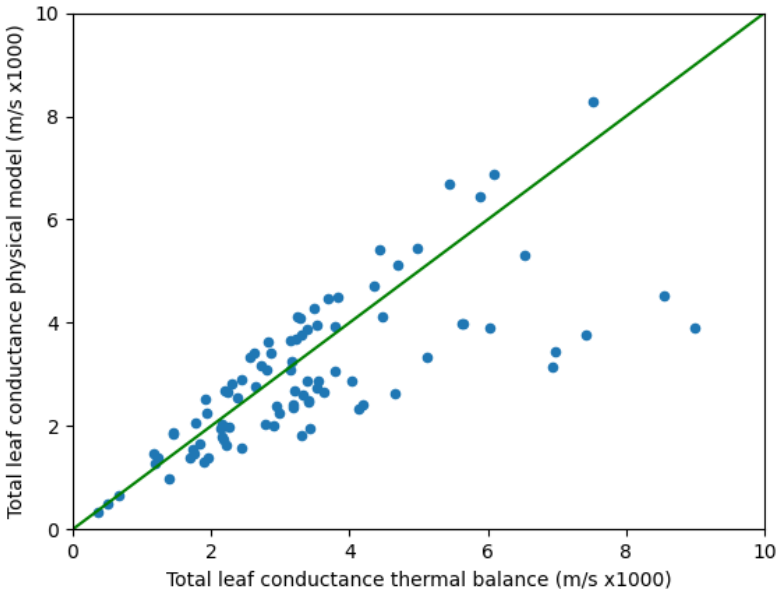

Figure 6-20: *Comparison between the predicted values of the total leaf conductance obtained by the physical model (Eq. 91) and the values obtained by the enthalpy balance model (Eq. 82).*

Although there is still a relative dispersion of the points, the adequacy is considered as fairly good. Prior to introduce surface tension effects, the former comparisons of transfer coefficients between model and experimental results were in a ratio 2 to 10 (Figure 6-14 and Figure 6-15). At least, this proves that the proposed approach, including capillarity and surface tension forces, cannot be discarded and should be continued in order to improve the model and the understanding of the physical phenomena controlling the process of evaporation.

6.4.5 Discussion on the mass transfer model

The approach followed here should be confirmed with other data obtained on other leaf replicas, by example modifying pores dimension and spacing in order to improve the prediction. Since the physical and geometric characteristics of the leaf replica were precisely defined and realized with the leaf replica used in this studies, it was possible to develop a

complete physical approach with reasonable predictions. The introduction of surface tension force balances into the model makes it possible to clarify certain points, such as the pore filling length or the fact that evaporation velocities reach a limit. By coupling with a diffusion model, it is thus possible to theoretically go back to the conductances. The final result is in good agreement with the enthalpy balance calculations. This seems to confirm that the model is robust. However, this requires further experimental confirmations.

It should be noted that the prediction results are highly sensitive to pore size and spacing: changes of 2 μm in pore diameter or 5 μm in pore spacing induce changes of more than 20% in conductances.

Finally, for the present study, it is important to outline that there is no influence of gravity on the conductance of the leaf replica itself. The only influence is on the boundary layer and it remains similar to the influence on heat transfer. This is probably one of the reasons why higher plants grow relatively well in space, their fundamental metabolic regulation of leaves temperature are marginally impacted by zero-gravity conditions, except when the gas boundary layer plays a significant role. This happens when the air velocity is too low. In that case, the BL resistance becomes important, impacting the global mass transfer performance.

6.5 Heat and mass transfer in transient parabolic experiments

6.5.1 Overview of experimental results obtained during parabolic flight

As previously presented, the thermal response for the upper and lower surfaces as well as the internal temperature of the leaf replica for non-evaporating leaf replica were almost linear (**Error! Reference source not found.**). An important observation is that the evolutions between the temperature on the upper and lower surface and in the median thermocouple are almost parallel (**Error! Reference source not found.**). Additionally, the effect of air velocity drastically reduces the increase of the temperatures. Considering the heat transfer model, this is a normal behaviour because in microgravity the gravity driven contribution is supressed, letting the heat exchange only driven by friction (Figure 6-11). For evaporating leaf replicas, the effects of

transient microgravity are less marked involving a complex behaviour when varying the air velocity and inclination angle.

The measurements of the slopes have been averaged for identical conditions. The results are reported in Figure 6-21 for non-evaporating horizontal leaf replicas (units 1 and 2) and in Figure 6-22 for evaporating horizontal leaf replicas (units 3 and 4).

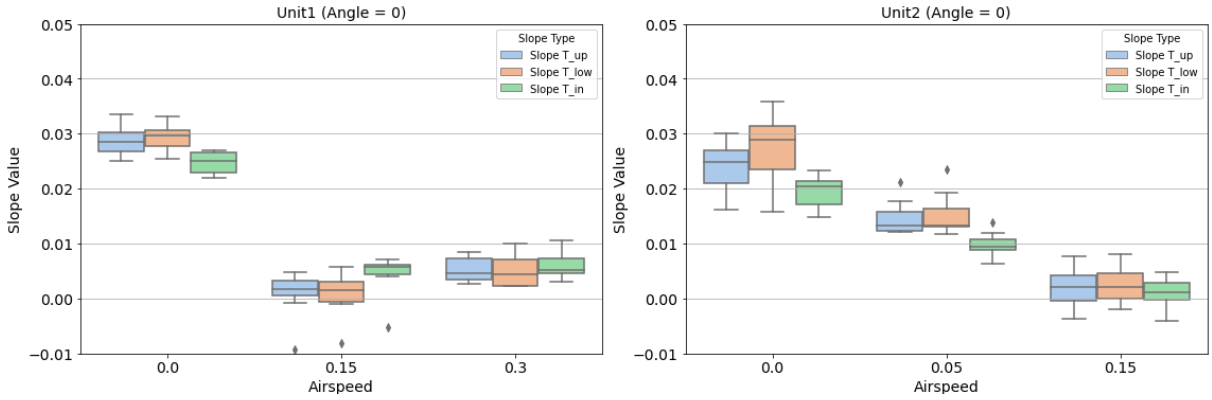

Figure 6-21: *Slopes of temperatures evolution during the 20 s parabolas: horizontal non-evaporating leaf replica*

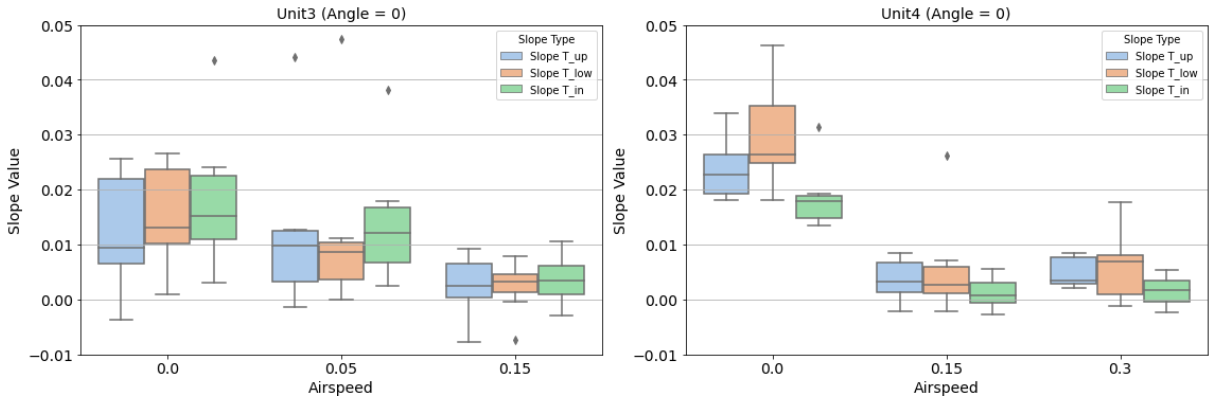

Figure 6-22: *Slopes of temperatures evolution during the 20 s parabolas: horizontal evaporating leaf replica*

As previously mentioned, the evolution of the slope for the non-evaporative replicas is consistently steeper (0.029 °C s^{-1}) than for the evaporative case (0.012 °C s^{-1}) for no airflow. It is also confirmed that the evolutions of the 3 temperatures (upper surface, lower surface, middle) are not significantly different. The other observation is that the airflow velocity almost clears the effects of zero gravity when it is higher than 0.15 m s^{-1}.

6.5.2 Stabilisation of temperatures and partial pressures profiles in the leaf replica and in the boundary layers at transient state during one parabola

The first thing to address is the transient behaviour of heat transfer inside the leaf replica and in the upper lower surface boundary layers. To investigate this point, the dimensionless Fourier number is the relevant variable (Beek et al., 2000):

$$Fo = \left(\frac{Penetration\ depth}{Thickness\ of\ the\ medium}\right)^2 = \frac{a\ t}{\delta^2}$$

a is the thermal diffusivity of the medium, t is the time, δ is the thickness of the medium. When Fo is greater than 0.1, it can be considered that the transient effects of thermal diffusion into the medium are negligible. In other words, the temperature profile can be considered to have reached steady state in the slide of thickness δ.

For the leaf replica, the thermal diffusivity is:

$$a_{LR} = \frac{\lambda_{LR}}{\rho_{LR}\ C_{p\_LR}}$$

With the data of Table 6-4, a_{LR}~$5\ 10^{-6}\ m^2\ s^{-1}$. The thickness of the leaf replica is lower that 1 mm. For $t = 1\ s$, $Fo_{LR} = 5$. Therefore, Fo_{LR} is well higher than 0.1, so that the temperature profile can be considered to have reached stationary heat penetration - heat penetration is a succession of steady state regimes during all the duration of a parabola (20 s). This means that the penetration of heat into the leaf replica has a rapid dynamic compared to duration of a parabola, so that the temperature profile instantaneously follows the dynamics of external conditions. This corresponds to a pseudo-steady state regime and this permits to ignore the internal dynamics of the leaf replica. As a result, the temperatures inside the leaf replica and on the external surfaces has parallel time-course evolutions. This is precisely that is observed, at least on non-evaporating leaf replica.

For the upper and lower surfaces gas boundary layers, the characteristic heat diffusion thickness is given by:

$$\delta_T = \frac{\lambda}{h}$$

Therefore, the Fourier numbers are:

$$Fo_{BL} = \frac{h^2\ t}{\rho_{air} C_{p\_air} \lambda_{air}}$$

With the data of Table 6-7, this leads to: $Fo_{BL} = 0.029\ h^2\ t$. This means that when the heat transfer coefficient is higher than $1.9\ W\ m^{-2} s^{-1}$, the Fourier number is higher than 0.1. Thus, in this case, the heat transfer temperature profile in the boundary layer reaches its stationary profile within less than 1 s. The situation is identical as the situation into the leaf replica itself. This condition is achieved for most situations both for h_{up} and h_{low}. However, it must be mentioned that the heat transfer coefficients that must be considered are the heat transfer coefficients after the onset of the parabola conditions, i.e., without gravity. The heat transfer is thus only associated to friction without any Grashof contribution, so that the transfer coefficients may become lower than $1\ W\ m^{-2} s^{-1}$ for the cases without any air velocity.

For the case of evaporating leaf replicas, the situation is less simple. After the onset the parabola conditions, the change of mass transfer behaviour in the boundary layer is similar to that of heat transfer. In most cases, it can be supposed that water partial pressure profile changes according to pseudo-steady state regime. The situation is still simple for the diffusion of water vapor at the output of the pore (in the cone separating the leaf replica surface from the entrance in the boundary layer): the length of the diffusion outside the pore is in the order of $L/2 = 190\ \mu m$. With an outside maximum velocity in the range of $v_\infty = 3\ 10^{-3}\ m\ s^{-1}$ (Eq. 83), it takes at least 0.06 s to get a stable diffusion regime. Even when the velocity is 2 to 3 times less, it can be considered that the stable regime for $\mathcal{R}_{end}$ is reached within 1 s. Inside the pore, the situation is more complex. According to Eq. 84, the length of diffusion of water vapor inside the pore l is linked to the velocity v_{bulk}. This leads to the fact that any change of the evaporating water flow rate would result in a change of liquid level inside the pore. This level cannot change rapidly: an estimation of the liquid level variation due to the evaporation is in the order $1 - 4\ \mu m\ s^{-1}$. The liquid water inside the pore is also submitted to high friction losses ($Re_L < 0.01$). The result is that the pore resistance $\mathcal{R}_{pores}$ changes slowly: several minutes for achieving a stable regime. Moreover, as the temperature increases, the water vapor pressure rises: Antoine law leads to almost $170\ Pa\ K^{-1}$. This results in a rapid increase of the difference of mass exchange potential (Eq. 82) which in turns results in the increase of heat removed by water evaporation. All the phenomena are strictly non-linear, which may even result in oscillating behaviours before the stable regime is reached, but, in any case,

within several minutes. Therefore, during the duration of one parabola, the stable regime is not reached. This is objectively observed with important variations in the slopes of the temperature profiles in the case of evaporating leaf replicas (Figure 6-22). The consequence is that the complete interpretation of the temperatures time-course evolution during the parabola would have to be done in the framework of integration of the transient evolution of the resistances. This part requires complex numerical developments, in order to introduce the time-course evolution of v_{bulk}, T_{low}, $P^0(T_{low})$, $\mathcal{R}_{pores}$,$\mathcal{R}_{end}$ and finally g_{tw}. It will not be developed in the framework of this study.

6.5.3 Pseudo-steady state evolution of temperature profiles during one parabola

The rapid evolution of temperature profiles inside the leaf replica and in the thermal boundary layers above and below has been considered. These profiles have sufficiently rapid dynamics to adapt to external conditions. However, mass transfer resistances in the leaf replica evolve more slowly due to complex couplings between diffusion phenomena, liquid vapor equilibrium and displacement of the interface inside the pore. Considering that the transfer coefficients are modified instantaneously during the transition to microgravity during a parabola, it is necessary to establish the slower dynamics of evolution of temperature profiles in the leaf replica. For that the hypothesis of a succession of permanent transfer regimes on which the slower dynamics of temperature evolution are superimposed was used. The framework of the pseudo-steady state transfer regime hypothesis to predict the evolution of temperature during a parabola was used. According to (Beek et al., 2000), the transient enthalpy balance is written as follows:

$$\frac{m}{A} C_p \frac{dT}{dt} = \phi_{up}^{rad} + \phi_{in}^{T} - \phi_{out}^{T} \qquad \textit{Eq. 92}$$

T is either T_{up},T_{low} or T_{in} knowing that pseudo-steady state assumption permits to consider that the time variation of the 3 temperatures is identical. As there is no heating of the leaf replica except by radiative flux, ϕ_{in}^{T} is zero. ϕ_{out}^{T} is given by:

$$\phi_{out}^{T} = h_{up}^{0g}\left(T_{up} - T_{bulk}\right) + h_{low}^{0g}(T_{low} - T_{bulk}) + g_{tw}^{0g} L^{V}\left(\frac{P^{0}(T_{low}) - \frac{\sigma}{d}}{T_{low}} - \frac{\mathcal{H}_{bulk} P^{0}(T_{bulk})}{T_{bulk}}\right)\frac{M_w}{R}$$

When the leaf replica is non-evaporating, the last right-hand term is cancelled. When the leaf evaporates, as already mentioned, the variation of g_{tw}^{0g} during the time-course of the parabola leads to complex behaviour.

The simplest case to treat, is the case with no airflow. The heat transfer model leads to $h_{up}^{0g} = h_{low}^{0g} = 0\ Wm^{-2}K^{1}$. In that case, Eq. 92 reduces to:

$$\frac{m}{A} C_p \frac{dT}{dt} = \phi_{up}^{rad} \qquad \textit{Eq. 93}$$

The factor in the left-hand side is a specific heat capacity per unit of surface: $C_p^{surf}\ (Jm^{-2}K^{-1})$. Considering the leaf replica thickness at the location where the thermocouples are installed is $e = 14\ mm$ and that the interstitial space is almost water, we obtain:

$$C_p^{surf} = \rho\ e\ C_p = 4765\ Jm^{-2}K^{-1}$$

With $\phi_{up}^{rad} = 156\ W\ m^{-2}$, this leads to a theoretical slope of $0.032\ K\ s^{-1}$. This is in fairly good agreement with the values reported in Figure 6-21 though this theoretical value is slightly over-estimated. But it must be considered that the pseudo-steady state hypothesis would have to be questioned when the air velocity is equal to 0. In this case, $h_{up}^{0g} = h_{low}^{0g} = 0\ Wm^{-2}K^{1}$, the Fourier number for 0 g conditions is also 0 (infinite boundary layer). The instantaneous variation of from the initial values of h to 0 is therefore not instantaneous. Using the penetration theory, it is shown that the average value of h during time t_e is (Beek et al., 2000):

$$< h > = 2\sqrt{\frac{\lambda_{air}\rho_{air}C_{p\ air}}{\pi\ t_e}}$$

For $t_e = 20\ s$, this leads to: $< h > = 1.5\ Wm^{-2}K^{1}$. Considering the temperature differences between the surfaces and the bulk remain almost constant during one parabola, this leads to decrease the value of ϕ_{up}^{rad} by about 15 % so that the estimated theoretical slope to 0.027 $K\ s^{-1}$ which is almost similar to what is observed (Figure 6-21) for both units 1 and 2. The

conclusion is that even in this simple case, the transient behaviour of boundary layers cannot be completely ignored.

In the case, the values of heat transfer coefficients are not 0 at 0 g, i.e., with a significant friction contribution, Eq. 93 is re-written as follows:

$$C_p^{surf}\frac{dT}{dt} = \phi_{up}^{rad} - h_{up}^{0g}\left(T_{up} - T_{bulk}\right) - h_{low}^{0g}(T_{low} - T_{bulk})$$

Knowing that T is both T_{up} and T_{low}, the previous relation defines a system of 2 differential equations possible to solve numerically. This leads to an evolution of the temperatures with an exponential decay towards the temperatures at $t \to \infty$. An approximation is derived at the origin, considering that the Taylor series development of the exact solution predicts a linear evolution of the temperatures. Let κ $(K\ s^{-1})$ the slope at the origin, neglecting the second-order terms, we get:

$$\kappa\ C_p^{surf} = \left(h_{up}^{1g} - h_{up}^{0g}\right)\left(T_{up}^{1g} - T_{bulk}\right) + \left(h_{low}^{1g} - h_{low}^{0g}\right)\left(T_{low}^{1g} - T_{bulk}\right)$$

T_{up}^{1g} and T_{low}^{1g} are the steady state temperatures for 1 g conditions. Considering that friction contributions are maintained between the phase 1 g and 0 g during the parabola, the differences $h_{up}^{1g} - h_{up}^{0g}$ and $h_{low}^{1g} - h_{low}^{0g}$ are the Grashof contributions during 1 g phase h_{up}^{Gr} and h_{low}^{Gr}. This leads to a simple, but approximate relationship:

$$\kappa\ C_p^{surf} = h_{up}^{Gr}\left(T_{up}^{1g} - T_{bulk}\right) + h_{low}^{Gr}\left(T_{low}^{1g} - T_{bulk}\right)$$

Considering the values reported in Figure 6-10 and Figure 6-11 and the previous value of C_p^{surf}, the results are 0.027, 0.022, 0.014 $K\ s^{-1}$ for air velocities $0.05,\ 0.15,\ 0.3\ m\ s^{-1}$. These results are in reasonable agreement with what is observed (Figure 6-21) although the estimates seem to be overestimated for the highest velocities. This is expected because the higher-order terms in the Taylor development decrease the average slopes calculated over the parabola. The other drawback of this estimation is related to the fact that it is assumed that the temperatures have returned to their steady-state 1 g values before starting the next parabola. This is not guaranteed by the experimental protocol during parabolic flight. All this should lead to a complete integration of the initial equation (Eq. 92) without making any first-order approximation. This part is not developed here, as this would require a complete calibration of the heat transfer model beforehand. However, the results obtained during parabolic flight

experiments are in good agreement with the developed model which leads to entirely plausible estimates of what actually happens during a 20 s transient phase in microgravity conditions.

For the evaporating leaf replica, the situation is more complex. As mentioned earlier, the variation of g_{tw}^{0g} during the time-course of the parabola leads to complex behaviour. However, it is possible to develop an approximate pseudo-steady state model of behaviour, considering that on average, 55% of the heat flux is removed by evaporation (Beek et al., 2000) for horizontal leaf replicas and assuming heat removal by evaporation of water is unaffected during the 20 s of one parabola. This assumption is based on the fact that the leaf replica's conductance and the change of the water evaporated flux have slow dynamics compared to the other phenomena. With these assumptions, the slopes would have the values 0.014, 0.012, 0.009, 0.007 $K\ s^{-1}$for air velocities 0, $0.05,\ \ 0.15,\ \ 0.3\ m\ s^{-1}$, respectively. These values are within the ranges of experimental errors that are reported in Figure 6-22. But as before, it would be necessary to develop a complete transient model, based on the time evolution of temperatures (Eq. 92) in order to control the fit of the curves to the experimental data. In the case of evaporating leaf replica, a significant uncertainty would remain on the initial conductance state of the leaf replica before the parabola, knowing that adaptation to steady-state transfer conditions probably takes at least several minutes.

6.5.4 Discussion on the transient model during the parabola experiments

The heat transfer model was adapted to transient conditions. First, it appears possible to assume a pseudo-steady state for the temperature profiles within the leaf replica. In the two boundary layers (upper and lower surfaces) characterizing heat transfer, the same hypothesis holds in most cases, except in the reference case at zero air velocity and for a horizontal leaf replica, where all transfers become negligible. In this case, it must be considered that the establishment of the boundary layer controls the dynamics of the phenomenon.

For the non-evaporating leaf replica, a simplified linearized model valid for the 20s during a parabola gave satisfactory results within the measurement accuracy.

For evaporating leaf replicas, the estimates presented are consistent with the experimental results. It appears that the observed nonlinearities are the result of relatively slow dynamics

of adaptation of the leaf replica conductance during the parabola. This slow variation is well explained by the water transfer model within the pore and at the surface of the leaf replica.

To go further, it would be necessary to develop the details of the dynamic models of temperature evolution, possibly taking into account the deformations of the profiles in the boundary layers. The mathematical description has been presented, but this work will require a specific study that will need to be developed later. For now, we can affirm that the presented model provides the correct trends and good orders of magnitude for short-term changes with relatively rapid dynamics.

6.6 Conclusion and perspectives for the modelling part

The experimental setup used was designed to be as simple as possible and provide cross-referencing experimental data. However, even with a simple design, representing experimental points with a physical model remains a difficult and complicated task.

The starting point was to understand and quantify the effect of gravity on mass and heat exchange. It should be noted that, except in very specific cases, in devices used at pilot and industrial scales, the effects of gravity are often lumped within semi-empirical correlations which are largely sufficient to understand and design industrial installations on Earth. It was therefore necessary to revisit in detail the separate contributions of friction and gravity phenomena in order to develop a physical model applicable to the very specific zero-gravity conditions during relatively short transient periods of parabolic flights. The objective is also to be able to extrapolate these conditions to longer durations of reduced gravity.

From the beginning, the difficulty was to work separately for the two surfaces of the leaf replica. Given the measured temperature gradients between the surfaces and the bulk liquid, the effects of natural convection (dependent on gravity) are reversed between the upper surface and the lower surface. The differences in density lead to convection beingfavoured above and damped below. It was necessary to model this to be able to quantify the effect of gravity. Moreover, since even if the effects of gravity are damped below, the leaf replica has pores located on the lower surface, so that an important part of heat removal is at the lower surface. This is a similar situation to that found on the leaves of higher plants. The physical understanding of the physical phenomena in the leaf replica we have used therefore has a

physiological counterpart that must be elucidated and quantified. From this point of view, the interest for studying the transfer mechanisms on the surfaces of our device goes far beyond the strict application to transient transfer conditions in reduced gravity on an leaf replica. The aim was to develop a precise mechanistic vision of the transfers from an artificial device (leaf replica). It must be outlined that the precise design and realization allowed to develop such a deep understanding.

There is no possible suitable consideration of gravity if we do not understand how the exchanges of heat and mass are carried out with a counter-gradient of density on the lower side of the leaf replica while these are carried out by natural convection on the upper side. To elucidate this apparent paradox and find a coherent physical representation, the exchanges of heat, matter and momentum were treated similarly via the Prandtl and Schmidt analogy.

The first work was to determine the heat exchange coefficients from the two surface temperature measurements. The simplest model accounting for the asymmetry of the exchanges between the two surfaces was a coupling model between radiative and conductive transfer inside the leaf replica. The results obtained, clearly indicate that there are strong differences between the exchange coefficients above and below and that these depend on the external conditions, inclination and air velocity. This indicates that the measured surface temperatures depend both on what happens inside the leaf replica (coupling radiative transfer and conduction) and what happens outside by convection in surrounding gas. To tackle these convective effects, the boundary layer concept was completely revisited, notably to link penetration theory and Blasius model-type simulations, given that the two approaches are each used for different specific cases, while there is approximately a factor of 2 between the predictions. Natural convection phenomena (upper surface) were then taken into account by introducing the Grashof number to the power of 1/3. Finally, to account for convection phenomena on vertical (or inclined) surfaces, it was shown that the Grashof number intervened to the power of 1/4. The result of this work is a single semi-empirical correlation obtained with all surface temperatures above and below the leaf replica. The result of this modelling exercise is the prediction of heat transfer coefficients as a function of external conditions. It should be noted that the ratio of the two transfer coefficients is very variable (between 1 and 9) depending on external conditions and on density differences and therefore on gravity. This justifies the previous deep investigation of the convective transfers, instead of

considering that the transfers are identical on the upper and lower surfaces of the leaf replica. In case of evaporating leaf replicas, taking into account the transfer phenomena in the surrounding gas boundary layer only allows us to represent 10 to 40% of the total conductance of the leaf replica according to our results. This has been already observed on the higher plants leaves and leaf replicas such as ones used in this study. Involving surface tension forces, it was possible to propose a complete model, which has the advantage of taking into account the geometry of the pores (diameter and depth) and their number. This aspect deserves confirmation but at least for the replicas that we have studied, it gives very satisfactory results. Finally, the model was confronted with transient regime conditions to test the predictions on transfers in parabolic flights. Although the model equations were not integrated over time, the results obtained for short durations of 20s in zero gravity are very satisfactory. The developed model appears to correctly account for temperature variations in the absence of gravity.

There are still points of fragility in the model, such as the determination of transfer coefficients on surfaces. It is likely that simulations using Computational Fluid Dynamics should bring new elements. However, it should be noted that the boundary layers are 1 to 4 mm thick, which will require having specific and fine gridding perpendicular to the surface level, and being able to take into account compressible fluids: the differences in densities on which gravity acts are barely 2% ($0.02\ kg\ m^{-3}$) of the average density. Also, the transversal transfers on the surface will have to be considered. This point was ignored in the framework of this study, considering that the transfers only took place perpendicular to the surfaces. Giving, the heat conductivities and diffusion coefficients, this seems to be a correct assumption but this would have to be more deeply investigated. All of these future improvements would require much more numerically intensive simulations, knowing that the extension to transient regimes must already be the subject of a specific study.

It must be outlined that the experimental results were sufficiently accurate for identifying the diversity of the relevant phenomena. Noticeably, the careful and accurate design of the Aluminium perforated foil on the lower surface of the leaf replica has permitted to develop the model for interfacial forces involvement. It would certainly be instructive to modify the density of the pores and eventually their diameter to test the ability of the model to represent the performances of different leaf replicas. Also, it is still possible to improve the experimental design. Characterizing the physical properties of the layer constituents has been a difficult

point, particularly for the absorption coefficients of radiative energy. Moreover, the use of thermocouples under the surface has certainly allowed for reliable temperature measurements, but even miniaturized, these thermocouples introduce an excess thickness ($400\ \mu m$) which introduces a bias in the calculation of the surface heat capacity (C_p^{surf}) which also affects the interpretation of the values of the slopes for transient experiments. It would probably be better to be satisfied with the temperatures measured by IR in zones where the thickness and composition of the layer are well controlled.

All these points constitute future improvement and refinement of the physical understanding of phenomena and their representation by digital simulations.

6.7 Outcomes of modelling part

A comprehensive knowledge model, based on various physical concepts and relying on energy conservation laws, was proposed to represent the experimental data obtained at the MELiSSA Pilot Plant in standard gravity conditions and in parabolic flight experiments. Basically, this model was conceived from chemical engineering principles, involving a large number of different concepts: boundary layer, heat and mass transfer, radiative transfer, flow in fixed-bed, momentum transfer and finally interfacial forces phenomena.

This model was designed to be fully predictive. This means that, given the configuration of the leaf replica, including its composition, the structure and size of the evaporation pores, and the operating variables, i.e., bulk temperature, humidity, air velocity, plate inclination, and incident radiative intensity, it is possible to predict surface temperatures and their evolutions when changing gravity.

This model aims to rigorously take into account the influence of gravity in presence of density gradients and might be applicable to space conditions. The results confirm that gravity may have a major importance on transfer intensity but, also, that precise knowledge of local density gradients is necessary for reliable simulations.

At the end, it opens the door to more complete simulations and modelling experiences in order to suitably simulate the behaviour of transport phenomena (radiative, heat and mass transfer by conduction and convection and momentum transfer) when operating in reduced gravity.

7 Conclusions

7.1 Summary of Key Points

7.1.1 Standard gravity conditions

Under normal gravity, the inclination of the leaf replica has a clear and consistent effect on the convective heat transfer. For a negative inclination (upper surface facing the stream), a buoyancy-driven component developed along the plate, promotes a boundary-layer flow that is faster and thinner. This leads to reduced wall temperatures and stronger convective exchange on the upper surface as was observed in the experiment. The effect is most visible under low air velocities (≤ 0.15 m s^{-1}), where natural convection remains dominant. Our observations confirm this behaviour, the term $Gr_{\perp\_up}^{1/3}$ bringing an important contribution at the lowest air velocities.

These findings are consistent with the work of (Pera and Gebhart, 1973), who analytically showed that introducing a buoyancy component parallel to the heated surface, even for small inclinations (2° to 6°), increases boundary layer flow and the local Nusselt number. Similar results were obtained by (Bilawane et al., 2021). In their studies, they observed that heat transfer coefficients increased with inclination from 0° to 90°, with maximum values when the plate is vertical. This study was done on roughened plates, but despite this, the overall dependence on inclination is consistent with the developed heat transfer model accounting for $Gr_{\parallel\_up}$ and $Gr_{\parallel\_low}$ contributions.

Similar results were obtained by (Ramirez et al., 2002). In this study, for inclinations up to 70°, and modelling a laminar flow, the average Nusselt numbers was up to 70% higher compared to the analytical value, mainly due to increased turbulence.

The lower temperature values observed for the inclined surface was also in line with results from (Corcione et al., 2011), who provided empirical correlations for natural convection from inclined plates across a wide range of Prandtl and Rayleigh numbers. When compared to Corcione's flat-plate data in air, the upper surface of the leaf replica showed local Nusselt numbers consistent with the expected values for inclination angles up to 30°, particularly under low air velocity.

More recent studies on leaf-like geometries have shown similar results. (Graefe et al., 2022) investigated elliptical leaf models under free convection and reported that boundary-layer conductance increases while the surface is angled. Although their setup focused on larger surfaces and used a different shape, the observed increase in conductance with inclination closely parallels the trends seen here.

One of the key findings of this study is the strong asymmetry between the two replica sides. In all configurations, more than 80% of the total convective flux occurred through the upper side, even when the lower side was facing the airflow. This implies that buoyancy alignment and boundary layer structure, not exposure alone, determine heat transfer efficiency.

The observed directional preference also corresponds to the physiological architecture of many terrestrial leaves. The adaxial surface (upper side), typically exposed to light and moving air, plays the main role in heat loss, while the abaxial surface (lower side), where most stomata are located, is structurally and functionally more sheltered. The results obtained here support the idea that this division of function is not only biological but also physically effective in controlling temperature through passive mechanisms.

7.1.2 Microgravity conditions

In the parabolic flight experiment, during the microgravity phase, the temperature of the upper side for the non-evaporative replica increased, compared to the preceding 1g phase. In the absence of airflow, this increase ranged between 0.3 and 0.7 °C and was consistently observed across multiple parabolas. The effect decreased with an increase in air velocity, and at a velocity of 0.3 m s^{-1}, the temperature difference between the 1g and microgravity phases became negligible (≤ 0.05 °C). This confirms that forced convection is able to compensate for the loss of buoyancy-driven exchange under microgravity. This is well correlated with the developed model prediction, showing that the Grashof contribution is relatively less important when air velocities are increased. Qualitatively, it was possible to find this trend and the orders of magnitude of the slopes of temperature evolution, which were measured during the microgravity phases.

The temperature increase observed in our study agrees with previous studies done on plant leaves during parabolic flights. (Kitaya et al., 2003) reported increases of up to 1.9 °C for real

leaves (sweet potato and barley), with typical values around 0.9–1.0 °C when gravity was reduced from 1g to 0.01g.

For the evaporative replica, in the performed experiment, temperature changes were smaller and more stable. In most cases, the temperature increase during the microgravity phase remained below 0.2 °C, and in several runs, the surface temperature remained slightly below the bulk air temperature throughout the entire microgravity phase. These results indicate that evaporative cooling effectively buffers the thermal response, even in the absence of buoyancy. This behaviour is in line with the findings of (Kitaya et al., 2003), who noted smaller temperature increases for wet paper replicas compared to real leaves or metal surfaces, and with (Hirai and Kitaya, 2009), who measured a 42% reduction in evaporation rate under microgravity at 0.2 m s^{-1} air velocity.

Air velocity was found to be the main parameter influencing the thermal and evaporative response under microgravity. As represented by the developed model, at 0.3 m s^{-1}, the non-evaporative replica showed almost no temperature rise during the parabola, and the evaporative replica maintained cooling performance comparable to 1g. This is consistent with results by (Tokuda et al., 2018), who demonstrated that applying a low-level air velocity (≥ 0.25 m s^{-1}) under microgravity conditions restored boundary-layer conductance and increased transpiration in real plants.

In addition, the behaviour observed at no-airflow conditions matches reported values for residual airflow in closed units. Under these conditions, estimated velocities within the test volume were 0.03 ± 0.01 m s^{-1}, similar to those reported by (Kimura et al., 2020), who showed that boundary-layer conductance can drop to the same order as stomatal conductance at low local wind speeds. This suggests that even very low air velocity can have a visible influence on exchange processes in microgravity environments. This is mainly due to the fact that leaf replica conductance is not affected by gravity. That is an important result confirmed by the model of leaf replica's conductance that has been developed in this work, involving a major influence of interfacial forces.

7.2 Limitation of the studies

Although this research provided data about heat and mass transfer between the leaf replica and the environment under different gravity conditions, there are several limitations in the experimental setup, methodology, modelling, and scope of the experiment. Those limitations are:

1. **Experimental Design Constraints**
    a. Variability in LED illumination - The LED modules used in each unit delivered slightly different power outputs. Additionally, light distribution across the leaf replica surface was not uniform. That led to inconsistent thermal input across the surface of the leaf replica. This has altered the possibility of studying the spatial distribution of temperature on the surface of the leaf replica.
    b. Unit-to-Unit mechanical tolerances - Differences in how replicas were mounted or connected to motors may have introduced uncontrolled variations between units.
    c. Aging and material behaviour - The materials used to make leaf replica, may have changed intrinsic properties over time - e.g., the water used for filling the leaf replica was milli-Q water, however, some minerals could have deposited on the hydrophilic filter and some pores could have clogged over time with this deposit, or with dirt from the outside. Knowing the influence of the pore diameter on the leaf replica's conductance, this finally could have modified the global characteristics of the leaf replica.
2. **Measurement Accuracy and Instrumentation**
    a. Thermocouple inertia - Due to the response time of thermocouples, they may have slightly underestimated temperatures during rapid increases and overestimated temperatures during cooling phases. This effect is particularly relevant for short-duration gravity transitions during parabolic flights.
    b. Lack of IR data analysis - Although the hardware incorporated four IR cameras, the study did not include any IR image analysis. This part of the interpretation of the experimental results remains to be done, requiring a preliminary selection of relevant data and a suitable calibration of the temperature readings.

c. Data dropouts during flight - Sensor readings were occasionally lost during parabolic flights.
d. No direct measurement of water loss rate - Actual water evaporation rate was not directly quantified. Including flow measurements could have strengthened the understanding of transpiration-like behaviour. It could confirm or contradict the calculation of water flux estimations. Conducted estimations show that the maximum mass evaporation flux of water is in the range of $500\ mg\ h^{-1} (59\ mg\ m^{-2} s^{-1})$ which determines the order of magnitude of water loss during fixed conditions. In any case, this could not have been applied for characterising the microgravity sequences that were too short to get a suitable accuracy.

3. Leaf Replica Design and Scope

a. Handmade replica imperfections - Each leaf replica was manually produced and may exhibit small geometric imperfections. These inconsistencies could impact flow resistance or surface temperature distributions.
b. The bloated surface at the location of the two thermocouples impairs the determination of specific heat capacity per unit of surface, that enters directly in the proportionality constant for the determination of the slopes during transient phases. This prevents the adequacy of the transfer model from being properly verified during transient phases during parabolic flights.
c. Ground experiment water leakage - During the ground reference experiment, unexpected evaporation might have occurred in the non-evaporative replica, likely due to inadequate sealing. This could have affected the comparative analysis between evaporative and non-evaporative conditions.

4. Environmental and Experimental Conditions

a. Limited gravity exposure - The microgravity data were collected only in transient conditions (~22 seconds per parabola). No data under steady-state microgravity or partial gravity were included. This is why an experiment for the ISS is underway.

7.3 Perspectives and future research directions

Building on the findings of this study, several improvements are proposed to improve the robustness, biological relevance, and applicability of the current work:

1. **Improvements in Experimental Design and Instrumentation**

    a. Enhanced light uniformity - Future experiments should implement a more precise lighting system with diffusers to provide uniform illumination across the leaf surface, or an inner resistor to heat the replica.

    b. Variation of light intensity – At the moment, we have used only one radiative energy flux of each leaf replica, corresponding to a precise mapping of the light flux distribution over the surface obtained with the lighting system. It will be instructive to vary the light energy input to achieve the effects on surface temperature distributions and the effects on the leaf replica evaporation capacities.

    c. Integrated water loss measurement - Incorporating flow meters would enable direct quantification of evaporative water loss at steady state during sufficiently long periods of stability of the environmental conditions (air velocity, relative humidity and bulk temperature).

    d. Full integration of IR imaging - Future experiments should fully utilize the IR camera to produce high-resolution thermal maps, allowing comparison of surface temperature distributions across conditions and replicas.

2. **Model improvement and extension**

    a. Up to now, the correlation of heat transfer coefficients has been done from a deep understanding of boundary layer theory. It appears necessary to associate CFD simulations in order to derive numerical predictions of heat and mass transfer coefficients on the basis of the resolution of the momentum balance equation, including momentum transfer in the vicinity of the surfaces. The influence of gravity that has been investigated with the Grashof number on the basis of the addition of hydrodynamic resistances in parallel needs to be confirmed. Normally CFD simulations are based on a complete momentum

balance including all contributions so that the present addition of transfer resistances in parallel would not be required.

b. The complex model developed here, including different contributions for representing measured surface temperatures, needs to be reversed. This means that knowing the physical characteristics of the leaf replica (light absorption in the different constitutive layers of the leaf replica, heat conductivities, thicknesses, pores length, diameter and spacing) and the operational conditions (air velocity, bulk temperature, relative humidity), the challenge is to use the model for predicting the surface temperatures. In principle, the resolution is possible, but the numerical developments are tedious considering that the resolution is highly non-linear, the temperature acting on density differences (therefore modelled with Grashof number), and vapor pressure. This part remains to be developed.

c. The proposed correlation for leaf replica conductance needs to be confirmed. The influence of surface tension forces appears to be intuitively correct, but this needs to be confirmed on the basis of new experiments and the configuration of leaf replica. In any case, the conductance of the leaf replica itself is the dominant controlling process in the case of the evaporating leaf replica. The importance in terms of physical understanding of water (and CO_2) transfer in the biological counterpart justifies such studies.

d. Integration of the model in transient state should be the only way to verify the ability to represent heat and mass transfers during parabolic flight experiments. The first evaluations seem to be correct. It seems that the influence of transient conditions in the boundary layers and in the leaf replica should remain insignificant. But this must be verified on a complete model with the ambiguity that the initial conditions are well defined before the start of the parabola.

3. Biological Integration and System Complexity

a. Validation with leaves - Parallel experiments using live plant leaves under similar conditions will help to integrate physical models into biological models

b. Multi-leaf or canopy models - Developing models that represent an entire plant canopy or use multiple interacting leaf replicas could provide insights into system-level dynamics, including mutual shading, airflow disturbance, and cumulative transpiration. This will require a reduction of the detailed transfer model. This is always possible provided that the model takes into account all the important contributions in the core equations.

c. Incorporating biological feedback mechanisms - Future research should aim to include biological elements that more closely simulate plant physiology or their responses, for example, dynamic stomatal apertures, which respond to environmental changes, or trichomes to simulate leaf surface more realistically. In light of the leaf replica conductance model, it will be interesting to look at the links between surface temperature, stomatal opening and relative humidity of ambient air.

4. Long-Duration and Steady-State Studies

a. Microgravity steady-state conditions - The current study was limited to transient conditions due to the short duration of microgravity phases during parabolic flights. However, future experiments should focus on the investigation of steady-state heat and mass transfer processes under long-duration microgravity conditions. In this context, an experiment proposal has been submitted and accepted for the ESA Reserved Pool of ISS experiments. This experiment would be conducted on the ISS, enabling the acquisition of steady-state data in true microgravity conditions. Discussions on the contract with ESA to proceed with hardware completion are currently ongoing.

b. Simulation-driven experiment design - Coupling CFD or thermal simulation tools with experimental planning could help predict outcomes, refine designs, and reduce the number of physical iterations needed.

5. **Application-Oriented Development**

    a. Design implications for LSS - Insights gained from this work should be progressively integrated into BLSS models, particularly for optimizing plant positioning, air velocity control, and heat management.

    b. Plant-inclusive environmental control systems - currently, plants grown in space are used either for food production studies or for fundamental research. They are not integrated as functional components of LSS. As scientific understanding of plant-environment interactions deepens, future systems should move toward incorporating plants as a part of the environmental control system.

7.4 General conclusion

Plants need to be integrated into hybrid LSS for long-term space missions as physicochemical systems are too costly and insufficient for long-duration space missions. In this framework, at the very beginning, the objective of this work was set within the framework of the study and understanding of heat and mass transfers on the surface of a plant leaf, in the case of cultivation of higher plants in a greenhouse integrated into an extra-terrestrial Life-support system. The major function of a greenhouse, considered as a unit operation in a Life-support system, is the production of oxygen, water, and food and the consumption of CO_2. A major gap in current higher plant growth models is the lack of gravity as a parameter. It is well known that gravity limits heat and mass exchange processes within plants, especially when ventilation is limited. However, the exact mechanisms, remain unknown, making it hard to incorporate stress factors into energy balance or transpiration rate models in a reduced gravity environment.

Knowing that models based on first principles are not easy to create but are more reliable, this is a critical challenge for life-support applications in space. Future solutions for Biological life-support systems may involve hybrid approaches that combine mechanistic understanding with data-driven adaptability, yet a strong physical foundation remains essential for ensuring safe and robust system designs. This is why leaf replicas were used, in which it was possible to control the physical characteristics and environmental variables of the leaf replicas. In this

context, the design of leaf replicas with fixed sizes and spacing of the pores has been carefully prepared. The design of the hardware that was built made it possible to fix the incident radiative flux of energy by the lighting system, the velocity of the surrounding air, the inclination of the leaf replica, the ambient temperature and relative humidity, as well as gravity during short phases (20s) in parabolic flight experiments. In total, this makes four main geometric parameters (surface area of the leaf replica, pore diameter, pore depth and spacing) and six operating variables (incident light flux, air velocity, leaf replica inclination, temperature and relative humidity of the surrounding air and gravity for short periods). Incident light flux was not varied, so that only five of six operating variables were used. Four-leaf replicas were installed inside units. The observed variables were mainly the temperatures of the upper and lower surfaces of the leaf replicas. This ultimately constituted a considerable set of data points. These data were processed to obtain average values for the same conditions to be able to establish a model supporting the physical understanding of the observed phenomena. This was the primary objective of this study.

Generally, it is well known that the exchanges between the leaf and its environment result from two types of convection: *i)* forced convection caused by the movement of wind or air and promotes heat transfer; *ii)* free convection that results from temperature differences between the surface of the plant and the ambient air; the latter depends on gravity and differences in air density between the surface and the surrounding air. Thus, the core of our modelling study had to incorporate the entanglement between forced and natural convection in order to get a chance to predict the effects of gravity. Although the density differences are small (1 to 2% of air density i.e., up to $0.02\ kg\ m^{-3}$), the effects of natural convection are strong enough to produce significant differences at the surface scale. This is what is observed during parabolic flights, with an increase in surface temperatures due to the absence of gravity during the parabolic maneuvers. However, these density differences act in terrestrial gravity in a favorable way on transfers on the upper surfaces by creating a convective movement between the surface and the bulk gas (higher density above the lower one) but unfavorably on the lower surface because the difference in densities creates a stabilizing effect which dampers the transfers (lower density above the higher one which results in a stable stratified thermal configuration). This last point requires considering that the transfers between the two surfaces are asymmetrical - properly taking into account the effects of gravity requires a

degree of refinement that allows the transfers on the upper surface and the lower surface to be treated differently. This is also consistent with the fact that the data obtained show the temperature gradients between the surfaces and the bulk are different on the two surfaces. Moreover, in the case of evaporating leaf replicas, an additional degree of complexity results from the fact that the evaporation of water takes place on the underside, as is generally the case for plant leaves. However, evaporation will reduce the momentum of the gravity stabilized thermal configuration mentioned above.

The model that was validated and implemented to represent the results takes into account these differences in behavior between the two surfaces. In the case of evaporating leaf replicas, the results indicate that between 35 and 65% of heat is removed by water evaporation. This is a typical result for this type of experiment. The calculations presented here allowed a precise evaluation of this contribution. Hence, it is shown that the proportion of energy evacuated by evaporation varies significantly with the experimental conditions (air velocity and inclination). Calculating the overall mass transfer conductance necessary to ensure such water fluxes, it appears that the overall conductance for mass transfer is located inside the leaf replica itself, the conductance in the gas boundary layer representing only a minor part. Proposed model is based on a fundamental contribution of surface tension forces inside the pores. It takes into account the morphology of the pores (length, diameter and spacing). The model was used to represent the results obtained during the transient phases of transition to zero gravity during parabolic flights. As expected, the extinction of the natural convection terms during the parabola leads to an increase in temperature. The kinetics of this increase are correctly predicted by the model under the various experimental conditions tested.

The design of the hardware and the development of the physical understanding of the model now allow to have a precise idea of the important mechanisms that control heat, mass, and radiative energy transfers inside this type of leaf replica. The results obtained were sufficiently reliable to develop a complete representation that takes into account the effects of gravity, that is to say, the phenomena of natural convection.

Still, the validity of the leaf replica conductance model remains to be confirmed. At least, as it stands, we fully understand why, under conditions of reduced or zero gravity, the leaf conductance is not significantly modified, the major determinant being the surface tension

forces and the geometry of the pores. This explains why in zero gravity, the aerial part of higher plants develops normally, provided that sufficient transfer conditions are maintained by forced convection in the environment of the plant canopy. This is confirmed by the higher plant growth experiments on ISS. Interestingly, the leaf conductance results from purely physical laws provided the pore geometry and spacing are fixed as it has been the case for the tested leaf replicas. For higher plants, biological control acts on stomata opening with a rather rapid retroaction, generally in a few seconds or minutes, with, among others, the temperature as the control variable. The density of the stomata results from a slower control and also acts on the capacity of the leaf to increase or reduce the evaporated water flux. All of this confirms the interest in strictly quantifying the links between pore diameter, depth and spacing with evaporated water flux and surface temperatures, the counterpart in the biological world being the stomata opening, depth and density.

On a more global perspective, this work opens new routes of exploration to understand and anticipate the functioning of higher plants in non-terrestrial environments. A deep understanding of the physical mechanisms is necessary because these are non-classical conditions, poorly described in standard correlations. When dealing with biological material, intricacies can become even more complex. But ultimately, this teaches a great deal about functioning under terrestrial conditions and should lead to the development of new perspectives both for terrestrial and space applications. It is within this framework that this study was developed.

The studies described here were presented during several conferences and so far, two papers have been published based on this research work. The detailed description can be found in Appendix F.

8 References

Albrecht, H., Fiorani, F., Pieruschka, R., Müller-Linow, M., Jedmowski, C., Schreiber, L., Schurr, U., Rascher, U., 2020. Quantitative Estimation of Leaf Heat Transfer Coefficients by Active Thermography at Varying Boundary Layer Conditions. Front. Plant Sci. 10, 1684. https://doi.org/10.3389/fpls.2019.01684

Alemany, L., Peiro, E., Arnau, C., Garcia, D., Poughon, L., Cornet, J.-F., Dussap, C.-G., Gerbi, O., Lamaze, B., Lasseur, C., Godia, F., 2019. Continuous controlled long-term operation and modeling of a closed loop connecting an air-lift photobioreactor and an animal compartment for the development of a life support system. Biochem. Eng. J. 151, 107323. https://doi.org/10.1016/j.bej.2019.107323

Amitrano, C., Chirico, G.B., De Pascale, S., Rouphael, Y., De Micco, V., 2020. Crop Management in Controlled Environment Agriculture (CEA) Systems Using Predictive Mathematical Models. Sensors 20, 3110. https://doi.org/10.3390/s20113110

Anderson, G., Martin, C., 2005. Evaluation and Application of Apollo ECLS/ATCS Systems to Future Manned Missions, in: 43rd AIAA Aerospace Sciences Meeting and Exhibit. Presented at the 43rd AIAA Aerospace Sciences Meeting and Exhibit, American Institute of Aeronautics and Astronautics, Reno, Nevada. https://doi.org/10.2514/6.2005-703

Beek, W.J., Muttzall, K.M.K., Heuven, J.W.V., 2000a. Transport Phenomena, 2nd edition. ed. Wiley, Chichester ; New York.

Beek, W.J., Muttzall, K.M.K., Heuven, J.W. van, 2000b. Transport phenomena, 2. ed., Repr. ed. Wiley, Chichester Weinheim.

Belew, L.F., Stuhlinger, E., 1973. Skylab : a guidebook. [National Aeronautics and Space Administration] : [For sale by the Supt. of Docs., U.S. Govt. Print. Off.] [Washington], [Washington].

Berry, W., Vernikos, J., Gaiser, K., Campbell, P., 1994. NASA's Advanced Life Support Technology Program, in: SAE Technical Paper Series. Presented at the International Conference On Environmental Systems, SAE International, 400 Commonwealth Drive, Warrendale, PA, United States. https://doi.org/10.4271/941290

Bilawane, R.R., Mandavgade, N.K., Kalbande, V.N., Patle, L.J., Kanojiya, M.T., Khorgade, R.D., 2021. Experimental investigation of natural convection heat transfer coefficient for roughed inclined plate. Mater. Today Proc. 46, 7926–7931. https://doi.org/10.1016/j.matpr.2021.02.639

Bird, R.B., Stewart, W.E., Lightfoot, E.N., 2007. Transport phenomena, Revised ed. ed. Wiley, New York.

Bobe, L., Samsonov, N., Gavrilov, L., Novikov, V., Tomashpolskiy, M., Andreychuk, P., Protasov, N., Synjak, Y., Skuratov, V., 2007. Regenerative water supply for an interplanetary space station: The experience gained on the space stations "Salut", "Mir", ISS and development prospects. Acta Astronaut. 61, 8–15. https://doi.org/10.1016/j.actaastro.2007.01.003

Brown, H.I., 1985. Galileo on the Telescope and the Eye. J. Hist. Ideas 46, 487. https://doi.org/10.2307/2709541

Ciurans Molist, C., 2023. Proposal of an Overall Control Architecture for the MELiSSA Loop (PhD Thesis).

References

Corcione, M., Habib, E., Campo, A., 2011. Natural convection from inclined plates to gases and liquids when both sides are uniformly heated at the same temperature. Int. J. Therm. Sci. 50, 1405–1416. https://doi.org/10.1016/j.ijthermalsci.2011.03.012

Cox, J.D., Wagman, D.D., Medvedev, V.A., 1989. CODATA key values for thermodynamics. Hemisphere Pub. Corp., New York.

Cramer, G.R., Urano, K., Delrot, S., Pezzotti, M., Shinozaki, K., 2011. Effects of abiotic stress on plants: a systems biology perspective. BMC Plant Biol. 11, 163. https://doi.org/10.1186/1471-2229-11-163

Creech, S., Guidi, J., Elburn, D., 2022. Artemis: An Overview of NASA's Activities to Return Humans to the Moon, in: 2022 IEEE Aerospace Conference (AERO). Presented at the 2022 IEEE Aerospace Conference (AERO), IEEE, Big Sky, MT, USA, pp. 1–7. https://doi.org/10.1109/AERO53065.2022.9843277

Crouch, T.D., 2002. Challenge to Apollo: The Soviet Union and the Space Race, 1945-1974 Asif A. Siddiqi. Public Hist. 24, 108–109. https://doi.org/10.2307/3379034

Daues, K.R., 2006. A history of spacecraft environmental control and life support systems.

De Boer, H.J., Lammertsma, E.I., Wagner-Cremer, F., Dilcher, D.L., Wassen, M.J., Dekker, S.C., 2011. Climate forcing due to optimization of maximal leaf conductance in subtropical vegetation under rising CO_2. Proc. Natl. Acad. Sci. 108, 4041–4046. https://doi.org/10.1073/pnas.1100555108

Defraeye, T., Verboven, P., Ho, Q.T., Nicolai, B., 2013. Convective heat and mass exchange predictions at leaf surfaces: Applications, methods and perspectives. Comput. Electron. Agric. 96, 180–201. https://doi.org/10.1016/j.compag.2013.05.008

DeYoung, G., 2000. Astronomy in Ancient Egypt, in: Selin, H., Xiaochun, S. (Eds.), Astronomy Across Cultures, Science Across Cultures: The History of Non-Western Science. Springer Netherlands, Dordrecht, pp. 475–508. https://doi.org/10.1007/978-94-011-4179-6_17

Diamant, B.L., Humphries, W.R., 1990. Past and Present Environmental Control and Life Support Systems on Manned Spacecraft. Presented at the International Conference On Environmental Systems, p. 901210. https://doi.org/10.4271/901210

Dow, G.J., Berry, J.A., Bergmann, D.C., 2014. The physiological importance of developmental mechanisms that enforce proper stomatal spacing in *A rabidopsis thaliana* . New Phytol. 201, 1205–1217. https://doi.org/10.1111/nph.12586

Eckart, P., 1996a. Spaceflight Life Support and Biospherics. Springer Netherlands, Dordrecht. https://doi.org/10.1007/978-94-017-3038-9

Eckart, P., 1996b. Fundamentals of Life Support Systems, in: Spaceflight Life Support and Biospherics. Springer Netherlands, Dordrecht, pp. 79–173. https://doi.org/10.1007/978-94-017-3038-9_4

ESA, 2022. ESA AGENDA 2025 Make space for Europe.

Ewert, M.K., Chen, T.T., Powell, C.D., 2022. Life Support Baseline Values and Assumptions Document.

Foin, G., Brunel, L., Cornet, J.-F., Dauchet, J., Gros, F., Vourc'h, T., 2024. Extending the use of normal hemispherical transmittance (T N H) measurements by modeling 3D multiple scattering radiative transfer. J. Quant. Spectrosc. Radiat. Transf. 327, 109124. https://doi.org/10.1016/j.jqsrt.2024.109124

Fu, Y., Li, L., Xie, B., Dong, C., Wang, M., Jia, B., Shao, L., Dong, Y., Deng, S., Liu, Hui, Liu, G., Liu, B., Hu, D., Liu, Hong, 2016. How to Establish a Bioregenerative Life Support

System for Long-Term Crewed Missions to the Moon or Mars. Astrobiology 16, 925–936. https://doi.org/10.1089/ast.2016.1477

Furfaro, R., Giacomelli, G., Sadler, P., Gellenbeck, S., 2017. The Mars-Lunar Greenhouse (M-LGH) Prototype for Bio Regenerative Life Support: Current Status and Future Efforts. 47th International Conference on Environmental Systems.

Galston, A.W., 1992. Photosynthesis as a basis for life support on Earth and in space: photosynthesis and transpiration in enclosed spaces. Bioscience 42, 490–493.

Garcia-Gragera, D., Arnau, C., Peiro, E., Dussap, C.-G., Poughon, L., Gerbi, O., Lamaze, B., Lasseur, C., Godia, F., 2021. Integration of Nitrifying, Photosynthetic and Animal Compartments at the MELiSSA Pilot Plant. Front. Astron. Space Sci. 8, 750616. https://doi.org/10.3389/fspas.2021.750616

Gingerich, O., 1974. The Astronomy and Cosmology of Copernicus. Highlights Astron. 3, 67–85. https://doi.org/10.1017/S1539299600001830

Gitelson, I.I., Terskov, I.A., Kovrov, B.G., Lisovskii, G.M., Okladnikov, Yu.N., Sid'ko, F.Ya., Trubachev, I.N., Shilenko, M.P., Alekseev, S.S., Pan'kova, I.M., Tirranen, L.S., 1989. Long-term experiments on man's stay in biological life-support system. Adv. Space Res. 9, 65–71. https://doi.org/10.1016/0273-1177(89)90030-6

Gitelson, J.I., Lisovsky, G.M., Tikhomirov, A.A., 1997. Optimal Structure of Plant Conveyor for Human Life Support in a Closed Ecosystem "Bios-3," in: Goto, E., Kurata, K., Hayashi, M., Sase, S. (Eds.), Plant Production in Closed Ecosystems. Springer Netherlands, Dordrecht, pp. 297–304. https://doi.org/10.1007/978-94-015-8889-8_18

Graefe, J., Grosch, R., Bitterlich, M., 2022. The boundary layer conductance of inclined elliptical leaves under free convection. Agric. For. Meteorol. 317, 108884. https://doi.org/10.1016/j.agrformet.2022.108884

Gribovskaya, I.V., Kudenko, Yu.A., Gitelson, J.I., 1997. Element exchange in a water-and gas-closed biological life support system. Adv. Space Res. 20, 2045–2048. https://doi.org/10.1016/s0273-1177(97)00939-3

Grimwood, J.M., Hacker, B.C., Vorzimmer, P.J., 1969. Project Gemini: Technology and Operations: A Chronology, NASA SP. Scientific and Technical Information Division, National Aeronautics and Space Administration.

Hannah, R., 2015. The Roles Of Observational Astronomy In Ancient Greece. https://doi.org/10.5281/ZENODO.34513

Hendrickx, L., De Wever, H., Hermans, V., Mastroleo, F., Morin, N., Wilmotte, A., Janssen, P., Mergeay, M., 2006. Microbial ecology of the closed artificial ecosystem MELiSSA (Micro-Ecological Life Support System Alternative): Reinventing and compartmentalizing the Earth's food and oxygen regeneration system for long-haul space exploration missions. Res. Microbiol. 157, 77–86. https://doi.org/10.1016/j.resmic.2005.06.014

Hetherington, A.M., Woodward, F.I., 2003. The role of stomata in sensing and driving environmental change. Nature 424, 901–908. https://doi.org/10.1038/nature01843

Hezard, P., 2012. Modélisation de la croissance des plantes supérieures pour les systèmes de support-vie : conception d'un modèle global et simulation des transferts de masse et d'énergie à l'échelle de la plante (PhD Thesis).

Hirai, H., Kitaya, Y., 2009. Effects of Gravity on Transpiration of Plant Leaves. Ann. N. Y. Acad. Sci. 1161, 166–172. https://doi.org/10.1111/j.1749-6632.2009.04093.x

Jenks, A.L., 2022. Collaboration in space and the search for peace on Earth. Anthem Press, London.

References

Johnson, C.M., Boles, H.O., Spencer, L.E., Poulet, L., Romeyn, M., Bunchek, J.M., Fritsche, R., Massa, G.D., O'Rourke, A., Wheeler, R.M., 2021. Supplemental Food Production With Plants: A Review of NASA Research. Front. Astron. Space Sci. 8, 734343. https://doi.org/10.3389/fspas.2021.734343

Jones, H., 2006. Evolution of Life Support from Apollo, Shuttle, and ISS to the Vision for the Moon and Mars. Presented at the International Conference On Environmental Systems, pp. 2006-01–2013. https://doi.org/10.4271/2006-01-2013

Jones, H.W., Kliss, M.H., 2010. Exploration life support technology challenges for the Crew Exploration Vehicle and future human missions. Adv. Space Res. 45, 917–928. https://doi.org/10.1016/j.asr.2009.10.018

Kimura, K., Yasutake, D., Yamanami, A., Kitano, M., 2020. Spatial examination of leaf-boundary-layer conductance using artificial leaves for assessment of light airflow within a plant canopy under different controlled greenhouse conditions. Agric. For. Meteorol. 280, 107773. https://doi.org/10.1016/j.agrformet.2019.107773

Kitaya, Y., Kawai, M., Tsuruyama, J., Takahashi, H., Tani, A., Goto, E., Saito, T., Kiyota, M., 2003. The effect of gravity on surface temperatures of plant leaves: Effect of gravity on leaf temperatures. Plant Cell Environ. 26, 497–503. https://doi.org/10.1046/j.1365-3040.2003.00980.x

Lambers, H., Chapin, F.S., Pons, T.L., 2008. The Plant's Energy Balance, in: Plant Physiological Ecology. Springer New York, New York, NY, pp. 225–236. https://doi.org/10.1007/978-0-387-78341-3_6

Lehmann, P., Or, D., 2015. Effects of stomata clustering on leaf gas exchange. New Phytol. 207, 1015–1025. https://doi.org/10.1111/nph.13442

LePage, A.J., 1999. Mercury: America's First Spaceship.

Liu, H., Yao, Z., Fu, Y., Feng, J., 2021. Review of research into bioregenerative life support system(s) which can support humans living in space. Life Sci. Space Res. 31, 113–120. https://doi.org/10.1016/j.lssr.2021.09.003

Liu, K., Wang, Y., Magney, T.S., Frankenberg, C., 2024. Non-steady-state stomatal conductance modeling and its implications: from leaf to ecosystem. Biogeosciences 21, 1501–1516. https://doi.org/10.5194/bg-21-1501-2024

MacElroy, R.D., Bredt, J., 1984. Current concepts and future directions of CELSS. Adv. Space Res. 4, 221–229. https://doi.org/10.1016/0273-1177(84)90566-0

Marino, B.D.V., Odum, H.T., 1999. Biosphere 2: Introduction and research progress.

Massa, G., Hummerick, M., Spencer, L., Smith, T., 2015. Veggie ISS Validation Test Results and Produce Consumption.

Mauri, R., 2013. Non-Equilibrium Thermodynamics in Multiphase Flows, Soft and Biological Matter. Springer Netherlands, Dordrecht. https://doi.org/10.1007/978-94-007-5461-4

McDougall, W.A., 1985. Sputnik, the space race, and the Cold War. Bull. At. Sci. 41, 20–25. https://doi.org/10.1080/00963402.1985.11455962

Mergeay, M., Verstraete, W., Dubertret, G., Lefort-Tran, M., Chipaux, C., Binot, R., 1988. MELiSSA: A micro-organisms-based model for CELSS development. Presented at the ESA, Third European Symposium on Space Thermal Control and Life Support Systems p 65-68(SEE N 89-28214 22-54).

Mitchell, K.L., 1994. Technical Assessment of Mir-1 Life Support Hardware for the International Space Station.

Monje, O., Bugbee, B., 2019. Radiometric Method for Determining Canopy Stomatal Conductance in Controlled Environments. Agronomy 9, 114. https://doi.org/10.3390/agronomy9030114

Monje, O., Richards, J.T., Carver, J.A., Dimapilis, D.I., Levine, H.G., Dufour, N.F., Onate, B.G., 2020. Hardware Validation of the Advanced Plant Habitat on ISS: Canopy Photosynthesis in Reduced Gravity. Front. Plant Sci. 11. https://doi.org/10.3389/fpls.2020.00673

Munns, D.P.D., Nickelsen, K., 2021. Far beyond the moon: a history of life support systems in the space age, Intersections histories of environment, science, and technology in the anthropocene. University of Pittsburgh Press, Pittsburgh, Pa.

NASA, 2018. Designing for Human Presence in Space: An Introduction to Environmental Control and Life Support Systems. CreateSpace Independent Publishing Platform.

Nelson, M., 2021. Biosphere 2's Lessons about Living on Earth and in Space. Space Sci. Technol. 2021. https://doi.org/10.34133/2021/8067539

Nelson, M., Dempster, W.F., Allen, J.P., 2008. "Modular Biospheres" – New testbed platforms for public environmental education and research. Adv. Space Res. 41, 787–797. https://doi.org/10.1016/j.asr.2007.03.002

Neufeld, M.J., 2023. Back to the Moon ... to stay? Phys. Today 76, 40–48. https://doi.org/10.1063/PT.3.5361

Ozgumus, T., Mobedi, M., Ozkol, U., 2014. Determination of Kozeny Constant Based on Porosity and Pore to Throat Size Ratio in Porous Medium with Rectangular Rods. Eng. Appl. Comput. Fluid Mech. 8, 308–318. https://doi.org/10.1080/19942060.2014.11015516

Pera, L., Gebhart, B., 1973. Natural convection boundary layer flow over horizontal and slightly inclined surfaces. Int. J. Heat Mass Transf. 16, 1131–1146. https://doi.org/10.1016/0017-9310(73)90126-9

Petersen, J.C.G., Hargens, A.R., Petersen, L.G., 2021. Parabolic Flight, in: Young, L.R., Sutton, J.P. (Eds.), Handbook of Bioastronautics. Springer International Publishing, Cham, pp. 489–498. https://doi.org/10.1007/978-3-319-12191-8_62

Pierre, L.M., Schultz, J.R., Johnson, S.M., Sauer, R.L., Sinyak, Y.E., Skuratov, V.M., Protasov, Nikoli N., Protasov, Nicolei N., 1996. Collection and Chemical Analysis of Reclaimed Water and Condensate from the Mir Space Station. SAE Trans. 105, 937–961.

Poughon, L., Farges, B., Dussap, C.G., Godia, F., Lasseur, C., 2009. Simulation of the MELiSSA closed loop system as a tool to define its integration strategy. Adv. Space Res. 44, 1392–1403. https://doi.org/10.1016/j.asr.2009.07.021

Poulet, L., 2018. Développement de modèles physiques pour comprendre la croissance des plantes en environnement de gravité réduite pour des apllications dans les systèmes support-vie (PhD Thesis).

Poulet, L., Dussap, C.-G., Fontaine, J.-P., 2020. Development of a mechanistic model of leaf surface gas exchange coupling mass and energy balances for life-support systems applications. Acta Astronaut. 175, 517–530. https://doi.org/10.1016/j.actaastro.2020.03.048

Poulet, L., Fontaine, J.-P., Dussap, C.-G., 2018. A Physical Modeling Approach for Higher Plant Growth in Reduced Gravity Environments. Astrobiology 18, 1093–1100. https://doi.org/10.1089/ast.2017.1804

References

Raghav, P., Kumar, M., Liu, Y., 2024. Structural Constraints in Current Stomatal Conductance Models Preclude Accurate Prediction of Evapotranspiration. Water Resour. Res. 60, e2024WR037652. https://doi.org/10.1029/2024WR037652

Ramirez, C., Murray, D.B., Fitzpatrick, J.A., 2002. CONVECTIVE HEAT TRANSFER OF AN INCLINED RECTANGULAR PLATE. Exp. Heat Transf. 15, 1–18. https://doi.org/10.1080/089161502753341834

Reid, R.C., Prausnitz, J.M., Sherwood, T.K., 1977. The properties of gases and liquids, 3. ed. ed, McGraw-Hill chemical engineering series. McGraw-Hill, New York.

Salisbury, F.B., Gitelson, J.I., Lisovsky, G.M., 1997. Bios-3: Siberian Experiments in Bioregenerative Life Support. BioScience 47, 575–585. https://doi.org/10.2307/1313164

Samsonov, N.M., Bobe, L.S., Novikov, V.M., Farafonov, N.S., Amiragov, M.S., Pinsky, B.Ja., Grigoriev, Ju.I., Romanov, S.Ju., Protasov, N.N., Sinyak, Ju.E., Baranov, V.M., 2000. Experience in Development and Operation of a Regenerative System for Water Supply on Mir Space Station. Presented at the International Conference On Environmental Systems, pp. 2000-01–2517. https://doi.org/10.4271/2000-01-2517

Sasidharan L., S., 2012a. Modélisation de la croissance des plantes supérieures pour les systèmes de support-vie : modèle métabolique de la feuille de laitue considérant la conversion d'énergie et le métabolisme central du carbone (PhD Thesis).

Sasidharan L., S., 2012b. Modélisation de la croissance des plantes supérieures pour les systèmes de support-vie : modèle métabolique de la feuille de laitue considérant la conversion d'énergie et le métabolisme central du carbone (PhD Thesis).

Sauer, R.L., Calley, D.J., Center (U.S.), M.S., 1973. Apollo Experience Report: Potable Water System, NASA TN D-7291. National Aeronautics and Space Administration.

Schymanski, S.J., Breitenstein, D., Or, D., 2017. Technical note: An experimental set-up to measure latent and sensible heat fluxes from (artificial) plant leaves. Hydrol. Earth Syst. Sci. 21, 3377–3400. https://doi.org/10.5194/hess-21-3377-2017

Schymanski, S.J., Or, D., 2016. Wind increases leaf water use efficiency. Plant Cell Environ. 39, 1448–1459. https://doi.org/10.1111/pce.12700

Smith, M., Craig, D., Herrmann, N., Mahoney, E., Krezel, J., McIntyre, N., Goodliff, K., 2020. The Artemis Program: An Overview of NASA's Activities to Return Humans to the Moon, in: 2020 IEEE Aerospace Conference. Presented at the 2020 IEEE Aerospace Conference, IEEE, Big Sky, MT, USA, pp. 1–10. https://doi.org/10.1109/AERO47225.2020.9172323

Steele, J.M., 2015. Babylonian Observational and Predictive Astronomy, in: Ruggles, C.L.N. (Ed.), Handbook of Archaeoastronomy and Ethnoastronomy. Springer New York, New York, NY, pp. 1855–1862. https://doi.org/10.1007/978-1-4614-6141-8_191

Stoiko, M., 1971. Soviet rocketry: the first decade of achievement. David & Charles, Newton Abbot, Eng.

Sunarseh, Daningsih, E., n.d. Analysis of Stomatal Number and Size in Six Species of Monocotiledon Plants. Presented at the Proceedings of KOBI 2nd International Conference on Management of Tropical Biodiversity for Human Welfare: From Ecosystem to Molecular, pp. 133–122. https://doi.org/10.29007/dndz

Tako, Y., Arai, R., Tsuga, S., Komatsubara, O., Masuda, T., Nozoe, S., Nitta, K., 2010. CEEF: closed ecology experiment facilities. Gravitational Space Res. 23.

Tesfamichael, T., Hoel, A., Niklasson, G.A., Wäckelgård, E., Gunde, M.K., Orel, Z.C., 2001. Optical characterization method for black pigments applied to solar-selective absorbing paints. Appl. Opt. 40, 1672. https://doi.org/10.1364/AO.40.001672

Tian, H., Zhang, T., Jia, Y., Peng, S., Yan, C., 2021. Zhurong: Features and mission of China's first Mars rover. The Innovation 2, 100121. https://doi.org/10.1016/j.xinn.2021.100121

TOKUDA, A., KITAYA, Y., HIRAI, H., HASHIMOTO, H., INATOMI, Y., 2018. Effects of Gravity on Stem Sap Flow and Water and Heat Exchange in the Leaves of Sweetpotato. https://doi.org/10.15011/jasma.35.3.350302

Vivin K., D., Daningsih, E., n.d. Description of Stomatal Sizes and Types From Several Shading and Ornamental Plants In Pontianak West Kalimantan. Presented at the Proceedings of KOBI 2nd International Conference on Management of Tropical Biodiversity for Human Welfare: From Ecosystem to Molecular, pp. 149–139. https://doi.org/10.29007/7hx3

Wang, C., Jia, Y., Xue, C., Lin, Y., Liu, J., Fu, X., Xu, L., Huang, Y., Zhao, Y., Xu, Y., Gao, R., Wei, Y., Tang, Y., Yu, D., Zou, Y., 2024. Scientific objectives and payload configuration of the Chang'E-7 mission. Natl. Sci. Rev. 11, nwad329. https://doi.org/10.1093/nsr/nwad329

Wang, M., Wei, H., Jeong, B.R., 2021. Lighting Direction Affects Leaf Morphology, Stomatal Characteristics, and Physiology of Head Lettuce (Lactuca sativa L.). Int. J. Mol. Sci. 22, 3157. https://doi.org/10.3390/ijms22063157

Wheeler, R., Sager, J., Prince, R., Knott, W., Mackowiak, C., Stutte, G., Yorio, N., Ruffe, L., Peterson, B., Goins, G., 2003. Crop Production for Advanced Life Support Systems - Observations From the Kennedy Space Center Breadboard Project.

Wheeler, R.M., 2009. Roadmaps and strategies for crop research for bioregenerative life support systems a compilation of findings from NASA's Advanced life support meetings.

Wheeler, R.M., Fitzpatrick, A.H., Tibbitts, T.W., 2019. Potatoes as a Crop for Space Life Support: Effect of CO2, Irradiance, and Photoperiod on Leaf Photosynthesis and Stomatal Conductance. Front. Plant Sci. 10, 1632. https://doi.org/10.3389/fpls.2019.01632

Wheeler, R.M., Mackowiak, C.L., Stutte, G.W., Sager, J.C., Yorio, N.C., Ruffe, L.M., Fortson, R.E., Dreschel, T.W., Knott, W.M., Corey, K.A., 1996. NASA's biomass production chamber: A testbed for bioregenerative life support studies. Adv. Space Res. 18, 215–224. https://doi.org/10.1016/0273-1177(95)00880-n

Williamson, M., 2006. Spacecraft technology: the early years, IEE history of technology series. Institution of Electrical Engineers, London.

Winkler, H.E., Cerna, N.F., Rotter, H.A., Ouellette, F.A., Hoy, D.M., Brasseaux, H.J., 1996. Shuttle Orbiter Environmental Control and Life Support System-Flight Experience. Presented at the International Conference On Environmental Systems, p. 961334. https://doi.org/10.4271/961334

Xu, L., Zou, Y., Jia, Y., 2018. China's Planning for Deep Space Exploration and Lunar Exploration before 2030. Chin. J. Space Sci. 38, 591. https://doi.org/10.11728/cjss2018.05.591

Xu, Z., Jiang, Y., Jia, B., Zhou, G., 2016. Elevated-CO2 Response of Stomata and Its Dependence on Environmental Factors. Front. Plant Sci. 7. https://doi.org/10.3389/fpls.2016.00657

Yuan, Ming, Custaud, M.-A., Xu, Z., Wang, J., Yuan, Min, Tafforin, C., Treffel, L., Arbeille, P., Nicolas, M., Gharib, C., Gauquelin-Koch, G., Arnaud, L., Lloret, J.-C., Li, Y., Navasiolava,

N., 2019. Multi-System Adaptation to Confinement During the 180-Day Controlled Ecological Life Support System (CELSS) Experiment. Front. Physiol. 10, 575. https://doi.org/10.3389/fphys.2019.00575

Zhang, H., Zhao, Y., Zhu, J.-K., 2020. Thriving under Stress: How Plants Balance Growth and the Stress Response. Dev. Cell 55, 529–543. https://doi.org/10.1016/j.devcel.2020.10.012

Zou, Y., Zhu, Y., Bai, Y., Wang, L., Jia, Y., Shen, W., Fan, Y., Liu, Y., Wang, C., Zhang, A., Yu, G., Dong, J., Shu, R., He, Z., Zhang, T., Du, A., Fan, M., Yang, J., Zhou, B., Wang, Y., Peng, Y., 2021. Scientific objectives and payloads of Tianwen-1, China's first Mars exploration mission. Adv. Space Res. 67, 812–823. https://doi.org/10.1016/j.asr.2020.11.005

9 Appendix

A Technical drawing of the rack

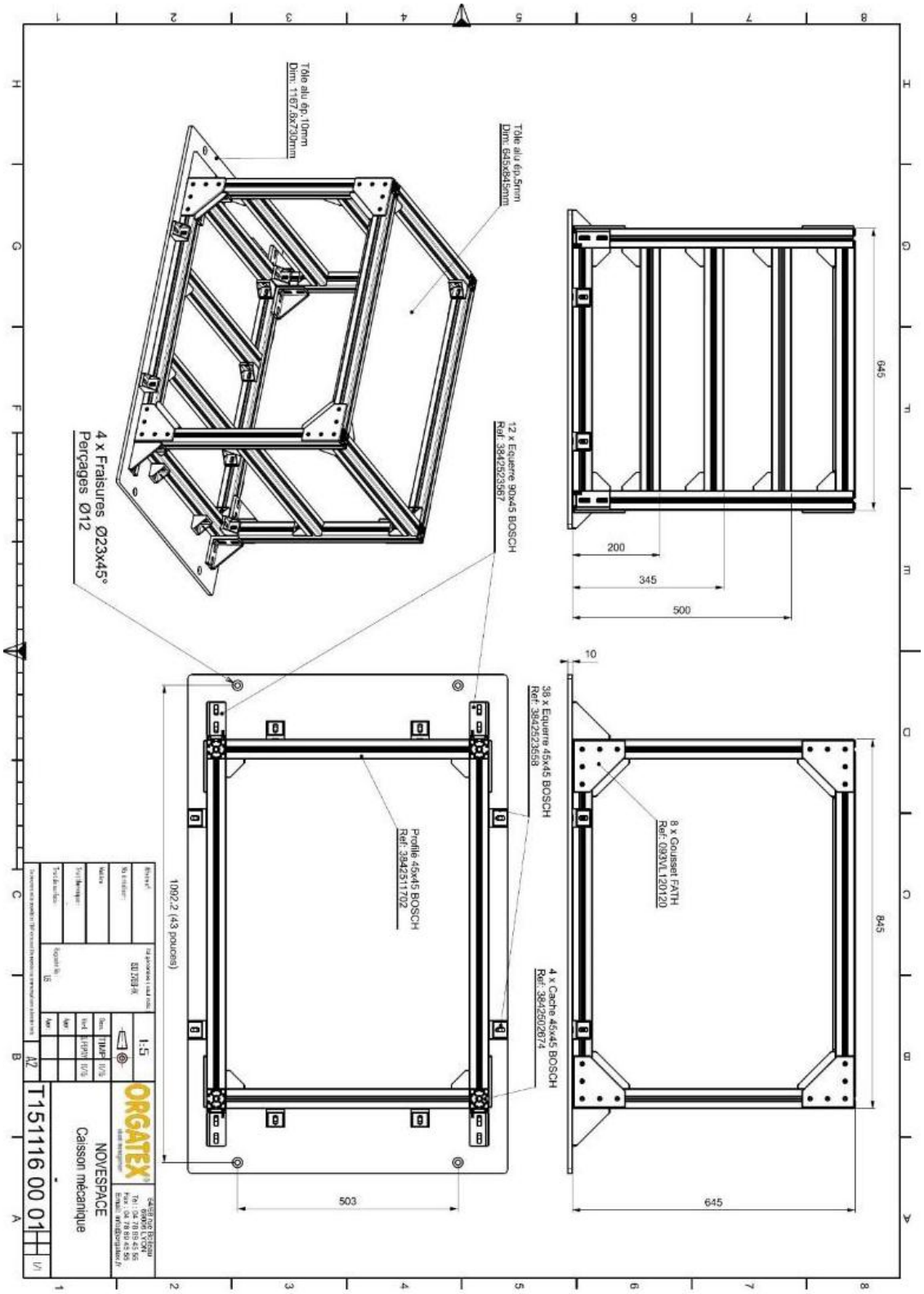

B Technical drawing of the experimental unit

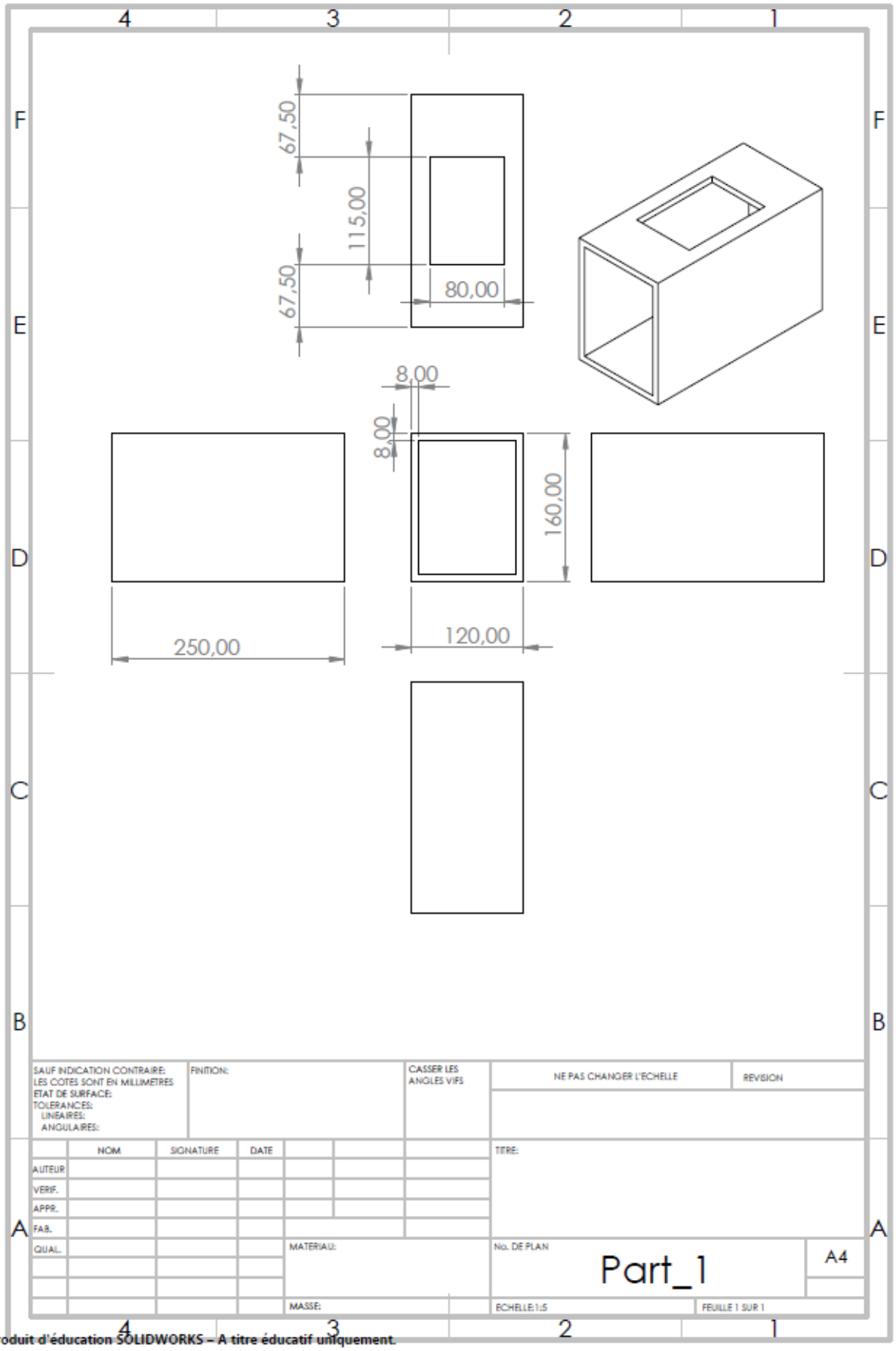

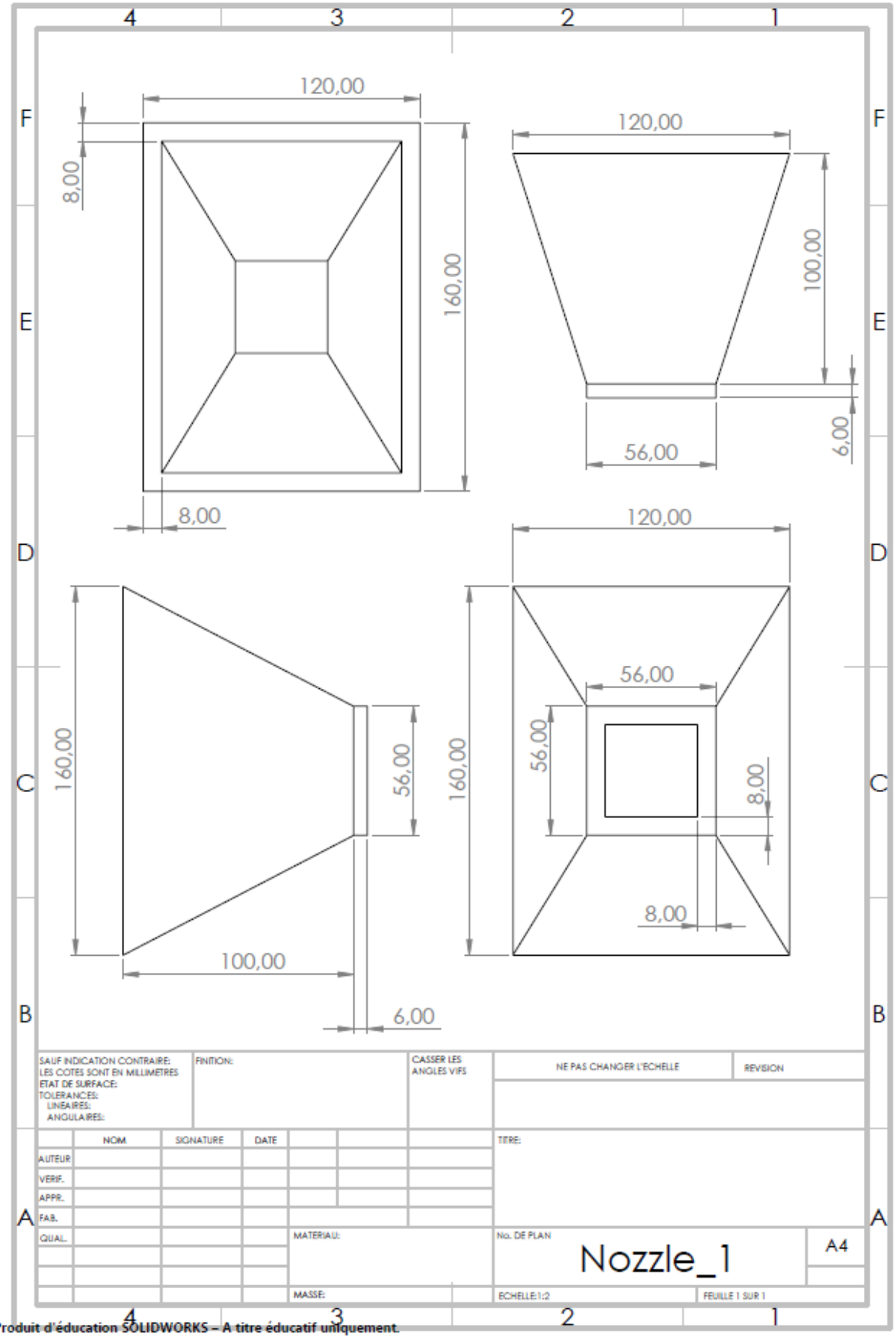

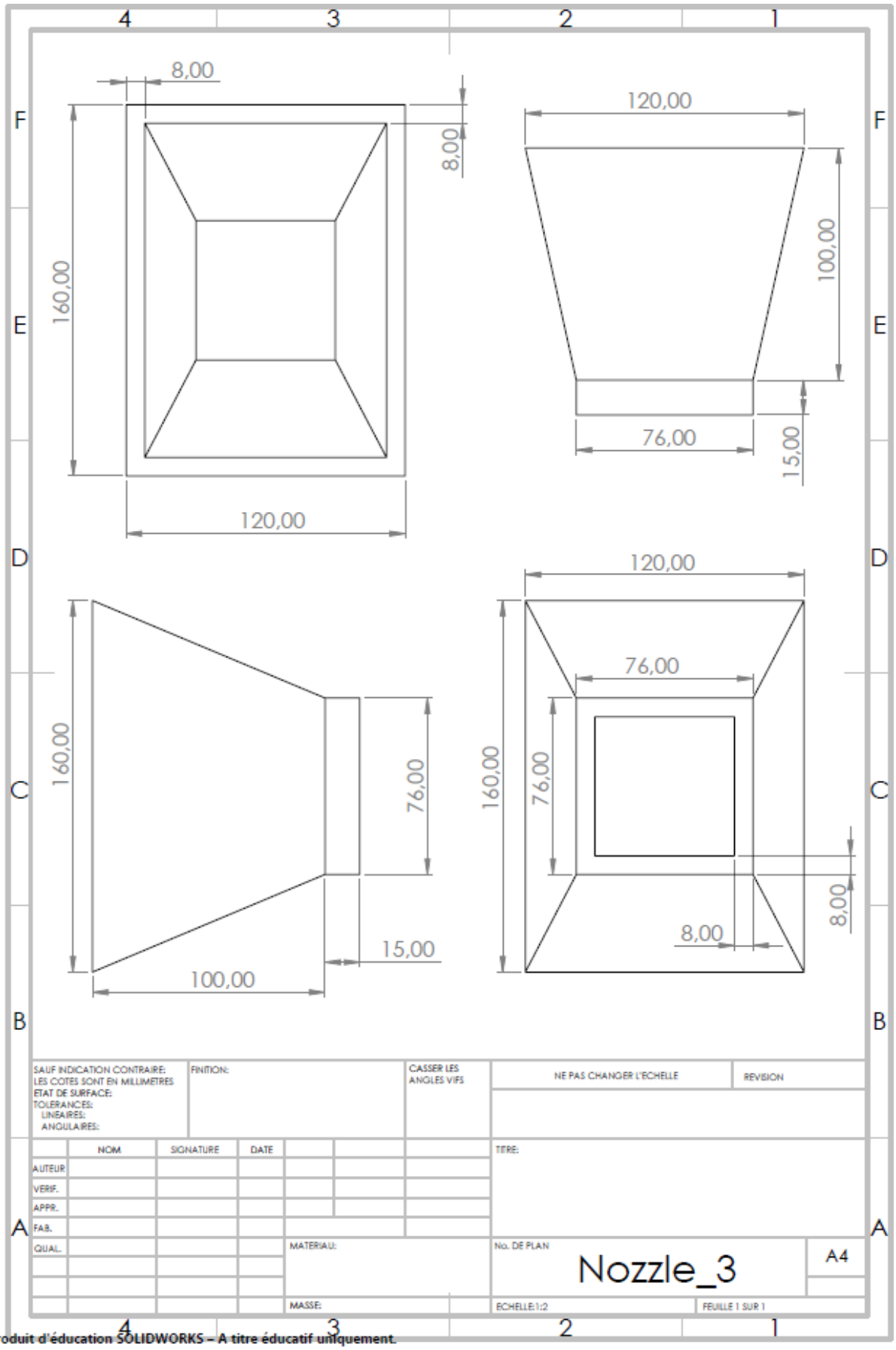

C Equations used for leaf replica conductance calculations

The calculations are based on the procedure described in Appendix A of

The total molar stomatal conductance is calculated from two main resistances:

1. Throat Resistance: due to diffusion through the pore itself
2. Vapor Shell Resistance: due to diffusion into the surrounding air

Molar pores conductance can be calculated:

$$g_{sw,mol} = \frac{1}{r_{sp} + r_{vs}}$$

Where:

r_{sp} - diffusive resistance of a pore [s·m2·mol^{-1}]

r_{vs} - Diffusive resistance of a pores vapour shell [s·m2·mol^{-1}]

$g_{sw,mol}$ - molar stomatal conductance [mol·m^{-2}·s^{-1}]

Mean radius of the conical pore:

$$r_{mean} = \frac{r_{top} + r_{bottom}}{2}$$

Where:

r_{mean} – average radius of the conical pore [m]

r_{top} - radius at the top of the pore [m]

r_{bottom} - - radius at the bottom of the pore [m]

Cross-sectional area of the pore is calculated with the equation:

$$A_p = \pi \cdot r_{mean}^2$$

Where:

A_p - cross-sectional area of the pore [m^2]

Pore density is calculated with the equation:

$$n_p = \frac{1}{spacing^2}$$

Where:

n_p - pore density [m^{-2}]

$spacing$ – spacing between the centres of the pores [m]

Spacing between pores is calculated with the equation:

$$s_p = \frac{1}{\sqrt{n_p}}$$

Where:

s_p - spacing between porous [m]

Diffusivity per unit molar volume is calculated with the equation:

$$k_{dv} = \frac{D_{va}}{V_m}$$

Where:

k_{dv} - diffusivity per unit molar volume [mol·m^{-1}·s^{-1}]

D_{va} - diffusivity of water vapor in air – $2.5 \cdot 10^{-5}$ [m^2·s]

V_m - Molar volume of air – 0.0245 [m^3·mol^{-1}]

Diffusive resistance of a pore is calculated with the equation:

$$r_{sp} = \frac{d_p}{A_p \cdot k_{dv} \cdot n_p}$$

Where:

d_p – pore depth [m]

Diffusive resistance of a pores vapour shell is calculated with the equation:

$$r_{vs} = \left(\frac{1}{4 \cdot r_{mean}} - \frac{1}{\pi \cdot s_p}\right)\frac{1}{k_{dv} \cdot n_p}$$

Pores conductance to water vapour is calculated with the equation:

$$g_{sw} = g_{sw,mol}\frac{R \cdot T}{P}$$

Where:

g_{sw} – pores conductance to water vapour [m·s^{-1}]

R – gas constant – 8.314 [J·mol^{-1}·K^{-1}]

T – temperature [K]

P – pressure [Pa]

D Calibration data for the anemometers

Vr: Reference velocity (m/s)

Vi: Average of the multimeter readings (V)

Vi conv: Average of the indicated velocities (m/s)

St Dev: Standard deviation calculated from the 3 values (m/s)

Error: Difference between Vi conv and Vr (m/s)

Uncertainty: Calibration uncertainty on the deviation (m/s)

Vr (m/s)	Vi (m/s)	Vi conv (m/s)	St Dev (m/s)	Error (Vi - Vr) (m/s)	Uncertainty (m/s)
0,080	2,113	0,081	0,007	0,001	0,025
0,221	2,256	0,218	0,010	-0,003	0,029
0,511	2,391	0,511	0,005	0,000	0,027
0,755	2,470	0,761	0,003	0,006	0,028
0,988	2,530	0,984	0,001	-0,004	0,030

Table 9-1 *Calibration data for the anemometer 1*

Vr (m/s)	Vi (V)	Vi conv (m/s)	St Dev (m/s)	Error (Vi - Vr) (m/s)	Uncertainty (m/s)
0,104	2,061	0,102	0,001	-0,002	0,021
0,229	2,209	0,235	0,012	0,006	0,033
0,508	2,327	0,505	0,020	-0,003	0,047
0,751	2,401	0,745	0,011	-0,006	0,035
0,976	2,460	0,981	0,005	0,005	0,031

Table 9-2 *Calibration data for the anemometer 2*

Vr (m/s)	Vi (V)	Vi conv (m/s)	St Dev (m/s)	Error (Vi - Vr) (m/s)	Uncertainty (m/s)
0,122	2,091	0,124	0,007	0,002	0,026
0,252	2,229	0,245	0,013	-0,007	0,034
0,516	2,361	0,526	0,008	0,010	0,029
0,762	2,435	0,756	0,001	-0,005	0,028
0,982	2,496	0,983	0,005	0,000	0,031

Table 9-3 *Calibration data for the anemometer 3*

Vr (m/s)	Vi (V)	Vi conv (m/s)	St Dev (m/s)	Error (Vi - Vr) (m/s)	Uncertainty (m/s)
0,094	2,147	0,090	0,002	-0,004	0,021
0,224	2,316	0,240	0,014	0,015	0,035
0,509	2,429	0,495	0,008	-0,013	0,030
0,752	2,508	0,747	0,013	-0,005	0,038
0,987	2,571	0,995	0,006	0,007	0,033

Table 9-4 *Calibration data for the anemometer 4*

E Angle and air velocity sequence during parabolic flight campaigns

Table 9-5 *Order of tested values inside all units during each day of the 1st parabolic flight campaign*

Day 1							
airflow [m/s]		0.5	0.15	0.5	0.25	0.3	0.25
angle sequence [°]	**Unit 1**	30, -30, 30, 0, -30	15, 0, -15, -30, 30	-30, 30, 30, 0, -30	-25, 25, -5, 25, 5	-15, 15, -15, 15, 15	5, 25, 5, -25, -5
	Unit 4	30, -30, -30, 0, 30	0, -30, -15, 30, 15	0, 30, -30, -30, 0	25, -25, -5, 5, -25	-15, 15, -15, -15, 15	25, -5, -25, -5, 5
airflow [m/s]		0	0.15	0.05	0.15	0.05	0
angle sequence [°]	**Unit 2**	15, -15, 15, -15, 0	15, -15, 30, 0, -30	-5, -25, -5, 25, 5	-25, -5, -25, 25, 5	15, -15, -15, 15, 0	15, -15, 30, -30, 0
	Unit 3	15, -15, 0, -15, 15	15, -20, -15, 30, 0	-25, 5, 5, 25, -5	25, 25, -25, 5, -5	-15, 15, 0, 15, -15	30, -30, -15, 0, 15
Day 2							
airflow [m/s]		0.15	0.3	0.25	0.5	0.25	0.25
angle sequence [°]	**Unit 1**	-30, 30, -15, 15, 15	15, 15, -15, 15, -15	25, -25, -5, 25, 5	-30, 30, 0, 30, 0	-25, 25, -5, 5, 5	25, -5, 5, 5, -25
	Unit 4	15, 30, -15, -15, 30	-15, 15, -15, 15, -15	-25, 25, 5, -5, -25	-30, 0, 30, 0, -30	-5, 25, -25, 5, -5	5, -5, -5, -25, 25
airflow [m/s]		0	0.05	0.15	0.05	0.15	0.05
angle sequence [°]	**Unit 2**	15, -15, 0, -15, 15	-5, 25, 5, -25, 25	-30, 15, -15, 30, 30	5, 25, -5, 5, -25	-15, 0, -30, 15, 30	25, -5, 5, -25, 25
	Unit 3	15, -15, -15, 15, 0	-5, 5, 25, -25, 25	15, -30, 0, 30, -30	5, -5, -25, -5, 25	-30, 15, 30, 0, -15	5, 25, -25, -5, -25
Day 3							
airflow [m/s]		0.5	0.15	0.25	0.3	0.25	0.3
angle sequence [°]	**Unit 1**	30, -30, 30, 0, -30	30, 0, -30, -15, 15	25, 5, -5, -25, 5	15, -15, 15, -15, 15	25, 5, -25, -5, 25	-15, -15, 15, 15, 15
	Unit 4	30, -30, 30, -30, 0	-30, -15, 30, 0, 15	5, 25, -25, -5, -5	-15, -15, 15, 15, -15	5, -25, 25, -5, -25	-15, 15, -15, 15, -15
airflow [m/s]		0.15	0.05	0.15	0	0.05	0
angle sequence [°]	**Unit 2**	30, -30, 15, -15, 0	5, 25, 5, -5, -25	-15, 0, -30, 30, 15	0, 0, 15, -15, 15	25, 5, -5, 5, -25	0, 15, 0, 15, -15
	Unit 3	30, 15, -15, 0, -30	5, -5, 25, -5, -25	15, -30, -15, 30, 0	0, 15, -15, 0, -15	25, -5, -5, -25, 5	-15, 0, 0, -15, 15

Table 9-6 *Order of tested values inside all units during each day of the 2nd parabolic flight campaign*

Day 1							
airflow [m/s]		0.3	0	0.15	0	0.3	0.15
angle sequence [°]	**Unit 1**	15, -30, 30, 0, -15	-30, 30, -15, 15, 0	-15, 30, 15, 0, -30	0, -30, -15, 15, 30	-15, 30, 0, 15, -30	-15, 15, 0, 30, -30
	Unit 4	-15, 15, -30, 0, 30	-15, -30, 15, 0, 30	15, 0, -30, -15, 30	30, 15, -30, 0, -15	0, 15, 30, -15, -30	30, -30, -15, 0, 15
airflow [m/s]		0.15	0	0.15	0.05	0	0.05
angle sequence [°]	**Unit 2**	-15, 0, 15, 30, -30	-15, 15, 0, 30, -30	-30, 15, 30, 0, -15	-30, 0, 15, -15, 30	-30, 15, -15, -30, 15	30, 0, -15, -30, 15
	Unit 3	15, -15, 30, -30, 0	30, -30, -15, 0, 15	-30, 30, 15, 0, -15	30, -15, 0, 15, -30	0, -15, 15, 30, -30	-30, -15, 30, 15, 0
Day 2							
airflow [m/s]		0.15	0	0.3	0	0.3	0.15
angle sequence [°]	**Unit 1**	30, -30, 0, 15, -15	15, 30, -15, 0, -30	-15, 0, -30, 30, 15	15, 0, 30, -30, -15	0, 30, -15, -30, 15	-30, 15, 30, -15, 0
	Unit 4	-15, -30, 0, 15, 30	0, -30, 15, -15, 30	30, -30, 15, -15, 0	15, -15, -30, 0, 30	30, -15, 15, 0, -30	-30, 30, -15, 15, 0
airflow [m/s]		0.15	0	0.05	0	0.05	0.15
angle sequence [°]	**Unit 2**	-15, -30, 30, 15, 0	-30, -15, 15, 0, 30	15, -15, 30, -30, 0	0, -30, 30, -15, 15	-30, 30, -15, 15, 0	0, 15, 30, -30, -15
	Unit 3	-30, 0, -15, 30, 15	-15, 30, 0, 15, -30	-30, -15, 15, 0, 30	30, -30, 0, 15, -15	15, 0, 30, -15, -30	30, -15, -30, 0, 15
Day 3							
airflow [m/s]		0.15	0.15	0	0.3	0	0.3
angle sequence [°]	**Unit 1**	30, 0, -30, -15, 15	-15, -30, 30, 0, 15	15, 30, -15, -30, 0	-30, -15, 30, 15, 0	0, -15, -30, 30, 15	15, 0, -30, -15, 30
	Unit 4	0, -30, -15, 30, -15	-30, 0, 30, 15, -15	-15, 15, -30, 30, 0	15, -15, 0, 30, -30	15, 30, 0, -30, -15	30, -30, 0, -15, 15
airflow [m/s]		0.15	0	0	0.05	0.15	0.05
angle sequence [°]	**Unit 2**	30, 15, -15, -30, 0	-15, 30, -30, 0, 15	15, 30, 0, -15, -30	-15, 0, 30, -30, 15	-15, 30, 0, -30, 15	-30, -15, 0, 15, 30
	Unit 3	-30, 0, -15, 15, 30	0, 30, -30, 15, -15	-15, 15, -30, 30, 0	-15, 30, 15, -30, 0	15, -30, 0, -15, 30	-30, 0, 30, -15, 15

F List of publications and conferences attended

Publications

Joanna Kuzma; Lucie Poulet; Jean-Pierre Fontaine; Claude-Gilles Dussap
Modelling physical processes in higher plants using leaf replicas for space applications. Comptes Rendus. Mécanique, Online first (2023), pp. 1-17. doi : 10.5802/crmeca.152

Joanna Kuzma; Jean-Pierre Fontaine; Lucie Poulet; Claude-Gilles Dussap
Main focusses on the use of higher plant growth models for life support systems; 51st International Conference on Environmental Systems (ICES 2022) Saint Paul (USA) 10th – 14th, 2022; https://hdl.handle.net/2346/89773

Conferences

Joanna Kuzma; Lucie Poulet; Alexis Paillet; Jean-Pierre Fontaine; Francesc Godia-Casablancas, Claude-Gilles Dussap (2024)
Heat and mass transfer study between a leaf replica and its environment in parabolic flight experiments
American Society for Gravitational and Space Research (ASGSR 2024), Conference, San Juan, Dec. 3th – 7th, 2024

Joanna Kuzma; Lucie Poulet; Jean-Pierre Fontaine; Francesc Godia-Casablancas, Claude-Gilles Dussap (2024)
Investigating heat and mass exchange between a leaf replica and Its environment in microgravity conditions
Journée scientifique du Comité de Développement du Génie des Procédés en Région Rhône Alpes Auvergne (CODEGEPRA), Villeurbanne, Nov. 28th, 2024

Joanna Kuzma; Jean-Pierre Fontaine; Lucie Poulet; Claude-Gilles Dussap (2023)
An experimental platform to study heat and mass exchange between the plants and the environment in microgravity conditions
Space Ecology Workshops, virtual, Oct. 13th – 14th, 2023

Joanna Kuzma; Jean-Pierre Fontaine; Lucie Poulet; Claude-Gilles Dussap (2022)
Modelling physical processes in higher plants using leaf replicas for space applications
MELiSSA Conference, Toulouse, Nov. 7th – 10th, 2022

Joanna Kuzma; Jean-Pierre Fontaine; Lucie Poulet; Claude-Gilles Dussap (2022)
Main focusses on the use of higher plant growth models for life support systems
51st International Conference on Environmental Systems (ICES 2022), Saint Paul 10th – 14th, 2022